

UNIVERSITY OF SOUTHAMPTON

**A HIGH ENERGY STUDY
OF ACTIVE GALACTIC NUCLEI**

by Angela Malizia

Doctor of Philosophy

Faculty of Science
Department of Physics and Astronomy

ACKNOWLEDGMENTS

It is a great pleasure for me to thank Loredana Bassani (more than a tutor), Professor Tony Dean, Guido Di Cocco and Giorgio Palumbo. I would not have been able to carry out this Ph.D. work without their strong encouragement and support during these years. I am very glad to have had their supervision and their precious advice, they are all for me models of professionalism and scientific passion.

I am grateful to the Science Faculty and the Physics Department of the University of Southampton as well as to the British Council for their financial support.

How can I forget Tony Bird who helped me a lot during my stay in Southampton, most of all for his efforts to explain to me the English life-style?

Special thanks go to my current colleagues in TeSRE-CNR in particular to John Stephen for his contribution to the evaluation of the BATSE systematic errors and his help in checking my English and to Marco Malaspina for his support in the implementation of the BATSE analysis package at TeSRE (at that time it was very difficult to work on BATSE data). Thanks also to the Director N. Mandolesi for his hospitality at TeSRE in the past few years, Massimo Cappi for his useful discussions, Pino Malaguti and Stefano Silvestri. Furthermore, I acknowledge the help of the BATSE team in Huntsville in particular Alan Harmon, Nan Zhang, Valerie Connaughton, Michael McCollough and Bill Paciesas who taught me all about the BATSE data analysis.

Another special thanks must go to Fabrizio Fiore and Paolo Giommi at BeppoSAX-SDC in Roma who gave me the opportunity to enjoy one of the most exciting professional experiences of my life.

Finally I would like to thank my husband Galileo because he was always close to me during these hard years of study, patiently waiting for me to arrive, first from Southampton then from Roma and encouraging me during my long stay far from home. Thanks also to my parents and to my entire family whose love and support has been so important during these busy years. But most of all my thanks to my baby who has shared his mother with a computer during his first year of life.

Thank you Andrea, this is dedicated to you.

UNIVERSITY OF SOUTHAMPTON

ABSTRACT

FACULTY OF SCIENCE
PHYSICS AND ASTRONOMY

Doctor of Philosophy

**A HIGH ENERGY STUDY
OF ACTIVE GALACTIC NUCLEI**

by Angela Malizia

This thesis contains a study of the hard X-ray properties of active galactic nuclei. The results have been obtained from the analysis of data sets from two different satellites: ComptonGRO-BATSE and BeppoSAX-PDS. The source sample used for this investigation is the Piccinotti sample of AGN, which is an X-ray selected sample and up to now the only complete sample in the 2-10 keV band. Nearly four years of BATSE observations have been analyzed to search for emission in the 20-100 keV band from all the sources and for the first time the whole sample was observed at higher energies, with most giving significant detections. Average fluxes have been estimated over the observing period while long term variability has been investigated for the brightest sources. The high-energy spectral characteristics of the Piccinotti sample have been studied using the BeppoSAX-PDS data in 20-200 keV band. With this analysis both the Compton reflection and the high energy cut-off have been investigated: both components are required by the high energy data; they are well constrained in the brightest sources (NGC4151 and IC4329A). Finally BeppoSAX MECS data together with the PDS data have been used to study the average 3-200 keV spectra of Seyfert 1 and Seyfert 2 galaxies in order to investigate their average spectral characteristics and the possible differences between the two classes. If an extra absorber that partially covers the source is added to the Seyfert 2 average spectrum then the primary continuum of both type of Seyferts is found to be similar: a power law with photon index 1.9 a reflection of ~ 1 and a high energy cut-off at around 200 keV.

Contents

| | | |
|----------|-----------------------------------------------------------------------------|-----------|
| 1 | AGNs | 7 |
| 1.1 | Introduction | 7 |
| 1.2 | Studies in the Hard X-Ray Band | 9 |
| 2 | BATSE | 15 |
| 2.1 | The Compton Gamma Ray Observatory | 15 |
| 2.2 | BATSE | 16 |
| 2.2.1 | BATSE Instrumentation | 17 |
| 2.2.2 | Data Selection | 18 |
| 2.3 | The Occultation Technique | 19 |
| 2.3.1 | Sensitivity | 21 |
| 2.3.2 | Systematic errors | 22 |
| 2.4 | Occultation Imaging | 24 |
| 2.5 | BATSE observations of AGN | 25 |
| 2.5.1 | BATSE observation of the high-redshift quasar 4C 71.07 | 28 |
| 3 | BeppoSAX | 33 |
| 3.1 | The satellite and the scientific instruments | 33 |
| 3.2 | The Phoswich Detector System | 35 |
| 3.3 | BeppoSAX scientific capabilities and its success of four years of mission . | 37 |
| 3.4 | BeppoSAX and AGN studies | 38 |
| 4 | BATSE OBSERVATIONS OF THE PICCINOTTI SAMPLE OF AGN | 47 |
| 4.1 | The Piccinotti Sample of AGN | 47 |
| 4.2 | BATSE Observations | 50 |
| 4.2.1 | <i>Systematic errors</i> | 51 |
| 4.3 | Results and Discussion | 56 |
| 4.4 | BATSE Light Curves | 58 |

| | | |
|----------|-----------------------------------------------------------------------|------------|
| 5 | BeppoSAX-PDS OBSERVATION OF THE PICCINOTTI SAMPLE | 69 |
| 5.1 | Introduction | 69 |
| 5.2 | Data Analysis | 70 |
| 5.3 | PDS Light Curves | 76 |
| 5.3.1 | <i>Results on variability</i> | 76 |
| 5.4 | PDS Spectra of the Piccinotti Sample | 79 |
| 5.4.1 | <i>Results of the spectral analysis of Seyfert galaxies</i> | 84 |
| 5.4.2 | <i>MCG-01-24-12</i> | 94 |
| 5.5 | Blazars | 95 |
| 5.5.1 | <i>3C273</i> | 98 |
| 5.5.2 | <i>MKN501</i> | 99 |
| 6 | BeppoSAX AVERAGE SPECTRA OF SEYFERT GALAXIES | 105 |
| 6.1 | Introduction | 105 |
| 6.2 | Average Spectra | 106 |
| 6.3 | Results of the average spectra | 107 |
| 6.4 | Discussion | 113 |
| 7 | Conclusions | 123 |
| 7.1 | BATSE results | 123 |
| 7.2 | <i>BeppoSAX</i> results | 125 |
| 7.3 | <i>BeppoSAX</i> average spectra | 127 |
| A | PDS Light Curves | 131 |
| B | PDS Spectra | 141 |

List of Figures

| | | |
|-----|-------------------------------------------------------------------------------------------------------------------------------------------------------------------------------------------------------------------------------------------------------------------------------------------------------------------------------------------------------------------------------------------------------------------------------------------------------------------------------------------------------------------------------------------------------------------------------------------------------------------------------------------------|----|
| 2.1 | The Compton Gamma Ray Observatory with the four instruments | 16 |
| 2.2 | Left: the co-alignment of the principal axes of the Compton Gamma Ray Observatory with the octahedron geometry of the BATSE detectors; Right: Pictorial representation of a BATSE detector module. | 17 |
| 2.3 | Sketch of the Earth Occultation Technique | 20 |
| 2.4 | Sensitivity (3σ) for a two week observation of a source averaging 16 occultations a day with contributions from two LADs, as a function of energy (Harmon et al. 2001) .The Crab Nebula total emission spectrum measured with HEAO-A4 experiment has been also reported for comparison. | 22 |
| 2.5 | Left: Sky region around Crab Nebula. Superimposed are shaded regions which are the portion of the sky subject to Earth occultation when the Earth's limb crosses the Crab. Sources which are routinely monitored by BATSE are also shown. Right: Angle between the closest approach points of a given source location, here 4U 0614+091, with the rising (top panel) and setting (middle panel) limbs of the Crab Nebula as a function of time. The corresponding light curve of 4U 0614+091 for the same period is also shown (bottom panel). Note that the setting limb of the Crab periodically crosses the location of 4U 0614+091. | 24 |
| 2.6 | Examples of BATSE images. On the left a $20^\circ \times 20^\circ$ image of the Sey2 galaxy NGC7582 obtained integrating 9 days of data (from TJD 8460 to TJD 8469). On the right a more accurate $10^\circ \times 10^\circ$ image of the high redshift quasar 4C71.07 obtained summing 35 days of data (from TJD 10,099 to TJD 10,134). | 25 |
| 2.7 | BATSE long term light curve of Cen A. The light curve plots 50 day average flux measurements over the period 1991-1998 (Westmore et al. 2000b). . | 27 |

| | | |
|-----|--------------------------------------------------------------------------------------------------------------------------------------------------------------------------------------------------------------------------------------------------------------------------------------------------------------------------------------------------------------------------------------------------------------------------------------------------------------------------------------------------------------------------------------------------------------------------------|----|
| 2.8 | Left: BATSE light curve over 3 years period; each bin corresponds to a 60 days integration time. The crosses superimposed on the BATSE data correspond to optical (R band) measurements; the optical minimum has been set to $R = 17.4$ based on von Linde et al. (1993) results. The two vertical lines indicate the period of the OSSE observation. Right: OSSE count spectrum with residuals for a simple power-law of slope $\Gamma=1.1\pm0.3$. | 29 |
| 2.9 | Overall spectral energy distribution of 4C71.07 adapted from Ghisellini et al. (1998) plus BATSE and OSSE measurements from Malizia et al. (2000) and V data point from McIntosh et al. (1999). The 12, 25 and 60 micron upper limits have been estimated by comparison with IRASFSC catalogue data obtained from objects located within 4 degrees of the QSO. The SSC and EC models are superimposed on the data as dotted and dashed lines respectively. | 31 |
| 3.1 | <i>BeppoSAX</i> payload accommodation | 34 |
| 3.2 | <i>BeppoSAX</i> broad band spectrum of the Seyfert 2 Mkn3 compared with the bright QSO 3C273 (Bassani et al. 1999) | 42 |
| 3.3 | 0.01-100 keV spectra of Mkn421 during three <i>BeppoSAX</i> observations multiplied by the frequency. | 44 |
| 4.1 | BATSE 20-100 keV weighted mean fluxes over ~ 3 years of observations with their relative errors, are plotted against 2-10 keV average fluxes. The horizontal bars in the figure are the 2-10 keV flux ranges (minimum and maximum value found in the literature). Lines plotted correspond to the ratio between fluxes expected for various values of photon index under the hypothesis of a single power law continuum from 2 to 100 keV. Although 3C445 has a slope flatter than 1.5, this is consistent with recent X-ray measurements (Sambruna et al. 1998). | 59 |
| 5.1 | Histogram of the photon indices of the power law fits. The solid line is for the observations of all sources while the dotted line is for the observations of Seyfert galaxies. | 82 |
| 5.2 | Histogram of the high energy cut-off for a cut-off power law model (model 1). | 84 |
| 5.3 | Histogram of the Compton reflection for the XSPEC <i>pexrav</i> model where $E=10000$ keV (model 2). | 85 |

| | | |
|------|--------------------------------------------------------------------------------------------------------------------------------------------------------------------------------------------------------------------------------------------------------------------------------------------------------------------|-----|
| 5.4 | Reflection versus high energy cut-off of the pexrav model fits. Open symbols are lower limits. Circles are objects of table 4 (model 3), squares are values of NGC4151 (model 5) and triangles are values of IC4329A (model 5). | 88 |
| 5.5 | Left: PDS light curve in the 20-200 keV energy range, the bin of 5700 seconds corresponds to a single <i>BeppoSAX</i> orbit. Right: PDS count spectrum with residuals for an absorbed power law model. | 94 |
| 5.6 | BATSE light curve. Twenty days intervals resulting from the rebinning of the daily data obtained with LADs in Earth Occultation Mode. The two vertical strips represent the windows of <i>BeppoSAX</i> observations during SVP and the AO1. | 97 |
| 5.7 | Photon index versus flux for all the <i>BeppoSAX</i> /PDS observations of 3C273. | 98 |
| 5.8 | BATSE light curve. 50 days intervals resulting from the rebinning of the daily data obtained with LADs in Earth Occultation Mode. | 100 |
| 5.9 | Comparison of the unfolded spectra of MKN501 in the highest state of April 97 (<i>"big flare"</i>) and in the lower state analyzed here of June 99. . . | 101 |
| 5.10 | Photon index versus flux of all the <i>BeppoSAX</i> /PDS observations analyzed here, filled symbols are the measurements during the big flare. The fluxes are in units of 10^{-11} erg cm $^{-2}$ s $^{-1}$ | 103 |
| 6.1 | Data to model (wa*po) ratio over the 3-200 keV energy range for Seyfert 1 (top) and Seyfert 2 (bottom). The figures show the major spectral characteristics to be investigated in both type of objects | 114 |
| 6.2 | Confidence contours of iron line sigma versus energy line for Seyfert 1 (top) and Seyfert 2 (bottom) | 115 |
| 6.3 | Data to model [wa*(po+ga)*highcut] ratio for Seyfert 1 (top) and Seyfert 2 (bottom). The Compton reflection component around 30 keV is well evident in both classes. | 116 |
| 6.4 | Confidence contours of high energy cut-off versus photon index. Solid lines are the 65%, 90% and 99% levels of the Seyfert 2s, the dashed lines are Seyfert 1s in edge-on configuration ($\cos\Theta=0.45$) and dotted lines are contours of Seyfert 1s in face-on configuration ($\cos\Theta=0.87$) | 117 |
| 6.5 | Confidence contours of Compton reflection versus photon index. Solid lines are the 65%, 90% and 99% levels of the Seyfert 2s, the dashed lines are Seyfert 1s in edge-on configuration ($\cos\Theta=0.45$) and dotted lines are contours of Seyfert 1s in face-on configuration ($\cos\Theta=0.87$) | 118 |

| | | |
|------|--------------------------------------------------------------------------------------------------------------------------------------------------------------------------------------------------------------------------------------------------------------------------------------------------------------------------------------------------------------------------|-----|
| 6.6 | Confidence contours of Compton reflection versus high energy cut-off. Solid lines are the 65%, 90% and 99% levels of the Seyfert 2s. The dashed lines are Seyfert 1s in edge-on configuration ($\cos\Theta=0.45$) and dotted lines are contours of Seyfert 1s in face-on configuration ($\cos\Theta=0.87$) | 119 |
| 6.7 | Confidence contours of Compton reflection versus high energy cut-off. Solid lines are the 65%, 90% and 99% levels of the Seyfert 2s with Γ fixed to 1.92 value, the dashed lines are Seyfert 1s in edge-on configura- tion ($\cos\Theta=0.45$) and dotted lines are contours of Seyfert 1s in face-on configuration ($\cos\Theta=0.87$) | 120 |
| 6.8 | Ratio of Seyfert 2s/Seyfert 1s spectra | 121 |
| 6.9 | Confidence contours of N_H vs Cf for a double absorption model | 122 |
| 6.10 | Combined unfolded spectra of Seyfert 1s fitted with pexrav and Seyfert 2s (squares) fitted with double absorption plus pexrav | 122 |

Chapter 1

AGNs

1.1 Introduction

Active galaxies (hereafter Active Galactic Nuclei (AGN)) are the most powerful objects known in the whole universe, especially in the X-ray band where their luminosities can reach $\sim 10^{47-48} \text{ erg s}^{-1}$. The origin of this strong X-ray emission may be directly related to the central engine powering the active galaxy, in fact the rapid X-ray variability detected in several sources (e.g. McHardy 1989) indicates that the X-ray production region is very close to the central regions of AGNs. The most fuel-efficient way to release such a large amount of energy is through the accretion of material onto a supermassive black hole. This is now a widely accepted picture supported also by the strong UV excess observed which is thought to be the signature of the accretion flow. In this picture the origin of the X-rays remains unclear, and any successful model needs to satisfy three main observational constraints:

1. the size of the X-ray production region must be small (a few gravitational radii) as indicated by the fast variability (McHardy 1989);
2. the X-ray spectrum in the 2-10 keV band is close to a power law with mean value of spectral index of $\simeq 0.7 \pm 0.15$ for Seyfert galaxies (Mushotzky 1984). At higher energies the power law shows a break with the e-folding energy between 50 and 300 keV (Madejski et al. 1995);
3. whatever produces the X-rays is close to cold reflecting matter. This material is optically thick subtending a substantial solid angle to the X-ray source, probably the putative accretion disk (e.g. Lightman and White 1988). This is inferred from the presence of fluorescent Fe line emission and Compton reflection hump peaked around

30 keV. Considering the latter component the slope of the underlying power law is revised to $\simeq 0.9$ (Pounds et al. 1995).

X-ray spectra of AGNs are clearly non-thermal but the problem that remains to be understood is whether the particle distribution responsible for such X-ray emission is thermal or non-thermal. Historically, two competing models have been proposed as an explanation of the source of X-rays: non-thermal pair (e^-e^+) models (e.g. Zdziarski & Lightman 1985) and thermal Comptonization models (e.g. Sunyaev & Titarchuk 1980, Haardt, Maraschi & Ghisellini 1994) which involve multiple Compton scattering of soft photons off of a thermal population of hot electrons. In the non-thermal models the gravitational power is channeled into a tiny fraction of the electrons (i.e., a non-thermal plasma) contrary to the case of thermal model where the power is equally channeled into all electrons (thermal plasma). Electromagnetic cascades occur in a compact region located (either as a cloud or a corona) above a cold accretion disk around a super-massive black hole. In a rough description, relativistic e^- Compton-upscatter the UV photons to γ -ray energies and γ -rays interact with X-rays to produce e^-e^+ pairs. This second injection of e^- can again Compton-upscatter the UV photons to produce the observed X-ray spectra (Svensson 1992). The e^-e^+ creation will be generally followed also by a e^-e^+ annihilation which produces line emission of the X-ray spectrum at ~ 511 keV. Furthermore, this model predicts a flattening of the X-ray spectrum at ~ 100 -200 keV. However, after that the OSSE results revealed in Seyfert 1 galaxies a high energy cut-off corresponding to e-folding energies of ~ 50 -300 keV and did not reveal the predicted annihilation line, consensus has thus been given to thermal models.

Thermal models generally assume that a substantial fraction of the gravitational energy is dissipated directly into a hot ($kT_e \sim 50$ -100 keV) corona placed above a cold ($kT_e \lesssim 1$ keV) accretion disk. The corona is an optically thin ($\tau_T < 1$, where τ_T is the optical depth to Thomson scattering) semi-relativistic plasma that Comptonizes (i.e. makes multiple Compton scatterings) seed UV and soft X-rays photons. The accretion disk is optically thick ($\tau_T > 1$) and has a double role: it is the source of the seed-photons that are Comptonized by the corona and is the medium responsible for the reprocessing and reflection features. The geometry of the system hot corona can vary and several models have been proposed to model it: extended corona (Haardt & Maraschi 1991, 1993), flaring blobs above the disk (Balbus et al. 1996), advection dominated accretion disks (Narayan & Yi 1995), and EUV cloudlets (Celotti et al. 1992, Kurcic et al. 1996). On the basis of currently available observations, it is difficult to favor one model with respect to the others, discriminating observations could come from timing properties of X-ray light curves, comparing properties as time-lags, power spectra and coherence in

different X-ray bands.

1.2 Studies in the Hard X-Ray Band

The study of astronomical objects at the highest energies of X-rays and gamma-rays really began only in the early 1960's. Before then, we knew only that the Sun was an intense source in these wavebands. The Earth's atmosphere absorbs most X-rays and gamma-rays and so rocket flights which could lift scientific payloads above the Earth's atmosphere were necessary. The first rocket flight which successfully detected a cosmic source of X-ray emission was launched in 1962. This rocket flight detected a very bright source named Scorpius X-1 (Sco X-1), because it was the first X-ray source found in the constellation Scorpius. Soon after this, the Crab Nebula supernova remnant was discovered to be a bright, extended X-ray source using lunar occultation techniques (Bowyer et al. 1964). Interestingly, the same technique, but using the Earth as the occultating disk, is exploited in this thesis to obtain data from extragalactic sources using observations with the BATSE instrument. The first 1-10 keV X-ray observations of extragalactic objects were performed using a collimated proportional counter flown on the Aerobee 150 rocket in 1969; the discrete sources detected were NGC5128 (Centaurus A), 3C273 and M87 in the Virgo cluster (Bowyer et al. 1970). On the same rocket, a scintillation counter sensitive to X-rays from 10 to 30 keV was also present but no sources were detected above the background noise. The launch in 1970 of the Uhuru Satellite, the first Earth orbiting mission entirely dedicated to X-ray astronomy, opened a new era not only because the number of X-ray emitting objects was enormously enlarged but because important characteristics such as the short and the long term variability and the spectral shape of the emission were for the first time revealed in galactic as well as extragalactic sources. In the following years dedicated X-ray astronomy satellites, such as Ariel-5, SAS-3 and OSO-8, developed this field of science at an astounding pace. Scientists began to believe that X-rays from stellar sources in our Galaxy were primarily coming from neutron stars in a binary system with a normal star. In these X-ray binaries, the X-rays originate from material falling from the normal star to the neutron star in a process called accretion. The binary nature of the system allowed the measurements of the mass of the neutron star. For some systems, the inferred mass of the degenerate object supported the idea of the existence of black holes, as they were too massive to be neutron stars. Some of the systems displayed a characteristic X-ray pulse, just as pulsars had been found to do in the radio regime, which allowed a determination of the spin rate of the neutron star. Finally, some of these galactic X-ray sources were found to be highly variable; in fact,

some sources would appear in the sky, remain bright for a few weeks, and then fade again from view. Such sources were called X-ray transients. The inner regions of some galaxies were also found to emit X-rays. The X-ray emission from these Active Galactic Nuclei (AGN) was soon associated with ultra-relativistic gas near a very massive black hole at the galaxy's centre. Lastly, a diffuse X-ray emission was found to exist all over the sky.

For energies >10 keV both satellites and balloon-born experiments, flown in the 1970s, provided information on the emission characteristics in the hard X-ray/gamma-ray domain for a very limited number of sources since measurements are much more difficult due to the higher instrumental background typical of these bands. Contrary to X-ray astronomy where the detected signal is source dominated, in these high energy bands the signal is background dominated making detections more difficult to obtain. Beginning in 1977, NASA launched a series of very large scientific payloads called High Energy Astronomy Observatories (HEAO). The first of these missions, HEAO-1 surveyed the X-ray sky almost three times over the 0.2 keV - 10 MeV energy band and provided nearly constant monitoring of X-ray sources near the ecliptic poles. More detailed studies of a number of objects were made through pointed observations lasting typically 3-6 hours. In particular, one of the instruments on-board, a hard X-ray/low energy gamma ray experiment called the A4 experiment, allowed for the first time the opportunity to study the extragalactic sky above 10 keV. This instrument performed an all sky survey in the range 13-180 keV at a limiting sensitivity of $\sim 3 \times 10^{-10}$ erg cm $^{-2}$ s $^{-1}$, detecting about 70 sources at a statistical significance level $\geq 6\sigma$, 44 of which were detected in the 40-80 keV energy range and 14 in the 80-180 keV band (Levine et al. 1984). Although most of the detected sources were galactic, seven were extragalactic: two were cluster of galaxies (Perseus and Virgo) and five AGN (NGC4151, 3C273, Cen A, NGC5548 and MKN509); only NGC4151, 3C273 and Cen A were also detected at $E > 80$ keV. This remains up to now the only survey of the entire sky at high energies (>10 keV). Note that the lower energy instrument on board HEAO-1 (A2) also performed an almost all sky survey at high galactic latitudes, providing a list of the brightest AGN in the 2-10 keV range (the Piccinotti sample, Piccinotti et al. 1982), and this too remains so far the only survey of the extragalactic sky at these intermediate X-ray energies. The A4 instrument also performed detailed studies of individual sources: in particular Rothschild et al. (1983) made the first study of the AGN spectral characteristics in the 2-165 keV band using a sample of 12 objects and by summing these data together, provided the first average AGN spectrum over this band. Before these measurements very few active galaxies were detected above 20 keV and their spectra were quite uncertain; furthermore knowledge of

the active galaxies' contribution to the diffuse X-ray background above 20 keV was hampered by the lack of sufficient information on their spectral behaviour at these energies. The mean photon index of the whole A4 sample was 1.55 ± 0.06 (or 1.59 ± 0.10 with the removal of NGC4151, the brightest source in the sample). Given the small dispersion, the active galaxies' spectra were combined to obtain an average spectrum which was best fitted in the A4 energy band (12-165 keV) with a power law of $\Gamma = 1.54 \pm 0.23$. Combining these data with the low energy A2 (2.1-32 keV) information, allowed the authors to test for the possible presence of spectral breaks. Although a simple power law of photon index $\Gamma = 1.62 \pm 0.04$ was the preferred fit, a break above 50 keV to an index $\Gamma = 2.67$, similar to the best fit power law index of the diffuse X-ray background, could not be ruled out at the 90% confidence level. The comparison of the mean active galaxies' spectrum to the diffuse X-ray background also measured by the A4 instrument, constrained the contribution of AGN to the diffuse flux to be $\sim 25\%$ below 10 keV increasing to 100% around 150 keV and located the spectral turnover in the range 50 keV to 4 MeV.

While at lower energies ($E < 10$ keV) the knowledge of the X-ray sky improved considerably, at higher energies the situation remained rather stalled until the 1990s. In fact, prior to these years, hard X-ray observations of the sky were performed only by the imaging telescope SIGMA on board the GRANAT satellite, operating in the 35 keV - 1.3 MeV energy band and by balloon borne detectors. Among the AGN, the well known hard X-ray emitting objects NGC4151, 3C273, Cen A were observed by SIGMA (Bassani et al. 1993). It is important to point out that SIGMA detected for the first time a break at around 50-60 keV in the spectrum of NGC4151 (Jourdain et al. 1992). This observation, if extended to the whole AGN class, had strong implications for Seyfert galaxies production mechanisms and for their contribution to the cosmic diffuse X/ γ -ray background. In fact, it ruled out pure non-thermal models as the production mechanisms of X-rays and solved the paradox of too much contribution from Seyfert galaxies to the Cosmic Diffuse Background at around a few hundreds of keV. SIGMA also observed variability on long timescales in the hard X-ray emission of 3C273, NGC4151 and Cen A and in this last object short term variability of the order of days was also found (Bassani et al. 1993). Finally SIGMA confirmed a previous SPACELAB observation of the Virgo cluster (Hanson et al. 1990) which indicated the presence of hard X-ray emission located at the position of the Seyfert galaxy NGC4388. These two observations were precursors of *BeppoSAX* measurements of heavily absorbed Seyfert 2 galaxies and indicated for the first time that to discover these type of objects and to measure $N_H > 10^{23} - 10^{24}$ atoms cm^{-2} , one must observe above ~ 10 keV.

The turning point for the study of AGN at hard X-ray energies is represented by the

Compton GRO satellite (see chapter 2) which thanks to its four instruments (BATSE, OSSE, COMPTEL and EGRET) observed the extragalactic sky from 20 keV to 10 GeV. These four instruments were much larger and more sensitive than any hard-X/gamma-ray telescopes previously flown allowing for the first time the detection of many more AGN than the three generally observed, i.e. NGC4151, 3C273 and Cen A. In the hard X-ray domain, two instruments were particularly suited for extragalactic observations, OSSE and BATSE.

OSSE has made an important contribution to the study of blazars as well as of Seyfert galaxies in the hard X-ray band. OSSE observations of a sample of blazars were analyzed by McNaron-Brown et al. (1995) and for the first time their spectral characteristics at energies >50 keV were investigated. The OSSE blazar sources were well described by a simple power-law model with photon indices Γ ranging from 1 to 2, while variability in the energy band 50-150 keV was observed in all the sample sources. When combined with available, although not necessarily contemporaneous, COMPTEL and EGRET observations, four to five detected blazars showed clear evidence for spectral breaks between the hard X-ray and medium-energy gamma-ray bands. The only exception was the combined OSSE/EGRET data for 3C279 during October of 1991, where a simple power law with $\Gamma \sim 1.9$ worked equally well. Gamma-ray evidence for beaming was detected in CTA 102, PFS 0528+134 and 3C 454.3. For the particular case of 3C273, variability by factors of ~ 3 on timescales of ~ 2 months and by a factor of 1.7 in $3/4$ days were detected in the energy band 50-150 keV (Johnson et al. 1995, McNaron-Brown et al. 1997). The data were well described by a single power law with photon index $\Gamma = 1.7 \pm 0.1$. No significant change of Γ was observed during changes in intensity. Thermal models did not provide acceptable fits to the data. When the OSSE data were combined with contemporaneous measurements by COMPTEL and EGRET, the spectrum was seen to break at an energy of $1.0^{+0.9}_{-0.4}$ MeV to a softer power law with $\Delta\Gamma = 0.7^{+0.06}_{-0.11}$, forming a power law with $\Gamma = 2.4$ between ~ 1 MeV and several GeV (Johnson et al. 1995). In a later observation, when the source flux was quite high, the data were however better described by a break at much lower energy (~ 300 keV), implying possible changes of the break energy with flux variations (McNaron-Brown et al. 1997).

The OSSE contribution to the high energy study of Seyfert galaxies is even more important. Thanks to its observations the number of these galaxies detected at high energies grew substantially and in particular observations of Seyfert 2 galaxies, limited to MCG-5-23-16 and NGC 1275 by HEAO/A4 and NGC 4388 and NGC 1068 by SIGMA, were considerably improved after the first measurement of NGC4507 (Bassani et al. 1995 and Johnson et al. 1994). One major result has been the discovery that the hard X-ray

spectra of Seyferts are significantly softer on average than the X-ray spectra since the mean OSSE photon index was $\Gamma_\gamma \simeq 2.2$ in the 50-150 keV range (Johnson et al. 1994), compared to $\Gamma_x \simeq 1.7$ or 1.9 in the 2-10 keV range (Nandra and Pounds 1994). This was taken as evidence for the presence of a break in the spectra of these sources in the range 20-50 keV (Johnson et al. 1994). These results have been recently confirmed by Zdziarski et al. (2000): OSSE data are best fitted with a thermal Comptonization model with $kT \simeq 50-150$ keV which corresponds to a Thomson optical depth of $\tau \simeq 0.3-1.5$ in spherical geometry and $\tau \simeq 0.1-0.6$ in slab geometry. The presence of a cut-off was detected in various observations of NGC4151, which was constantly monitored by OSSE during its lifetime. These observations showed a photon spectrum in the 50-800 keV band that was well described by an exponentially cut-off power law of the form $\Phi(E) \propto E^{-1.6} e^{-E/100\text{keV}}$. Long-term luminosity changes of no more than a factor of 2 were observed with only modest changes in the spectral shape. With these data it was possible to set the most stringent upper limits on any positron annihilation radiation from a Seyfert nucleus further limiting the role of pair production and non-thermal processes in this and similar sources (Johnson et al. 1997). Also the OSSE observation of Cen A was particularly interesting (Kinzer et al. 1995). Long-term intensity changes by a factor of 2-3 were measured over a period of three years. Short term variations by as much as 25% on timescales as short as 12 hours were detected in most of the observations. No evidence for gamma-ray line emission was detected at sensitivities much improved over previous observations. An intensity dependent evolution of the 50-1000 keV spectral shape was observed which could be characterized as an exponentially cut-off power law with an intensity dependent cut-off energy ranging from ~ 300 keV at the highest observed level to ~ 700 keV at the lowest level. A broken power law model with an intensity correlated break above ~ 120 keV described the observed spectral changes equally well. Below 120 keV the spectra at all intensities can be fitted with photon index $\Gamma \sim 1.7 \pm 0.08$, in agreement with previous measurements. Contemporaneous measurements by the EGRET instrument require additional softening in the MeV measurements.

Having a large sample of Seyferts it was possible to search for possible observational differences between the two classes which are unified according to a simple model (Antonucci and Miller 1985). According to this model Seyfert 2 galaxies harbor a bright Seyfert 1 nucleus hidden from our view by an optically and geometrically thick obscuring torus. OSSE data have shown that hard X-ray spectra for different types of AGN are different contrary to the expectation of the Unified Theory. By combining Ginga with OSSE data of type 2 sources, Zdziarski et al. (1995) provided evidence for a harder intrinsic power law, less reflection and a cut-off at lower energies in type 2 objects with respect to that

observed in type 1 sources.

Seyfert 2 galaxies are generally heavily absorbed in soft X-rays, plausibly because of obscuration of the Seyfert nucleus by a thick molecular torus. With a high torus column, $10^{23} < N_H < 10^{25} \text{ cm}^{-2}$, the observed flux in the classical 2-10 keV X-ray band can be strongly suppressed, while at higher energies the photoelectric absorption becomes less important and the true nuclear luminosity can be seen. In this context, it is interesting to highlight the OSSE detection of NGC4945 which is the first Compton thick Seyfert 2 galaxy observed at high energies. The OSSE observation confirmed the GINGA prediction of an active galactic nucleus in NGC4945 strongly obscured by a column density of $N_H = 4 \times 10^{25} \text{ cm}^{-2}$. The OSSE spectrum was fitted with a power law of photon index $\Gamma = 2.2 \pm 0.3$, and a 50-150 keV photon flux of $13.3 \pm 1.4 \times 10^{-4} \text{ photons cm}^{-2} \text{ s}^{-1}$ ($1.7 \pm 0.2 \times 10^{-10} \text{ ergs cm}^{-2} \text{ s}^{-1}$), making this the second brightest radio-quiet AGN (after NGC 4151) in the sky at 100 keV, detected by OSSE (Done et al. 1996).

Although less limited in sensitivity than OSSE, BATSE had nevertheless the appealing capability of observing the whole sky continuously and it did that for almost 10 years (see chapter 2). This allowed the possibility of performing an all sky survey at high galactic latitudes at a sensitivity limit a factor of 10 or more deeper than HEAO1-A4, providing information on new sources, some of which were unexpected. BATSE observations of AGN are briefly discussed in chapter 2, while the observations of all the sources in the Piccinotti sample, i.e. the brightest AGN in the sky in the 2-10 keV band, are an important part of this thesis and are discussed in chapter 4.

A further step forward in extragalactic studies was provided by the launch of *BeppoSAX*. This satellite thanks to its broad band capabilities and the good sensitivity of its instruments (see chapter 3) above 10 keV, allowed for the first time the measurement of various spectral components with great accuracy: the strength of the Compton reflection component as well as the shape of the intrinsic power law emission (photon index and high energy cut-off) were determined in the spectra of various AGN. It also enabled tests for possible correlations between these components (Perola et al. 2001). Furthermore, *BeppoSAX* has allowed for the first time the study of heavily obscured sources and the estimate of the Seyfert 2 column density distribution. Finally, by monitoring blazar-type objects, it has provided information on their various spectral behaviors and has permitted their classification into blue or red objects (Ghisellini et al. 1998). The main results of AGN studies performed by *BeppoSAX* are described in chapter 3, while *BeppoSAX* -PDS observations of all the Piccinotti sample sources already present in the public archive are discussed in general in chapter 5, while in chapter 6 the average spectra of type 1 and 2 Seyferts are discussed and compared.

Chapter 2

BATSE

2.1 The Compton Gamma Ray Observatory

The Compton Gamma Ray Observatory (CGRO) was the first NASA gamma-ray observatory. It was launched on April 5, 1991 aboard the space shuttle Atlantis and it was safely deorbited and re-entered the Earth's atmosphere on June 4, 2000. CGRO was responsible for many discoveries in the study of gamma ray bursts, accreting binaries, active galaxies and pulsars. Compton had four instruments that covered an unprecedented six decades of the electromagnetic spectrum, from 20 keV to 30 GeV:

- The Burst And Transient Source Experiment (BATSE), an all sky monitor in the energy range 20-1000 keV;
- The Oriented Scintillation Spectrometer Experiment (OSSE), operating in the 0.05-10 MeV energy range;
- The Imaging Compton Telescope (COMPTEL), operating in 0.8-30 MeV band, capable of imaging 1 steradian of the sky;
- The Energetic Gamma Ray Experiment Telescope (EGRET), which worked in 30 MeV-10 GeV part of the electromagnetic spectrum.

For each of the instruments, an improvement in sensitivity of better than a factor of ten was realized over previous missions. In figure 2.1, Compton Gamma Ray Observatory and the placement of the four instruments on the spacecraft is shown.

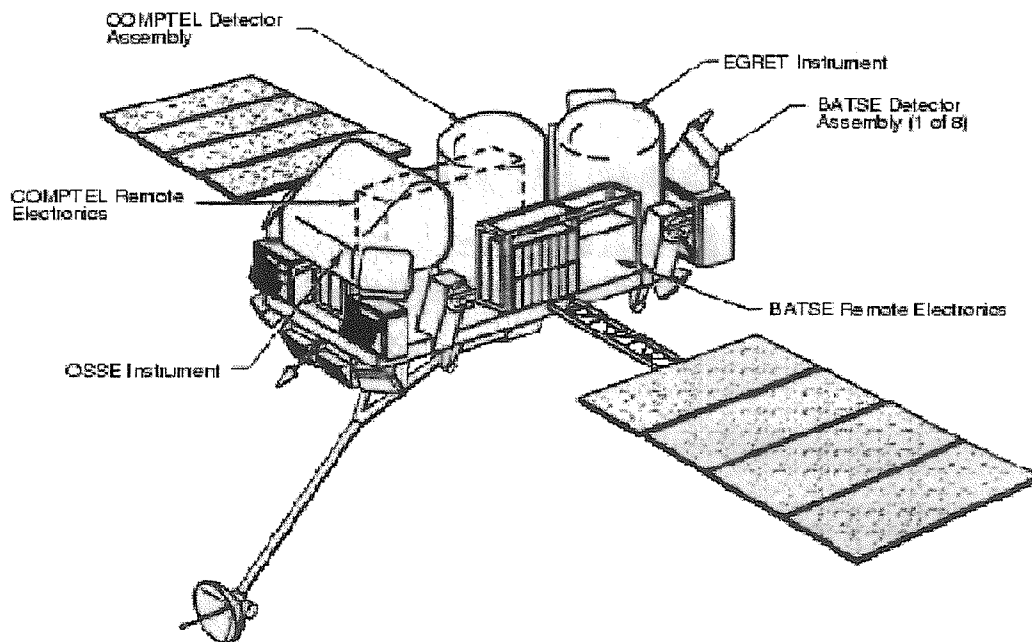


Figure 2.1: The Compton Gamma Ray Observatory with the four instruments

2.2 BATSE

It was the quest to understanding the origin of gamma ray bursts that led to the development and the flight of The Burst and Transient Source Experiment (BATSE) on CGRO. In fact, as expected, BATSE pointed the way to the extragalactic origin of gamma ray bursts through the mapping of burst locations and number-brightness distribution (Meehan et al. 1992). Also, in addition to this BATSE's primary scientific goal, its nine years of nearly continuous operation and all-sky capability allowed monitoring of the low energy gamma-ray/hard X-ray sky, using the Earth occultation technique (see below). Furthermore, the high energy sky has been monitored with a daily sensitivity of about 100 mCrab for non-pulsating sources and 25 mCrab for pulsars, performing the second all sky survey in the 20-100 keV band (after the A4 instrument on HEAO-1) and the first one above these energies. This has resulted in the detection of many relatively bright pulsars, for which variations on timescales of hours to years has been investigated, new transient sources, which show unusual intensity and spectral changes, black hole candidates and AGNs of various classes, as well as clusters of galaxies.

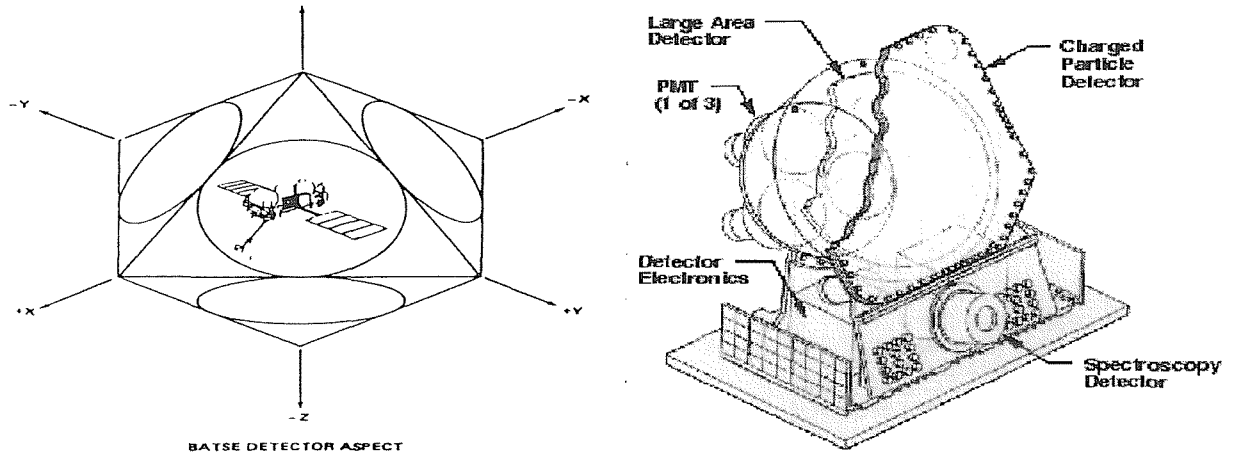


Figure 2.2: Left: the co-alignment of the principal axes of the Compton Gamma Ray Observatory with the octahedron geometry of the BATSE detectors; Right: Pictorial representation of a BATSE detector module.

2.2.1 BATSE Instrumentation

BATSE consists of eight uncollimated detector modules arranged on the corners of CGRO so as to provide the maximum unobstructed view of the celestial sphere. Each module has two detectors, a large-area detector (LAD) which is thinner but has a geometrically larger area for high counting statistics between 20-1800 keV and is optimized for sensitivity and directional response, and a spectroscopy detector (SD) which is thicker but has a smaller area for higher energy resolution and higher detection efficiency up to 10 MeV and is optimized for broad energy coverage and energy resolution.

In this thesis only observations from the large area detectors LADs have been analyzed. The eight planes of the LADs are parallel to the eight faces of a regular octahedron, thus providing nearly uniform sky coverage. As shown in figure 2.2 (left), the three primary axes of the octahedron are parallel to the three principal axes of the spacecraft. Since the faces of a regular octahedron comprise four pairs of intersecting planes, every detected burst is viewed by four detectors. The LADs are composed of sodium iodide (NaI(Tl)) crystal 50.8 cm in diameter and 1.27 cm thick with a front area of 2025 cm². Scintillators work by the conversion of X-ray energy into visible light. In the case of BATSE detectors, the alkali halides NaI are activated by the introduction of 10⁻²-10⁻³ mole thallium (impurities). Light production in the activated alkali halides results from a complex sequence of excitation and de-excitation processes. The role of the impurity is to produce luminiscent centres energetically intermediate between the valence and conduction band of the host crystal. At energy below 100 keV, X-ray interactions with NaI are still predominantly by photoelectric effect. The photoelectrons produce secondary

electron/hole pairs, which diffuse to the neighbourhood of luminiscent centres and form a long-lived ($\sim 10^{-6}$ s) excited Tl^+ states which decay with emission of visible light. Scintillation light from the detector crystal is viewed by three 12.7 cm photomultiplier tubes (PMTs), with the signals from the three tubes being summed. The light collection technique is different from that usually used with crystal scintillation detectors. Instead of directly coupling the PMTs to the crystal window, a large light-integrating housing is used. In figure 2.2 (right) is shown a schematic view of a single detector module. The front of the LAD is covered by a plastic scintillator that rejects charged particle induced events in the LAD.

2.2.2 Data Selection

The LADs are well-suited to Earth occultation measurements because of their sensitivity, uniformity in energy range, and stabilized gain. Data from two or more LADs can be easily fitted jointly in two different types: DISCLA (LAD discriminator data) and CONT (LAD continuous data) which both cover the energy range between 20 keV - 1 MeV. The DISCLA data type provides four energy channels binned every 1.024 seconds, while CONT data type provides 16 channels every 2.048 seconds. Prior to the application of the Earth occultation method, proper data selection is required to remove large fluctuations that may affect the fitting of the occultation steps. Therefore when data are flagged in one stage of the selection process, they are then excluded from the occultation analysis. The first stage of the data selection is performed onboard. An event may “trigger” the gamma ray burst (GRB) acquisition mode, when a high data rate is measured compared to the background in two or more LADs (Meegan et al. 1992). High rate events may be caused by bursts, solar flares, bremsstrahlung from electron precipitation (Aschwanden, Schwartz & Dennis 1998), or even flaring galactic sources (Mallozzi et al. 1993). Any trigger events are flagged automatically in the data-stream and identified later. Only the brightest and most variable galactic sources such as A0535+262 (Finger, Wilson & Harmon 1996), Cygnus X-1 (Fishman et al. 1994) GRO J0422+32 (Mallozzi et al. 1993), GRO J1744-28 (Kouveliotou et al 1996), and 4U 1700-377 (Rubin et al. 1996) and the soft gamma ray repeaters (Woods et al. 1999) have been detected via the burst trigger. The second stage of the selection process consists of manual inspection for other events that may escape the burst trigger, but can yet generate large transient flares. These are on a somewhat longer timescale than GRBs, usually a few tens of seconds to minutes. The fluxes from these sources are generally easy to identify based on their observed timing and spectral properties. Time periods containing transient background features large enough to be detected visually (about 10% of the total background counting rate) are

flagged and excluded from occultation analysis along with the triggered events. Finally, additional flagging of very short (< 1 sec) cosmic ray events appearing in only one LAD is performed using a spike filter prior to the occultation measurements.

2.3 The Occultation Technique

The occultation technique uses the Earth's limb as a well defined, stable occulting disk for measuring source intensity and spectra and for locating new sources. In one orbit, two occultations of the hard X-ray source in the sky by the Earth, produces a step-like feature, a rise and a set pair, superimposed on the background counting rates. In figure 2.3 a sketch of this method has been shown. A measurement can be made of the intensity of a source in each energy channel both when rising and setting; in fact, when the Earth's limb (an arc) sweeps through a chosen region of the sky, the detectors record the counting rate as a function of time. The attenuation of gamma rays by the Earth's atmosphere and the variation in thickness of the air mass along the line of sight to the X-ray source, produce a step-like feature in the detector count rate as a function of time. The attenuation is 50% for 100 keV photons that pass through the atmosphere along a line of sight with minimum altitude of 70 km. For a typical orbital speed of 8 km/s, the duration of the occultation step for a source rising or setting in the plane of the spacecraft orbit is about 10 seconds. Therefore occultations are relatively sharp features superimposed on the generally slower background variations caused by orbital motion around the Earth. The location of the spacecraft is well known and thus the location and orientation of the limb projected on the sky can be determined accurately. In practice, both measurements per orbit are not always achieved. The most common reasons are passages through the lower Van Allen radiation belt at the South Atlantic Anomaly when the detector voltage is turned off, or where CGRO is out of the line of sight contact with the NASA Tracking & Data Relay Satellites. Also high declination sources ($\sim |\delta| \geq 41^\circ$) experience an interruption of occultations near the orbital poles. A deep discussion of the Earth occultation technique with the developing of the mathematical framework for the Earth occultation from an orbiting spacecraft can be found in Harmon et al. (2001).

It is also worth noting that source confusion, where occultations of one source are indistinguishable from another, limits the number of usable occultation steps. All these effects combined causes Earth occultation coverage averaged over one precession cycle (53 days) to range between 80-90%, at best, and at worst, to about 50%. The count rate for a source in the LAD is extracted by simultaneously fitting occultation step features with terms for each source in the fit and a quadratic polynomial is used to represent

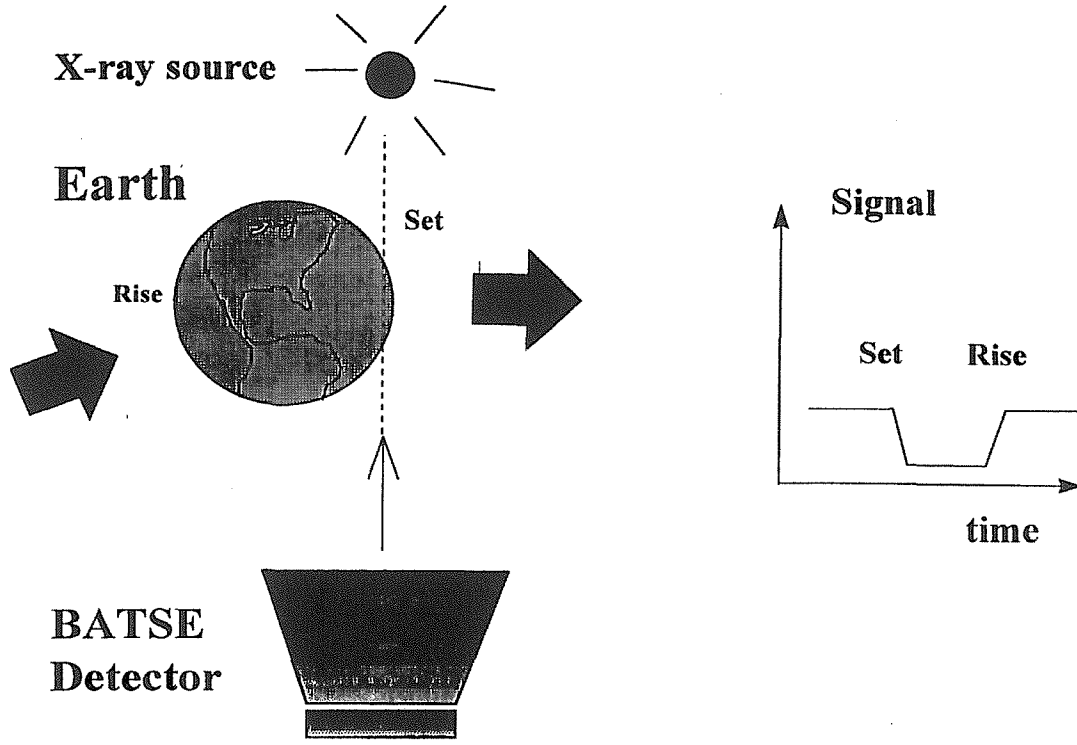


Figure 2.3: Sketch of the Earth Occultation Technique

the detector background. Each occultation step, rise or set, is fitted over a time $t_{occ}-\tau$ to $t_{occ}+\tau$, called the *fitting window*. t_{occ} represents the occultation time of the source of interest and also the center of the time window and τ is the half-width of the fitting window. The modeled detector count rate $R(t)$ in each energy channel can be represented as

$$R(t) = \sum_{i=0}^2 b_i(t - t_{occ})^i + \sum_{j=1}^n r_j T_j(t) \quad (2.1)$$

where b_i are the coefficients of the background model (to second order) and r_j are source terms including the source of interest and other bright sources within the fitting window, and $T_j(t)$ are the atmospheric transmission functions. A database of source locations, outburst times, and intensities provides information to determine whether terms for sources should be included in the fitting window. This database is built up as new sources are found either through occultation analysis (light curves and images) or from other instrument measurements. Each energy channel in the source-pointed LADs is fitted independently to derive a count rate in each CONT channel for all the sources r_j as a function of time. The statistical error (δr_j) of the r_j th term at time t_{occ} is computed from the least square fit of Eq. (2.1).

2.3.1 Sensitivity

The sensitivity of the Earth occultation technique depends on several factors. Essentially the uncollimated detector geometry of the LADs and the fixed orientation of CGRO with respect to the sky for a single pointing period, generates continuously varying backgrounds which range over a factor of two or more. At energies up to ~ 100 keV, the background is dominated by the modulation of the diffuse sky flux by the Earth while at higher energies by the cosmic ray secondary radiation. Therefore at lower energies the background exhibit a slow sinusoidal variation with the orbital period of the spacecraft and at high energy it is modulated more rapidly, due to the changes in magnetic field strength and direction. Furthermore, with BATSE a given source exposes a combination of several detectors at different angles so all these factors combine to produce complex energy and time-dependent variations in the background. Nevertheless, the Crab Nebula flux is used as a standard candle to perform an empirical calculation of the sensitivity as a function of energy, angle and detector combination (Harmon et al. 2001). A basic representation of the instrument sensitivity to a point source of continuum emission over a specified energy range is:

$$F_{min} = \frac{N_{\sigma}}{A\epsilon} \sqrt{\frac{R_B}{T_{live}}} \quad (2.2)$$

where F_{min} is the minimum detectable flux for N_{σ} standard deviations, R_B is the background count rate, ϵ is the detector efficiency, A the geometric area of the detector and T_{live} is the duration of the observation. To apply this formula to the calculation of sensitivity of the Earth occultation technique, we need to substitute the term $\sqrt{\frac{R_B}{T_{live}}}$ with the uncertainty δr_s of the detector count rate $R(t)$ (Eq. (2.1)) since in this case the background changes within the fitting region and T_{live} is not a well defined quantity. Therefore the minimum detectable flux of a source is given as:

$$F_{min} = \frac{N_{\sigma}}{A\epsilon} \delta r_s \quad (2.3)$$

Using the Crab Nebula we can relate the flux to the measured Crab count rate r_{Crab} as:

$$r_{Crab} = A\epsilon F_{Crab} \quad (2.4)$$

which allow us to eliminate the area and efficiency factors; in fact Eq. (2.2) can be written as:

$$F_{min} = \delta r_{Crab} \frac{N_{\sigma} F_{Crab}}{r_{Crab}} \quad (2.5)$$

The Crab occultation data were obtained in all eight detectors in the 16 CONT data channels and at many CGRO orientation angles over a period of about five years.

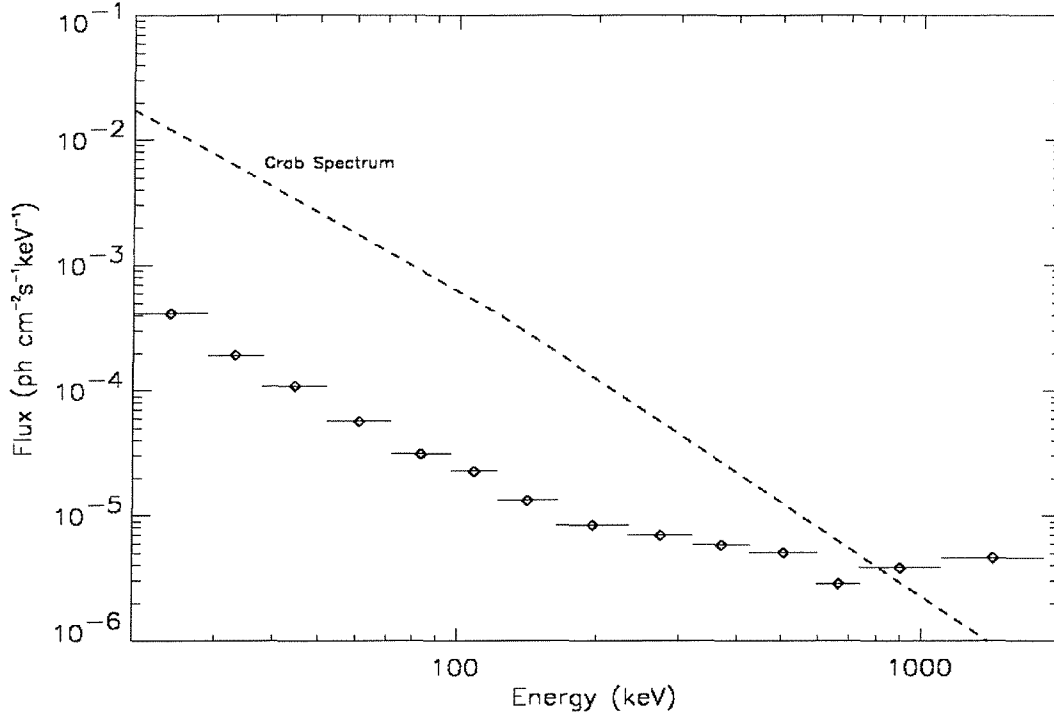


Figure 2.4: Sensitivity (3σ) for a two week observation of a source averaging 16 occultations a day with contributions from two LADs, as a function of energy (Harmon et al. 2001). The Crab Nebula total emission spectrum measured with HEAO-A4 experiment has been also reported for comparison.

Therefore, the Crab Nebula count rate at any angle or energy in the LADs could be determined and this automatically contained the background effects. The point source 3σ sensitivity of a typical CGRO observation of two weeks is shown as a function of energy in figure 2.4 where the Crab Nebula total emission spectrum measured with HEAO-A4 experiment has been also reported for comparison. In the 20-100 keV region this corresponds to a limiting flux of $\sim 8 \times 10^{-5} - 1 \times 10^{-4} \text{ ph cm}^{-2} \text{ s}^{-1} \text{ keV}^{-1}$ (or $\sim 6 - 8 \times 10^{-10} \text{ erg cm}^{-2} \text{ s}^{-1}$) indicating that in order to observe AGN dimmer than 3C273 and/or NGC4151 (which have a flux of $\sim 4 \times 10^{-10} \text{ erg cm}^{-2} \text{ s}^{-1}$ and $\sim 8 \times 10^{-10} \text{ erg cm}^{-2} \text{ s}^{-1}$ respectively in this energy band), data have to be integrated over much longer period (months to years).

2.3.2 Systematic errors

The use of the Earth occultation technique imposes a number of systematic errors based on source location in the sky combined with orbital precession effects plus the variations in the background. One of the major errors may be done in the method of extracting flux,

in particular in relation to the decision that must be made as to what sources must be included in Eq. (2.1). Therefore, the selection of which sources are included in the fitting window is an important determiner of the systematic error, and so it is necessary to keep a controlled database of bright sources information. Generally, sources that exceed ~ 0.02 photons $\text{cm}^2 \text{s}^{-1}$ in the 20-100 keV band (about 75 mCrab for a source with a Crab-like spectrum) are considered as sufficiently bright to be included in the fitting window. The Crab Nebula and the black hole system Cyg X-1 generally are the most persistently bright hard X-ray to low gamma ray emitters in the sky and therefore dominant contributors to systematic errors in their respective sky regions when their occultation steps fall into the fitting window of the source of interest. Of course in the extragalactic sky NGC4151, 3C273 and Centaurus A (Cen A) are the most contaminating sources.

Another type of systematic errors are the ones that can be considered by examining the limb geometry as a function of time. In figure 2.5 (left), taken by Harmon et al. (2001), the sky region around the Crab Nebula and the surrounding sources monitored by BATSE is shown. The two shaded regions correspond to the set of projections of the setting limb of the Earth as the spacecraft moves through one precession cycle of its orbit (dashed lines) and the equivalent regions for the rising limb (solid lines). There are some regions of the sky that are not swept by the Earth's limb at times of occultation, for example as in the case of GROJ0422+32 in the Crab occultation shown in figure 2.5. In contrast 4U 0614+091 is located such that the projection setting and rising limbs of the Crab both cross it at certain times during the precession cycle. This is equivalent to saying that the Crab and 4U 0614+091 are occulted at the same time for a period of 1-2 days. As a consequence, the light curve of 4U 0614+091 will exhibit significant systematic deviations of and around these times. This is illustrated on the right of figure 2.5, where the time dependence of the angle between the location of the source 4U 0614+091 and the closest approach points of the Earth's limb projection that intersect the Crab Nebula over a period of 200 days, has been shown (Harmon et al. 2001). It is evident that when the setting limb of the Crab crosses the location of 4U 0614+091, the occultations become superimposed for a few days every precession cycle (for example around TJD 9900) and so the light curve of 4U 0614+091 shows systematic deviations at these times. Generally the light curves are cleaned of these effects (*bad limbs removed*) with the rejection of the measurements at contaminated times. As reported by Harmon et al. (2001) it is difficult to quantify the total systematic error precisely. For example an additional source of systematic error, is the presence of non-statistical background fluctuations from bright X-ray sources which is considered, in practice, unpredictable.

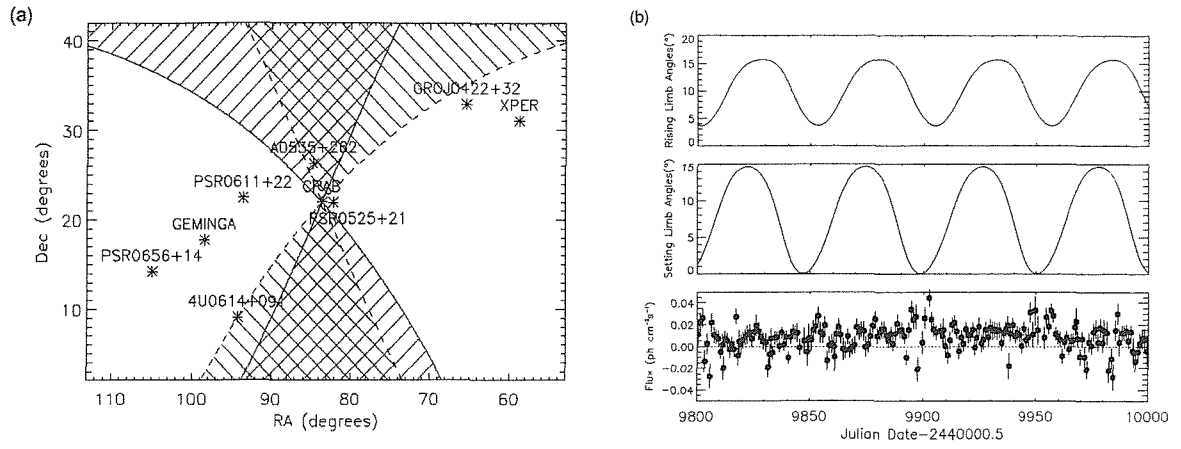


Figure 2.5: Left: Sky region around Crab Nebula. Superimposed are shaded regions which are the portion of the sky subject to Earth occultation when the Earth’s limb crosses the Crab. Sources which are routinely monitored by BATSE are also shown. Right: Angle between the closest approach points of a given source location, here 4U 0614+091, with the rising (top panel) and setting (middle panel) limbs of the Crab Nebula as a function of time. The corresponding light curve of 4U 0614+091 for the same period is also shown (bottom panel). Note that the setting limb of the Crab periodically crosses the location of 4U 0614+091.

2.4 Occultation Imaging

It is not easy to image high energy astrophysical sources since photons with energies above ~ 5 keV are hard to focus. Coded masks or moving collimators are generally used to modulate the flux received by the detectors and then the resulting signals are deconvolved to form images. BATSE team has developed a technique to transform the occultation features in the time domain into spatial information for the imaging construction (Zhang et al. 1993). As the spacecraft moves in its orbit, the Earth itself can be considered as a stable occulting disk. Changes in the measured signal during a single occultation step correspond to the integrated intensity of a source positioned along the arc described by the Earth’s edge (limb). The location of the spacecraft is well known and thus the location of the limb projected on the sky can be determined accurately. The angle at which the limb traverses each source region varies between occultations and thus data from a series of occultations can be transformed into an image. Occultation transform imaging is conceptually similar to techniques used for many years in radio astronomy and medical X-ray tomography to convert essentially one-dimensional scanning measurements into two-dimensional images. Image reconstruction is achieved via Radon transformation (Deans 1983) and the Maximum Entropy Method (Huesman et al. 1977). Use of the

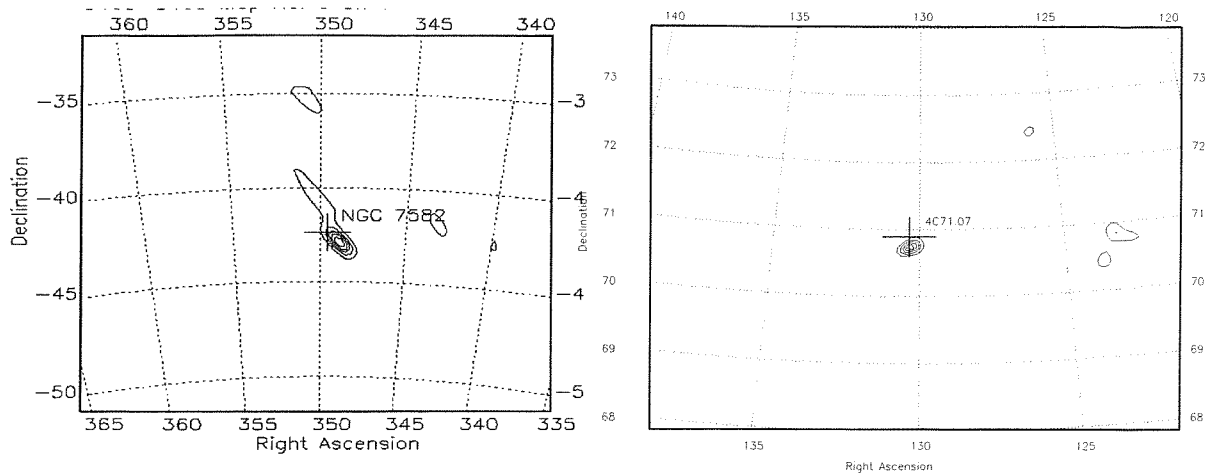


Figure 2.6: Examples of BATSE images. On the left a $20^\circ \times 20^\circ$ image of the Sey2 galaxy NGC7582 obtained integrating 9 days of data (from TJD 8460 to TJD 8469). On the right a more accurate $10^\circ \times 10^\circ$ image of the high redshift quasar 4C71.07 obtained summing 35 days of data (from TJD 10,099 to TJD 10,134).

Radon transformation to represent the limb projection produces a field of view of $20^\circ \times 20^\circ$, while the Maximum Entropy Method is used as stopping criteria since an exact reconstruction is not achievable due to the presence of noise. The location accuracy near the center of $10^\circ \times 10^\circ$ image, figure 2.6 (left), is $\geq 0.3^\circ$ for a best case geometry (nearly perpendicular limb sampling), with a sensitivity in the 20-100 keV range of about $\sim 1.1 \times 10^{-9} \text{ erg cm}^{-2} \text{ s}^{-1}$ (75 mCrab for a source with a Crab-like spectrum) for one day of integration. Computer memory requirements limit the number of days that can be combined into one image, although an integration of 15-35 days has been achieved with a sensitivity of 10 and 20 mCrab (Harmon et al. 2001). The occultation imaging enhanced the ability of BATSE to locate and identify much weaker sources than step search algorithm permitted, and also allowed positional information for the transient sources to be obtained, allowing discrimination between sources in crowded regions such as the galactic center. Examples of images obtained with the Radon transformation, are shown in figure 2.6 for the Seyfert 2 galaxy NGC7582 and the high redshift quasar 4C71.07 (see next section).

2.5 BATSE observations of AGN

The challenging project to exploit the BATSE capabilities to study extragalactic objects, started in 1996 with a sample of Seyfert 2 galaxies studied by Bassani et al. (1996); this was the beginning of a large series of studies some of which are included in this thesis.

Of this first sample of 17 Seyfert 2 galaxies, BATSE detected in the 20-100 keV energy range, 59% of the observed objects at a confidence level $> 3\sigma$, giving for the first time a clear indication that Seyfert 2 are high-energy emitters, as expected by the unified theory (Bassani et al. 1996). This first sample has been widened and so far a total of 24 Seyfert 2s has been detected, among these are 6 new hard X-ray detections: MKN78, NGC3185, NGC4579, NGC7465, NGC7496 and NGC4395 (Westmore et al. 2000a). Some of these detections are from low luminosity Seyfert 2 galaxies like M51 (Westmore 2001) and NGC4258 (Dean et al. 2001). It is interesting to observe that these and other objects detected by BATSE (such as NGC4579 and NGC4395) have a very low Eddington luminosity ratio ($L/L_{Edd} \sim 10^{-3}$ - 10^{-4}) and yet they emit hard X-rays/gamma-rays. The ADAF models generally used to explain the emission from low luminosity AGNs are not always able to explain these observations (see also Fiore et al. 2001 for *BeppoSAX* data on NGC4258) indicating that some other mechanisms may be at work in these systems. An important result obtained with BATSE is the long term hard X-ray (~ 20 -1000 keV) study of the radio galaxy Cen A. This is the nearest AGN (< 5 Mpc) and so high quality data are available. BATSE detection of Cen A ($> 100\sigma$) allows us to perform a timing as well as a spectral analysis of the source. In fact, in this case a long term average spectrum has been obtained. This is well fitted with a broken power law with a cut-off energy at around 160 ± 30 keV, also it appears to vary such that the spectrum seems flatter (harder) when brighter and conversely steeper (softer) when fainter (Westmore et al. 2000b). BATSE monitoring of Cen A indicates two distinct timescales of variability and in figure 2.7 the long term light curve over the period 1991-1998 has been reported (Westmore et al. 2000b).

The date and time convention generally used for the BATSE data analysis is *Truncated Julian Date* (TJD) = Julian Date (JD) - 2,440,000.5 and therefore this will be used here and elsewhere. Inspection of figure 2.7 reveals a long term decline in mean flux over the 8 years of BATSE observation of approximately a factor of 4. Superimposed on the long term decrease, it is possible to observe flaring like activity with a timescale of a few hundreds days.

Similarly the long term monitoring of NGC4151 over ~ 6 years period, has been presented by Parsons et al. (1998). The source has been monitored both in 20-70 keV and 70-200 keV band and in both light curves intrinsic variability is observed with a fractional variation ratio of 2, or alternatively with difference between extrema normalized to the average flux of ~ 2 . The hardness ratio in these two bands further provides indication for a power law of photon index 1.6 exponentially cut-off as observed by OSSE (Johnson et al. 1997). No periodicity was found in the light curves.

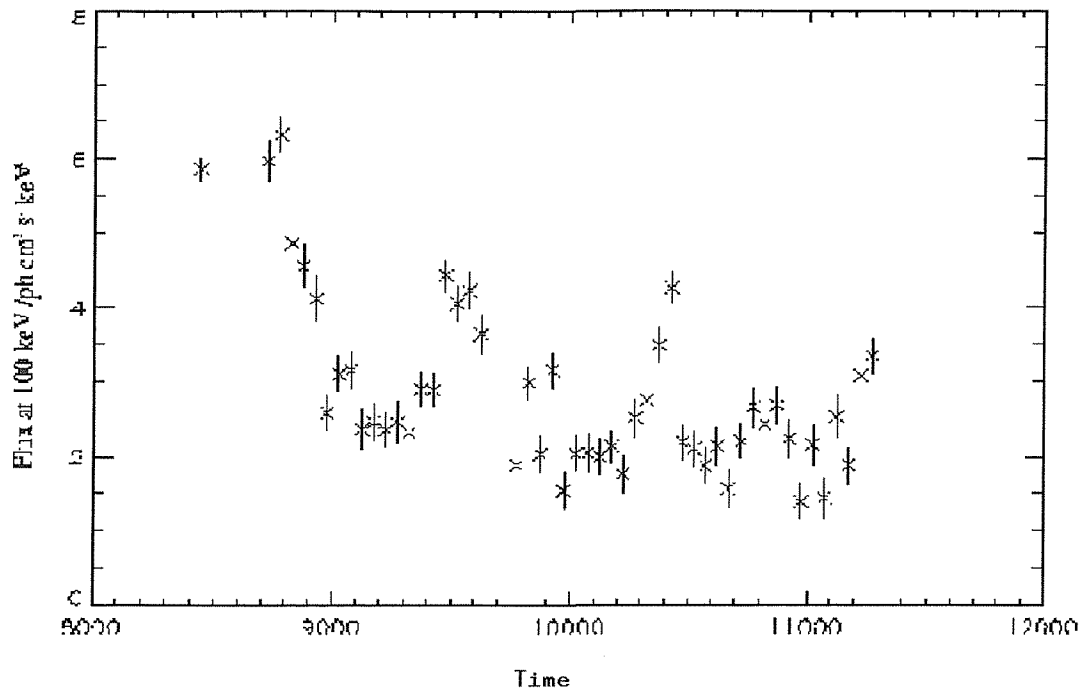


Figure 2.7: BATSE long term light curve of Cen A. The light curve plots 50 day average flux measurements over the period 1991-1998 (Westmore et al. 2000b).

Among AGN, blazars represent the most extreme and powerful sources. Their fundamental property is the beamed continuum due to plasma moving relativistically along the line of sight. This scenario is adopted to explain objects with somewhat different observational properties leading to different classifications/definitions. Objects with significant emission-line equivalent widths are usually classified as flat spectrum radio quasars (FSRQ), while objects without emission lines are classified as BL Lac objects. Different flavors of BL Lac objects have been found in radio and X-ray surveys and these also correspond to differences in the overall spectral energy distribution which have been interpreted either as due to orientation (Ghisellini & Maraschi 1989, Urry & Padovani 1995), or as intrinsic (Padovani & Giommi 1995). Nevertheless, while different sub-classes have different average properties, the actual distinction among them is certainly unclear and so far several sources have shown intermediate behavior. In fact, a continuity in the continuum spectral properties of BL Lac and FSRQ has been recently found (Fossati et al. 1998 and Ghisellini et al. 1998). BATSE is also well suited for the observations of blazar type objects which are well known to show flaring activity. In this context BATSE provides the opportunity to monitor large samples over a long time period in the hard X-rays. BATSE average fluxes between 20 and 200 keV range for a complete radio- and

X-ray selected BL Lac sample integrated over a 2 year period of observations, have been reported by Connaughton et al. (1998). A recent update of that study indicates that 31 BL Lac objects have fluxes of more than 7.0×10^{-4} ph cm $^{-2}$ s $^{-1}$ and are selected at a statistical significance of at least 6σ between 20 and 200 keV (Connaughton et al. 2001 private communication). Of course bright gamma-ray sources such as MKN501 and 1ES2344+514 are included. It is evident that BATSE offers the unique opportunity to detect some sources in high intensity state over timescales of years and this can be used to monitor for strong, hard flares that can trigger multi-wavelength campaigns. An important example of the kind of study that could be performed by BATSE in the blazars field, is the observation of the high-redshift quasar 4C 71.07 (Malizia et al. 2000a), reported in the following subsection.

2.5.1 BATSE observation of the high-redshift quasar 4C 71.07

BATSE observations of 4C71.07 supported by the OSSE data, indicated that this quasar was the brightest and farthest ($z=2.172$) active galactic nucleus detected above 20 keV at the time of the data analysis. BATSE occultation data over 3 years of observations (1994 December-1997 October) have been analyzed. The mean source flux over this period is $(1.32 \pm 0.11) \times 10^{-10}$ erg cm $^{-2}$ s $^{-1}$, implying a flux measurement of 12σ ; even increasing the error by 80% to account for residual systematic uncertainties evaluated by examining “blank sky field” (see chapter 4), the detection remains at a 7σ level and so it is highly significant. The flux estimations have been obtained converting the counts by folding a power-law model of photon index of 1.5 (similar to that observed in X-rays). However, to further check the reality of the detection an image of the sky region around 4C 71.07 has been produced (see figure 2.6, right). The long term light curve of 4C 71.07 is shown in figure 2.8 (left), where BATSE data have been combined in 60 days bins to enhance the statistical significance. A few flare like events are visible around 1995 April (TJD 9750-9900), 1996 January (TJD 10,000-10,200), 1996 November (TJD 10,350-10,400), and 1997 May (TJD 10,500- 10,600) separated by periods of low flux when the source is barely visible by BATSE. The crosses in figure 2.8 (left) correspond to the optical (R -band) measurements (Raiteri et al. 1998) that have been superimposed on the BATSE data to better investigate possible correlations. In fact, the first event corresponds to a period of medium brightness in optical (i.e., the flux in R was $\sim 20\%$ lower than observed during the big flare of 1992 reported by von Linde et al. 1993) and so it is compatible with the BATSE high state. More interesting is the second flare which corresponds to a period of optical flaring activity monitored in the R band (Raiteri et al. 1998); the source was at its historical maximum ($R=16.1$) on 1995 November 20 (TJD 10,042) about 55

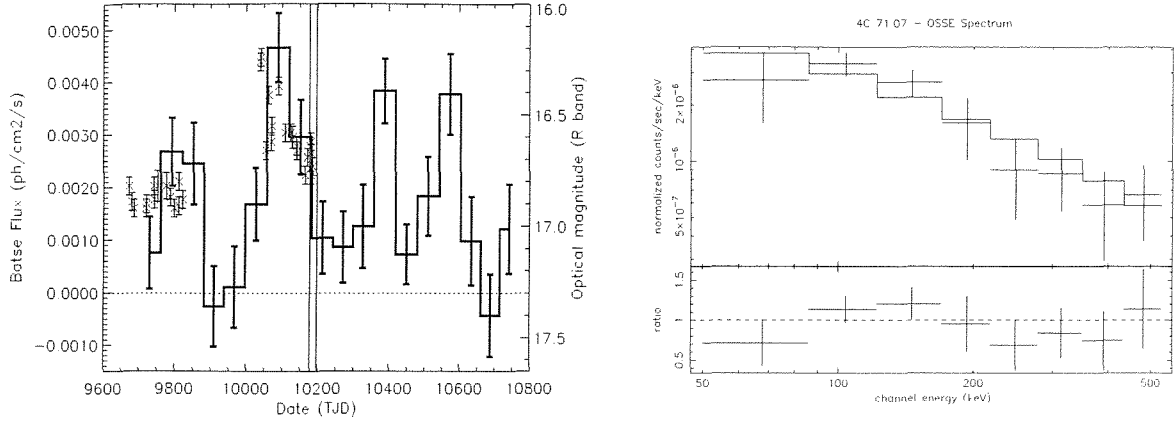


Figure 2.8: Left: BATSE light curve over 3 years period; each bin corresponds to a 60 days integration time. The crosses superimposed on the BATSE data correspond to optical (R band) measurements; the optical minimum has been set to $R = 17.4$ based on von Linde et al. (1993) results. The two vertical lines indicate the period of the OSSE observation. Right: OSSE count spectrum with residuals for a simple power-law of slope $\Gamma = 1.1 \pm 0.3$.

days before the BATSE peak on 1996 January 14 (TJD 10,097).

The optical peak is, however, highly structured with the second peak on 1995 December 8 and a third one on 1996 January 7; both peaks are characterized by a lower intensity in R than the first one. BATSE data do not have the same statistical quality of the optical monitoring to resolve these structures, but data are indicative of a similar broad structure. Unfortunately, no optical coverage is available during the other flare like events detected by BATSE. The source reached a 20-100 keV flux of $\sim 3 \times 10^{-10}$ erg cm⁻² s⁻¹ during the peak, but was back to its mean flux about 3 months later; the upper limit on the minimum timescale to double the flux is ~ 60 days, implying a size for the emission region of $\leq 5 \times 10^{16}$ cm. Also note that the change in flux observed during the 1995 November/1996 January event is a factor of 4.5 ± 0.5 in hard X-rays and 1.6 in optical. The mean observed 20-100 keV flux translates to a luminosity of 2.6×10^{48} erg s⁻¹. The BATSE/OSSE spectral analysis indicates that the source is characterized by a flat power law spectrum ($\Gamma \sim 1.1-1.3$) when in a low state; this spectral form is consistent within errors with the X-ray spectra, e.g. ASCA (Cappi et al. 1997) and ROSAT (Brunner et al. 1994). The data indicate that the power law observed from 0.1 to 10 keV extends up to 600 keV (or about 2 MeV in the QSO rest frame), but steepens soon after to meet EGRET high energy data (Thompson et al. 1993, Mukherjee et al. 1997). The OSSE count-rate spectrum and the data-to-folded model ratio is

shown in figure 2.8 (right). Furthermore, BATSE data taken around the 1996 January flare suggest that the spectrum could be steeper when the source is in a bright state. This is in contrast with the typical “flatter when brighter” behaviour of blazars, and this was the second source in which such behavior is observed (see Ghisellini et al. 1999 for the case of PKS 0528+134). BATSE/OSSE data have recently been confirmed by *BeppoSAX* measurements of the source, in which a similar spectral slope and luminosity have been found (Tavecchio et al. 2000). Several models have been put forward to explain the overall broad band spectral energy distribution (SED) of blazars. In the widely adopted scenario, a single population of high-energy electrons in a relativistic jet radiate from radio/FIR to UV-soft X-ray by the synchrotron process and at higher frequencies by Compton scattering soft-target photons present either in the jet (synchrotron self-Compton [SSC] model), in the surrounding medium (external Compton [EC] model), or in both (Ghisellini et al. 1998 and references therein). Then in the νF_ν representation of blazar SED, two peaks corresponding to the synchrotron and inverse Compton emission should be evident. The non simultaneous broad band spectral energy distribution of 4C71.07, adapted from Ghisellini et al (1998) is shown in figure 2.9 with the inclusion of OSSE, BATSE, and other data (Malizia et al. 2000a). A broad hump associated with the Compton peak is strongly inferred by the high energy data (OSSE/BATSE vs EGRET) and localized in the 10^{20} - 10^{22} Hz band; the corresponding synchrotron peak falls in a region of the spectrum localized between 10^{12} and 10^{14} Hz, where only upper limits from IRAS are available. Nevertheless, the data are consistent with the object being a low-frequency peaked or *red* blazar: the synchrotron and Compton spectra peak in the millimeter-FIR and MeV bands, respectively, and the X/gamma radiation completely dominate the radiative output. In these powerful blazars, the contribution from the external radiation to the cooling is supposed to be the greatest (Ghisellini et al. 1998); thus the EC model should be favored with respect to the SSC model. In figure 2.9 the SED from the SSC and EC models are superimposed on the data of 4C71.07. It is evident from the figure that neither version of the theoretical modeling fits the data well, since both models are unable to reproduce the radio data below 100 GHz. Furthermore, while the IRAS upper limits favor the SSC model over the EC, the high-energy data support the inverse. A major drawback in such type of analysis, and also a possible explanation for obtaining contradictory results, is the fact that the broad-band data come from different epochs: source variability, which is extreme in 4C71.07, may invalidate tests based on non contemporaneous measurements. Nevertheless, we can rely on alternative ways to constrain models, for example by examining the possible flatter state of the source when brighter.

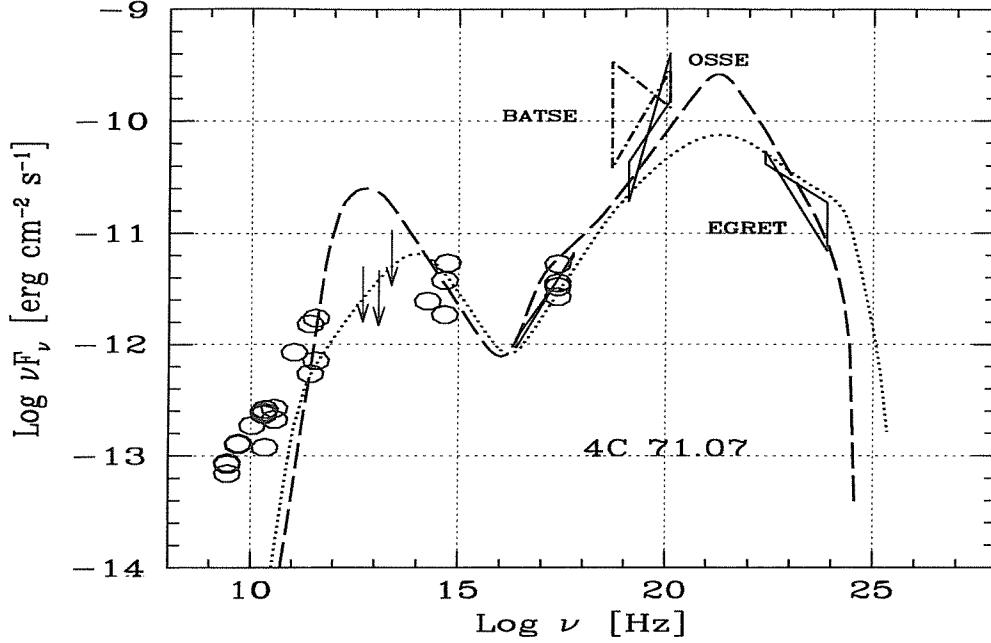


Figure 2.9: Overall spectral energy distribution of 4C71.07 adapted from Ghisellini et al. (1998) plus BATSE and OSSE measurements from Malizia et al. (2000) and V data point from McIntosh et al. (1999). The 12, 25 and 60 micron upper limits have been estimated by comparison with IRASFSC catalogue data obtained from objects located within 4 degrees of the QSO. The SSC and EC models are superimposed on the data as dotted and dashed lines respectively.

Ghisellini et al. (1999) have recently proposed a scenario to explain this behaviour in PKS0528+134, a source very similar to 4C71.07 (i.e. a low-frequency-peaked/gamma-ray-dominated blazar). Their suggestion is that the high-energy flux is produced by both the SSC and EC processes. If the radiation densities of these two components are compatible, then the EC component dominates and is entirely responsible for the gamma-ray emission. If, on the other hand, the source power increases, then the SSC component becomes more important and therefore it becomes the main contributor to the high energy flux over a larger energy range. If this also happens in 4C71.07, then the two gamma ray states could correspond to different electron injected powers (larger and flatter in the high state). In any case, a contribution from both the SSC and EC components is required in each state.

Chapter 3

BeppoSAX

3.1 The satellite and the scientific instruments

The Italian-Dutch X-ray satellite SAX (*Satellite italiano per Astronomia X*), later named *BeppoSAX* in honor of Giuseppe (Beppo) Occhialini, was successfully launched in April 1996 (Boella et al. 1997a) directly into a 600 km, 96 min orbit at 3.9° inclination. This is a very important technical characteristic of *BeppoSAX* in particular for the capabilities of the high energy instruments, since it nearly avoids the South Atlantic Anomaly and takes full advantage of the screening effects of the Earth's magnetic field in reducing the amplitude and modulation of the cosmic-ray induced background. *BeppoSAX* is the first X-ray satellite covering more than three decades of energy (0.1-300 keV) with a relatively large area and low background, good energy resolution and imaging capabilities (resolution of $\sim 1'.5$) in the energy range 0.1-10 keV, and unprecedented sensitivity above 20 keV. These unique capabilities are provided by a set of 4 instruments co-aligned with the Z-axis of the satellite (see figure 3.1), called Narrow Field Instruments (NFI).

The NFI consist of:

- LECS (Low Energy Concentrator Spectrometer, Parmar et al. 1997) a low energy telescope sensitive between 0.1 and 10 keV, with a thin-window position-sensitive gas scintillation proportional counter in its focal plane.
- MECS (Medium Energy Concentrator Spectrometers, Boella et al. 1997b), a medium energy (1.5-10 keV) set of three identical telescopes with position-sensitive gas scintillation proportional counters in their focal plane. Unfortunately on 1997 May 6th a technical failure caused the switch off of unit MECS1 and all observations after this date are performed with two units (MECS2 and MECS3).

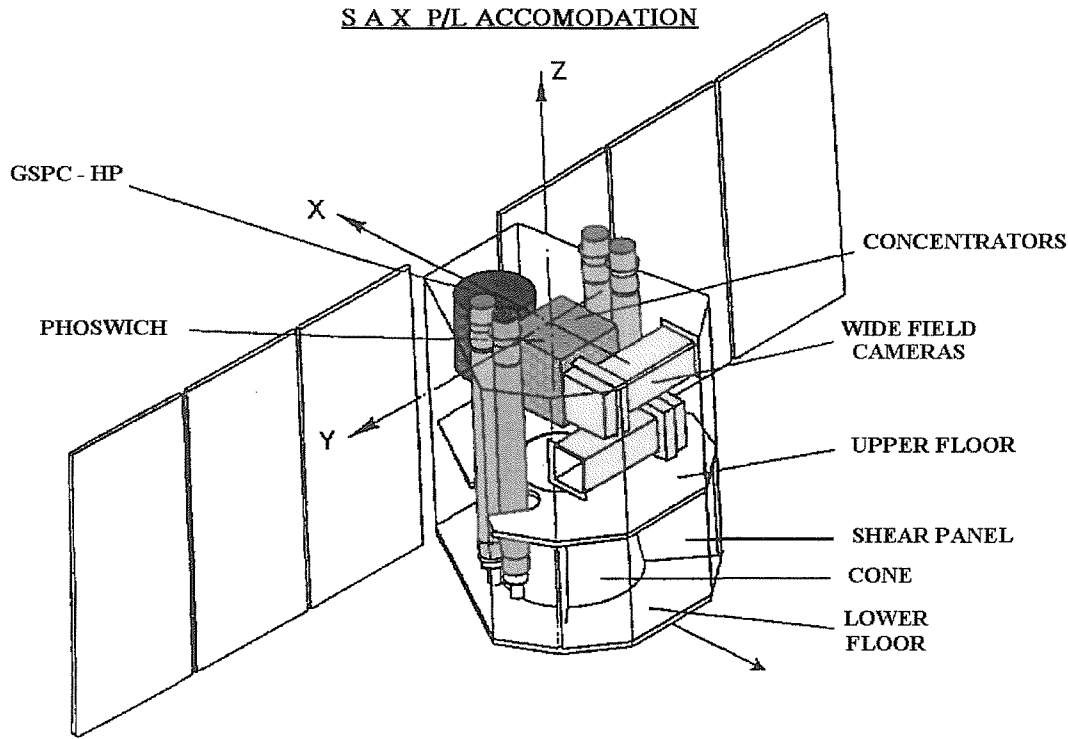


Figure 3.1: *BeppoSAX* payload accommodation

- HPGSPC, a collimated High Pressure Gas Scintillator Proportional Counter (Manzo et al. 1997) operating in the energy range 4-120 keV.
- PDS, a collimated Phoswich Detector System (Frontera et al. 1997) operating at higher energies: higher then 15 keV (see next section).

Perpendicular to the NFI axis there are two coded mask proportional counters: the Wide Field Cameras (WFC, Jager et al. 1996). They point at the opposite directions of the NFI and provide observations of large regions of the sky in the energy band 2-30 keV. Each WFC has a field of view of $20^\circ \times 20^\circ$ (FWHM) with a resolution of $5'$. Finally, the anticoincidence scintillator shields of the PDS are used as monitor of gamma-ray bursts in the band 40-700 keV with a fluence greater than about 10^{-6} erg cm $^{-2}$ and with a temporal resolution of about 1 ms.

In table 3.1 the main characteristics of the *BeppoSAX* instruments have been summarized.

Table 3.1: *Beppo*SAX Instruments

| Instrument | Range (keV) | Field (° FWHM) | Angul. Res. (arcmin) | Area (cm ⁻²) | Energy Res. (%FWHM) |
|------------|----------------|-------------------|-------------------------|-----------------------------|---------------------------|
| 1 LECS | 0.1-10 | 0.5 | 3.5@0.25 keV | 22@0.25 keV | $8 \times (E/6)^{-0.5}$ |
| 3 MECS | 1.3-10 | 0.5 | 1.2@6 keV | 150@6 keV | $8 \times (E/6)^{-0.5}$ |
| 1 HPGSPC | 4-120 | 1.1 | collimated | 240@30 keV | $4 \times (E/60)^{-0.5}$ |
| 1 PDS | 15-300 | 1.3 | collimated | 600@80 keV | $15 \times (E/60)^{-0.5}$ |
| 2 WFC | 2-30 | 20×20 | 5 | 140@80 keV | $18 \times (E/6)^{-0.5}$ |

3.2 The Phoswich Detector System

In this thesis the PDS data will be used to investigate the spectroscopic properties of active galactic nuclei at high energies. Therefore, in this section the main technical characteristics of the PDS instrument will be briefly illustrated.

The PDS operates in the hard X-ray band (15-300 keV) and allows high sensitivity spectroscopy and temporal studies of X-ray sources to be performed at this energy range. It consists of a square array of four independent scintillation detectors each of them comprising two crystals of NaI(Tl) and CsI(Na) optically coupled and forming a detector system named PHOSWICH, acronym of PHOSphor sandWICH (PHW). Among the events (photons or charged particles) detected in each phoswich, those with energy deposited only in the NaI crystal are considered *good*, while those that deposit their energy only in the CsI crystal or in both crystals are rejected. A Pulse Shape Analyzer (PSA) can electronically discriminate between events of these three classes. The phoswich configuration is well known to provide a high detection efficiency and a very low background level. Furthermore, since the accepted photons lose energy in the NaI(Tl) alone, the energy spectra provided by phoswiches are not affected by biases as in a single crystal detector. The total geometric area is 795 cm².

In order to further reduce the PHW background level, an anticoincidence (AC) shield system is implemented to surround the sides and the front of the detector and the two collimators (lateral, top and PHW shields). As already mentioned, the AC lateral shields are also used as Gamma-Ray Burst Monitors (GRBM). The signals from each slab are sent both to a Pulse Height Analyser and a GRBM logical unit, where the trigger condition is checked. A GRB event is triggered when at least two of the four lateral shields satisfy the trigger condition.

Between the top shield and the phoswich detector units there are two X-ray collimators, one for each pair of detectors. They define a hexagonal field of view which is on the

Table 3.2: PDS main characteristics

| Parameter | Value |
|-----------------------------------------|------------------------------------|
| Energy range | 15-300 keV |
| Total area through collimator | 640 cm ⁻² |
| Field of view (FWHM) | 1.3 degrees (hexagonal) |
| Detection plane | 4 NaI(Tl)/CsI(Na) square PHW units |
| Energy resolution at 60 keV | ≤15% (average) |
| Maximum time resolution | 16 μs |
| Gain control accuracy | 0.25% |
| In-flight calibration accuracy | 0.1% |
| Minimum channel width of energy spectra | 0.3 keV |
| Maximum throughput | 4000 events s ⁻¹ |

average 1.3 degrees Full Width at Half Maximum (FWHM) along the normal direction. Each of the two collimators can be rocked back and forth with respect to its normal position independently of the other. The maximum rocking angle is ± 3.5 degrees ($210'$) with intermediate steps of $\pm 30'$, $\pm 60'$, $\pm 90'$ and $\pm 150'$, the minimum dwell time in each step is 50s and a transit time from one position to another is less than 3 seconds. The collimator rocking allows the X-ray source and the background levels to be almost simultaneously monitored at various offset angles.

The standard observation strategy is to continuously monitor background and source+background with both collimators following a cyclic law: while one collimator points at the source the other points at the blank (non source-contaminated) sky field for background measurement. After each cycle the two collimators are swapped. The default collimator law samples alternatively two background fields on opposite sides of the target source at the maximum rocking angle, that is ON/ $+210'$ (OFF)/ON/ $-210'$ (OFF). The collimator law is fully programmable, therefore any other convenient choice can be made.

Apart from the low background, the PDS functional performance is guaranteed by the well known detector window transparency and by a good energy resolution defined as $R(E) = \Delta E/E$ where ΔE is the FWHM of a line at energy E seen by the detector. The energy resolution of the NaI(Tl) detector units is 15% at 60 keV with a dependence on energy that can be approximated by the function.

$$R(E) = K(E/60)^\alpha \quad (3.1)$$

where $K=0.15$, $\alpha=0.5$ and E is expressed in keV.

The main characteristics of the PDS are summarized in table 3.2.

3.3 BeppoSAX scientific capabilities and its success of four years of mission

The main scientific capabilities of the *BeppoSAX* mission are the unprecedented combination of the following characteristics:

- Spectroscopy and timing of galactic and extragalactic sources over a very wide energy band from 0.1 to 300 keV
- Relatively large area and low background
- Spatially resolved spectroscopy of 1 *arcmin* in the 0.1-10 keV range
- Good sensitivity of the scientific payload and balanced performances of the low energy and high energy instruments. (This allows the exploitation of the full band of *BeppoSAX* for sources as weak as 1 mCrab)
- Monitoring of wide regions of the sky in the range 2-30 keV and 40-700 keV for the search of X-ray transients and gamma ray bursts, precise localization of these events with the WFC and fast follow up with NFI instruments. The importance of the Target of Opportunities (TOO) triggered so far, is successfully demonstrated by the gamma-ray burst experience (Costa 1998).

Thanks to its very good scientific performances, *BeppoSAX* has made a large contribution to the field of X-ray astronomy. During the five years of the mission, *BeppoSAX* observations have not only helped in clarifying the X-ray properties of well known classes of X-ray emitting sources like galactic pulsars, black hole candidates, AGN and clusters of galaxies, but allowed advances to be made in the field of X-ray bursters and especially in the field of GRB science. For more than twenty years after their discovery, the origin of gamma-ray bursts has remained one of the unresolved questions in astrophysics. This has been largely due to difficulties in identifying a counterpart and to the absence of an accurate position of the source, except for a few cases. Combining instrumental and operational capabilities, with *BeppoSAX* it is possible to detect the gamma-ray event just with the GRBM, determine its position within a few *arcmin* with the WFCs in less than 2-4 hours and finally carry out a fast (within 6-8 hours after the event) follow up observation with the NFI instruments. This procedure led to the first discovery of an X-ray afterglow in GRB970228 (Costa et al. 1997). From the launch date up to Sept 2000, *BeppoSAX* has observed 46 GRB, in 31 of them it was possible to observe the X-ray afterglow, and for a $\sim 50\%$ of them the optical counterpart has been identified. For

the work on the gamma-ray bursts, the *BeppoSAX* Team was awarded the "Bruno Rossi 1998" prize by the American Astronomical Society. Finally, it is worth noting the large number of Targets Of Opportunity (TOO) and coordinated observations with on-ground and space observatories performed by *BeppoSAX*. These are of extreme importance, firstly to promptly observe a source in a particular state, see the X-ray transients (e.g. Campana et al. 1998) and the BL Lacs cases (Pian et al. 1998, Malizia et al. 2000b) and secondly to identify counterparts of new hard X-ray sources or study the complex physics occurring in them (i.e. Israel et al. 2001, Covino et al. 2001, Malizia et al. 2000c). Until September 2000 *BeppoSAX* NFIs have performed more than 1150 observations of every kind of X-ray emitter.

3.4 *BeppoSAX* and AGN studies

BeppoSAX is providing a great contribution to our knowledge of active galactic nuclei. Since its best characteristics are the wide energy band and the high sensitivity, the results obtained so far mainly concern the broad band spectra of the bright AGN and the identification of weak sources at high energies. In this context the greatest contribution comes from the observations of Seyfert galaxies. Their X-ray spectra can be described in terms of a complex model, with broad and narrow components, which can be variable, and which are generally interpreted as due to accretion onto a supermassive black hole within a structured gaseous environment. The *BeppoSAX* Narrow Field Instruments offer the first and the unique opportunity to cover simultaneously all these model components. In five years of the mission we have had the opportunity to investigate each of them deeply. Aspects such as the nature of the circumnuclear matter surrounding the black hole responsible for soft excess, warm and cold absorption, iron line, Compton reflection as well as high energy cut-off of the primary power law component can all be studied. However due to the poorer energy resolution of *BeppoSAX* with respect to ASCA, no major advances about the iron line, especially for the narrow ones, have been made. Where *BeppoSAX* is giving its greatest improvement to previous knowledge is in the high energy part of the spectrum i.e. in the measurements of the Compton reflection and the high energy cut-off as well as in the measurement of absorbing column densities in excess of 10^{24} atoms cm^{-2} . In fact, the first is revealed by a broad bump emerging on top the primary power law at energies greater than 10 keV; the second is expected to occur above a few tens of keV, while the third one can only be evaluated by observing the source above ~ 10 keV. In table 3.3 we report the *BeppoSAX* measurements of the primary power-law slope (Γ), the amount of the reflected radiation (R), the iron-line

Table 3.3: Seyfert 1s Broad Band Results

| Source | Γ | R | EW (eV) | E_c (keV) | Ref |
|-------------|------------------------|------------------------|---------------------|---------------------|-----|
| Fairall 9 | $2.05^{+0.11}_{-0.09}$ | $1.2^{+0.7}_{-0.5}$ | 220^{+60}_{-100} | >220 | 1 |
| NGC 4151 | $1.35^{+0.20}_{-0.20}$ | $0.45^{+0.20}_{-0.20}$ | 240 ± 70 | 70 ± 20 | 2 |
| NGC5548 | $1.63^{+0.04}_{-0.03}$ | $0.44^{+0.18}_{-0.18}$ | 120 ± 40 | 160^{+50}_{-70} | 3 |
| NGC5506 | $2.02^{+0.09}_{-0.08}$ | $1.20^{+0.45}_{-0.35}$ | 152^{+45}_{-35} | >298 | 4 |
| NGC7469 | $1.97^{+0.05}_{-0.10}$ | $0.66^{+0.37}_{-0.30}$ | 146^{+48}_{-53} | 235^{+594}_{-110} | 4 |
| IC4329A (1) | $1.86^{+0.03}_{-0.03}$ | $0.55^{+0.15}_{-0.13}$ | 110^{+50}_{-40} | 270^{+170}_{-80} | 5 |
| IC4329A (2) | $1.90^{+0.05}_{-0.05}$ | $0.73^{+0.22}_{-0.18}$ | 123^{+46}_{-36} | 262^{+204}_{-84} | 4 |
| MCG-6-30-15 | $2.06^{+0.03}_{-0.03}$ | $1.2^{+0.4}_{-0.2}$ | 200^{+50}_{-60} | 160^{+130}_{-60} | 6 |
| NGC 4593 | $1.87^{+0.05}_{-0.05}$ | $1.1^{+0.4}_{-0.4}$ | 190^{+90}_{-6} | >150 | 7 |
| NGC 3516 | $2.07^{+0.20}_{-0.08}$ | $1.4^{+1.8}_{-0.9}$ | 100^{+50}_{-60} | >250 | 8 |
| MKN 509 | $1.62^{+0.04}_{-0.05}$ | $0.6^{+0.4}_{-0.3}$ | 120 ± 60 | 80^{+20}_{-30} | 9 |
| MCG+8-11-11 | $1.84^{+0.05}_{-0.05}$ | $0.98^{+0.56}_{-0.39}$ | 130^{+80}_{-60} | 170^{+300}_{-80} | 9 |
| MKN 841 | $2.16^{+0.07}_{-0.05}$ | $3.9^{+1.2}_{-1.2}$ | 290^{+210}_{-220} | >150 | 1 |
| NGC 3783 | $1.77^{+0.04}_{-0.04}$ | $0.63^{+0.20}_{-0.17}$ | 161^{+39}_{-37} | 156^{+37}_{-40} | 4 |

Ref: 1) Matt 2000a, 2) Piro et al. 2001, 3) Nicastro et al. 2000, 4) Perola et al. 2001, 5) Perola et al. 1999, 6) Guainazzi et al. 1999a, 7) Guainazzi et al. 1999b, 8) Costantini et al. 2000, 9) Perola et al. 2000

equivalent width (EW) and the high energy cut-off E_c for the brightest Seyfert 1s which have so far been reported in the literature (see table for references).

Only in a couple of Seyfert 1s (NGC7469 and MKN 509) has *BeppoSAX* found a soft excess component, while for a few of them (NGC4593, IC4329A, MKN509, MCG+8-11-11, NGC5548) absorption edges at low energies (0.7-1 keV) from ionized species of oxygen have been detected and interpreted as evidence for the existence of warm gas in the AGN. Before *BeppoSAX*, the high energy cut-off was unambiguously detected only in NGC4151 (i.e. Jourdain et al. 1992). Zdziarski et al. (2000) have estimated an average cut-off energy of a few hundreds of keV by summing several spectra obtained from OSSE observations. As shown in table 3.3, the high-energy cut-off is now positively detected in about half of the sample sources and the values range from 70 keV (NGC4151) to 270 keV (IC4329A). Recently *BeppoSAX* results indicate the existence of a possible correlation between the cut-off energy (E_c) and the photon index, with E_c increasing on average with Γ (Perola et al. 2001).

Also the Compton reflection R seems to correlate with Γ in the sense that flatter ob-

Table 3.4: Radio Galaxies Broad Band Results

| Source | Γ | N_H^* | EW (eV) | R | E_c (KeV) |
|--------------|------------------------|---------------------|-------------------|---------------------|--------------------|
| Pictor A | 1.63 ± 0.06 | 0.42(fixed) | <102 | - | - |
| 3C120 | $1.80^{+0.12}_{-0.30}$ | $2.4^{+1.8}_{-1.3}$ | 59^{+82}_{-42} | 0.7 ± 0.4 | 1.9^{+125}_{-77} |
| 3C111 | 1.65 ± 0.04 | $7.1^{+0.9}_{-0.8}$ | 58^{+31}_{-55} | <0.3 | >90 |
| 3C390.3 | $1.80^{+0.05}_{-0.04}$ | 1.3 ± 0.2 | 136^{+40}_{-36} | $1.2^{+0.4}_{-0.3}$ | >123 |
| 3C382 | 1.79 ± 0.04 | 0.88(fixed) | 31^{+44}_{-15} | $0.4^{+0.3}_{-0.2}$ | 155^{+148}_{-59} |
| Cen A (1997) | $1.76^{+0.04}_{-0.06}$ | 98^{+20}_{-30} | 166^{+38}_{-32} | 0.2 ± 0.1 | 286^{+257}_{-94} |
| Cen A (1998) | $1.73^{+0.05}_{-0.04}$ | 92^{+30}_{-10} | 57 ± 18 | 0.1 ± 0.1 | 297^{+156}_{-79} |

(\star) in units of 10^{21} cm^{-2}

jects have less reflection than steep ones (Perola et al. 2001), whether these correlations are real or an effect of the poor statistics still affecting the high-energy band is not clear, and we need more sensitive observations to confirm these preliminary results.

Furthermore, a powerful tool for studying the underlying emission mechanism within a source is the broad-band spectral variability which allows us the study of correlations between different components and hence their origin and location. *BeppoSAX* is very well suited for this purpose and in fact a few of the brightest Seyferts have been systematically monitored (see NGC4151, Piro et al. 2001; NGC7469, De Rosa et al. 1999; NGC5548, Nicastro et al. 2000). In particular in the case of NGC4151 the broad band spectral coverage combined with the variability analysis has allowed us to characterize the intrinsic continuum and the various spectral components (Piro et al. 2001). Piro et al. (2001) found that the intrinsic power law steepens when the luminosity increases, in agreement with previous results. During these variations an increase in the cut-off energy from $50 \pm 10 \text{ keV}$ to $80^{+40}_{-20} \text{ keV}$ when the spectrum gets steeper has also been found. The authors confirmed the presence of a complex absorption which varies on timescales of months-years; finally new evidence for variations in the absorption on timescales as short as a day has been reported.

The exceptional case of NGC4051, a well known Seyfert 1 galaxy with a large X-ray flux variability on relatively short ($\sim 10^4 \text{ s}$) timescales (Lawrence et al 1987, Matsuoka et al. 1990, Guainazzi et al. 1996, Uttley et al. 1998) is of particular interest. *BeppoSAX* observed NGC4051 in an ultra-dim and steady state; the 2-10 keV flux ($1.26 \times 10^{-12} \text{ erg cm}^{-2} \text{ s}^{-1}$) was about 20 times fainter than its historical average value. Its flat spectrum ($\Gamma \simeq 0.8$) and the intense iron line ($\text{EW} \simeq 600 \text{ eV}$) are best explained with a switched off active nucleus. What *BeppoSAX* observed was only the Compton reflection component

Table 3.5: Compton thin Broad Band Results

| Source | Γ | N_H^* | EW (eV) | R | Ref |
|-------------|------------------------|------------------------|---------------------|------------------------|-----|
| NGC2110 | 1.7 ± 0.1 | $4.1 \pm 0.2^\dagger$ | 180 ± 30 | < 0.2 | 1 |
| NGC7582 | $1.95^{+0.09}_{-0.18}$ | $14.4^{+0.9}_{-1.0}$ | 100-150 | - | 2 |
| NGC7172 | 1.90 ± 0.3 | $11.5^{+12.5}_{-10.5}$ | 224^{+650}_{-54} | $1.0^{+2.7}_{-0.4}$ | 1 |
| NGC4507 | 2.00 ± 0.1 | 70 ± 15 | 120^{+292}_{-68} | 0.4 ± 0.1 | 1 |
| MKN3 | 1.80 ± 0.1 | 130^{+15}_{-25} | 997^{+300}_{-307} | 0.9 ± 0.1 | 1 |
| MCG-5-23-16 | 1.81 ± 0.05 | $1.63^{+0.9}_{-0.9}$ | 96^{+37}_{-28} | $0.66^{+0.25}_{-0.20}$ | 3 |

(\star) in units of 10^{22} cm^{-2}

Ref: 1) Bassani et al. 1999a and references therein, 2) Turner et al. 2000, 3) Perola et al. 2001.

arising from a reflector far away from the nucleus (the "torus" or the dust lanes visible in the high-resolution optical images) which can lag the primary emission by weeks or more (Guainazzi et al. 1998).

In the unified schemes of AGN, the radio-loud counterpart of Seyfert 1s are the Broad Line Radio Galaxies (BLRG). In table 3.4 the *BeppoSAX* results on a sample of 5 BLRG plus one Narrow Line Radio Galaxy (NLRG), Centaurus A taken from Grandi (2000), have been reported. From the spectral parameters shown in table 3.4 it is evident that the broad-band spectra of radio-galaxies are complex and varied. *BeppoSAX* analysis of this class of AGN shows that, while the BLRGs are quite similar to Seyfert 1s (see Perola et al. 2001) for their continua and cutoff energies (when detected), the iron line, always detected in Seyfert 1s, is measured only in a half of the BLRGs observed and no signature of warm absorber, rather common in type 1 objects, has been detected. Moreover, a cold absorbing column in excess of the Galactic one is observed not only in Centaurus A, but in half of the BLRGs.

The PDS turns out to be of primary importance especially for the study of the type 2 objects whose spectra in the X-ray band show absorption by neutral matter significantly in excess of the Galactic one along the line of sight. A large observation time has already been dedicated to the study of the type 2 objects. The Seyfert 2 objects can be divided in Compton thin sources where the nucleus is obscured along our line of sight by cold and dense matter whose density can range from a few $10^{22-24} \text{ cm}^{-2}$ and Compton thick sources with column densities greater than $1.5 \times 10^{24} \text{ cm}^{-2}$. In table 3.5 the major results of *BeppoSAX* for the Compton thin Seyfert 2 have been summarized from the literature. One striking *BeppoSAX* result evident from table 3.5, is the wide range of absorption

found: although the sample is small, the column densities span 2 order of magnitudes and 4 out of 6 objects have $N_H > 10^{23} \text{ cm}^{-2}$. Note that in the case of NGC2110 and NGC7582 the value of the column density is referred to the total absorption, in fact in these sources the best favored model is the "dual absorber" whereby the line of sight passes through two absorbers (Malaguti et al. 1999, Turner et al. 2000).

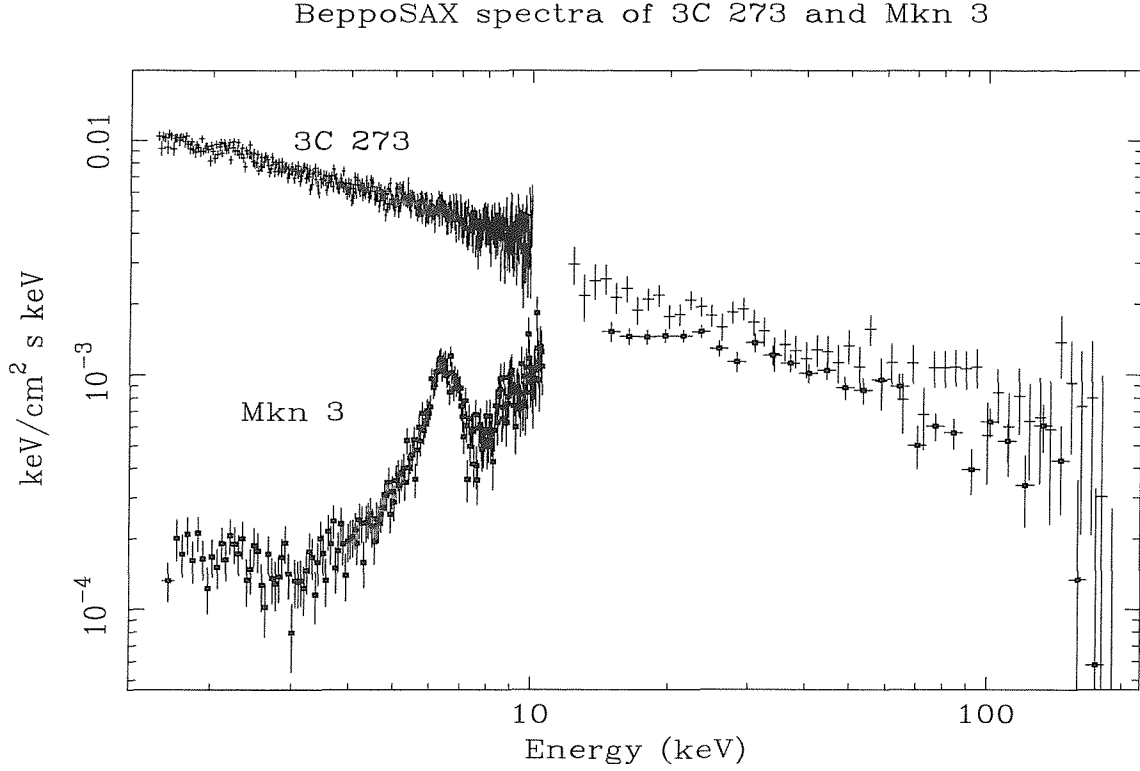


Figure 3.2: *BeppoSAX* broad band spectrum of the Seyfert 2 Mkn3 compared with the bright QSO 3C273 (Bassani et al. 1999)

For N_H in the range 10^{24} - 10^{25} cm^{-2} , the source is thick in the 2-10 keV band but still "thin" to Compton scattering in the 10-100 keV range as X-rays of these energies can still penetrate the torus allowing an estimate of the source column density to be made. These borderline objects are well represented by MKN3 (Cappi et al. 1999a) which turns out to be particularly bright in hard X-rays (above 10 keV). At these energies the transparency effect is coupled with a strong reflection but at lower energies the primary continuum is totally absorbed and only emission reflected by the torus reaches the observer. In figure 3.2 the *BeppoSAX* broad band spectrum of MKN3 by Bassani et al. (1999a) is compared to that of 3C273 to show that the emission is absorbed below 10 keV, but similar to the bright QSO above this energy. *BeppoSAX* observations of Seyfert 2 indicate that,

Table 3.6: Compton thick main properties

| Source | N_H^* | CR | WR | L_X^\dagger |
|-----------------|---------|--------|--------|---------------|
| NGC1068 | >10 | Yes | Yes | ?(>1) |
| Circinus Galaxy | 4.3 | Yes | No(?) | ~0.01 |
| NGC6240 | 2.2 | Yes(?) | Yes | ~1.2 |
| MKN3 | 1.1 | Yes | Yes | 0.9 |
| NGC7674 | >10 | Yes | No(?) | ? |
| NGC4945 | 2.2 | No | No | ~0.03 |
| TOL 0109-383 | 2.0 | Yes | Yes(?) | ~0.2 |

(\star) in units of 10^{24} cm^{-2} , (\dagger) 2-10 keV luminosity in units of $10^{44} \text{ erg s}^{-1}$

on average, these objects are intrinsically similar to Seyfert 1 galaxies and that the main differences are due to the different amount of absorbing material along the line of sight. This proves, at least qualitatively, what is expected from the "0th-order" version of the unified model (Cappi et al. 1999b). MKN3 is one of the 7 Compton thick sources so far detected by *BeppoSAX*: they are listed in table 3.6 together with their associated column densities N_H , cold reflection (CF), warm reflection (WR) and X-ray luminosities (Matt et al. 2000b and references therein). *BeppoSAX* has investigated the spatial distribution of the X-ray absorption matter and, in particular, the covering factor as it changes the importance of Compton scattering into our line of sight of photons initially emitted in other directions (Matt, Pompilio and La Franca 1999). In 5 out of the 7 observed sources, the nucleus is directly visible at high energies where the photons penetrate the absorbers, while in NGC 1068 and NGC 7674, the nucleus is totally obscured at all energies implying even larger column densities. In most sources there is unambiguous evidence of a reflection from optically thick cold matter; while in two (or maybe four) cases there is also evidence of reflection from ionized matter.

Finally, *BeppoSAX* has demonstrated that the average N_H of type 2 Seyfert is very much higher than that deduced from previous surveys. Maiolino et al. (1998) have performed *BeppoSAX* observations of a sample of Seyfert 2 selected according to their [OIII] optical emission flux, to avoid biases against obscuration on pc scale. The sample objects turn out to be weak AGN characterized by prominent iron lines (at 6.4-7 keV) and flat observed X-ray continua. All of the 8 targets have been detected in the 2-10 keV band but only two of them have also a detection in the 20-100 keV band. All the sources exhibit column densities larger than $4 \times 10^{23} \text{ cm}^{-2}$ along the line of sight and most of them appear to be thick to Compton scattering with $N_H > 10^{24} \text{ cm}^{-2}$. This result is

of tremendous importance in the study of the hard X-ray background, as it provides for the first time the distribution of column densities in Seyfert 2 galaxies. In fact, using *BeppoSAX* data Risaliti et al. (1999) derived the distribution of the absorbing column densities among Seyfert 2 galaxies in the local universe: 75% of all Seyfert 2 galaxies in their sample resulted heavily obscured ($N_H > 10^{23} \text{ cm}^{-2}$) and about half are Compton thick ($N_H > 10^{24} \text{ cm}^{-2}$).

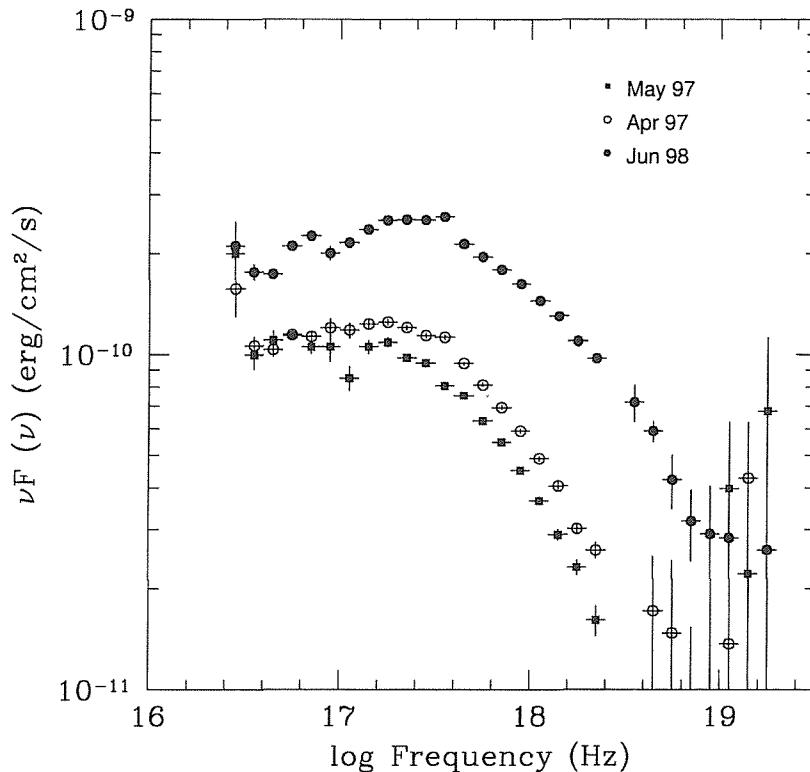


Figure 3.3: 0.01-100 keV spectra of Mkn421 during three *BeppoSAX* observations multiplied by the frequency.

Among AGN, blazars are the objects most dominated by non thermal continuum emission, which extends from radio to gamma rays (see section 2.5.1) and among blazars, BL Lacertae objects are the sources with the highest variety of synchrotron peak frequencies, ranging from IR-optical to UV-soft-X ray bands, called Low- or High-energy peak BL Lacs, i.e. LBL or HBL respectively (Padovani & Giommi 1995). *BeppoSAX* turns out to be very well suited for the study of the Blazars objects, and in particular for the BL

Lac subset. In fact direct measurements of the Compton part of the spectrum have been obtained for a number of LBLs (e.g. Padovani et al. 1999), and the variable tail of the synchrotron component has been studied in several HBLs (e.g. Pian et al. 1998, Wolter et al. 1998, Giommi et al. 1999, Chiappetti et al. 1999). In the case of two intermediate BL Lacs S5 0716+714 and ON 231, *BeppoSAX*, for the first time, was able to detect both spectral components within a single instrument (Giommi et al. 1999, Tagliaferri et al. 2000). Recently a study of extreme synchrotron BL Lac objects ($\nu_{peak} > 1$ keV) observed by *BeppoSAX*, has been reported by Costamante et al. (2001). Of the seven sources analyzed by Costamante et al. (2001), five revealed or confirmed their extreme nature. Four showed peak frequencies in the range 1-5 keV, while one (1ES 1426+428) displayed a flat power law spectrum ($\alpha_X = 0.92 \pm 0.04$) which locates its synchrotron peak at or above 100 keV. This is the third source of this type ever found after MKN501 and 1ES 2344+514. Furthermore, BL Lac objects are characterized by strong variability both in the amplitude of the flux and in the shape of the continuum. In this respect, *BeppoSAX* has monitored the brightest BL Lacs in their low and high states, following the changing spectral shape during a flare event (see for example the cases of MKN 501, Pian et al. 1998; ON 231, Tagliaferri et al. 2000; MKN 421, Guainazzi et al. 1999c, Malizia et al. 2000b, Fossati et al. 2000a,b). Just in the case of MKN 421 we have exploited the full *BeppoSAX* capabilities. The source was detected in a dim state during the April 1997 observation (Guainazzi et al. 1999) and one year later (June 1998) a TOO was performed, thanks to a trigger in the WFC when MKN 421 was at a flux level of ~ 20 mCrab. Historically that was the highest state detected for this source (Malizia et al. 2000b). In figure 3.4 the 0.01-100 keV *BeppoSAX* spectra of MKN 421 obtained in the period May 1997-June 1998 multiplied by the frequency are shown.

Finally, it is worth noticing that many serendipitous hard sources have been discovered in the MECS field of view. Sometimes these have been observed only above a few keV, and later classified as AGN by means of follow-up optical identifications. In particular, the good sensitivity of the MECS detectors (5-10 keV flux limit of 0.002 mCrab in 100 Ks, Boella et al. 1997b) and their improved point spread function (PSF), provided an ideal tool for the High Energy Large Area Survey (HELLAS) project. The HELLAS survey has so far catalogued 180 sources (Fiore et al. 1999) in about 50 deg^2 of the sky down to a limiting flux of $5 \times 10^{-14} \text{ erg cm}^{-2} \text{ s}^{-1}$. Most of these sources are identified with AGN, which corresponds to resolving about 30% of the hard XRB. Furthermore, a great majority of them turned out to be absorbed by column densities in the range 10^{22} - 10^{23} cm^{-2} , even though they may be highly different in their optical and/or near-infrared properties. Fabian (2000) has recently pointed out that if absorbed AGN are

the major contributors to the hard XRB then about 85% of the accretion power in the Universe is absorbed. The author has exploited this *Beppo*SAX capability by studying the serendipitous source in the MECS field of view when pointing at the Seyfert 2 galaxy NGC7314 (Malizia et al. 2000c). Also in this particular case, the source has been identified with a type 2 Seyfert with a column density of $2 \times 10^{22} \text{ cm}^{-2}$.

Chapter 4

BATSE OBSERVATIONS OF THE PICCINOTTI SAMPLE OF AGN

4.1 The Piccinotti Sample of AGN

The only statistically complete and large sample of X-ray sources in the energy range 2-10 keV was obtained using data from the A2 experiment on the HEAO-1 satellite (Piccinotti et al. 1982). This instrument performed a survey of 8.3 sr of the sky (65.5% coverage) at $|b| \geq 20^\circ$. Sources were included in the catalogue if they were detected with a significance greater than or equal to 5σ . The Piccinotti sample contains 85 sources (excluding the LMC and SMC sources) down to a limiting flux of 3.1×10^{-11} erg cm $^{-2}$ s $^{-1}$. Of the 68 objects of extragalactic origin, 36 have been identified with active galaxies while the remaining sources were found to be associated with clusters of galaxies. The AGN sample is composed of 30 Seyfert galaxies (of which 23 are of type 1 and 7 of type 2), one starburst galaxy (M82), 4 BL Lac objects and one QSO (3C 273). Some objects which were left unidentified in the original Piccinotti list have been subsequently identified (Miyaji and Boldt 1990, Giommi et al. 1991, Fairall, McHardy and Pye 1982); these are H0111-149 (MKN1152, $z=0.0536$), H0235-52 (ESO198-G24, $z=0.045$), H0557-385 (IRAS F05563-3820, $z=0.034$), H0917-074 (EXO0917.3-0722, $z=0.169$; but see section 5.4.2 for more details and a different source identification), H1829-591 (F49, $z=0.02$) and H1846-768 (1M1849-781, $z=0.074$). Only one object (H1325-020) is still unidentified but it is probably associated with a galaxy cluster (A1750, Marshall et al. 1979) and therefore has been excluded from the present study. Three objects in the sample have the X-ray emission contaminated by a nearby source (IIIZW2 by the visual binary HD560, Tagliaferri et al. 1988, IRAS F05563-3820 by the BL Lac object EXO055625-3838.6,

Giommi et al. 1989 and 3C445 by the cluster of galaxies A2440, Pounds 1990); however, since these nearby objects should only give a negligible contribution to the emission above 20 keV, none of these sources have been excluded from the present analysis. All the sample sources together with their coordinates (J2000.0), optical classification and redshift are reported in table 4.1. The Piccinotti sample is the hard X-ray selected sample of AGN best studied at all wavelengths below 10-20 keV and as such has been used to study AGN X-ray spectral characteristics, the LogN-logS relationship and luminosity function and hence to determine the contribution of active galaxies to the cosmic diffuse X-ray background in the 2-10 keV energy range. In the X-ray band most of the AGNs in the sample have been observed several times individually with various space borne experiments. Spectral data in the 2-10 keV range obtained over the last 20 years have been summarized in Ciliegi et al. (1993), Malaguti et al. (1994) and Malizia et al. (1997) for all objects except H0557–385 and H0917–074; the spectrum of the former can be found in Turner et al. (1996) while no spectral data have so far been reported for the latter object. More recently, intrinsic absorption and soft excesses have been studied for 31 of the Piccinotti sources (the 4 BL Lacs and the starburst galaxy M82 were not considered) using all-sky survey data from the ROSAT satellite in the 0.1-2 keV band (Schartel et al. 1997). A systematic study of the X-ray variability of the sample has been performed by Turner & Pounds (1989), Giommi et al. (1990) and Grandi et al. (1992) with the Low Energy (LE) (0.05-2 keV) and Medium Energy (ME) (2-50 keV) experiments on board EXOSAT. Only in the last few years, have high energy observations of individual objects in the sample been started. Prior to CGRO and BeppoSAX, a handful of objects were detected above 10 keV by balloon borne telescopes, HEAO A-4 and Sigma/GRANAT (Rothschild et al. 1983, Bassani et al. 1985, Bassani et al. 1993). More recently, data on most of these galaxies have been obtained both by OSSE/CGRO and BeppoSAX/PDS. Twenty-seven of the Piccinotti objects have so far been observed by OSSE, 11 with detection above $\geq 5\sigma$ level (McNaron-Brown et al. 1995 and Johnson, 1997 private communication, Zdziarski et al. 2000) while BeppoSAX reported high energy emission from many of the sample sources (BeppoSAX public archive). *BeppoSAX* high energy (PDS) data of the Piccinotti sample of AGN will be reported and illustrated in the next chapter. The BATSE data reported in the ApJ publication (Malizia et al. 1999) provided, for the first time, a systematic coverage at high energies of the whole sample.

Table 4.1: The Piccinotti sample of AGN

| | Source | RA | Dec | Class | z |
|----|---------------|------------|-----------|---------|--------|
| 1 | III Zw 2 | 00 10 31.0 | 10 58 29 | Sey 1 | 0.0893 |
| 2 | Mrk 1152 | 01 23 45.5 | −14 50 44 | Sey 1.5 | 0.0527 |
| 3 | Fairall 9 | 01 23 45.5 | −58 48 16 | Sey 1 | 0.0470 |
| 4 | NGC 526A | 01 23 55.1 | −35 04 04 | Sey 1.5 | 0.0191 |
| 5 | Mrk 590 | 02 14 33.6 | −00 46 01 | Sey 1.2 | 0.0264 |
| 6 | ESO 198 − G24 | 02 38 19.9 | −52 11 23 | Sey 1 | 0.0455 |
| 7 | 3C 120 | 04 33 11.1 | 05 21 16 | Sey 1 | 0.0330 |
| 8 | PKS 0548−322 | 05 50 40.8 | −32 16 18 | BL Lac | 0.0690 |
| 9 | H0557−385 | 05 58 02.1 | −38 20 03 | Sey 1 | 0.0344 |
| 10 | H0917−074 | 09 19 50.7 | −07 35 42 | Sey 1/Q | 0.1690 |
| 11 | NGC 2992 | 09 45 42.0 | −14 19 35 | Sey 2 | 0.0077 |
| 12 | M 82 | 09 55 52.3 | 69 40 46 | SB | 0.0007 |
| 13 | NGC 3227 | 10 23 30.6 | 19 51 54 | Sey 1.5 | 0.0038 |
| 14 | NGC 3783 | 11 39 01.8 | −37 44 20 | Sey 1 | 0.0097 |
| 15 | NGC 4151 | 12 10 32.5 | 39 24 21 | Sey 1.5 | 0.0033 |
| 16 | 2A 1219+305 | 12 21 21.9 | 30 10 37 | BL Lac | 0.1820 |
| 17 | 3C 273 | 12 29 06.6 | 02 03 88 | QSO | 0.1583 |
| 18 | NGC 4593 | 12 39 39.4 | −05 20 39 | Sey 1 | 0.0090 |
| 19 | MCG−6−30−15 | 13 35 53.7 | −34 17 45 | Sey 1 | 0.0077 |
| 20 | IC 4329A | 13 49 18.4 | −30 18 34 | Sey 1 | 0.0160 |
| 21 | NGC 5506 | 14 13 14.8 | −03 12 27 | Sey 1.9 | 0.0620 |
| 22 | NGC 5548 | 14 17 59.5 | 25 08 12 | Sey 1.5 | 0.0171 |
| 23 | Mrk 501 | 16 53 52.2 | 39 45 37 | BL Lac | 0.0337 |
| 24 | Fairall 49 | 18 36 58.1 | −59 24 08 | Sey 2 | 0.0202 |
| 25 | ESO 103−G35 | 18 38 20.3 | −60 25 42 | Sey 2 | 0.0133 |
| 26 | H1846−786 | 18 47 06.7 | −78 31 55 | Sey 1 | 0.0740 |
| 27 | ESO 141−G55 | 19 21 14.3 | −58 40 15 | Sey 1 | 0.0360 |
| 28 | Mrk 509 | 20 44 09.8 | −10 43 24 | Sey 1 | 0.0344 |
| 29 | PKS 2155−304 | 21 58 52.0 | −30 13 32 | BL Lac | 0.1160 |
| 30 | NGC 7172 | 22 02 02.1 | −31 52 12 | Sey 2 | 0.0087 |
| 31 | NGC 7213 | 22 09 16.2 | −47 10 00 | Sey 1 | 0.0059 |
| 32 | 3C 445 | 22 23 49.5 | −02 06 12 | Sey 1 | 0.0562 |
| 33 | NGC 7314 | 22 35 45.7 | −26 03 03 | Sey 1.9 | 0.0047 |
| 34 | NGC 7469 | 23 03 15.6 | 08 52 26 | Sey 1 | 0.0163 |
| 35 | MCG−2−58−22 | 23 04 43.4 | −08 41 08 | Sey 1.5 | 0.0473 |
| 36 | NGC 7582 | 23 18 23.2 | −42 22 11 | Sey 2 | 0.0053 |

4.2 BATSE Observations

We have exploited the BATSE Earth occultation technique to search for emission by AGN in the Piccinotti sample, and since this technique reaches its peak sensitivity below ~ 140 keV, the study was carried out in the range between 20 and 100 keV. BATSE data from nearly four years of observations (November 93 - September 97) have been analyzed to extract a signal from sources in the Piccinotti sample. Interference from bright sources flaring or occulted at the same time as the object being studied are the major source of systematic errors in the flux measurement (see chapter 2), and so careful cleaning of the data is necessary before estimating the flux. Two types of cleaning procedures have been applied to the data. First the median statistic has been applied to remove about 5% of data points as outlier individual occultation steps; these outliers are generally due to pulsar activity in individual detectors. Second, contaminating objects in the limbs of the source being studied have been identified using a catalogue of flaring and bright objects detected at high energies. If present, these contaminating sources were included in the occultation step fit, and subsequently data corresponding to contaminating periods were removed (see chapter 2). In 7 cases (ESO 103-G35, IC 4329A, MCG-6-30-15, MKN 501, NGC 4593, NGC 7172 and PKS 2155-304) contamination was found and the above procedure applied. Of course any interfering sources that are not taken into account (i.e. those not included in the database) will systematically increase the flux estimate. This maybe particularly important for sources closer than 5° to the galactic plane or within a cone of 45° around the galactic center up to 30° (Connaughton et al. 1998). Since we are probing the extragalactic sky, only a handful of sources (ESO103-G35, ESO141-G55, Fairall 49 and MKN509) fall within the above cone and in any case, all of them are located at the extreme boundaries of the cone and therefore they have not been excluded from the present analysis. Moreover, comparison of our fluxes with OSSE and BeppoSAX data for two of the above sources suggests that contamination from galactic objects was in these cases negligible.

Fluxes in the 20-100 keV energy band have been obtained by folding a single power law of photon index 1.75 for Seyfert galaxies, 3C273 and M82, and 2.25 for BL Lac objects, with the BATSE instrumental response function and then computing weighted mean flux values over the whole observation period. Although these mean estimates depend on the choice of the photon index, the differences in fluxes are of the order of 10-20% around the values reported in table 4.2 for $\Delta \Gamma = \pm 0.25$.

4.2.1 *Systematic errors*

Besides the standard correction of the data by the systematic errors discussed in chapter 2, before proceeding with the discussion of our results and in view of the difficulties associated with the data analysis, it is important to search for more possible systematic effects on the flux measurements. Two types of systematic errors are particularly relevant: those affecting the overall normalization (which are particularly important for comparison with other instruments), and those affecting the size of the fluctuations (which are relevant to estimate the confidence level of a detection). Comparison of BATSE occultation results with contemporaneous observations with other CGRO instruments have indicated that the BATSE flux values maybe systematically higher. In the most extensive study published to date, Much et al. (1996) found that the BATSE Crab Nebula flux was $\sim 20\%$ higher than OSSE flux in the same energy range. More recently, Parsons et al. (1998) compared BATSE measurements of NGC 4151 with those of OSSE and derived a BATSE/OSSE flux ratio of 1.45 ± 0.08 . In view of the relevance of the Parsons et al. study to the present one, we have performed a similar analysis on all the sample sources for which contemporaneous BATSE/OSSE data (kindly provided to us by the OSSE team, Johnson 1997, private communication) could be analyzed. The results of this analysis are summarized in the parameter R reported in table 4.2. For every contemporaneous BATSE/OSSE observation we have estimated the relative flux ratio in the 20-100 keV band and then we have calculated R which represents the weighted mean value, with its associated error, of all the available flux ratios. The numbers in parentheses indicate how many periods were examined (first quote) and the total number of observation days analyzed over those periods (second quote). It is evident from table 4.2 that R is ≥ 1 in most cases, the weighted mean value of R being 1.36 ± 0.03 (this value becomes 1.5 ± 0.13 if the two strongest sources, NGC4151 and 3C273, are removed). Thus our result confirms previous reports of a BATSE/OSSE normalization discrepancy (Much et al. 1996, Parsons et al. 1998) and further indicates that in the particular case of extragalactic studies the BATSE flux can be systematically higher than that seen by OSSE by as much as 35%. The possible origin for this normalization problem is at the moment under investigation and will hopefully be solved in the near future. A possible explanation may be source interference which is not taken into account in the data cleaning. This is an important problem to address if BATSE light curves are to be used in combination with observations taken by other hard X-ray observations to monitor bright source behaviour at high energies.

We have also compared BATSE data to BeppoSAX observations (see next chapter for more details) although in this case the comparison is hampered by the lack of simul-

taneous data. The results are summarized in the parameter R1 in table 4.2. In this case we get many cases ($\sim 50\%$) in which BATSE/SAX flux ratio is ~ 1 ; only in 8 cases the flux is higher in BATSE than in SAX by a factor of 2. We know, however, that in some of these sources (as in 3C273) variability could well explain this flux difference. In other cases, contamination by nearby objects could be responsible for excess emission in BATSE. Therefore, a check of possible contaminations by hard X-ray emitters located at around 1 degree (see Harmon et al. 2001) from each Piccinotti source has been performed. No possible contaminations have been found except for M82 and 2A1219+305. In fact, the starburst galaxy M82 is very close to M81 (about 37 arcmin): both these two objects were observed by *BeppoSAX* (Pellegrini et al. 2000, Cappi et al. 1999c). Due to their nearness, the spectral characteristics are confused; they are both in the PDS field of view, and, given the PDS triangular response ($1^\circ.3$ FWHM), half of the M82 flux between 13–300 keV could contaminate the M81 observation. In any case *BeppoSAX* data indicate that M82 has a steeper spectrum than M81; Cappi et al. (1999c) reported a photon index of 3.8 ± 1.8 in the PDS energy band and a 13–50 keV flux $\lesssim 1.7 \times 10^{-11}$ erg $\text{cm}^{-2} \text{s}^{-1}$ (i.e. a factor of $\gtrsim 2$ lower than M81 in the same energy band). Pellegrini et al. (2000) estimated that M81 could be contaminated by M82 at most by 25%. Finally, in 1 degree field around 2A1219+305 there is the BL Lac object ON 325 (20 arcmin) and the Seyfert 1 galaxy MKN766 (44 arcmin). From the *BeppoSAX* observations we know that although there is no possible contamination by ON 325, it is highly possible that being a hard X-ray emitter, Mkn 766 (Matt et al. 2000c) contaminates the BATSE flux. In the remaining sources it is possible that either variability and/or contamination by nearby objects is responsible for the excess flux seen in BATSE. In particular, unknown hard X-ray emitting sources just outside the 1 degree error circle taken here, could produce such an effect. However, since for individual sources the discrepancies found can be less than quoted and in fact ~ 1 (see for example 3C273 with respect to OSSE or various others with respect to *BeppoSAX*) no correction is applied to the BATSE data. Furthermore, as the errors are also affected in the same way as the fluxes, this normalization problem has no impact on the detection level of a given source.

The effects of systematic errors have also been carefully considered by examining "blank fields" randomly distributed around the sky. It was found that while the flux values for each field were consistent with the quoted errors, the spread around zero of the mean fluxes from a large number of these empty fields was about 80% higher than would be expected by the statistical errors alone (Stephen 1998, private communication). For this reason all the errors on the mean fluxes were adjusted by 80% so as to be conservative in the source detection estimate. This estimate of the systematic errors is slightly higher

than the 65% obtained by Connaughton et al. (1998), but compatible given the difference in the number of fields analysed.

Table 4.2: Results

| Source | Low Energy | | High Energy | | | |
|--------------|-----------------------------------|-----------------|--------------------------------------|----------------------|------------------------|-----------|
| | F_{MEAN}^{\dagger} (2-10)keV | VR^{\ddagger} | F_{BATSE}^{\dagger} (20-100)keV | N_{σ}^{BATSE} | R^* | $R1^{**}$ |
| III ZW 2 | 2.93 | 0.64 | 4.88 ± 1.62 | 3.02 | 1.80 ± 1.0 (1-13) | ... |
| MKN 1152 | 2.02 | 1.22 | 5.99 ± 1.51 | 3.96 | ... | 7.99 |
| FAIRALL 9 | 2.89 | 2.15 | 3.80 ± 1.70 | 2.24 | 1.65 ± 1.37 (1-13) | 1.16 |
| NGC 526A | 3.13 | 2.43 | 12.44 ± 1.54 | 8.07 | 4.40 ± 1.5 (1-13) | 3.30 |
| MKN 590 | 1.97 | 0.94 | 6.75 ± 1.47 | 4.59 | 4.67 ± 4.8 (1-14) | ... |
| ESO 198-G24 | 3.30 | 1.31 | 5.27 ± 1.66 | 3.18 | ... | ... |
| 3C 120 | 3.94 | 1.26 | 4.84 ± 1.58 | 3.07 | 3.41 ± 2.5 (2-18) | 0.8 |
| PKS 0548-322 | 2.73 | 1.17 | < 3.76 | ... | ... | < 4 |
| H0557-385 | 3.17 | 1.75 | 4.74 ± 1.53 | 3.09 | ... | 1.4 |
| H0917-074 | 1.88 | 1.08 | 5.63 ± 1.55 | 3.63 | ... | ... |
| NGC 2992 | 5.03 | 4.58 | < 3.18 | ... | ... | 2.2 |
| M 82 | 2.52 | 0.16 | 5.94 ± 1.12 | 3.08 | ... | 10.24 |
| NGC 3227 | 3.15 | 2.35 | 11.26 ± 1.53 | 7.36 | 1.67 ± 0.6 (4-51) | ... |
| NGC 3783 | 4.69 | 3.35 | 13.00 ± 1.64 | 7.91 | ... | 1.31 |
| NGC 4151 | 22.55 | 15.05 | 77.46 ± 1.59 | 48.77 | 1.37 ± 0.03 (6-94) | 1.79 |
| 2A 1219+305 | 2.98 | 1.38 | 5.70 ± 2.29 | 2.48 | ... | 4.91 |
| 3C 273 | 11.68 | 6.14 | 39.13 ± 1.59 | 24.58 | 1.04 ± 0.1 (5-43) | 2.19 |
| NGC 4593 | 3.17 | 1.17 | 9.81 ± 1.59 | 6.16 | ... | 1.42 |
| MCG-6-30-15 | 5.77 | 1.51 | < 4.30 | | 1.08 ± 1.6 (1-7) | < 0.7 |
| IC 4329A | 12.15 | 7.05 | 19.44 ± 1.99 | 9.78 | 1.34 ± 1.19 (6-71) | 1.17 |
| NGC 5506 | 6.52 | 4.75 | 19.16 ± 1.60 | 11.97 | 2.57 ± 0.56 (3-29) | 1.48 |

Table 4.2 - Continued

| Source | Low Energy | | High Energy | | | |
|--------------|-----------------------------------|------------------|--------------------------------------|----------------------|------------------------|--------------------|
| | F_{MEAN}^{\dagger} (2-10)keV | VR ‡ | F_{BATSE}^{\dagger} (20-100)keV | N_{σ}^{BATSE} | R * | R1 ** |
| NGC 5548 | 4.35 | 2.37 | 10.53 \pm 1.58 | 6.67 | 1.45 \pm 0.63 (3-26) | 1.52 |
| MKN 501 | 3.40 | 1.25 | 10.31 \pm 2.77 | 3.71 | | 1.17 |
| FAIRALL 49 | 1.94 | 1.43 | 3.98 \pm 1.86 | 2.14 | ... | ... |
| ESO 103-G35 | 2.09 | 0.89 | 7.92 \pm 1.86 | 4.26 | ... | 1.40 |
| H1846-786 | 2.46 | 0.76 | 5.99 \pm 1.76 | 3.39 | ... | ... |
| ESO 141-G55 | 3.26 | 0.44 | <3.50 | ... | ... | <0.9 |
| MKN 509 | 4.41 | 1.29 | 12.47 \pm 1.52 | 8.18 | 0.96 \pm 0.6 (2-20) | 1.85 |
| PKS 2155-304 | 9.29 | 5.21 | 7.70 \pm 1.94 | 3.97 | 1.19 \pm 0.82 (2-14) | 6.47 |
| NGC 7172 | 3.06 | 1.29 | 8.00 \pm 1.55 | 5.15 | 1.16 \pm 0.37 (3-26) | 2.68 |
| NGC 7213 | 3.66 | 1.34 | 3.39 \pm 1.65 | 2.05 | 2.23 \pm 1.5 (1-7) | 0.80 |
| 3C 445 | 2.28 | 1.09 | 12.15 \pm 1.54 | 7.88 | ... | 3.92 |
| NGC 7314 | 2.76 | 1.46 | 4.19 \pm 1.58 | 2.66 | ... | 0.92 |
| NGC 7469 | 3.02 | 1.22 | 7.77 \pm 1.51 | 5.15 | 2.39 \pm 2.05 (1-7) | 1.85 |
| MCG-2-58-22 | 4.08 | 2.32 | 7.53 \pm 1.53 | 4.93 | ... | ... |
| NGC 7582 | 3.60 | 3.00 | 8.97 \pm 1.65 | 5.43 | <2.14 (1-7) | 1.11 |

Notes: (\dagger) = flux in units of 10^{-11} erg cm $^{-2}$ s $^{-1}$, (\ddagger) = fluxes variability range in the 2-10 keV energy band

(\star) = weighted mean value of the BATSE/OSSE flux ratios in the 20-100 keV with its associated error for contemporaneous observations. The numbers in parentheses indicate how many periods were examined (first quote) and the total number of observation days analyzed over those periods (second quote). BATSE fluxes are the weighted mean calculated over nearly four year of observations. Upper limits are at 2σ level

($\star\star$) BATSE/SAX flux ratio in the 20-100 keV.

4.3 Results and Discussion

Table 4.2 lists all sources contained in the sample together with their X-ray data in the 2-10 keV band, a compendium of the results of the BATSE data analysis (flux and significance of detection), the BATSE/OSSE flux ratio, R and BATSE/SAX flux ratio, R_1 . Significant detection at $\geq 10\sigma$ level has been found for three sources (NGC 4151, 3C 273 and NGC5506), while at the 5σ level the number of detected sources grows to 14. Marginal detections ($3 < \sigma < 5$) can be claimed for 13 sources while only 9 galaxies were observed below the 3σ confidence level.

The main result of BATSE data analysis is the detection of high-energy emission from the majority of the sample sources. Comparison between OSSE and BATSE data indicates that 6 objects are reported as hard X-ray emitting sources for the first time: ESO198-G24, H0917-074, ESO 103-G35, H1846-786, 3C 445 and MKN1152, all detected above the 3σ confidence level (Malizia et al. 1999); only successively *BeppoSAX* -PDS observations have confirmed these high energy emitters (see next chapter for a compendium of the PDS observations). It is also interesting to note that 5 out of 8 Seyferts 2's in the sample have been detected, in agreement with the expectation of the unified theory, which predicts similar energy output for type 1 and type 2 Seyferts at high energies. Particularly interesting is also the BATSE detection of two BL Lac objects out of four in the sample: MKN 501 and PKS 2155-304. Due to the steepness of their spectra compared to Seyferts, BL Lacs have less probability of being detected by BATSE unless higher than expected brightness was present during BATSE monitoring (see below).

In order to assess the reliability of our results and to investigate the approximate spectral shape of AGN in the BATSE energy band, a comparison with soft X-ray fluxes has been performed. BATSE flux estimates, however, are the result of a long integration period (years) and thus represent averaged values over this period, while observations with pointed instruments provide instantaneous flux measurements. This has been taken into account by using in the 2–10 keV band mean flux values as estimated from data in the literature (Ciliegi et al. 1993, Malaguti et al. 1994, Malizia et al. 1997, Polletta et al. 1996). The errors on this mean flux has been set equal to the observed range of X-ray variability or VR in table 4.2.

In figure 4.1, BATSE flux values are plotted against these 2-10 keV flux measurements. Lines plotted in the figure correspond to the ratio expected for two values of the photon index (1.5 and 2) under the hypothesis of a single power law continuum from 2 to 100 keV. It is interesting to find that a good fraction of galaxies fall within the region constrained by these two spectral indices, particularly if the range of X-ray flux variability is taken into

account. More specifically the broad-band (2-100 keV) power-law slope can be estimated from the fluxes emitted in the two bands: while the average photon index is 1.7, the weighted mean value is 1.6 ± 0.1 (considering only detections above 3σ and excluding BL Lacs); removal of NGC4151 and 3C273 from the sample does not change this mean. Decreasing the BATSE fluxes by the amount required by the BATSE/OSSE comparison would make this mean photon index slightly steeper. Therefore the canonical 1.7 power law which best represents the X-ray data gives also a good description of the spectrum in the 20-100 keV band. This result indicates that the reflection component which is responsible for flattening the intrinsic $\Gamma=1.9$ spectrum in the 2-10 keV band, is relevant also above 20 keV and present in most sample sources. Furthermore, BATSE observations imply that spectral breaks and/or steepening must occur preferentially above about 100 keV for consistency with our findings. This is in line with BeppoSAX results discussed in the next chapter.

A couple of exceptions are however worthy of note. Two sources, MCG-6-30-15 and NGC2992, are located in the region characterized by spectral indices greater than 2.0 (or, alternatively, in these sources the BATSE flux is underestimated, which would be surprising in view of the above discussion). NGC2992 is however compatible with flatter indices, if one considers the source's large range in variability and, in particular, the gradual decline in flux by a factor of ~ 20 monitored over the last 10 years (Polletta et al. 1996): by sampling the last part of this period BATSE probably underestimates the source average flux. The case of MCG-6-30-15 is less obvious and deserves further investigation: either the source was dimmer during the BATSE coverage with respect to previous 2-10 keV observations or a break below 100 keV must be postulated. Since BeppoSAX observation of this source locates the break at energies ≥ 100 keV (see next chapter and Guainazzi et al. 1999a), the first alternative is more plausible suggesting that BATSE can indeed be used as a monitor of bright source states. The location of MKN501 and 2A 1219+305 is also peculiar as these two objects have unusually flat spectra for BL Lac objects (Ciliegi et al. 1995). The case of MKN501 is particularly interesting. Strong flaring activity has been reported from this source at high energies during the BATSE monitoring period (Pian et al. 1998 and Catanese et al. 1997, Lamer et al. 1998); analysis of the BATSE light curve indicates indeed that flare-like events are present together with a gradual increase in flux during April-July 1997 (Connaughton et al. 1998, Petry et al. 2000). During at least one such event (in April) the source spectrum was flatter than previously reported (Pian et al. 1998). Given the peculiar behaviour observed during the BATSE coverage, a proper comparison between low and high energy bands should use contemporaneous data.

Finally, BATSE results have been compared with previous studies of the average AGN flux at high energies; the average flux of the Seyfert galaxy population as a whole has been found to be $(1.74 \pm 0.05) \times 10^{-5}$ photons/cm² s keV in the 20-100 keV band, and if strong sources such as NGC 4151, 3C 273 and IC 4329A are excluded, the mean flux reduces to $(1.24 \pm 0.05) \times 10^{-5}$ photons/cm² s keV. Dividing the sample in classes gives a mean flux of $(1.88 \pm 0.05) \times 10^{-5}$ photons/cm² s keV for Seyfert 1, $(1.31 \pm 0.11) \times 10^{-5}$ photons/cm² s keV for Seyfert 2 and $(1.03 \pm 0.19) \times 10^{-5}$ photons/cm² s keV for BL Lac objects, in agreement with the results of Maisack, Wood and Gruber (1994) based on HEAO A4 data; a 40% reduction in the BATSE fluxes improves the comparison. Also, if only the radio-quiet Seyfert 1 galaxies in the sample (12 objects) are taken into account, the average flux is $(1.22 \pm 0.08) \times 10^{-5}$ photons/cm² s keV, compatible within errors with the value obtained by Gondek et al. (1996) for the same class of objects; in this case no correction to a lower flux level is required by the comparison. While the agreement found gives confidence to our data analysis (the level of each detection is a sound result, while the flux estimate maybe in some cases slightly overestimated) it also demonstrates the potential of BATSE for cumulative studies of selected samples of objects for example in search of a population of objects bright at high energies. Down to a limiting flux of 7.8×10^{-11} erg cm⁻² s⁻¹, reached integrating data over four years of data, BATSE was able to detect 14 objects above 5σ level over 8.2 sr. This is to be considered a lower limit to the number of high-energy emitting AGN as highly absorbed objects, i.e. objects missed in the Piccinotti survey for their absorption in excess of 10^{24} cm⁻² but visible above 10 keV (Bassani et al. 1998b) are probably not included. This suggests that an improvement in sensitivity of a factor of ~ 10 as foreseen for the next generation of high energy telescopes such as INTEGRAL (Winkler 1996) would allow more than 600 objects to be visible over the entire sky at $\geq 5 \sigma$ level.

4.4 BATSE Light Curves

Here the BATSE light curves of the Piccinotti sample of AGN are reported, 30 days binning has been used to plot the four years of observations for all the sample sources. Note that the gaps present in a few of the light curves are due to a lack of data. Searching for variability of the Piccinotti sample with the BATSE data is not an easy test mainly due to the poor statistics found in a large fraction of the sources. However, a timing analysis has been attempted using a χ^2 test on the whole data of each source. To be conservative, for each source only the daily positive detections have been considered and

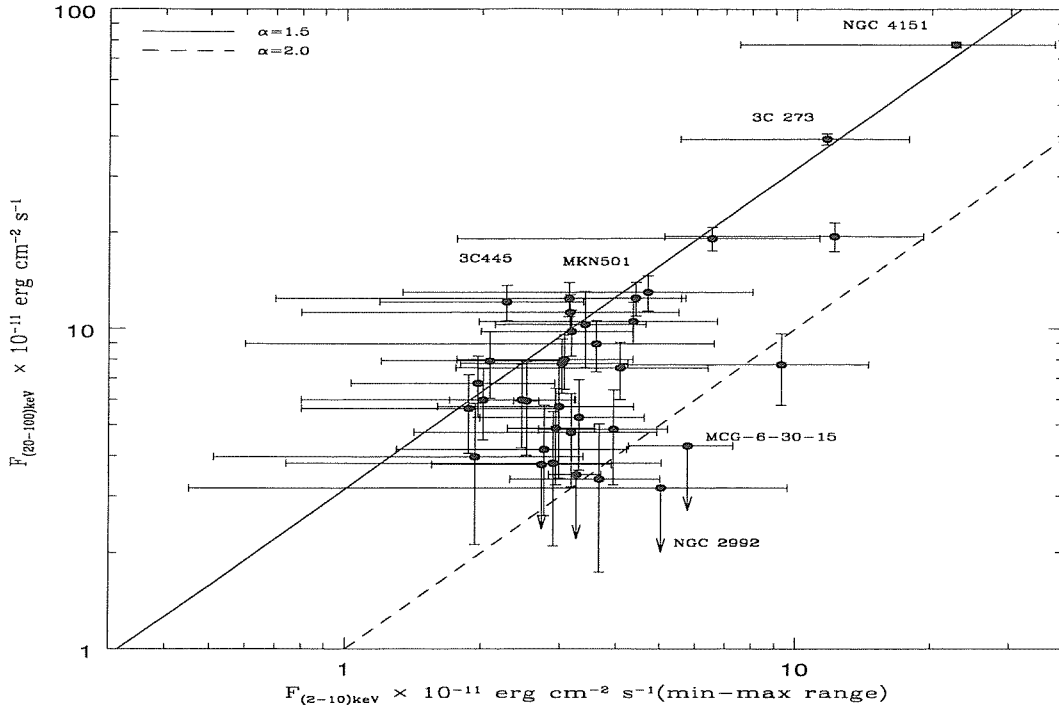


Figure 4.1: BATSE 20-100 keV weighted mean fluxes over ~ 3 years of observations with their relative errors, are plotted against 2-10 keV average fluxes. The horizontal bars in the figure are the 2-10 keV flux ranges (minimum and maximum value found in the literature). Lines plotted correspond to the ratio between fluxes expected for various values of photon index under the hypothesis of a single power law continuum from 2 to 100 keV. Although 3C445 has a slope flatter than 1.5, this is consistent with recent X-ray measurements (Sambruna et al. 1998).

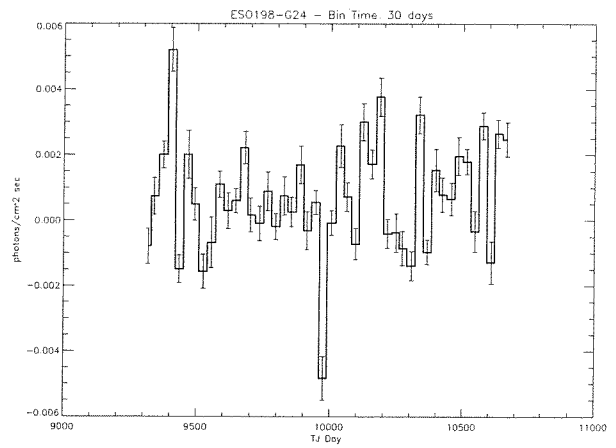
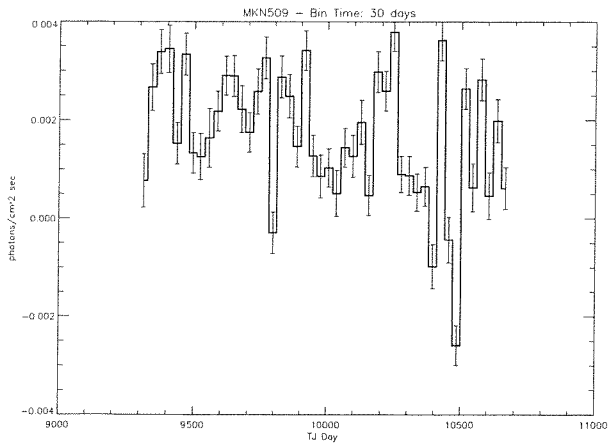
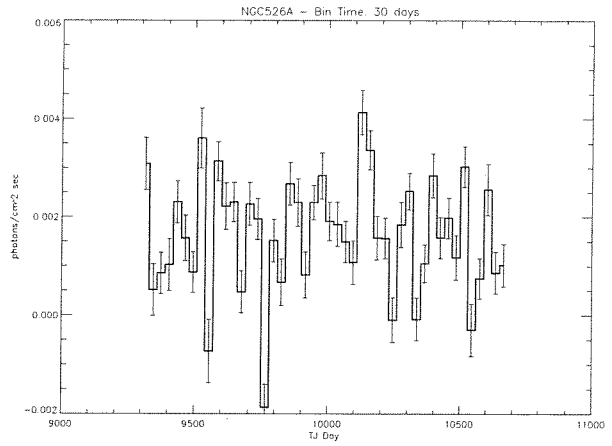
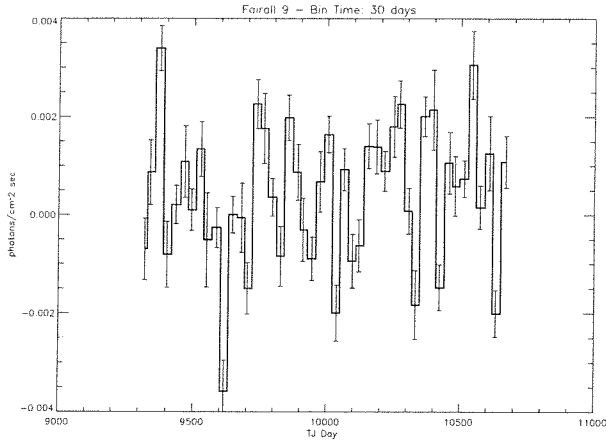
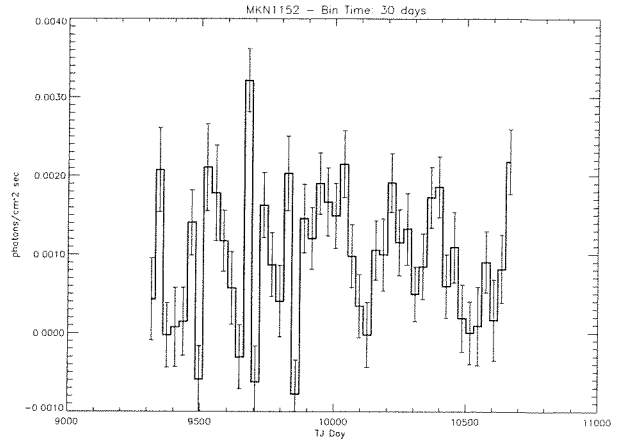
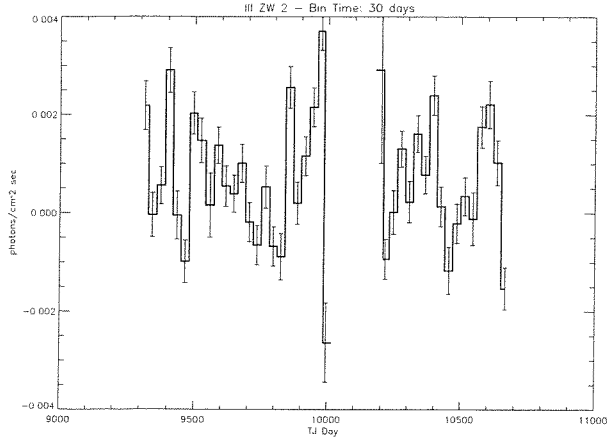
then a bin of 30 days has been applied to improve the statistics. Afterward with the χ^2 test we have verified if the selected data showed variations from the weighted mean value and so the associated probability of variability has been calculated. In table 4.3 the χ^2 test results have been reported; for each source the average and the weighted mean count rate (photons/cm² s), the resultant χ^2 , the degrees of freedom (number of bins - 1), and the associated probability of variation have been listed. Among all 36 Piccinotti sources only NGC4151 and 3C273 are variable with a probability $>90\%$, but on the other hand only NGC4151, 3C273 and NGC5506, which is not found variable, have a detection $>10\sigma$ over the whole observing period. Therefore, conclusive results on long time scale variability can not be given for the rest of the sample sources. On the other hand long term variability of the high energy emission is well known in NGC4151 (Johnson et al. 1997, Parsons et al. 1998) and in 3C273 (Johnson et al. 1995, McNaron-Brown et al. 1997),

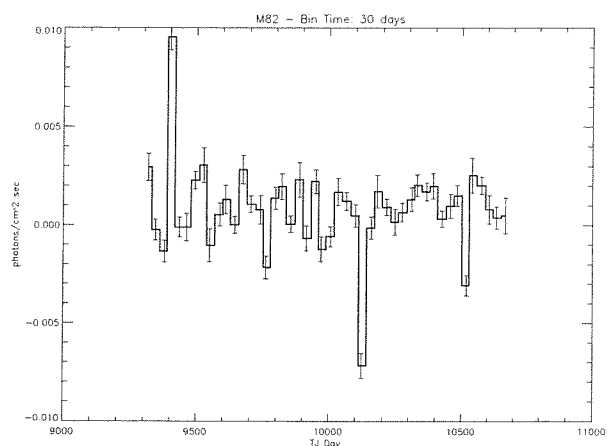
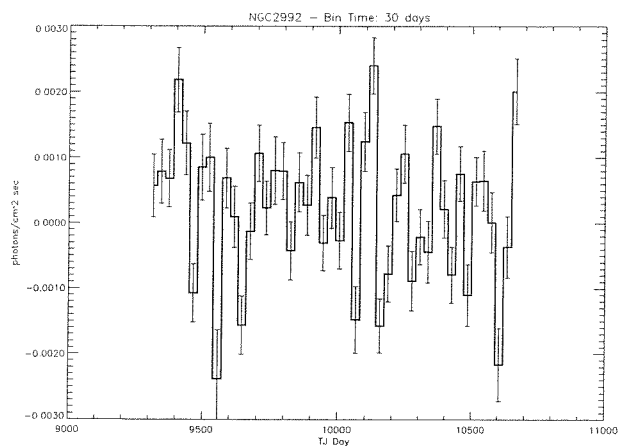
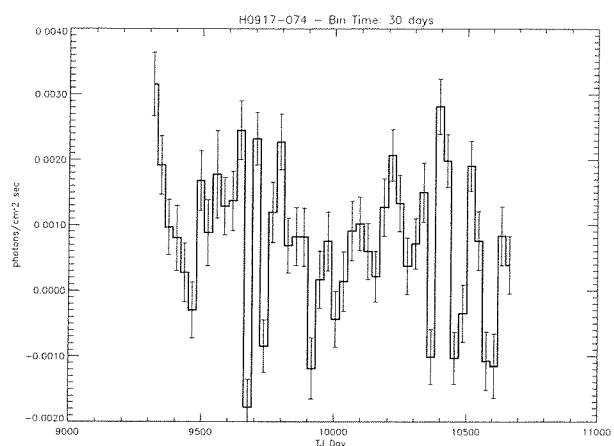
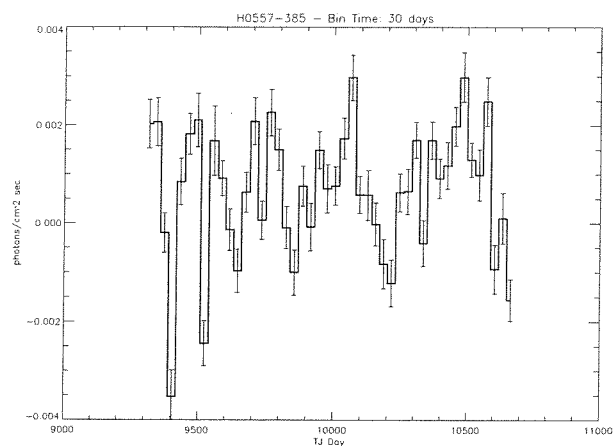
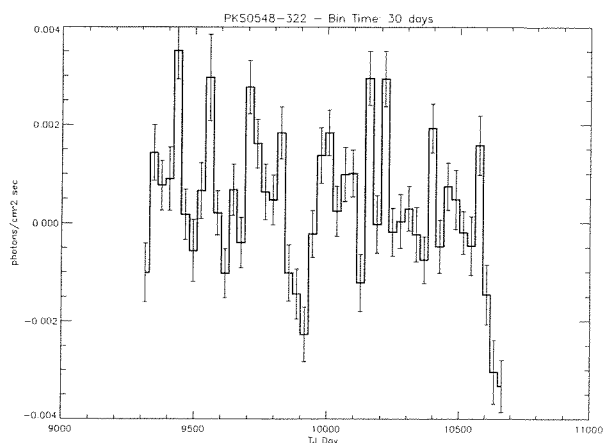
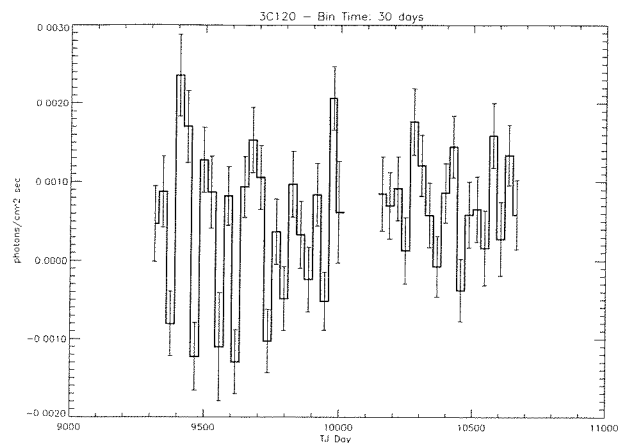
however here for the first time the complete light curves over four years time span have been reported. In these light curves, flare-like events are clearly visible superimposed, in the case of 3C273, on a long term of flux decrease. Although comparison with other instruments is hampered by the possible flux over-estimation problem of BATSE, OSSE and *Beppo*SAX results alone and/or combined, indicate that variations of the hard X-ray emission is more the rule than the exception (see next chapter), further confirming that the high-energy sky is continuously changing in time. With the BATSE overall database containing 9 years of data of the whole sky, and with the BATSE all sky survey (BASS = BATSE All Sky Survey), at the moment under construction at Southampton University (Shaw et al. 2000), it will be possible to search for variability of bright sources over this long time span by highlighting flares or high states of the emission. Also it will be possible to decrease the sensitivity threshold to include in the detection all the Piccinotti sources as well as lower-luminosity AGNs which have already started to emerge in preliminary data analysis (Westmore et al. 2001).

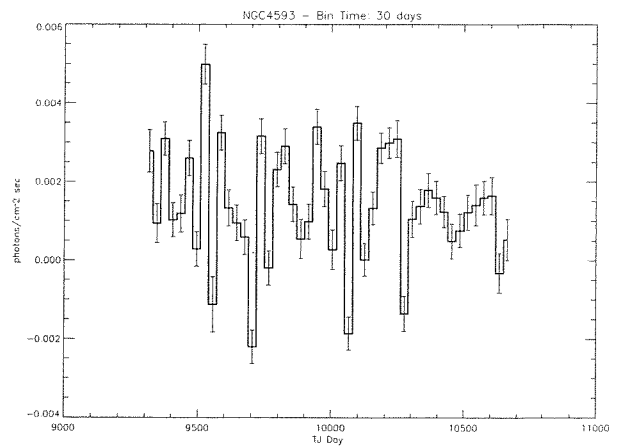
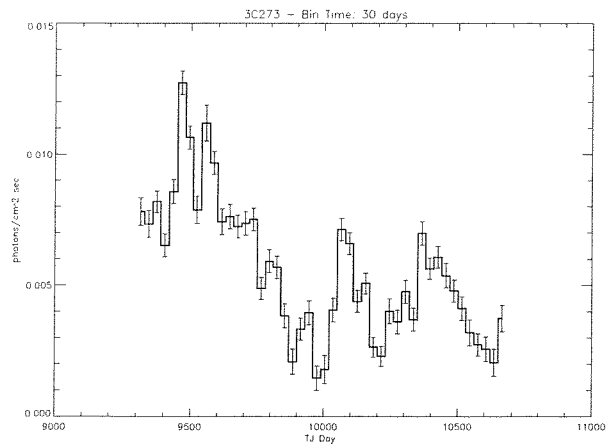
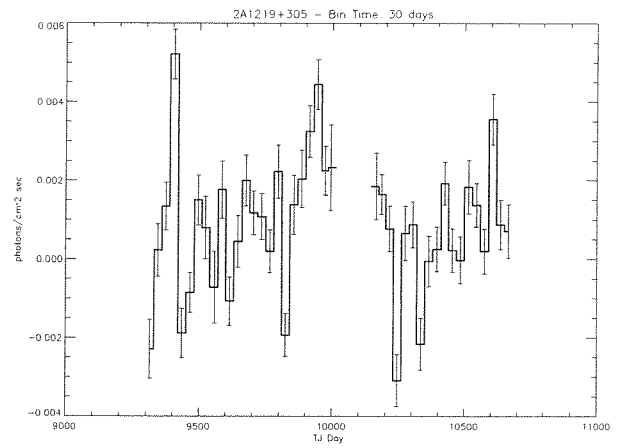
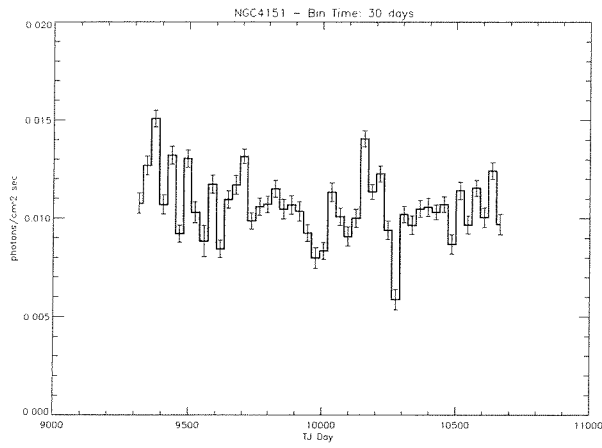
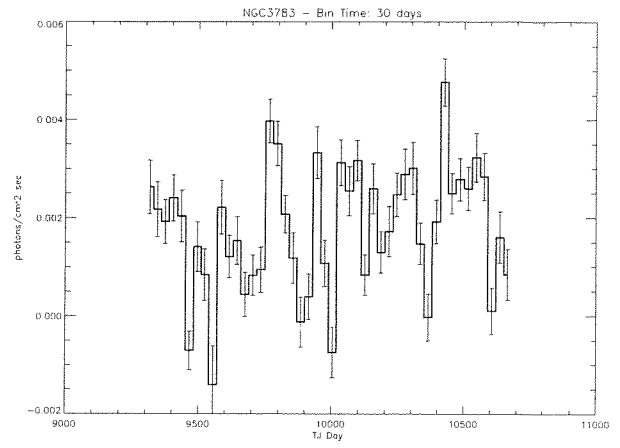
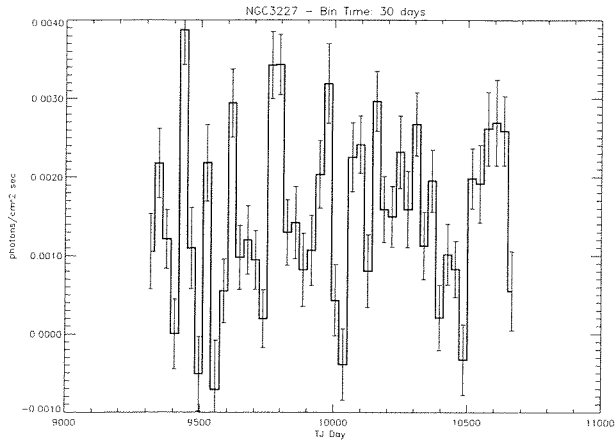
Table 4.3: Timing analysis results

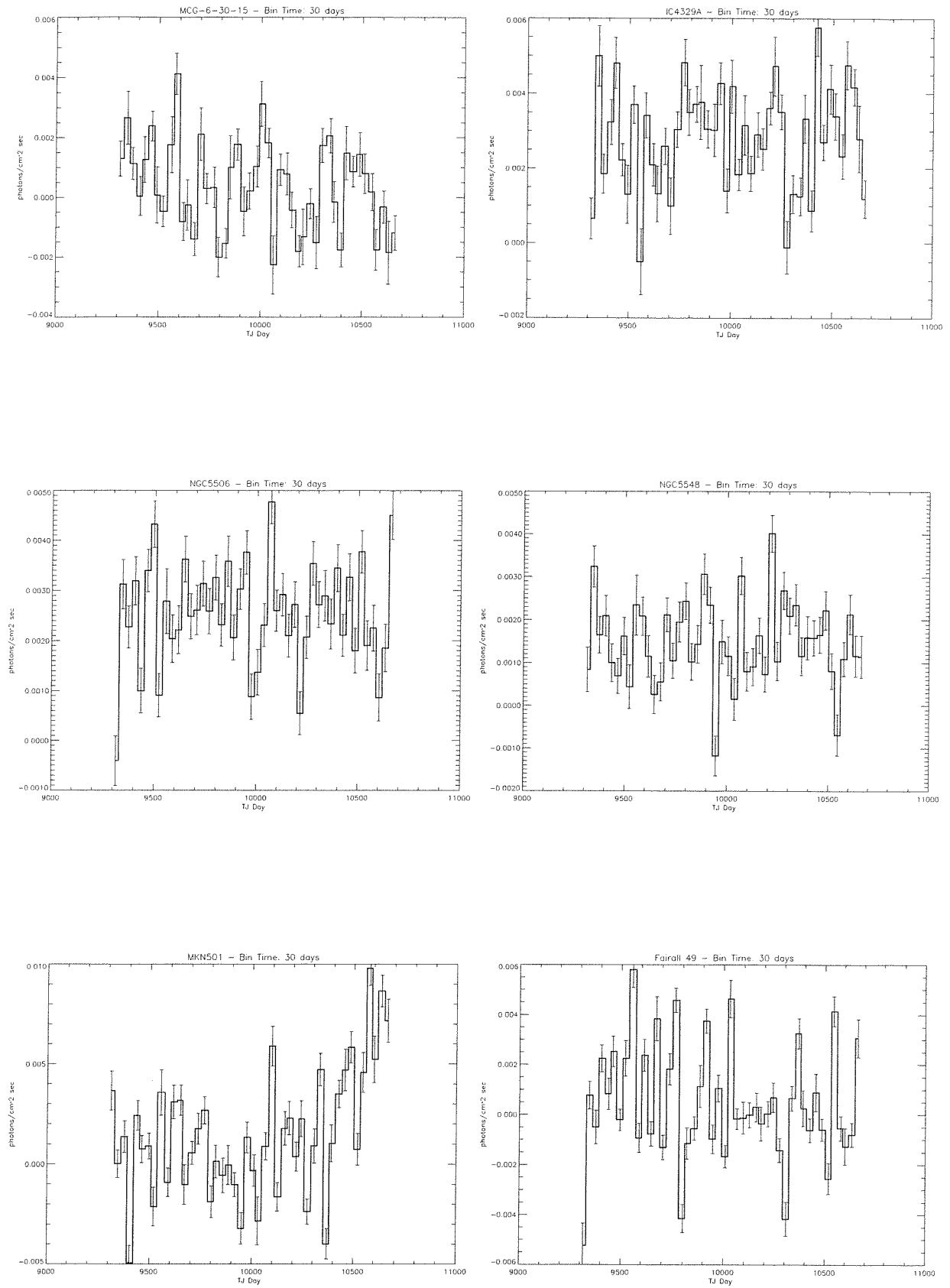
| Source | Average [†] | Weighted Mean [†] | χ^2 | d.o.f. | Prob |
|---------------|----------------------|----------------------------|----------|--------|------|
| III Zw 2 | 0.038 | 0.022 | 32.7 | 28 | 75% |
| Mrk 1152 | 0.035 | 0.034 | 20.1 | 40 | <1% |
| Fairall 9 | 0.037 | 0.031 | 16.2 | 26 | 7% |
| NGC 526A | 0.060 | 0.055 | 29.2 | 41 | 8% |
| Mrk 590 | 0.042 | 0.036 | 23.2 | 39 | 2% |
| ESO 198 – G24 | 0.049 | 0.038 | 20.1 | 29 | 11% |
| 3C 120 | 0.030 | 0.028 | 9.3 | 32 | <1% |
| PKS 0548–322 | 0.041 | 0.035 | 9.0 | 26 | <1% |
| H0557–385 | 0.046 | 0.038 | 10.2 | 30 | <1% |
| H0917–074 | 0.039 | 0.038 | 14.4 | 36 | <1% |
| NGC 2992 | 0.030 | 0.026 | 5.5 | 29 | <1% |
| M 82 | 0.037 | 0.027 | 13.9 | 33 | <1% |
| NGC 3227 | 0.058 | 0.054 | 34.2 | 41 | 24% |
| NGC 3783 | 0.067 | 0.062 | 22.9 | 41 | <1% |
| NGC 4151 | 0.338 | 0.309 | 59.5 | 46 | 91% |
| 2A 1219+305 | 0.047 | 0.040 | 12.8 | 32 | <1% |
| 3C 273 | 0.171 | 0.140 | 109.9 | 46 | >99% |
| NGC 4593 | 0.056 | 0.051 | 27.3 | 40 | 6% |
| MCG–6–30–15 | 0.029 | 0.027 | 12.6 | 26 | 1% |
| IC 4329A | 0.064 | 0.054 | 36.9 | 44 | 23% |
| NGC 5506 | 0.082 | 0.076 | 30.4 | 45 | 5% |
| NGC 5548 | 0.049 | 0.045 | 21.8 | 43 | <1% |
| Mrk 501 | 0.068 | 0.045 | 31.5 | 32 | 51% |
| Fairall 49 | 0.050 | 0.038 | 18.0 | 23 | 24% |
| ESO 103–G35 | 0.063 | 0.046 | 20.3 | 27 | 18% |
| H1846–786 | 0.054 | 0.044 | 17.2 | 29 | 4% |
| ESO 141–G55 | 0.028 | 0.025 | 7.26 | 25 | <1% |
| Mrk 509 | 0.062 | 0.057 | 30.8 | 42 | 10% |
| PKS 2155–304 | 0.056 | 0.049 | 26.5 | 34 | 18% |
| NGC 7172 | 0.046 | 0.041 | 19.6 | 38 | <1% |
| NGC 7213 | 0.033 | 0.028 | 13.4 | 32 | <1% |
| 3C 445 | 0.058 | 0.051 | 39.0 | 44 | 32% |
| NGC 7314 | 0.031 | 0.028 | 15.3 | 36 | <1% |
| NGC 7469 | 0.047 | 0.041 | 23.2 | 37 | 4% |
| MCG–2–58–22 | 0.049 | 0.042 | 22.7 | 35 | 5% |
| NGC 7582 | 0.055 | 0.040 | 26.8 | 35 | 16% |

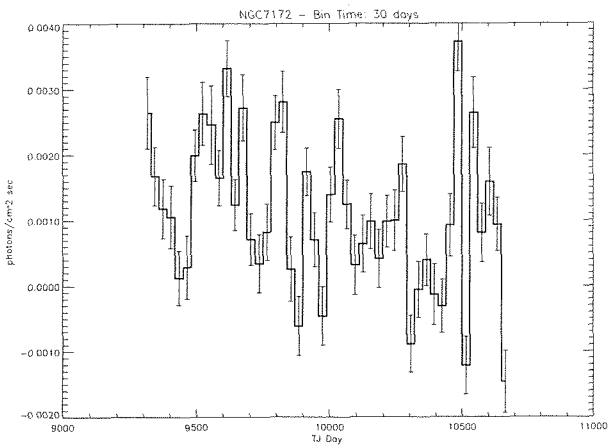
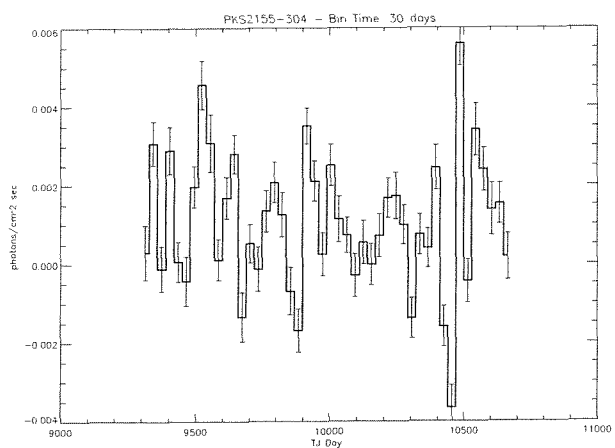
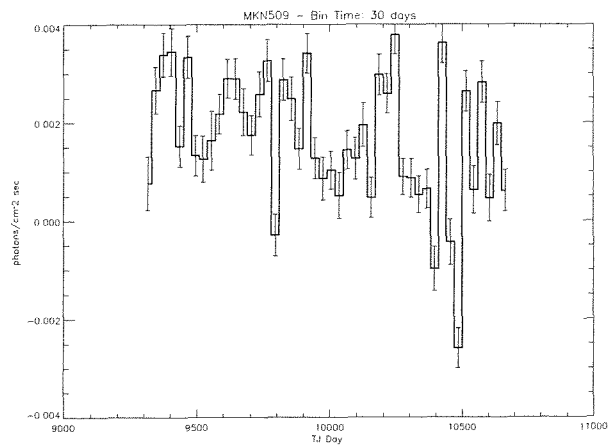
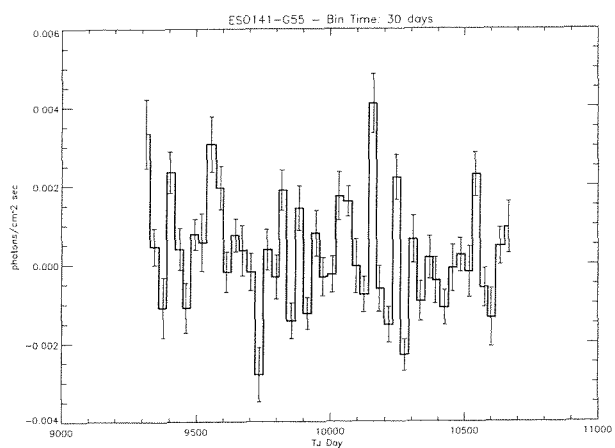
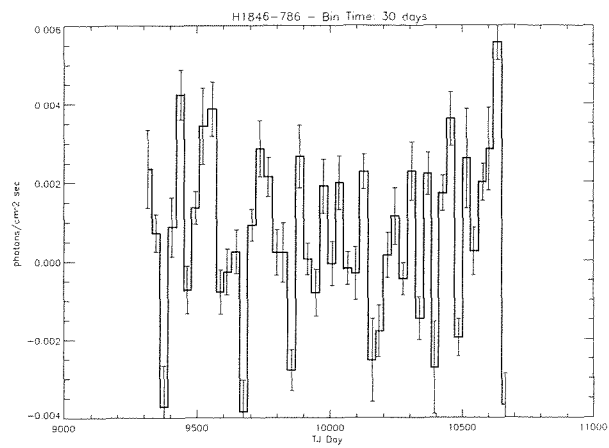
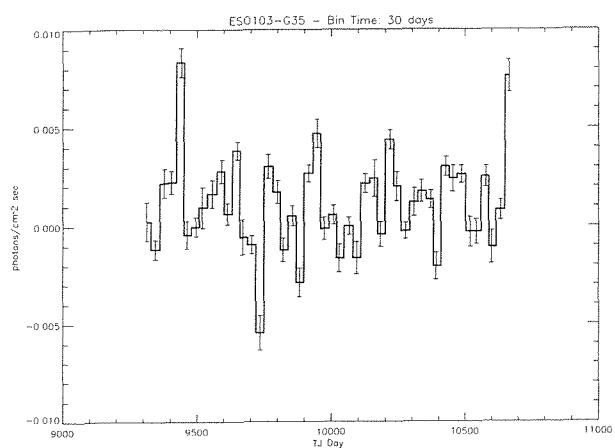
(†) = photons/cm²s

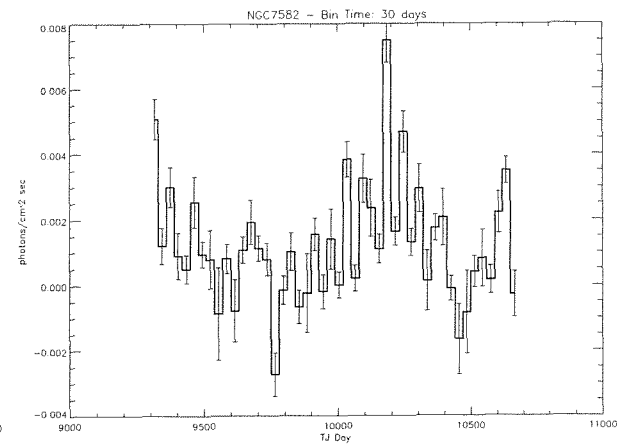
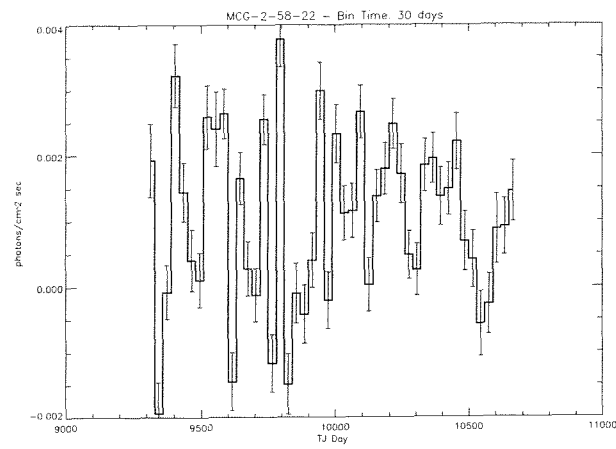
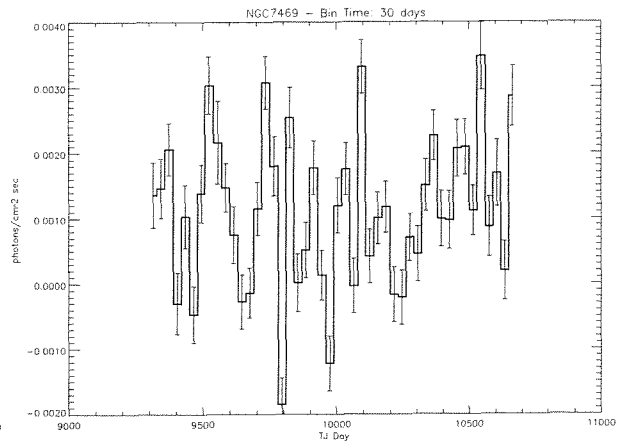
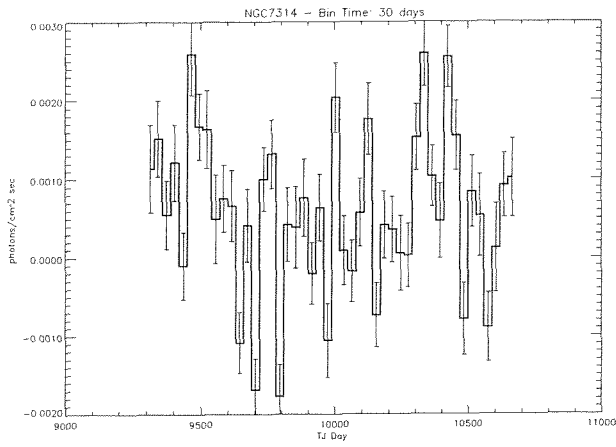
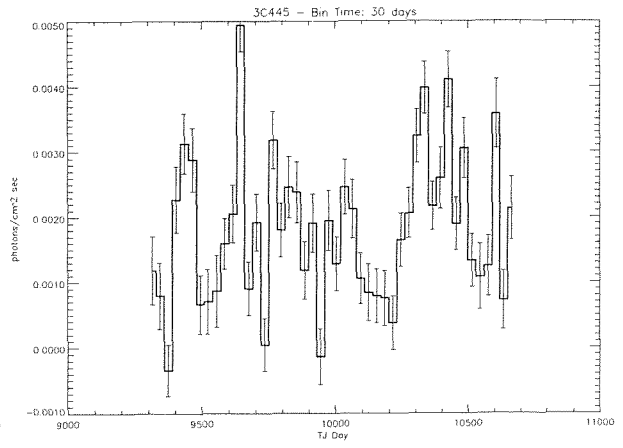
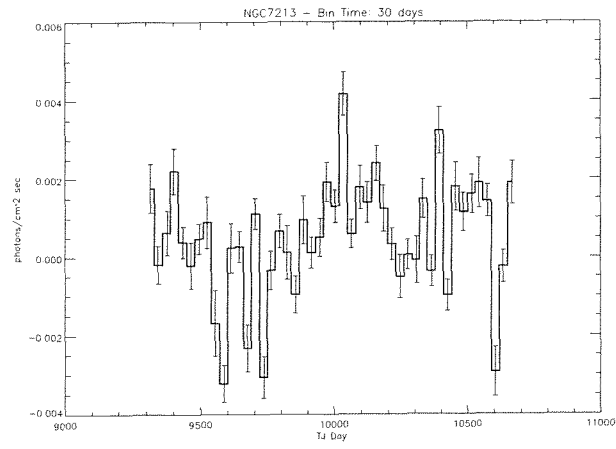












Chapter 5

BeppoSAX-PDS OBSERVATION OF THE PICCINOTTI SAMPLE

5.1 Introduction

In the previous chapter, BATSE results of the observations of the Piccinotti sample of AGN were presented. BATSE detected a good fraction of the sources above its sensitivity limit (see chapter 2) with only 9 objects out of 36 having a detection $<3\sigma$, but it was only possible to measure an average flux over the observing period. The good sensitivity of *BeppoSAX* -PDS has been exploited in this chapter in order to study the spectral characteristics of all the Piccinotti AGN observed and available in the public archive as of December 2000. Moreover, while with BATSE it was possible to study only the long-term variability (timescale of months/years) of the brightest sources, with the PDS observations it is possible to detect high-energy variability on shorter timescales (hours/day). The comparison of the variability results between *BeppoSAX* and BATSE will provide an opportunity to evaluate the behaviour of the brightest sources of the Piccinotti sample on long timescales; furthermore a cross-calibration between these two satellites can be performed.

In table 5.1 we list all the publically available *BeppoSAX* observations of the Piccinotti sample of AGN plus a few sources for which we have proprietary data. Among the missing sources the data of Fairall 49 and MCG-2-58-22 are still private and unfortunately the pointing of IIZW2 is not centered on the source. The remaining two sources, MKN 590 and NGC 3227 are going to be observed in the coming AO5. The Piccinotti source H0917-074 identified with EXO0917.3-0722 has been observed twice by *BeppoSAX* in 1999, but the PDS data was found to be contaminated by another hard X-ray source. Among

the possible sources around EXO0917.3-0722 in the PDS field of view, there was just one good candidate: the Seyfert 2 galaxy MCG-01-24-12 ($z=0.0198$) at RA (2000)=09 20 46.3 and Dec.(2000)=-08 03 22. We obtained a *Beppo*SAX observation pointed at this source and found that this Seyfert 2 was indeed the hard X-ray emitter (Malizia et al. in preparation). Both EXO0917.3-0722 and MCG-01-24-12 are in the HEAO-1 A2 error box, but the Piccinotti flux is mostly due to the Seyfert 2 galaxy according to the *Beppo*SAX results, therefore we conclude that the previous identification was most probably wrong. The *Beppo*SAX data of both sources are discussed in detail in Malizia et al. (in preparation). The PDS spectrum of MCG-01-24-12 is briefly presented in a subsection for completeness but it is not included in the overall sample characteristics. For several sources more than one observation is available. In table 5.1 the PDS observation Log is presented; note that each measurement represents a distinct observation data set within the *Beppo*SAX archive. All sources except for PKS0548-322 were detected at $\geq 3\sigma$ confidence level and the 20-200 keV flux is reported for each individual observation while for PKS0548-322 a 2σ upper limit on the flux is listed.

5.2 Data Analysis

The PDS data analysis of all the Piccinotti sources available from the *Beppo*SAX public archive, has been performed using the software package "SAXDAS" (see <http://www.sdc.asi.it/> software and the Cookbook for *Beppo*SAX NFI spectral analysis, Fiore, Guainazzi & Grandi 1998). Data were telemetred in direct modes; the PDS instrument provides full information about the arrival time, energy, burst length/rise time (RT) and, when available, position for each photon. Standard reduction procedures and screening criteria have been adopted to produce linearized and equalized event files. In particular, time intervals have been excluded from the scientific product accumulation when the angle between the pointing direction and the Earth's limb was $< 5^\circ$; the momentum associated with Geomagnetic Cutoff Rigidity was > 6 GeV/c or when the satellite passed through the South Atlantic Geomagnetic Anomaly (SAGA). The PDS data have been further screened with respect to the other NFI instruments, by eliminating the 5 minutes after any SAGA passage to avoid gain instabilities due to the recovery to the nominal voltage after instrumental switch-on. Particular care was given to the background rejection. Background due to high-energy particles strongly limits the high-energy study of faint extragalactic sources like AGNs. For the PDS, particle background events are rejected through an analysis of their Rise Time signal. At the moment two different strategies are available in SAXDAS for Rise Time based background rejection:

Table 5.1: PDS observation Log

| Source | Fux [†] (20-200)keV | Obs. Date | Exp. Time (x 10 ⁴ sec) | Count Rate | σ |
|--------------|---------------------------------|-----------|--------------------------------------|------------|----------|
| Mrk 1152 | 1.01 | 04-01-00 | 3.97 | 0.09±0.026 | 4 |
| Fairall 9 | 4.85 | 25-08-96 | 4.08 | 0.36±0.028 | 13 |
| NGC 526A | 5.99 | 31-12-98 | 4.42 | 0.40±0.026 | 15 |
| 3C 120 | 6.10 | 20-08-97 | 3.57 | 0.72±0.031 | 23 |
| PKS 0548–322 | <1.84 | 20-02-99 | 0.93 | 0.11±0.050 | 2 |
| | <1.38 | 08-04-99 | 1.02 | 0.11±0.050 | 2 |
| H0557-385 | 4.07 | 19-12-00 | 1.47 | 0.43±0.042 | 10 |
| | 8.14 | 26-01-01 | 0.58 | 0.61±0.067 | 9 |
| NGC 2992 | 2.12 | 01-12-97 | 3.32 | 0.17±0.032 | 5 |
| | 16.06 | 25-11-98 | 2.71 | 1.28±0.035 | 36 |
| M 82 | 0.62 | 06-11-97 | 3.85 | 0.13±0.029 | 4 |
| NGC 3783 | 13.78 | 06-06-98 | 7.04 | 1.16±0.022 | 53 |
| NGC 4151 | 61.45 | 06-07-96 | 2.75 | 4.79±0.047 | 102 |
| | 59.18 | 09-07-96 | 0.78 | 4.85±0.080 | 61 |
| | 59.09 | 04-12-96 | 1.12 | 4.45±0.058 | 77 |
| | 56.15 | 06-12-96 | 1.08 | 4.34±0.059 | 73 |
| | 68.60 | 04-01-99 | 3.85 | 5.23±0.031 | 169 |
| 2A 1219+305 | 1.56 | 12-07-99 | 2.07 | 0.12±0.038 | 3 |
| 3C 273 | 23.12 | 18-07-96 | 6.06 | 1.56±0.031 | 50 |
| | 41.60 | 13-01-97 | 1.14 | 2.71±0.070 | 39 |
| | 36.93 | 15-01-97 | 1.08 | 2.48±0.059 | 42 |
| | 32.89 | 17-01-97 | 1.25 | 2.22±0.054 | 41 |
| | 30.00 | 24-06-98 | 3.38 | 2.19±0.032 | 68 |
| NGC 4593 | 10.12 | 31-12-97 | 3.85 | 0.75±0.030 | 25 |
| MCG–6–30–15 | 7.98 | 29-07-96 | 8.57 | 0.72±0.026 | 28 |
| IC 4329A | 26.34 | 02-01-98 | 3.76 | 2.12±0.031 | 68 |
| | 18.27 | 17-07-98 | 1.83 | 1.44±0.043 | 33 |
| | 22.82 | 21-07-98 | 1.78 | 1.89±0.044 | 47 |
| | 20.19 | 27-07-98 | 1.12 | 1.70±0.056 | 30 |
| NGC 5506 | 17.39 | 30-01-97 | 1.70 | 1.44±0.046 | 31 |
| | 20.03 | 14-01-98 | 1.75 | 1.61±0.061 | 26 |
| NGC 5548 | 10.24 | 14-08-97 | 12.0 | 0.81±0.017 | 48 |

Table 5.1–Continued

| Source | Fux [†] (20-200)keV | Obs. Date | Exp. Time (x 10 ⁴ sec) | Count Rate | σ |
|--------------|---------------------------------|-----------|--------------------------------------|------------|----------|
| Mrk 501 | 23.79 | 07-04-97 | 0.89 | 2.18±0.064 | 34 |
| | 34.84 | 11-04-97 | 0.87 | 2.77±0.067 | 41 |
| | 115 | 16-04-97 | 0.73 | 8.98±0.079 | 114 |
| | 18.07 | 28-04-98 | 0.98 | 1.85±0.078 | 24 |
| | 22.54 | 29-04-98 | 0.96 | 2.30±0.079 | 29 |
| | 11.64 | 01-05-98 | 0.84 | 1.13±0.083 | 13 |
| | 4.78 | 20-06-98 | 1.16 | 0.48±0.054 | 9 |
| | 4.63 | 29-06-98 | 0.75 | 0.71±0.089 | 8 |
| | 8.41 | 16-07-98 | 0.69 | 0.83±0.093 | 10 |
| | 4.67 | 25-07-98 | 1.45 | 0.53±0.063 | 9 |
| | 1.53 | 10-06-99 | 7.84 | 0.14±0.020 | 7 |
| ESO 103–G35 | 7.59 | 03-10-96 | 2.10 | 0.74±0.041 | 18 |
| | 6.95 | 14-10-97 | 0.59 | 0.56±0.077 | 7 |
| H1846–786 | 1.38 | 08-03-01 | 1.79 | 0.16±0.050 | 3 |
| ESO 141–G55 | 5.89 | 01-11-99 | 3.92 | 0.50±0.028 | 17 |
| Mrk 509 | 8.52 | 18-05-98 | 2.40 | 0.75±0.038 | 20 |
| | 9.88 | 11-10-98 | 1.70 | 0.89±0.044 | 20 |
| PKS 2155–304 | 2.10 | 20-11-96 | 4.33 | 0.18±0.028 | 6 |
| | 2.43 | 22-11-97 | 2.80 | 0.18±0.035 | 5 |
| NGC 7172 | 6.41 | 16-10-96 | 1.73 | 0.42±0.044 | 9 |
| | 3.43 | 07-11-97 | 2.11 | 0.27±0.041 | 7 |
| 3C 445 | 4.21 | 30-11-99 | 4.65 | 0.33±0.025 | 13 |
| NGC 7314 | 6.40 | 09-06-99 | 4.25 | 0.54±0.027 | 20 |
| NGC 7469 | 7.31 | 14-12-97 | 3.21 | 0.62±0.033 | 19 |
| | 5.33 | 29-11-99 | 12.15 | 0.46±0.016 | 29 |
| NGC 7582 | 10.65 | 09-11-98 | 2.61 | 0.85±0.035 | 24 |

Notes: (†)Flux $\times 10^{-11}$ erg cm⁻² s⁻¹

1. fixed Rise Time thresholds
2. variable Rise Time thresholds as a function of the PHA channel of the event and of the temperature of the phoswiches.

The default strategy is the former and the PDS response matrix has been calibrated using data reduced in this way. The average, full band (13-300 keV) PDS residual background is about 34 counts s^{-1} . The background is considerably reduced, by 30-50% depending on the energy, if the second strategy is applied. The variable Rise Time strategy reduces the count rates of a "Crab like" spectral source by about 7% giving a much better signal to noise ratio for faint sources. The method has been developed and calibrated by the PDS team at TESRE/CNR using Crab data and does not introduce systematic spectral effects for a "Crab like" spectral source (power law spectrum with energy index $\alpha = 1.1$). However the method is recommended for faint sources only, i.e. sources for which the uncertainty on the best-fit slope is higher than 0.1 or so (corresponding to a count rate smaller than 0.5-1 s^{-1}). For sources with better statistics, and intrinsic spectral shape very different from the Crab, the use of this method may introduce a systematic error in the spectral shape. The Piccinotti sources have been analyzed using the variable Rise Time method. The background subtraction in the PDS light curves and spectra was performed by plain subtraction of the *off-source* from the *on-source* products. The systematic uncertainties of this method are lower than $\simeq 0.03 \text{ s}^{-1}$ in the full PDS sensitive energy band-pass (Guainazzi & Matteuzzi 1997). Another correction applied to the PDS data is the screening for "spikes". The PDS light curves are well known to exhibit "spikes" on timescales between a fraction of a second to a few seconds. These spikes are due to single particle hits, which illuminate one crystal and create fluorescence cascades. The average occurrence rate varies strongly from observation to observation and can be as high as a few events per orbit. Typical count rates range between a few tens up to several hundreds or even thousands of counts per second. The spectrum of the spikes is soft and usually most counts from spikes are recorded below 30 keV.

Spectral fits were performed using the XSPEC 10.0 software package and public response matrices as from the 1998 November issue. PI (Pulse Invariant) channels are rebinned by sampling the instrument resolution with the same number of channels at all energies when possible and ensuring at least 20 counts per bin. This guarantees the use of the χ^2 method in determining the best-fit parameters, since the distribution in each channel can be considered Gaussian. Errors are quoted at 90% level of confidence.

Table 5.2: Timing Analysis Results

| Source | | Average | χ^2 | d.o.f. | Prob |
|--------------|------------|---------|----------|--------|------|
| Fairall 9 | | 0.159 | 37.11 | 31 | 79% |
| NGC 526A | | 0.156 | 58.64 | 34 | 99% |
| 3C 120 | | 0.336 | 60.12 | 27 | >99% |
| PKS 0548–322 | (20-02-99) | -0.01 | 5.87 | 6 | 56% |
| | (08-04-99) | 0.09 | 6.60 | 8 | 42% |
| H0557-385 | (19-12-00) | 0.198 | 14.66 | 14 | 60% |
| | (26-01-01) | 0.251 | 13.65 | 8 | 91% |
| NGC 2992 | (01-12-97) | 0.07 | 17.20 | 25 | 12% |
| | (25-11-98) | 0.501 | 31.06 | 20 | 94% |
| M82 | | 0.04 | 8.63 | 24 | <1% |
| NGC 3783 | | 0.459 | 75.51 | 59 | 93% |
| NGC 4151 | (06-07-96) | 1.811 | 28.55 | 24 | 76% |
| | (09-07-96) | 2.016 | 242.3 | 6 | >99% |
| | (04-12-96) | 1.770 | 13.62 | 6 | 96% |
| | (06-12-96) | 1.894 | 4.87 | 6 | 44% |
| | (04-01-99) | 2.070 | 214.2 | 28 | >99% |
| 2A 1219+305 | | 0.04 | 23.01 | 16 | 89% |
| 3C 273 | (18-07-96) | 0.530 | 52.91 | 49 | 67% |
| | (13-01-97) | 0.818 | 5.12 | 8 | 25% |
| | (15-01-97) | 0.960 | 17.72 | 8 | 98% |
| | (17-01-97) | 0.867 | 8.64 | 8 | 63% |
| | (24-06-98) | 0.699 | 42.27 | 28 | 96% |
| NGC 4593 | | 0.296 | 36.95 | 30 | 82% |
| IC 4329A | (02-01-98) | 0.904 | 37.25 | 29 | 86% |
| | (17-07-98) | 0.471 | 3.19 | 15 | <1% |
| | (21-07-98) | 0.795 | 14.65 | 14 | 60% |
| | (27-07-98) | 0.720 | 13.59 | 9 | 86% |
| NGC 5506 | (30-01-97) | 0.619 | 12.47 | 13 | 51% |
| | (14-01-98) | 0.678 | 17.14 | 15 | 69% |
| NGC 5548 | | 0.321 | 16.39 | 35 | <1% |
| | | 0.253 | 33.43 | 34 | 50% |
| | | 0.319 | 23.94 | 32 | 15% |
| | | 0.309 | 24.81 | 18 | 87% |

Table 5:2–Continued

| Source | | Average | χ^2 | d.o.f. | Prob |
|-------------|------------|---------|----------|--------|------|
| Mrk 501 | (07-04-97) | 0.887 | 9.11 | 6 | 83% |
| | (11-04-97) | 1.091 | 11.29 | 6 | 92% |
| | (16-04-97) | 3.139 | 80.65 | 6 | >99% |
| | (28-04-98) | 0.470 | 9.37 | 10 | 50% |
| | (29-04-98) | 0.596 | 19.98 | 10 | 97% |
| | (20-06-98) | 0.106 | 9.29 | 10 | 49% |
| | (16-07-98) | 0.175 | 8.29 | 9 | 49% |
| | (25-07-98) | 0.167 | 11.31 | 16 | 21% |
| | (10-06-99) | 0.060 | 101.6 | 77 | 97% |
| H1846-786 | | 0.08 | 13.50 | 12 | 67% |
| ESO 141–G55 | (01-11-99) | 0.192 | 26.09 | 33 | 20% |
| Mrk 509 | (18-05-98) | 0.325 | 3.99 | 19 | <1% |
| | (11-10-98) | 0.387 | 7.99 | 13 | 15% |
| PKS2155-304 | (20-11-96) | 0.08 | 44.7 | 34 | 90% |
| | (22-11-97) | 0.03 | 17.98 | 21 | 35% |
| NGC 7172 | (16-10-96) | 0.187 | 10.03 | 13 | 31% |
| | (07-11-97) | 0.09 | 14.42 | 17 | 36% |
| 3C 445 | | 0.134 | 82.61 | 35 | 99% |
| NGC 7314 | | 0.271 | 38.03 | 33 | 75% |
| NGC 7469 | (29-11-99) | 0.193 | 112 | 94 | 90% |
| NGC 7582 | | 0.377 | 24.86 | 18 | 87% |

5.3 PDS Light Curves

As for the BATSE data the χ^2 test has been used on all the PDS observations of the Piccinotti sources available in the *BeppoSAX* public archive, for a preliminary investigation of possible variations in the high energy flux. In fact, although the following analysis is not deep it can help to investigate the presence of variability on shorter timescales than possible with BATSE (note that a deeper study on the variability is beyond the scope of this thesis). In table 5.2 the average count rate for all observations together with the χ^2 value, the degree of freedom (*d.o.f.*, number of bins -1) and the relative probability of variation, are shown. For consistency, the temporal bin size used in the χ^2 test is always of 5700 seconds which corresponds to a single *BeppoSAX* orbit. The light curves of sources having detection $\geq 10\sigma$ are included in appendix A. Also for the light curve plots, the bin size corresponds to 5700 seconds, except for very short observations (such those performed on NGC4151 and MKN501) where it is halved and conversely for the very long observation (such as that of NGC7469, ~ 150 ks) where it is doubled. Note that for sources with more than one observation, light curves with the same y -scale have been plotted in order to best identify the possible variations between various pointings. In the first observation of NGC7469 there are data missing due to telemetry problems and for this reason the light curve has not been considered.

5.3.1 Results on variability

Among all the Piccinotti sources observed by *BeppoSAX*, only 11 proved to be variable with probability $\geq 90\%$ in the 20-200 keV band, for a total of 17 observations (see table 5.2). To verify these results, the χ^2 test with different temporal bin size (1000, 4000 and 8000 seconds) has been applied to all the light curves which were variable with a 5700 seconds bin size. Only for three of them, the well known variable sources NGC4151, 3C273 and MKN501, is variability on different timescales discussed here. In fact, short timescale variability (hours-days) can be searched for by analyzing the single pointings while longer variations on timescales of months-years can be investigated by looking at different pointings.

Of the 5 *BeppoSAX* observations of NGC4151 analyzed here, three were found to be variable using different bin sizes. Variations between the different *BeppoSAX* pointings are also evident. In particular, the July 1996 light curves show a clear trend with an increase of $\sim 15\%$ between the first and the second pointings. The variation in the second observation of July has been confirmed with a probability $> 99\%$ by using other bin sizes. The intensity during the Dec 1996 observations was low and constant and quite similar

to the first part of the July 1996 observation. However, in the Dec 4th 1996 observation a flare like event of about 3 hours duration is detectable (see light curve in appendix A). Finally in Jan 1999 the source exhibits a few variations of ~ 1 day timescale confirmed at $>99\%$ probability also with other bin sizes. Comparison of all 5 observations (light curves and average count rates in the table) helps to detect high states of the source and indicates a months/years variability as already found in the BATSE data (see previous chapter). It is important to note that the LECS-MECS (0.1-20 keV) light curves of the discussed observations follow almost the same pattern of variability as the PDS, but with a greater amplitude (Piro et al. 2001).

In the case of 3C273, variations between different pointings have been found, but short time scale variability has been detected only in a couple of observations out of the 5 analyzed here. In particular daily variability has been found among the January 1997 observations, in fact, there is a monotonically decreasing flux with a difference in the count rate between the first and the last observation of more than 20%. Shorter timescale variability (~ 8 hours) is present in the first part of the Jun 24th 1998 pointing, which is also confirmed using different bin sizes. Also for 3C273 variability on longer timescales (months-years) is present (see average count rates in table 5.2) confirming again the BATSE results.

During 1997, the BL Lac object MKN501 showed extremely strong emission and a high variability as has been reported by various authors (see for example Pian et al. 1998). In particular *BeppoSAX* caught a big flare from this source on April 16th. In the first three light curves of MKN501 reported in appendix A (7th, 11th and 16th April 1997), the *BeppoSAX* -PDS pointings of this flare are shown. A huge increase of the flux (more than 4 times) is evident on April 16th with respect to the 7th and 11th of the same month. Spectral variations have also been found and they will be discussed in section 5.5.2. It is interesting to note that after this extremely high activity the source became more and more dim, so much that one year later (April 1998) the 20-200 keV flux was about 6 times fainter than the big flare flux, continuing to decrease in just one month by a factor of 3 (May-Jun 1998) and again by a factor of 3 one year later (June 1999). Apart from this long-timescale variability, from the χ^2 test there is evidence of variation on a timescale of hours in the April 29th 1998 observation, and marginal fluctuations around the mean value have been detected in the last observation (Jun 1999) but both of these were not confirmed using different bin time sizes. PDS light curves of MKN501 relating to observations with detection $>10\sigma$ are reported in appendix A.

Variability on timescales of hours/day can be investigated also in the remaining sources which were found to be variable in table 5.3. For three objects: NGC526A, 3C120

and 3C445 the variability found in table 5.2 has been confirmed only when using large temporal bin sizes (4000-8000 seconds). In the case of 3C120 variations at lower energies in the LECS and MECS data have recently been reported by Zdziarski & Grandi (2001), while for NGC526A even if no variability has been reported by Landi et al. (2001) in the lower energy band, variations seem to be present in the high energy band (5-10 keV) of the MECS data (*BeppoSAX* public archive). On the contrary for 3C445 no *BeppoSAX* broad band analysis is available yet but ASCA-SIS and GIS light curves were inspected for variability, and none was found (Sambruna et al. 1998). A sinusoidal trend seems to characterize the light curve of NGC3783 at different bin sizes but a probability of variation $>90\%$ has been found only with bin sizes greater than 5700 seconds. Finally variability was not confirmed using different temporal bin sizes than 5700 seconds for H0557-385, NGC2992, PKS2155-304 and NGC7469. Probably for all these sources, except for NGC7469, the poor statistics play an important role. In the case of NGC2992 which does not show short timescale variability, the flux changed by a factor of 6 between the two PDS observations, taken in one year and analyzed in this thesis, confirming also the broad-band results (Gilli et al. 2000). In fact, at lower energies (2-10 keV) this is one of the most variable Seyferts ever observed (Polletta et al. 1996).

The variability study performed in this thesis, although not highly detailed, provides some interesting results: variation of the high energy emission is probably ubiquitous in Seyfert galaxies being present on both short and long timescales. There is a range of variability amplitudes observed as well as patterns; although a comparison with low-luminosity emission (< 10 keV) is not discussed in this thesis, very likely the changes seen at high energies are correlated with these observed at low energies.

Variability studies of AGN are an important tool for the investigation of the region where the radiation is produced, and since in the standard picture it is assumed that the X-rays are produced by accretion onto a massive black hole (Rees 1984), evaluation of the minimum timescale of variations provides information on the size of the central region. In particular, the timescale of the variations is roughly equal to the light travel time across the innermost stable orbit in a Schwarzschild geometry, or:

$$\Delta t \sim R/c \sim 50M_6 \quad (seconds) \quad (5.1)$$

where M_6 is the mass of the black hole in units of 10^6 Solar masses. Besides providing an estimation of the black hole mass, the variability can give important information about the accretion rate. If the observed luminosity is compared to the maximum luminosity of an AGN emitting isotropically which is given by the Eddington luminosity, L_{EDD} ; this maximum luminosity is related to the minimum timescale variability by the following

relationship:

$$\text{Log}L_{EDD} \leq 41.3 + \text{Log}\Delta t_{(sec)} \quad (5.2)$$

Finally, knowing the X-ray luminosity (L_x) and the size of the emitting region (R), we can estimate the degree of absorption of the γ -ray photons or the compactness parameter defined as:

$$\tau_{\gamma\gamma} \propto \frac{L_x(20 - 200\text{keV})}{R} \quad (5.3)$$

This must be <1 for γ -rays not to be absorbed. Since the hard X-ray luminosity represents a higher source output with respect to the emission below 10 keV, it is obvious that flux variations at higher energies provide the most stringent constraints on the above discussed parameters. For example, using the minimum variability timescale obtained from the PDS observations (say a few hours or so) we can estimate a typical black hole mass of the order of $\sim 10^8 M_\odot$, an Eddington luminosity of less than $\sim 10^{45} \text{ erg s}^{-1}$, or alternatively an Eddington ratio ($L_{(20-200\text{keV})}/L_{EDD}$) which is greater than 10^{-2} – 10^{-3} , or close to the Eddington rate expected in the standard accretion disc model. The compactness parameter τ is greater than one, which may explain why in Seyfert galaxies γ -rays above a few hundred keV are not strongly detected.

5.4 PDS Spectra of the Piccinotti Sample

The PDS spectral analysis of the Piccinotti sample has been performed for all the *BeppoSAX* observations with detection $>5 \sigma$ for Seyfert galaxies and whenever possible for blazars. A simple power-law model was used to fit the data in the 20–200 keV energy band; the goodness of fit is given by the χ^2 statistics:

$$\chi^2 = \sum (C(I) - C_p(I))^2 / (\sigma(I))^2 \quad (5.4)$$

where $C(I)$ are the photon counts within specific instrument channels (I), $C_p(I)$ is the predicted count spectrum and $\sigma(I)$ is the error for channel I (e.g. if $C(I)$ are counts $\sigma(I)$ is usually estimated by $\sqrt{C(I)}$). The fit parameters and the reduced χ^2 are listed in table 5.3 for Seyferts and in table 5.7 for blazars (the 20–200 keV fluxes for this model are reported in table 5.1 for all the Piccinotti sources observed by *BeppoSAX*). In the cases of sources with more than one observation, the spectra have been summed in order to improve the statistics. In particular we summed together observations of the Seyfert galaxies H0557-385, NGC2992, NGC4151, 3C273, IC4329A, NGC5506, ESO103-G35, MKN509, NGC7172 and NGC7469 even if in many of them flux and/or spectral variations are well known. We also summed the data of blazars when possible except

Table 5.3: Simple Power Law Spectra of Seyfert galaxies

| Source | | A_{pl}^{\dagger} | Γ | χ^2 | d.o.f. |
|-------------|------------|------------------------|------------------------|----------|--------|
| Fairall 9 | | $0.86^{+0.02}_{-0.01}$ | $1.89^{+0.34}_{-0.25}$ | 12.32 | 14 |
| NGC 526A | | $0.50^{+0.40}_{-0.01}$ | $1.72^{+0.24}_{-0.20}$ | 14.42 | 14 |
| 3C 120 | | $3.62^{+0.03}_{-0.01}$ | $2.11^{+0.17}_{-0.15}$ | 13.16 | 14 |
| H0557-322 | (19-12-00) | $6.99^{+0.20}_{-0.04}$ | $2.46^{+0.44}_{-0.32}$ | 14.28 | 14 |
| | (26-01-01) | $1.29^{+0.04}_{-0.01}$ | $1.87^{+0.43}_{-0.34}$ | 14.54 | 14 |
| | (Sum) | $3.64^{+0.06}_{-0.06}$ | $2.23^{+0.29}_{-0.25}$ | 18.48 | 14 |
| NGC 2992 | (01-12-97) | $0.40^{+0.08}_{-0.04}$ | $1.91^{+0.99}_{-0.30}$ | 6.02 | 14 |
| | (25-11-98) | $3.37^{+0.02}_{-0.01}$ | $1.94^{+0.11}_{-0.08}$ | 12.46 | 14 |
| | (Sum) | $1.72^{+0.01}_{-0.01}$ | $1.93^{+0.15}_{-0.13}$ | 8.26 | 14 |
| NGC 3783 | | $3.75^{+0.01}_{-0.01}$ | $2.00^{+0.07}_{-0.07}$ | 25.48 | 14 |
| NGC 4151 | (06-07-96) | $12.0^{+0.01}_{-0.01}$ | $1.92^{+0.04}_{-0.03}$ | 236.18 | 14 |
| | (09-07-96) | $15.5^{+0.03}_{-0.02}$ | $1.99^{+0.06}_{-0.04}$ | 114.38 | 14 |
| | (04-12-96) | $9.23^{+0.01}_{-0.01}$ | $1.87^{+0.05}_{-0.04}$ | 103.88 | 14 |
| | (06-12-96) | $9.73^{+0.02}_{-0.01}$ | $1.89^{+0.05}_{-0.04}$ | 123.76 | 14 |
| | (04-01-99) | $10.3^{+0.01}_{-0.01}$ | $1.86^{+0.02}_{-0.03}$ | 156.24 | 14 |
| | (Sum) | $10.9^{+0.01}_{-0.01}$ | $1.90^{+0.01}_{-0.01}$ | 757.96 | 14 |
| NGC 4593 | | $1.31^{+0.01}_{-0.01}$ | $1.82^{+0.16}_{-0.13}$ | 16.10 | 14 |
| MCG-6-30-15 | | $4.21^{+0.02}_{-0.01}$ | $2.16^{+0.15}_{-0.12}$ | 34.44 | 14 |
| IC 4329A | (02-01-98) | $5.91^{+0.01}_{-0.01}$ | $1.96^{+0.14}_{-0.05}$ | 38.92 | 14 |
| | (17-07-98) | $3.83^{+0.02}_{-0.01}$ | $1.94^{+0.11}_{-0.11}$ | 52.78 | 14 |
| | (21-07-98) | $6.03^{+0.02}_{-0.01}$ | $1.99^{+0.07}_{-0.08}$ | 32.34 | 14 |
| | (27-07-98) | $5.72^{+0.03}_{-0.02}$ | $2.01^{+0.19}_{-0.11}$ | 21.14 | 14 |
| | (Sum) | $5.44^{+0.01}_{-0.02}$ | $1.97^{+0.04}_{-0.04}$ | 99.69 | 14 |
| NGC 5506 | (30-01-97) | $4.37^{+0.02}_{-0.01}$ | $1.98^{+0.13}_{-0.11}$ | 19.32 | 14 |
| | (14-01-98) | $4.77^{+0.02}_{-0.01}$ | $1.99^{+0.12}_{-0.11}$ | 30.52 | 14 |
| | (Sum) | $4.59^{+0.01}_{-0.01}$ | $1.99^{+0.06}_{-0.08}$ | 36.68 | 14 |
| NGC 5548 | | $1.76^{+0.01}_{-0.01}$ | $1.89^{+0.08}_{-0.07}$ | 18.34 | 14 |
| ESO 103-G35 | (03-10-96) | $5.09^{+0.05}_{-0.02}$ | $2.22^{+0.26}_{-0.18}$ | 24.08 | 14 |
| | (14-10-97) | $2.21^{+0.09}_{-0.09}$ | $2.04^{+0.52}_{-0.24}$ | 10.78 | 14 |
| | (Sum) | $4.31^{+0.04}_{-0.02}$ | $2.19^{+0.19}_{-0.19}$ | 12.54 | 14 |
| ESO 141-G55 | (01-11-99) | $1.48^{+0.01}_{-0.01}$ | $1.98^{+0.02}_{-0.02}$ | 16.66 | 14 |
| Mrk 509 | (18-05-98) | $3.34^{+0.03}_{-0.01}$ | $2.09^{+0.21}_{-0.17}$ | 24.78 | 14 |
| | (11-10-98) | $5.65^{+0.05}_{-0.03}$ | $2.19^{+0.19}_{-0.18}$ | 28.56 | 14 |
| | (Sum) | $3.79^{+0.02}_{-0.01}$ | $2.11^{+0.17}_{-0.13}$ | 29.54 | 14 |

Table 5.3:–Continued

| Source | | A_{pl}^{\dagger} | Γ | χ^2 | d.o.f. |
|----------|------------|------------------------|------------------------|----------|--------|
| NGC 7172 | (16-10-96) | $0.36^{+0.01}_{-0.03}$ | $1.63^{+0.37}_{-0.33}$ | 12.04 | 14 |
| | (07-11-97) | $0.67^{+0.05}_{-0.06}$ | $1.93^{+0.72}_{-0.53}$ | 15.12 | 14 |
| | (Sum) | $0.44^{+0.01}_{-0.03}$ | $1.75^{+0.33}_{-0.34}$ | 14.14 | 14 |
| 3C 445 | | $1.19^{+0.02}_{-0.01}$ | $2.01^{+0.28}_{-0.24}$ | 21.14 | 14 |
| NGC 7314 | | $1.83^{+0.02}_{-0.01}$ | $2.02^{+0.20}_{-0.18}$ | 19.60 | 14 |
| NGC 7469 | (14-12-97) | $2.42^{+0.02}_{-0.02}$ | $2.05^{+0.23}_{-0.19}$ | 11.90 | 14 |
| | (29-11-99) | $1.84^{+0.01}_{-0.01}$ | $2.06^{+0.12}_{-0.12}$ | 20.03 | 14 |
| | (Sum) | $1.88^{+0.01}_{-0.01}$ | $2.05^{+0.12}_{-0.10}$ | 22.96 | 14 |
| NGC 7582 | | $2.85^{+0.02}_{-0.01}$ | $2.00^{+0.16}_{-0.14}$ | 39.62 | 14 |

Notes: (\dagger) $A \times 10^{-2}$

for the BL Lac object MKN501 April 1997 observations, when a big flare occurred (see section 5.5). The spectrum and data to model ratio for all the observations are shown in appendix B. Inspection of tables 5.3 and 5.7 shows that considering the PDS (20-200 keV) data only and using a simple power law model, the photon indices are generally steep. Only three sources, 3C273, NGC526A and NGC7172 (only the first observation) have $\Gamma < 1.8$, while most BL Lacs have observations with steep spectral index. In the case of BL Lac objects the steepness of the spectrum is not a surprise, typically in these objects the spectrum is $\Gamma > 2$ (i.e. Ciliegi et al 1995). In the case of 3C273 the spectrum is known to be intrinsically flat and this is probably true also for the Seyfert 1.9 galaxy NGC526A (Landi et al. 2001); in the first observation of NGC7172 the flatness of the spectrum could be due to a stronger amount of Compton reflection implied by the broad-band data (Dadina et al. 2001). A histogram of the photon indices is shown in figure 5.1, where the solid histogram represents the distribution of photon indices for all the Piccinotti sources observed by *BeppoSAX* (Seyferts and blazars), while the dotted histogram represents the Seyfert galaxies only. The estimated weighted mean of all the observations of table 5.1 is $\Gamma_{mean} = 1.93 \pm 0.01$ which becomes 1.98 ± 0.02 if the three flatter objects, NGC4151 and the BL Lac objects (in particular MKN501) are not considered. There is no difference between the two classes of Seyfert, we obtain 1.98 ± 0.02 for the Seyfert 1s and 1.97 ± 0.08 for the Seyfert 2s (again NGC4151 has not been considered). The steep photon index found from the PDS data is not consistent with the results of the first spectral studies on Seyfert galaxies in the high energy band performed by Rothschild et al. (1983) with the HEAO 1-A4 (12-165 keV).

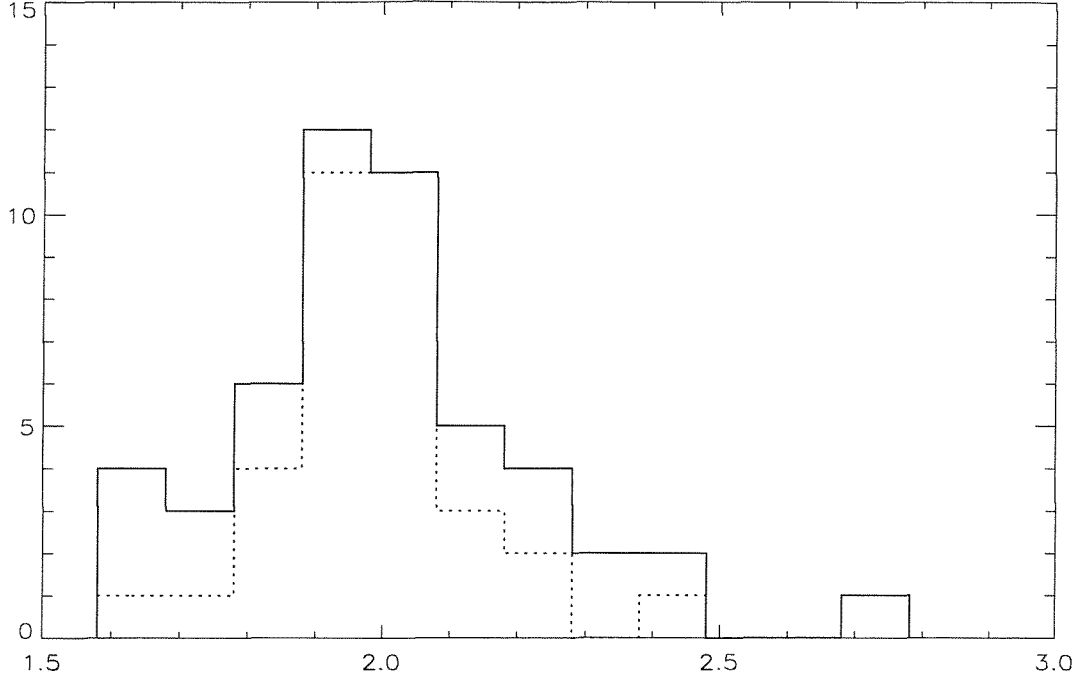


Figure 5.1: Histogram of the photon indices of the power law fits. The solid line is for the observations of all sources while the dotted line is for the observations of Seyfert galaxies.

Observations of 12 AGN provided a mean photon index of $\Gamma=1.54\pm0.23$, or 1.62 ± 0.04 if the A2 (2.1-50 keV) data were also considered. On the other hand, in the harder energy range of OSSE (~ 50 -500 keV) Zdziarski et al. (2000) find that the average data of a sample of Seyfert 1 and Seyfert 2 galaxies, when fitted with a simple power law give spectral indices significantly higher than 1.9 (2.50 ± 0.09 for Seyfert 1s and 2.05 ± 0.09 for Seyfert 2s). Clearly the average spectrum of Seyferts is not well represented by a single power law as argued by Rothshield et al. in 1983 using the limited sensitivity of HEAO 1. Comparison between our *BeppoSAX* -PDS and OSSE/A4 results strongly suggest that at high energies the steepness of the spectra are probably due to the presence of a high energy cut-off while the flatness at low energies may be explained by the presence of a reflection component. This is also evident from the model to data ratio obtained by this preliminary analysis of the PDS data (see table 5.3 and figures in appendix B). In fact, while in some cases the simple power law model fits the high energy data satisfactorily, in others this model is not sufficient; clearly in these last cases the contribution of spectral components like Compton reflection and/or a high energy cut-off are probably present. Note, however, that in the case of the three blazar objects with high statistics analyzed in

section 5.5, MKN501, 3C273 and PKS2155-304, the high energy data are well fitted by a power law model. *BeppoSAX* observations of MKN501 and 3C273 and their comparison with BATSE results and other high energy observations, will be presented in section 5.5 while in the following the Seyfert galaxies will be discussed. To investigate more complex spectral shapes, a deeper analysis has been performed for all the Seyfert galaxies listed in table 5.3, which have a value of a χ^2 greater than 21; this corresponds to a 90% probability that the power law model is not a good fit to the data. For this sub-sample of 10 objects three more complex models have been used to fit the high energy data. In table 5.4 all the parameters for each of the above models are reported (errors are quoted at 90% confidence level). **Model 1** in the tables corresponds in the XSPEC package to the HIGHECUT model i.e. a power law with a high energy cut-off (i.e. with no reflection), **model 2** is the PEXRAV model, i.e. an exponentially cut-off power law spectrum reflected from neutral material (Magdziarz & Zdziarski 1995) where the high energy cut-off has been frozen to a value of 10000 keV (i.e. only a Compton reflection component has been assumed) and **model 3** is again PEXRAV model with both the reflection and the high energy cut-off included but with the photon index fixed to 1.9 which is the average value for Seyfert 1s and 2s previously found. With the pexrav model the output spectrum is the sum of an e-folded power law and the reflection component. The reflection component ($R=\Omega/2\pi$) is characterized by two parameters: the solid angle fraction of a neutral, plane parallel slab illuminated by the power-law photons, and its inclination angle to the line of sight. Nominally it can vary only between 0 and 2, $R=1$ for an isotropic source above disc. If this parameter is left free to vary up to values >2 , then one can assume source anisotropy and/or time lag. If $E_c=0$ there is no cutoff in the power-law. This model allows variable iron abundance and opacities of Balucinska & McCammon (1994). As expected in AGNs, H and He are assumed to be fully ionized. The parameters of the pexrav model are: Γ , the power-law photon index; E_c , the e-folding energy in keV (if $E_c=0$ there is no cut-off); R , if $R<0$ there is no direct component; z , the redshift; iron abundance relative to the solar iron abundance; $\cos \theta$, the cosine of inclination angle and K , the photon flux at 1 keV of the power-law.

NGC4151 and IC4329A have been studied separately since they are the brightest Seyferts of the sample and allow a more detailed analysis (tables 5.5 and 5.6 respectively). In these cases thanks to the good statistics available, the pexrav model with the photon index free to vary has also been performed (**model 4**). In the pexrav model, the inclination angle of the disc is fixed to $\cos \theta=0.45$ for all the sources except NGC4151 for which a value of 0.85 (i.e. a face-on disc configuration) has been assumed following Piro et al. (2001). In this last case, a further check has been performed also for $\cos \theta=0.45$, but the

best fit values are those corresponding to $\cos \theta = 0.85$. Another exception for NGC4151 is the inclusion in the model of neutral absorption; in fact this is strongly required by the data. For all the other observations, including those of type 2 objects, absorption is ruled out by the data. It is worth noting that all the Seyfert 2s of the Piccinotti sample have column densities $\leq 10^{23}$ atoms cm^{-2} and this value of N_H is not enough to absorb photons in the PDS energy band.

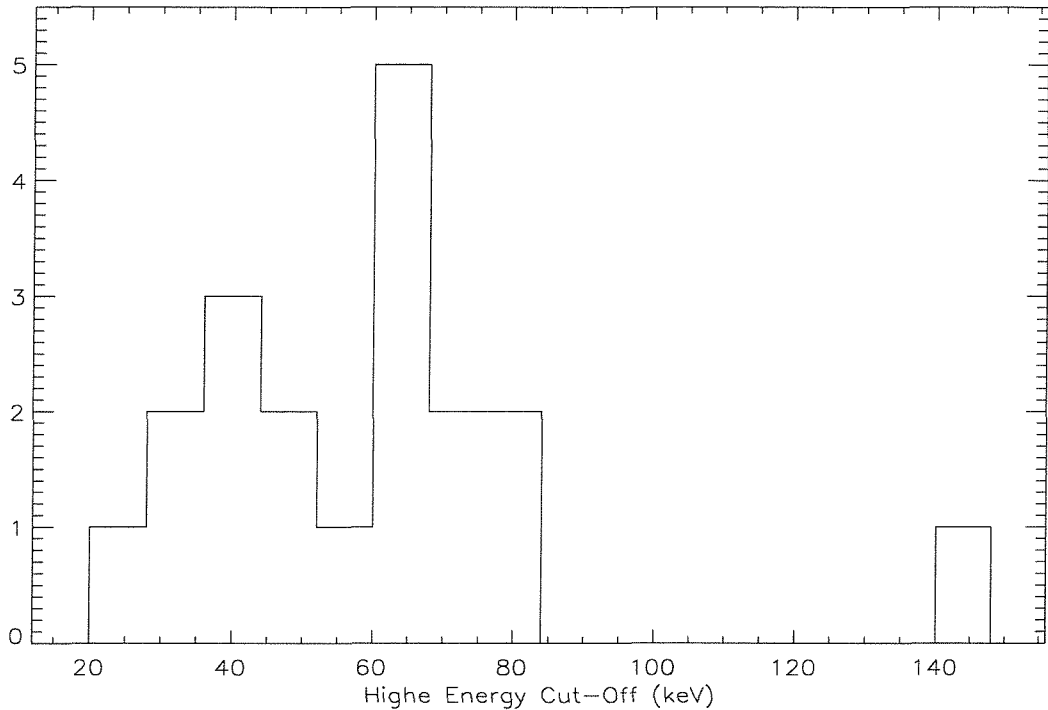


Figure 5.2: Histogram of the high energy cut-off for a cut-off power law model (model 1).

5.4.1 Results of the spectral analysis of Seyfert galaxies

In model 1 only the high energy cut-off was considered and this is well constrained in all the sources of the sample analyzed with the only exception being the first observation of NGC7469 (see table 5.4 column 1). The histogram of the high energy cut-off values found is shown in figure 5.2. The cut-off is required by the data at 91-99% probability ($4.93 < \Delta\chi^2 < 31.1$ for one degree of freedom (d.o.f.)) for almost all the sample objects and at >99% probability ($93.71 < \Delta\chi^2 < 230.37$ for two d.o.f., here the column density is also considered) in the case of NGC4151. The values range between 24^{+30}_{-9} keV in MCG-6-30-15 to 142^{+8}_{-27} keV in the last observation of NGC4151. It is worth noting

that the photon indices found are however unusually flat and in a few cases they have unacceptably low values, indicating that this model is not correct. For this reason in model 2, the high energy cut-off was fixed to 10000 keV in order to analyze the relevance of the Compton reflection component. Comparing these fits with those of the power law of table 5.3, we find that this component is required by the data at 96-99% probability ($6 < \Delta\chi^2 < 26$ for one d.o.f.) for all the sources analyzed and at >99% probability for two d.o.f. in the case of NGC4151. Using this model the spectra are steep ($\Gamma > 2$) and with a large amount of reflection that cannot be constrained in a large fraction of the observations. The values of R measured are all > 1.5 with the only exception being NGC4151 (April 99's observation) which has $R=0.6$. The histogram of the values of R resulting from model 2 fits are reported in figure 5.3. Considering the results obtained using models 1 and 2 (the photon index either too flat or too steep, a too low value of the cut-off energy and higher reflection than expected) as well as the high probability that these components are separately required by the data, we can argue that both are probably present in the 20-200 keV spectra. Note that when *BeppoSAX* broad band data of Seyfert 1 galaxies are considered, R is about 1 or less in most objects (Perola et al. 2001).

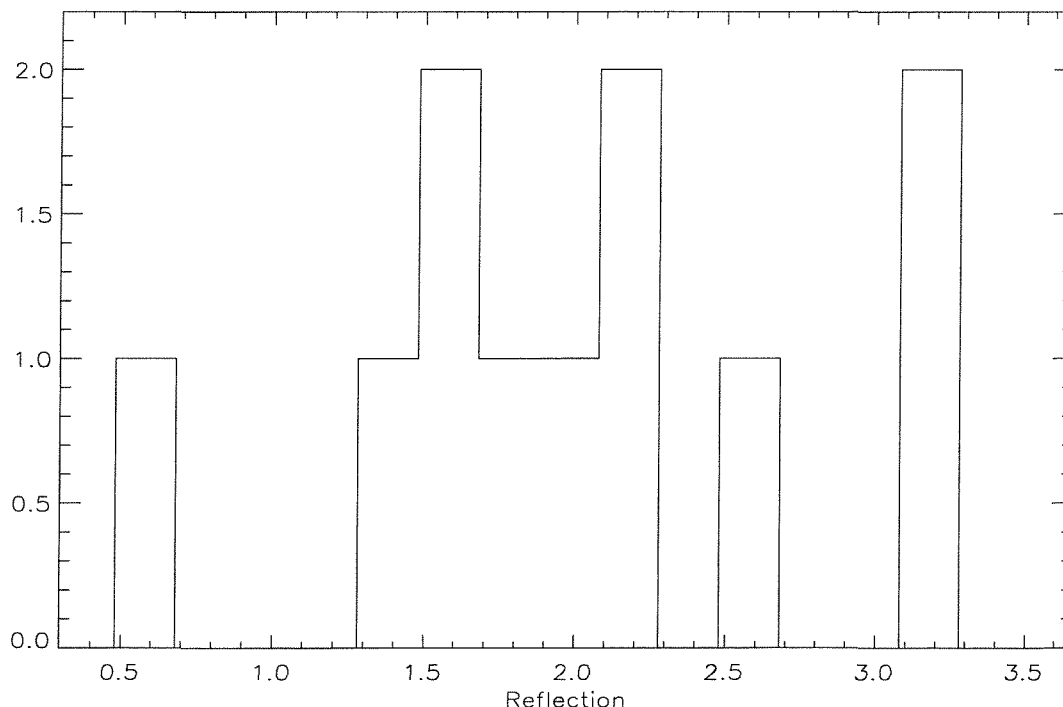


Figure 5.3: Histogram of the Compton reflection for the XSPEC *pexrav* model where $E=10000$ keV (model 2).

Therefore both the reflection and the high energy cut-off have been considered in model 3 where the photon index has been frozen to the PDS average value of 1.9 as we do not have enough statistics to constrain all parameters on the basis of the PDS data only. If we compare model 3 fits with the power law, we find that both components considered together are required by the data at 97-99% probability ($7 < \Delta\chi^2 < 28$ for 1 d.o.f.) and at >99% for NGC4151 and IC4329A. However, the best way to evaluate how strongly each component is required by the data is to compare for each source model 1 with model 3 (or model 4 for NGC4151 and IC4329A) i.e. by adding the Compton reflection in a spectrum where the high energy cut-off is already present and model 2 with model 3/4, i.e. by adding the high energy cut-off in a spectrum with the Compton reflection component. Unfortunately due to the poor statistics, these comparisons cannot be conclusive for the majority of the sources analyzed. The method used works well in the case of NGC4151; in fact from the comparisons between models 1 and 4 and models 2 and 4 it is clear that when the Compton reflection is added in the spectrum with the high energy cut-off the fits improve by a $\Delta\chi^2$ of 2.31 (70%) for 1 d.o.f., but $\Delta\chi^2$ goes from 2.92 to 17.57 (95-99%) for 1 d.o.f. when the high energy cut-off is added in the spectrum with the Compton reflection component already included. For the rest of the sources in some cases the fit significantly improves ($\Delta\chi^2 > 2$, same d.o.f.) when adding the reflection (model 1-3) as in the case of MCG-6-30-15, ESO103-G55, MKN509 (first observation) and IC4329A (second observation) and in other cases the fits significantly improve ($\Delta\chi^2 > 2$, same d.o.f.) when adding the high energy cut-off (model 2-3) as for NGC5506 (second and total observation) NGC7582 and IC4329A (first and total observation). The best fit logarithmic values of the high energy cut-off (E_c) versus the logarithmic values of reflection (R) have been plotted in figure 5.4. For NGC4151 and IC4329A the best fit values of model 4 in tables 5.5 and 5.6 have been considered. Due to the poor statistics the quoted errors are huge and so this plot cannot give useful information on any possible correlation but it can help in defining at least the dynamical range of the Compton reflection component and of the high energy cut-off of the sample analyzed. The cut-off energy E_c ranges from 50 keV (NGC4151) to 255 keV (NGC5506), while the reflection component lies in the interval 0-2: these values are reasonable and close to theoretical expectations, but also are obtained with a power-law index of canonical value. Note that, in general the spectral parameters found with the pexrav model (model 3-4) are in agreement with previous *BeppoSAX* results based on broad band data 0.1-200 keV (see chapter 3). There are a couple of exceptions in table 5.4 that need to be discussed: MKN509 and ESO103-G35. Studying the *BeppoSAX* broad band spectrum of

MKN509, Perola et al. (2000, 2001), reported an unusually flat continuum (~ 1.6) and a cutoff at 70 keV. The authors argued that this source is similar to NGC4151, suggesting that, generally speaking, Seyferts with flat continua have also low cut-off energies. In fact, the PDS data when fitted with only the pexrav model, leaving all the parameters free to vary, confirm these broad band result; the values found here are $\Gamma = 1.6^{+0.55}_{-0.60}$, $E_c > 30$ keV but with an amount of reflection which is unconstrained ($R < 9.71$). In the case of ESO103-G35, Wilkes et al. (2001) found that the best fitting spectrum is that of a power law of $\Gamma = 1.74$ with an unusual cutoff at 29 ± 10 keV. The same model used to analyze only the PDS data of the first *BeppoSAX* observation of ESO103-G35 (model 1 in table 5.4) provides an unacceptable value of the photon index; if Γ is fixed to 1.7 a cutoff at 61^{+30}_{-17} keV is found. For a steeper power law of $\Gamma = 2.39^{+0.33}_{-0.53}$, an unconstrained reflection compatible with zero and a cut-off $E_c > 80$ keV are found if the pexrav with all the parameters free to vary is used.

The pexrav fit (model 4 of table 5.5 and 5.6) works well in the case of NGC4151 and IC4529A. Analyzing the 5 single *BeppoSAX* observations of NGC4151 fitted with the pexrav model a steepening of the intrinsic power law is found when the luminosity increases. During this variation there is also evidence for a change of the high energy cut-off from a minimum of 52^{+26}_{-12} keV (July 96) to a maximum of 144^{+56}_{-34} keV (April 99). This observational result is in agreement with the OSSE finding of a photon index $\Gamma = 1.6^{+0.2}_{-0.3}$ and a cut-off $E_c = 96^{+28}_{-19}$ obtained over 5 years monitoring of the source; also comparing OSSE data taken in different viewing periods, there was an indication of softening of the spectrum when the source brightens (Johnson et al. 1997). Significant changes in the column density and the Compton reflection component are also seen. In particular the N_H has a maximum value of $121^{+21}_{-3} \times 10^{22}$ atoms cm^{-2} in the first observation and it is completely ruled out three days later. The amount of the reflection is always small ($R < 0.5$) and in the case of the April '99 observation it is not required at all. The analysis of the sum of all five observations has also been performed in order to improve the statistics and the average parameters of the fits are in agreement with previous findings especially if the last observation is not considered (Sum (a) in table 5.5). The results found here are in agreement with the broad band study of NGC4151 recently performed by Piro et al. (2001).

In the case of IC4329A only the sum of the four available observations will be discussed since *BeppoSAX* caught the source at almost the same intensity state, showing only marginal spectral changes between different observations. However the PDS results confirm the presence of a Compton reflection of $R \sim 0.6$ but with a lower high energy cutoff ($E_c = 115^{+15}_{-10}$ keV) than previously found on the basis of the broad band data (Perola et

al. 1999).

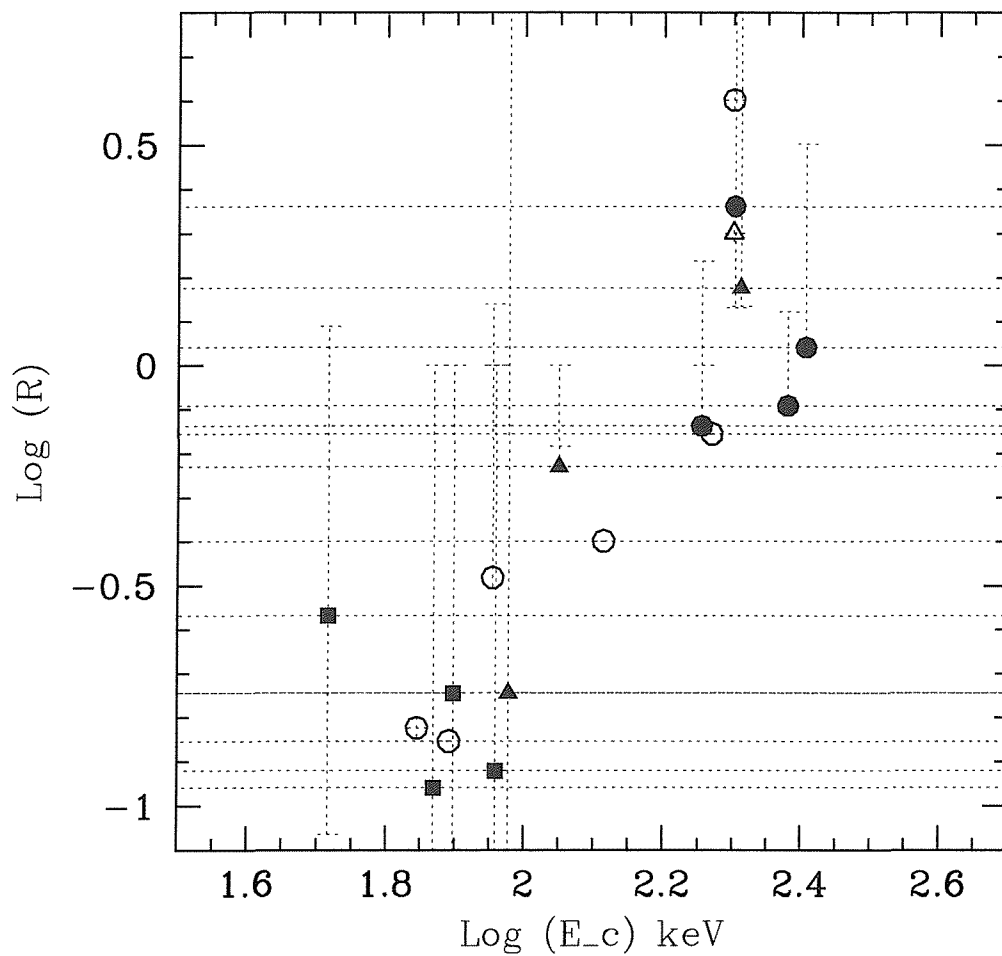


Figure 5.4: Reflection versus high energy cut-off of the pexrav model fits. Open symbols are lower limits. Circles are objects of table 4 (model 3), squares are values of NGC4151 (model 5) and triangles are values of IC4329A (model 5).

Table 5.4

| Source | PARAMETERS | MODEL 1 | MODEL 2 | MODEL 3 |
|---------------------------------|------------------|------------------------|------------------------|------------------------|
| NGC3783 | Γ | $1.52^{+0.28}_{-0.55}$ | $2.12^{+0.08}_{-0.07}$ | 1.9 |
| | E_{fold} | $76.5^{+93.5}_{-31.5}$ | - | 240^{+210}_{-60} |
| | R | - | $1.63^{+1.77}_{-0.89}$ | $0.81^{+0.99}_{-0.61}$ |
| | χ^2 (d.o.f) | 9.30 (13) | 7.59 (13) | 7.68 (13) |
| | χ^2/ν | 0.71 | 0.58 | 0.63 |
| MCG-6-30-15 | Γ | $0.8^{+0.8}_{-0.7}$ | $2.46^{+0.08}_{-0.17}$ | 1.9 |
| | E_{fold} | 24^{+30}_{-9} | - | >200 |
| | R | - | >2.4 | >4 |
| | χ^2 (d.o.f) | 14.63 (13) | 11.92 (13) | 11.91 (13) |
| | χ^2/ν | 1.12 | 0.92 | 0.99 |
| NGC5506 (30-01-97) | Γ | $1.38^{+0.48}_{-0.53}$ | $2.07^{+0.12}_{-0.11}$ | 1.9 |
| | E_{fold} | 62^{+190}_{-32} | - | 255^{+695}_{-105} |
| | R | - | $1.98^{+6.65}_{-1.49}$ | $1.1^{+2.9}_{-1}$ |
| | χ^2 (d.o.f) | 11.07 (13) | 11.57 (13) | 10.85 (13) |
| | χ^2/ν | 0.85 | 0.89 | 0.83 |
| NGC5506 (14-01-98) | Γ | $0.96^{+0.5}_{-0.47}$ | $2.12^{+0.18}_{-0.12}$ | 1.9 |
| | E_{fold} | 36^{+34}_{-13} | - | 201^{+249}_{-71} |
| | R | - | >1.2 | $2.3^{+7.7}_{-1.7}$ |
| | χ^2 (d.o.f) | 6.35 (13) | 12.83 (13) | 10.28 (13) |
| | χ^2/ν | 0.49 | 0.99 | 0.79 |
| NGC5506 (Sum) | Γ | $1.15^{+0.35}_{-0.35}$ | $2.13^{+0.09}_{-0.07}$ | 1.9 |
| | E_{fold} | 45^{+33}_{-15} | - | 221^{+179}_{-71} |
| | R | - | $2.9^{+4.65}_{-1.60}$ | $1.64^{+2.36}_{-1.04}$ |
| | χ^2 (d.o.f) | 5.60 (13) | 11.14 (13) | 8.62 (13) |
| | χ^2/ν | 0.43 | 0.86 | 0.72 |
| ESO103-G35 (03-10-96) | Γ | 1.7* | $2.49^{+0.26}_{-0.21}$ | 1.9 |
| | E_{fold} | 61^{+30}_{-17} | - | 78^{+101}_{-10} |
| | R | - | >1.5 | >0.14 |
| | χ^2 (d.o.f) | 19.11 (14) | 16.80 (13) | 16.9 (13) |
| | χ^2/ν | 1.36 | 1.29 | 1.3 |
| MKN509 (18-05-98) | Γ | 1.6 * | $2.29^{+0.22}_{-0.64}$ | 1.9 |
| | E_{fold} | 69^{+29}_{-17} | - | 130^{+220}_{-57} |
| | R | - | >3 | >0.4 |
| | χ^2 (d.o.f) | 17.91 (14) | 14.80 (13) | 13.97 (13) |
| | χ^2/ν | 1.19 | 1.14 | 1.07 |

Note: (*) Fixed because when left free the fit gives unacceptable values

Table 5.4–Continued

| Source | PARAMETERS | MODEL 1 | MODEL 2 | MODEL 3 |
|------------------------------|------------------|------------------------|------------------------|------------------------|
| MKN509 (11-10-98) | Γ | $1.42^{+0.59}_{-0.14}$ | $2.4^{+0.26}_{-0.25}$ | 1.9 |
| | E_{fold} | 44^{+556}_{-29} | - | 98^{+122}_{-33} |
| | R | - | >1 | - |
| | χ^2 (d.o.f) | 22.9 (13) | 22.15 (13) | 21.55 (13) |
| | χ^2/ν | 1.77 | 1.7 | 1.66 |
| MKN509 (Sum) | Γ | $1.01^{+0.53}_{-0.73}$ | $2.31^{+0.19}_{-0.20}$ | 1.9 |
| | E_{fold} | 31^{+48}_{-13} | - | 121^{+119}_{-41} |
| | R | - | >1.5 | >0.5 |
| | χ^2 (d.o.f) | 14.4 (13) | 14.82 (13) | 14.02 (13) |
| | χ^2/ν | 1.11 | 1.14 | 1.08 |
| 3C445 | Γ | $0.95^{+0.84}_{-0.95}$ | $2.23^{+0.30}_{-0.33}$ | 1.9 |
| | E_{fold} | 33^{+117}_{-19} | - | >70 |
| | R | - | >0.6 | >0.15 |
| | χ^2 (d.o.f) | 16.21 (13) | 14.19 (13) | 14.46 (13) |
| | χ^2/ν | 1.25 | 1.09 | 1.11 |
| NGC7469 (14-12-97) | Γ | $1.79^{+0.36}_{-0.89}$ | $2.13^{+0.27}_{-0.23}$ | 1.9 |
| | E_{fold} | >27 | - | >90 |
| | R | - | - | $0.33^{+4.17}_{-0.33}$ |
| | χ^2 (d.o.f) | 11.29 (13) | 10.85 (13) | 11.07 (13) |
| | χ^2/ν | 0.87 | 0.83 | 0.85 |
| NGC7469 (29-11-99) | Γ | $1.49^{+0.49}_{-0.51}$ | $2.17^{+0.18}_{-0.13}$ | 1.9 |
| | E_{fold} | 65^{+255}_{-35} | - | 180^{+260}_{-60} |
| | R | - | $1.64^{+9.36}_{-0.64}$ | $0.73^{+2.37}_{-0.73}$ |
| | χ^2 (d.o.f) | 12.81 (13) | 14.14 (13) | 13.27 (13) |
| | χ^2/ν | 0.98 | 1.09 | 1.02 |
| NGC7469 (Sum) | Γ | $1.56^{+0.40}_{-0.30}$ | $2.16^{+0.16}_{-0.14}$ | 1.9 |
| | E_{fold} | 73^{+247}_{-28} | - | 185^{+215}_{-60} |
| | R | - | $1.41^{+4.59}_{-1.21}$ | $0.62^{+1.58}_{-0.62}$ |
| | χ^2 (d.o.f) | 15.44 (13) | 16.14 (13) | 15.46 (13) |
| | χ^2/ν | 1.19 | 1.24 | 1.19 |
| NGC7582 | Γ | $0.75^{+0.65}_{-0.65}$ | $2.17^{+0.11}_{-0.17}$ | 1.9 |
| | E_{fold} | 30^{+30}_{-10} | - | 186^{+304}_{-71} |
| | R | - | >1 | >0.7 |
| | χ^2 (d.o.f) | 17.15 (13) | 24.81 (13) | 22.33 (13) |
| | χ^2/ν | 1.32 | 1.91 | 1.72 |

Table 5.5: NGC4151

| Source | PARAMETERS | MODEL 1 | MODEL 2 | MODEL 3 | MODEL 4 |
|------------------------------|------------------|------------------------|------------------------|------------------------|------------------------|
| NGC4151 (06-07-96) | Γ | $1.59^{+0.23}_{-0.23}$ | $2.11^{+0.04}_{-0.04}$ | 1.9 | $1.61^{+0.14}_{-1.36}$ |
| | N_H^\dagger | 140^{+47}_{-46} | - | 60^{+30}_{-25} | 121^{+21}_{-3} |
| | E_{fold} | 67^{+30}_{-16} | - | 206^{+42}_{-26} | 74^{+26}_{-14} |
| | R | - | $3.25^{+1.85}_{-1.05}$ | $0.96^{+0.37}_{-0.21}$ | $0.11^{+0.19}_{-0.11}$ |
| | χ^2 (d.o.f) | 5.81 (12) | 12.67 (12) | 8.14 (12) | 5.7 (11) |
| | χ^2/ν | 0.48 | 1.06 | 0.68 | 0.52 |
| NGC4151 (09-07-96) | Γ | $0.98^{+0.19}_{-0.20}$ | $2.14^{+0.06}_{-0.06}$ | 1.9 | $1.26^{+0.07}_{-0.06}$ |
| | N_H^\dagger | - | - | - | - |
| | E_{fold} | 37^{+23}_{-7} | - | 226^{+84}_{-46} | 52^{+26}_{-12} |
| | R | - | $2.12^{+2.48}_{-0.78}$ | $1.33^{+0.97}_{-0.43}$ | $0.27^{+0.32}_{-0.22}$ |
| | χ^2 (d.o.f) | 15.67 (12) | 23.42 (12) | 18.53 (13) | 14.5 (11) |
| | χ^2/ν | 1.31 | 1.95 | 1.42 | 1.32 |
| NGC4151 (04-12-96) | Γ | $1.5^{+0.32}_{-0.33}$ | $1.99^{+0.06}_{-0.05}$ | 1.9 | $1.54^{+0.20}_{-0.19}$ |
| | N_H^\dagger | 93^{+71}_{-68} | - | - | 74^{+37}_{-39} |
| | E_{fold} | 78^{+71}_{-27} | - | >400 | 91^{+68}_{-28} |
| | R | - | $1.7^{+1.30}_{-0.70}$ | $1.36^{+0.84}_{-0.41}$ | $0.12^{+0.3}_{-0.12}$ |
| | χ^2 (d.o.f) | 10.17 (12) | 13.16 (12) | 11.86 (12) | 10.09 (11) |
| | χ^2/ν | 0.85 | 1.1 | 0.99 | 0.92 |
| NGC4151 (06-12-96) | Γ | $1.48^{+0.37}_{-0.37}$ | $2.04^{+0.06}_{-0.06}$ | 1.9 | $1.52^{+0.22}_{-0.22}$ |
| | N_H^\dagger | 116^{+40}_{-72} | - | 19^{+41}_{-19} | 86^{+36}_{-36} |
| | E_{fold} | 66^{+61}_{-21} | - | 379^{+241}_{-79} | 79^{+51}_{-24} |
| | R | - | $2.62^{+2.78}_{-1.12}$ | $1.48^{+1}_{-0.58}$ | $0.18^{+0.33}_{-0.18}$ |
| | χ^2 (d.o.f) | 6.51 (12) | 9.31 (12) | 7.78 (12) | 6.39 (11) |
| | χ^2/ν | 0.54 | 0.77 | 0.65 | 0.58 |
| NGC4151 (Apr 99) | Γ | $1.64^{+0.14}_{-0.13}$ | $1.93^{+0.02}_{-0.03}$ | 1.9 | $1.65^{+0.08}_{-0.08}$ |
| | N_H^\dagger | 46^{+29}_{-28} | - | 13^{+27}_{-13} | 46^{+24}_{-22} |
| | E_{fold} | 142^{+81}_{-37} | - | >800 | 144^{+56}_{-34} |
| | R | - | $0.58^{+0.17}_{-0.16}$ | $0.44^{+0.24}_{-0.19}$ | - |
| | χ^2 (d.o.f) | 16.32 (12) | 23.27 (12) | 21.97 (12) | 16.31 (11) |
| | χ^2/ν | 1.36 | 1.94 | 1.83 | 1.48 |

Table 5.5–Continued

| | | | | | |
|------------------|------------------|------------------------|------------------------|------------------------|------------------------|
| NGC4151 | Γ | $1.58^{+0.14}_{-0.10}$ | $2.01^{+0.02}_{-0.02}$ | 1.9 | $1.68^{+0.05}_{-0.06}$ |
| <i>(Sum)</i> | N_H^\dagger | 83^{+29}_{-28} | - | $0.15^{+18}_{-0.15}$ | 40^{+10}_{-14} |
| | E_{fold} | 88^{+30}_{-18} | - | 510^{+100}_{-75} | 134^{+28}_{-22} |
| | R | - | $1.35^{+0.25}_{-0.15}$ | $1.02^{+0.18}_{-0.12}$ | $0.31^{+0.10}_{-0.11}$ |
| | χ^2 (d.o.f) | 24.11 (12) | 39.37 (12) | 29.12 (12) | 21.8 (11) |
| | χ^2/ν | 2.01 | 3.28 | 2.43 | 1.98 |
| NGC4151 | Γ | $1.50^{+0.14}_{-0.17}$ | $2.07^{+0.03}_{-0.02}$ | 1.9 | $1.62^{+0.18}_{-0.24}$ |
| <i>(Sum (a))</i> | N_H^\dagger | 106^{+34}_{-29} | - | - | 30^{+18}_{-19} |
| | E_{fold} | 63^{+16}_{-10} | - | 330^{+60}_{-50} | 105^{+25}_{-17} |
| | R | - | $2.53^{+0.87}_{-0.83}$ | $1.65^{+0.4}_{-0.3}$ | $0.61^{+0.26}_{-0.16}$ |
| | χ^2 (d.o.f) | 13.04 (12) | 26.3 (12) | 15.13 (12) | 10.47 (11) |
| | χ^2/ν | 1.09 | 2.19 | 1.26 | 0.95 |

Note: (\dagger)= N_H is in units of 10^{22} atoms cm^{-2}

Table 5.6: IC4329A

| Source | PARAMETERS | MODEL 1 | MODEL 2 | MODEL 3 | MODEL 4 |
|------------------------------|------------------|------------------------|------------------------|------------------------|------------------------|
| IC4329A (02-01-98) | Γ | $1.44^{+0.20}_{-0.20}$ | $2.05^{+0.06}_{-0.06}$ | 1.9 | $1.55^{+0.46}_{-0.28}$ |
| | E_{fold} | 74^{+46}_{-19} | - | 339^{+261}_{-99} | 95^{+13}_{-7} |
| | R | - | $1.42^{+0.02}_{-0.63}$ | $0.91^{+0.89}_{-0.41}$ | 0.18^{+42}_{-18} |
| | χ^2 (d.o.f) | 7.69 (13) | 10.82 (13) | 8.95 (13) | 7.46 (12) |
| | χ^2/ν | 0.59 | 0.83 | 0.69 | 0.62 |
| IC4329A (17-07-98) | Γ | $1.05^{+0.45}_{-0.45}$ | $2.14^{+0.14}_{-0.12}$ | 1.9 | $1.5^{+0.45}_{-0.30}$ |
| | E_{fold} | 42^{+46}_{-17} | - | 245^{+405}_{-75} | >200 |
| | R | - | >3 | >1 | >2 |
| | χ^2 (d.o.f) | 32.29 (13) | 27.45 (13) | 28.2 (13) | 27.48 (12) |
| | χ^2/ν | 2.49 | 2.11 | 2.17 | 2.29 |
| IC4329A (21-07-98) | Γ | $1.37^{+0.34}_{-0.37}$ | $2.12^{+0.10}_{-0.10}$ | 1.9 | $1.68^{+0.52}_{-0.57}$ |
| | E_{fold} | 59^{+71}_{-24} | - | 236^{+254}_{-56} | 112^{+44}_{-62} |
| | R | - | $2.23^{+6.27}_{-0.73}$ | $1.2^{+2}_{-0.8}$ | $0.59^{+1.11}_{-0.59}$ |
| | χ^2 (d.o.f) | 14.64 (13) | 15.11 (13) | 14.29 (13) | 14.09 (12) |
| | χ^2/ν | 1.12 | 1.16 | 1.1 | 1.17 |
| IC4329A (27-07-98) | Γ | $1.27^{+0.38}_{-0.57}$ | $2.15^{+0.14}_{-0.12}$ | 1.9 | $1.3^{+0.5}_{-0.55}$ |
| | E_{fold} | 50^{+88}_{-25} | - | 205^{+285}_{-75} | 53^{+97}_{-23} |
| | R | - | $3.09^{+7.06}_{-2.21}$ | $1.5^{+5}_{-1.1}$ | - |
| | χ^2 (d.o.f) | 8.20 (13) | 9.62 (13) | 8.83 (13) | 8.20 (12) |
| | χ^2/ν | 0.33 | 0.74 | 0.68 | 0.68 |
| IC4329A (Sum) | Γ | $1.34^{+0.16}_{-0.17}$ | $2.09^{+0.04}_{-0.04}$ | 1.9 | $1.66^{+0.37}_{-0.37}$ |
| | E_{fold} | $59.6^{+10.4}_{-15.6}$ | - | 275^{+15}_{-55} | 115^{+15}_{-10} |
| | R | - | $2.28^{+1.18}_{-0.76}$ | $1.3^{+0.7}_{-0.8}$ | $0.6^{+0.4}_{-0.35}$ |
| | χ^2 (d.o.f) | 16.88 (13) | 18.63 (13) | 15.57 (13) | 14.52 (12) |
| | χ^2/ν | 1.3 | 1.43 | 1.2 | 1.12 |

5.4.2 MCG-01-24-12

From the quick look inspection of the MECS-PDS broad band spectrum of H0917-074 there was the indication of an apparent mismatch between MECS and PDS data. A simple power law fit requires a MECS-PDS constant of 8-10, i.e. an order of magnitude greater than that normally used (Fiore, Guainazzi & Grandi 1998). The simplest explanation for this phenomenon is the presence of a contaminating serendipitous source in the PDS field of view. The region of the sky around H0917-074 was searched for possible high energy sources, and only one candidate was found, the Seyfert 2 galaxy MCG-01-24-12 which lies also within the original HEAO1-A2 error box (Piccinotti et al. 1982). MCG-01-24-12 was then pointed with *BeppoSAX* NFI from May 15th to May 17th, 2001. The broad-band spectrum of the source is analyzed in detail in Malizia et al. (in preparation), here only the PDS data will be briefly presented. Inspection of the MECS data indicate for this source a 2-10 keV flux similar to that reported in the original Piccinotti source list (Piccinotti et al. 1982), confirming that MCG-01-12-24 is indeed the right identification. The net count rate in the PDS instrument was 0.43 ± 0.04 ($\sim 11\sigma$ of detection) accumulated on a total exposure time of 3.6×10^4 seconds which corresponds to a flux in the 20-200 keV band of $\sim 5 \times 10^{-11}$ erg cm $^{-2}$ s $^{-1}$. In figure 5.5 (left) the light curve of MCG-01-24-12 in the 20-200 keV energy range is shown. No evidence of variability is found even using different bin sizes.

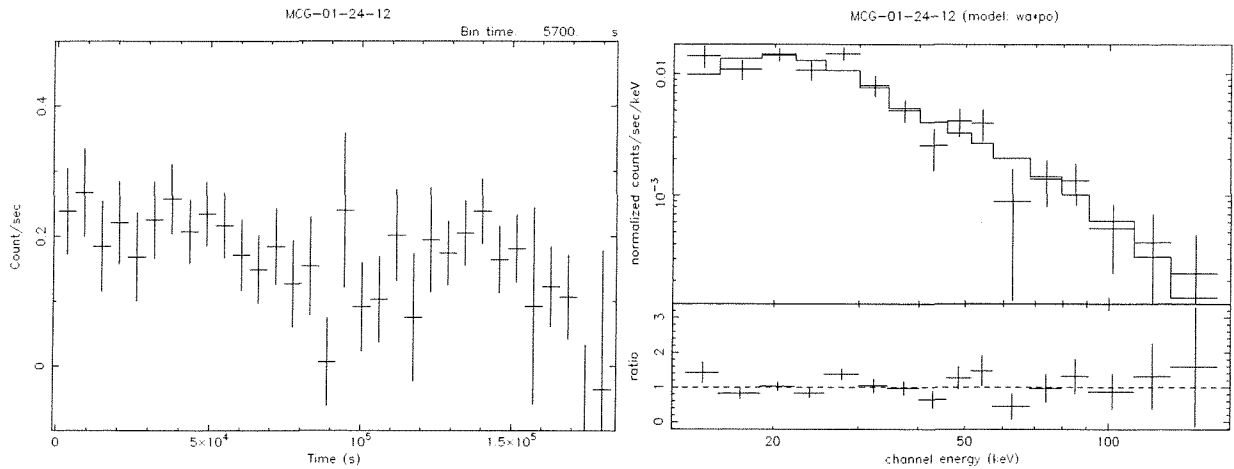


Figure 5.5: Left: PDS light curve in the 20-200 keV energy range, the bin of 5700 seconds corresponds to a single *BeppoSAX* orbit. Right: PDS count spectrum with residuals for an absorbed power law model.

To study the high energy (20-200 keV) spectral characteristics of MCG-01-24-12, a simple power-law fit was first performed. This fit gives a spectrum of photon index of $\Gamma=1.82\pm0.18$ with a marginally acceptable $\chi^2=21.46$ with 14 d.o.f.. As before, the errors are quoted at 90% confidence level. We then considered the column density, and the introduction of this component improves the fit by about 95% ($\chi^2=17.04$ with 13 d.o.f.) resulting in a spectrum having a photon index of $\Gamma=2.23_{+0.58}^{-0.57}$ and a column density $N_H < 7 \times 10^{24} \text{ cm}^{-2}$. The presence of the Compton reflection and high-energy cut-off are also investigated. In particular, using the XSPEC pexrav model, the presence of a high energy cut-off is completely ruled out by the data, while a strong amount of reflection ($R\sim4$) is required. The introduction of both a column density and a Compton reflection component, provides $R>0.05$ and $N_H < 8 \times 10^{24} \text{ cm}^{-2}$ while the photon index is $\Gamma=2.08_{+0.48}^{-0.12}$. It is worth noting that also considering a different inclination angle ($\Theta=0.87$) the spectral parameters do not change significantly.

5.5 Blazars

All the five blazars objects (PKS0548-322, 2A1219+305, 3C273, MKN501 and PKS2155-304) belonging to the Piccinotti sample have been observed with *BeppoSAX*.

PKS0548-322, 2A1219+305, MKN501 and PKS2155-304 are all extreme synchrotron BL Lac objects, that is those HBL (see chapter 3) which have the synchrotron peak that not only reaches the 2-10 keV band, but can go even further, up to or above 100 keV, at least during the flaring state, and consequently the Compton peak can reach TeV energies. Quite different is the nature of 3C273; in fact multifrequency campaigns (e.g. Courvoisier et al. 1987) showed that the broad-band spectral energy distribution is rather complex, with two clear peaks at UV ($\sim 10 \text{ eV}$) and γ -ray ($\sim 1\text{-}10 \text{ MeV}$) energies (Ramos et al. 1997, von Montigny et al. 1997). 3C273 and MKN501 are the only two blazars of the Piccinotti sample which have a PDS detection $>10\sigma$ and so they will be discussed in detail below. The log of *BeppoSAX* PDS observations of all blazars are reported in table 5.1. Due to the poor statistics, only the sum of the two observations of PKS0548-322 provides a positive detection, in any case a sum of all observations has been performed also for the other sources. A simple power law describes well the data in all cases although the constraints on the parameters are not always good (see table 5.7). The power-law slopes found are, in any case, consistent with the values obtained using the *BeppoSAX* broad band data (Costamante et al. 2001, Chiappetti et al. 1999) and in line with those expected for their classification. In fact, the spectral index α_x ($\Gamma - 1$) is considered the parameter by which to classify the source: LBLs, which have

Table 5.7.- Blazars

| Source | | A_{pl}^{\dagger} | Γ | χ^2 | d.o.f. |
|--------------|------------------|-------------------------|------------------------|----------|--------|
| PKS0548-322 | (Sum) | $6.50^{+2.43}_{-0.06}$ | $2.79^{+0.93}_{-0.67}$ | 11.44 | 14 |
| 3C 273 | (18-07-96) | $1.51^{+0.01}_{-0.01}$ | $1.66^{+0.10}_{-0.08}$ | 7.70 | 14 |
| | (13-01-97) | $2.57^{+0.01}_{-0.01}$ | $1.65^{+0.11}_{-0.11}$ | 11.02 | 14 |
| | (15-01-97) | $2.50^{+0.01}_{-0.01}$ | $1.67^{+0.09}_{-0.08}$ | 26.43 | 14 |
| | (17-01-97) | $2.41^{+0.01}_{-0.01}$ | $1.69^{+0.08}_{-0.08}$ | 16.59 | 14 |
| | (24-06-98) | $3.15^{+0.01}_{-0.01}$ | $1.77^{+0.07}_{-0.06}$ | 12.04 | 14 |
| | (Sum) | $2.17^{+0.01}_{-0.01}$ | $1.70^{+0.04}_{-0.04}$ | 19.72 | 14 |
| 2A1219+305 | | $1.02^{+26}_{-0.93}$ | $2.23^{+1.57}_{-0.83}$ | 7.77 | 14 |
| Mrk 501 | (07-04-97) | $0.93^{+0.05}_{-0.03}$ | $2.09^{+0.12}_{-0.11}$ | 9.52 | 14 |
| | (11-04-97) | $5.25^{+0.02}_{-0.01}$ | $1.86^{+0.10}_{-0.09}$ | 18.06 | 14 |
| | (16-04-97) | $18.72^{+0.02}_{-0.02}$ | $1.87^{+0.03}_{-0.04}$ | 16.66 | 14 |
| | (28-04-98) | $16.21^{+0.14}_{-0.07}$ | $2.29^{+0.21}_{-0.18}$ | 8.40 | 14 |
| | (29-04-98) | $16.17^{+0.11}_{-0.05}$ | $2.24^{+0.16}_{-0.14}$ | 16.94 | 14 |
| | (01-05-98) | $11.06^{+0.19}_{-0.07}$ | $2.32^{+0.34}_{-0.28}$ | 11.76 | 14 |
| | (Sum Apr-May 98) | $14.67^{+0.06}_{-0.05}$ | $2.28^{+0.13}_{-0.09}$ | 6.30 | 14 |
| | (20-06-98) | $5.74^{+0.22}_{-0.04}$ | $2.27^{+0.53}_{-0.37}$ | 17.22 | 14 |
| | (29-06-98) | $23.99^{+2.56}_{-0.14}$ | $2.73^{+0.87}_{-0.33}$ | 11.62 | 14 |
| | (16-07-98) | $4.62^{+0.39}_{-0.05}$ | $2.17^{+0.73}_{-0.39}$ | 12.60 | 14 |
| | (25-07-98) | $7.21^{+0.37}_{-0.06}$ | $2.43^{+0.62}_{-0.38}$ | 7.98 | 14 |
| | (Sum Jun-Jul 98) | $7.83^{+0.12}_{-0.07}$ | $2.42^{+0.29}_{-0.27}$ | 13.72 | 14 |
| | (10-06-99) | $1.06^{+0.01}_{-0.01}$ | 2.23^{\dagger} | 13.05 | 15 |
| PKS 2155-304 | (20-11-96) | $0.42^{+0.04}_{-0.01}$ | $1.92^{+0.78}_{-0.52}$ | 9.53 | 14 |
| | (Sum) | $0.4^{+0.03}_{-0.01}$ | $1.91^{+0.69}_{-0.41}$ | 10.88 | 14 |

Notes: (\dagger) $A \times 10^{-2}$ (\dagger) Photon Index fixed to 2.23 which is the average value of all the observations.

the synchrotron peak in the IR band, have a flat ($\alpha_x < 1$) X-ray spectral index, due to inverse Compton emission (the same is true for the FSRQ): this is observed in 3C273. As the peak shifts toward higher energies, the synchrotron emission becomes more and more dominant in the X-ray band and so the HBLs, where the X-ray emission is completely dominated by the synchrotron emission, show a steep spectral index ($\alpha_x > 1$): this is observed in all the rest of the BL Lac objects of table 5.7 (Costamante et al. 2001). No timing variability has been investigated in section 5.3 ($\sigma < 10$), however significant variation (χ^2 -test constant probability $> 80\%$) has been detected in the PDS data of 2A1219+305 and in the first observation of PKS2155-304.

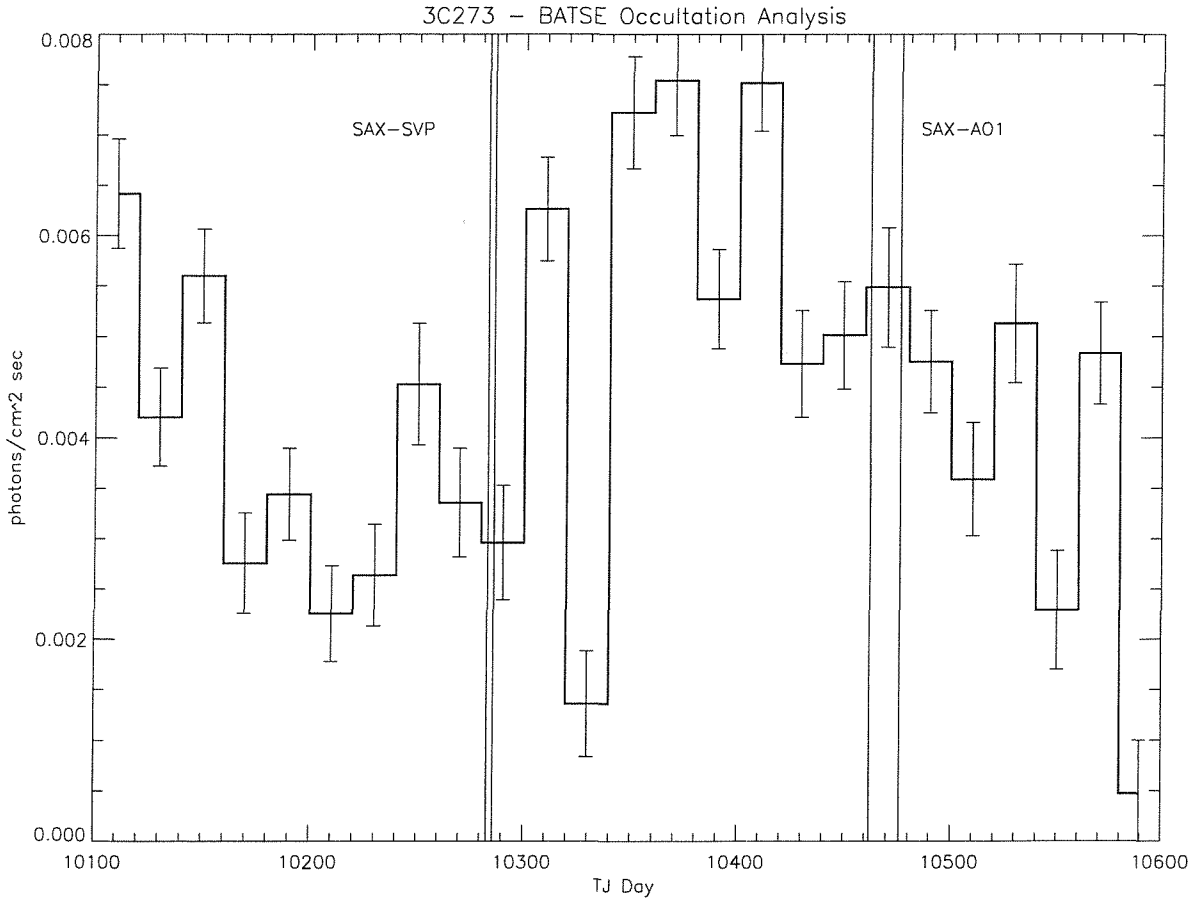


Figure 5.6: BATSE light curve. Twenty days intervals resulting from the rebinning of the daily data obtained with LADs in Earth Occultation Mode. The two vertical strips represent the windows of *BeppoSAX* observations during SVP and the AO1.

5.5.1 3C273

3C273 is a nearby ($z=0.158$) quasar and is one of the best studied extragalactic objects in the entire electromagnetic spectrum. *BeppoSAX* has observed 3C273 several times, but here we will consider only PDS observations taken in 1996-97 and 98. Unfortunately the last observation of 1997 was not available in the public archive and so is not considered here. It is well known that 3C273 is variable at high energies: just considering *BeppoSAX* observations, we found that in 1997 it was a factor of 2 brighter than in the first observation of 1996, and during the January 1997 observations there is a change in the flux of about 15%. In fact, 3C273 is one of the most variable sources on time scales of months of the entire Piccinotti sample on the basis of the PDS results (see timing analysis, section 5.3). The PDS light curves of all five observations analyzed are included in appendix A.

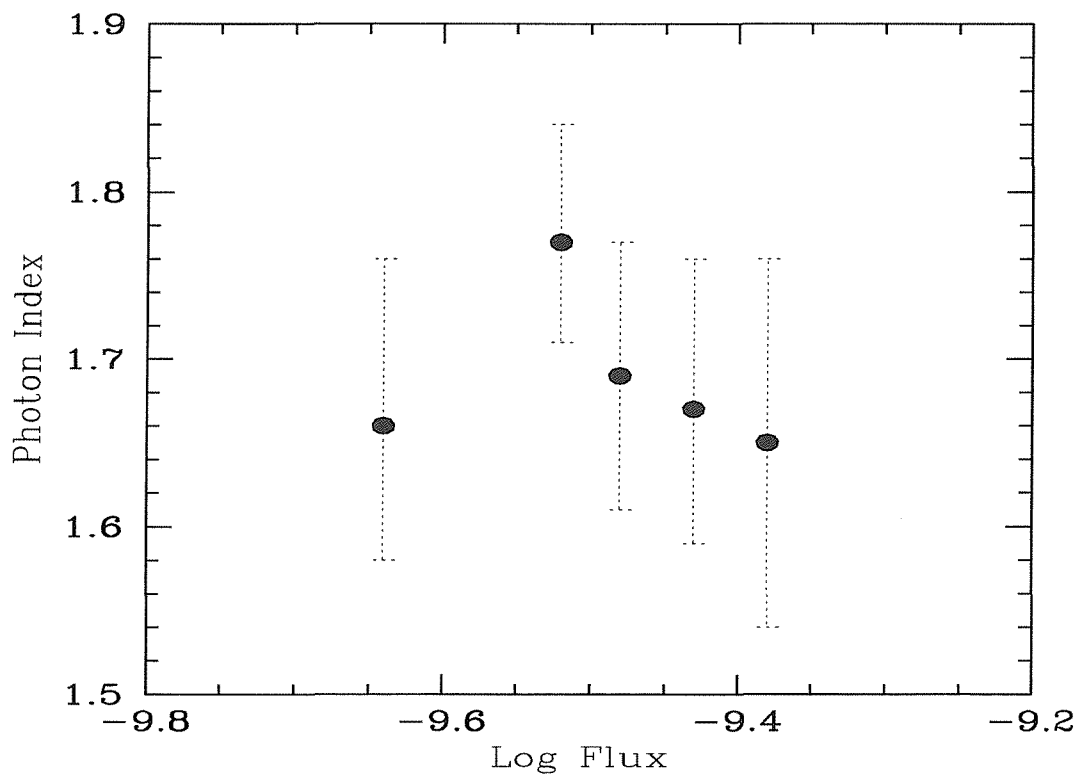


Figure 5.7: Photon index versus flux for all the *BeppoSAX*/PDS observations of 3C273.

3C273 is one of the most variable sources even over longer time scales of years; from the BATSE data set analyzed here, i.e. more than three years of observations (November 93 - September 97), it is the only variable source at >99% probability. The BATSE timing analysis reported in chapter 4, clearly indicates a trend with a flux gradually decreasing during the observed period. Fortunately the BATSE monitoring includes also the time of the *BeppoSAX* observations and so here the simultaneous data will be considered in order to frame the *BeppoSAX* -PDS observations into the long look of the source performed by BATSE. In figure 5.6 the BATSE light curve over 500 days covering the *BeppoSAX* observations of 1996 (SVP observation) and 1997 (AO1 observation) has been reported. The BATSE fluxes in the 20-100 keV energy band have been obtained by folding a single power law of photon index 1.7, which is the average value of the PDS data (see table 5.7). In the light curve a bin of 20 days of the daily data has been applied in order to improve the statistics and highlight the trend of the source over longer time scales. Despite the fact that local minima or maxima are present in the BATSE light curve on monthly scales, figure 5.6 shows that the *BeppoSAX* 1996 observation was performed during a period of a long term increase of the source, while the 1997 observation occurred in a period of long term decrease. As already discussed the high energy data (20-200 keV) of 3C273 are satisfactorily fitted with a single power law with the exception of the third observation (15-01-97) where the exceedingly large χ^2 value of the fit is essentially due to a single bin at ~ 100 keV and is probably related to a poorly calibrated background subtraction (see table 5.7 and figure in appendix A). However a deep spectral analysis has been performed on the average spectrum obtained by summing all the available observations. Using the pexrav model the lack of a high-energy cut-off has been confirmed, as well as a photon index of $\Gamma = 1.7^{+0.03}_{-0.03}$ and only an upper limit on the Compton reflection ($R < 0.1$) can be estimated. Also fixing the photon index to 1.7, a typical value for this source, the cut-off is always ruled out and the reflection unconstrained. The large errors in the determination of the slope do not allow any investigation of possible spectral variation in the PDS data (see figure 5.7). The PDS spectral indices found are consistent with the OSSE results (Johnson et al. 1995).

5.5.2 MKN501

MKN501 is one of the closest ($z=0.034$) BL Lacertae objects and one of the brightest at all wavelengths. It is classified as HBL (High energy peaked BL Lac, Padovani & Giommi 1996) since its Spectral Energy Distribution (SED) peaks (in a $\nu f(\nu)$ vs ν representation) in the UV/X-rays energy band. The spectral energy distribution of high-energy peaked BL Lacs, from radio to γ -ray energy, in the ν - νF_ν representation, is characterized by

two peaks: one in the UV/soft X-ray band and the second at the GeV to TeV energies. This spectral energy distribution is generally interpreted as due to incoherent synchrotron radiation followed by Inverse Compton emission (e.g. Ghisellini, Maraschi & Dondi 1996). The radio to X-ray emission is produced by the synchrotron process as strongly suggested by the connection of the X-ray and IR, optical, UV spectra. On the contrary the inverse Compton is responsible for the γ -ray emission and the correlated flaring at X-ray and TeV energies (Takahashi et al. 1996). Many theoretical models have been proposed to explain the spectral and the timing variability observed in the high-energy peaked BL Lac. The comparison between different spectral states can give us information on the source electron distribution.

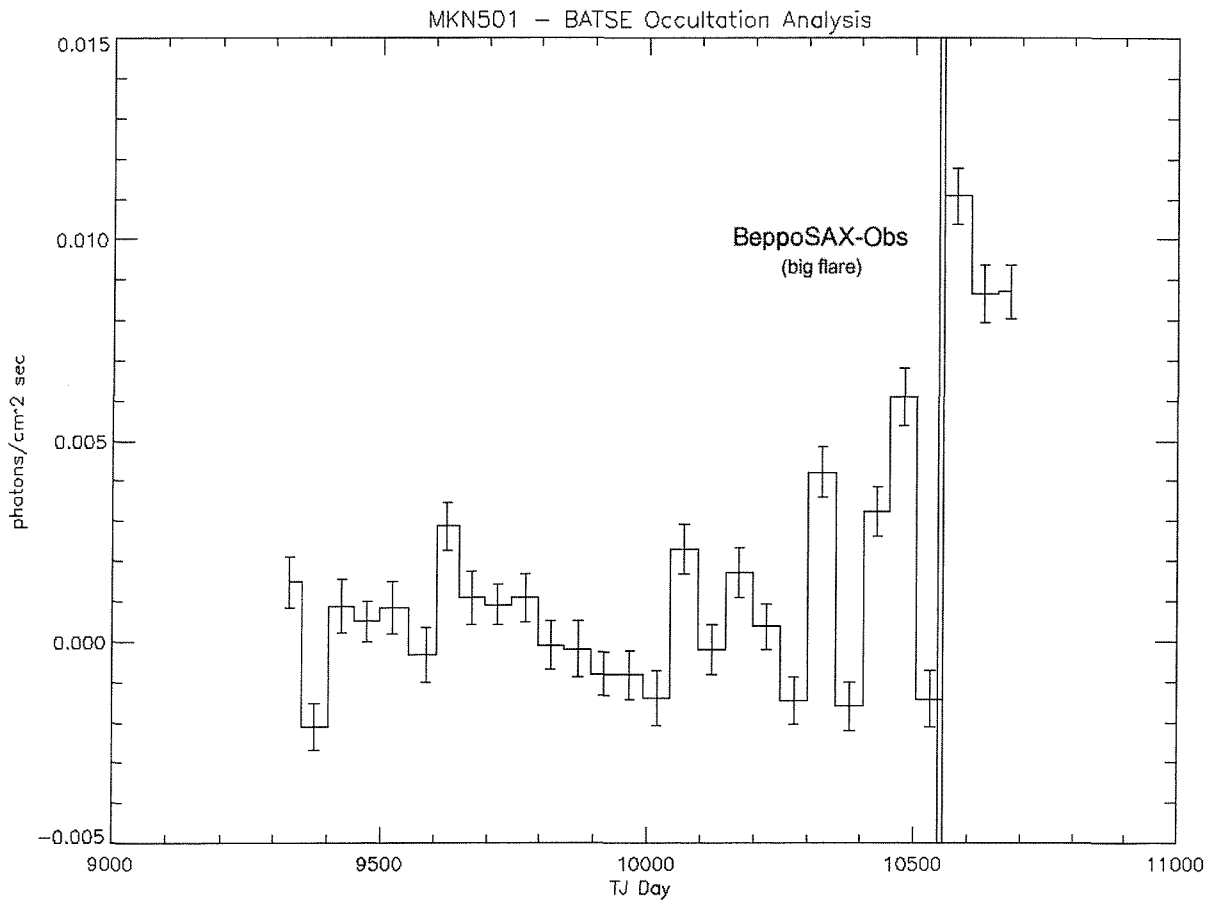


Figure 5.8: BATSE light curve. 50 days intervals resulting from the rebinning of the daily data obtained with LADs in Earth Occultation Mode.

BeppoSAX has observed MKN501 several times in 1997, 1998 and 1999. In the spring of 1997, the source exhibited a phase of very high activity and showed the most extreme

X-ray/TeV flare ever recorded (Catanese et al. 1997, Pian et al. 1998). Since that time, MKN501, has been the target of numerous observations at all wavelengths, in particular at high energies. Here *BeppoSAX* -PDS observations of MKN501 in 1997 April, the period of the big flare, 1998 April-May-June-July and 1999 June have been considered. In figure 5.8 the BATSE light curve over 3 years of observations is shown, in the figure is also highlighted the period of the *big flare* of April 1997 observed by *BeppoSAX* again to frame the short variability in the long term behaviour of the source studied by BATSE. While the broad X-ray spectra of the HBL present a large convex curvature fitted with a power law which is gradually steepening with energy in line with the SSC scenario (Ghisellini et al. 1998), a single power law represents well the PDS data only. The results of the *BeppoSAX* /PDS analysis of MKN501 are reported in table 5.7 while the spectra of all the observations have been included in appendix B.

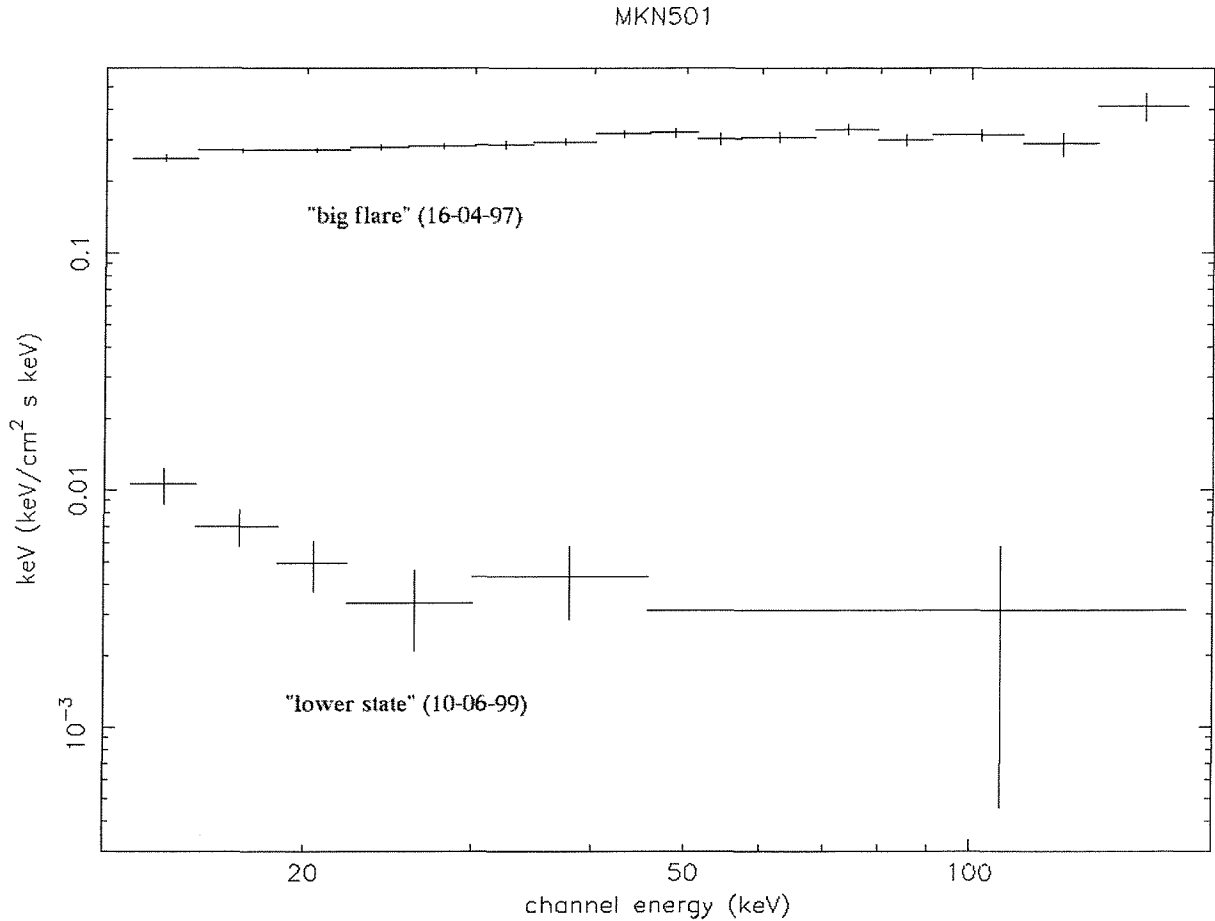


Figure 5.9: Comparison of the unfolded spectra of MKN501 in the highest state of April 97 (*"big flare"*) and in the lower state analyzed here of June 99.

It is clear from the data analyzed here (table 5.7) that a significant spectral variability is present; in fact, during the flare of April 1997 the spectrum of the source was exceptionally hard ($\alpha \leq 1$, with $F_\nu \propto \nu^{-\alpha}$), indicating that the X-ray power output peaked at ~ 100 keV. This corresponds to a shift of at least 2 orders of magnitude with respect to previous observations of MKN501. This behaviour has never been seen before in this or any other blazar, and for the first time in any blazar the synchrotron power is observed to peak at hard X-ray energies. The high spectral variability is clearly shown in figure 5.9 where the PDS unfolded spectra of the maximum and minimum state of the *BeppoSAX* observations analyzed here have been plotted together for comparison. In figure 5.10 the photon indices of the *BeppoSAX* /PDS spectra have been plotted against the fluxes in 20-200 keV energy band. It is evident that the source significantly hardened when it brightened and this is in line with the expectations of the SSC model.

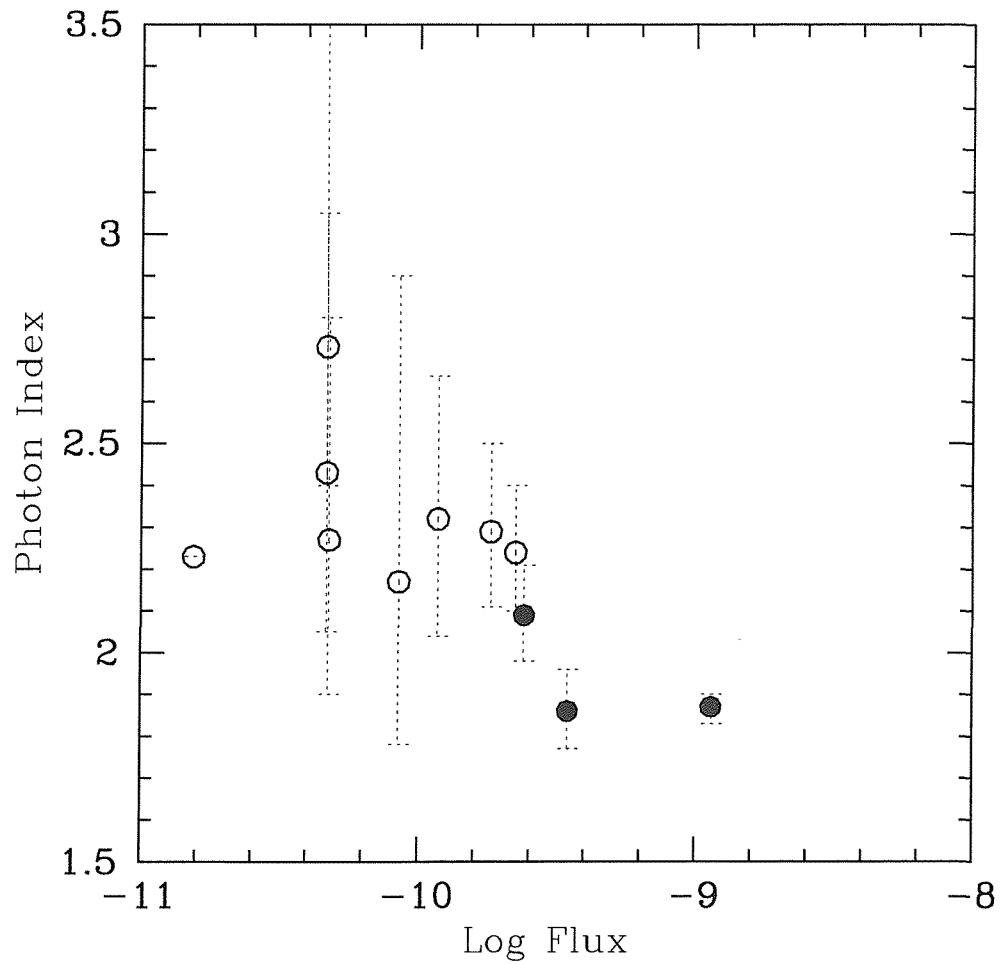


Figure 5.10: Photon index versus flux of all the BeppoSAX/PDS observations analyzed here, filled symbols are the measurements during the big flare. The fluxes are in units of $10^{-11} \text{ erg cm}^{-2} \text{ s}^{-1}$.

Chapter 6

BeppoSAX AVERAGE SPECTRA OF SEYFERT GALAXIES

6.1 Introduction

The discovery of broad emission lines in the polarized spectrum of a number of Seyfert 2 galaxies (Antonucci and Miller 1985) has provided the basis for a unification model of Seyfert galaxies in which the main discriminating parameter is the inclination of our line of sight with respect to an obscuring torus surrounding the source. In the simple version of this model, one then expects the direct continuum of type 1 and 2 objects to be the same except for the effects of obscuration by the torus material. The X-ray spectra of type 1 objects are relatively well known and consist of a power law of index ~ 2 , a Fe K α feature, a cut-off at around 200 keV plus a Compton reflection component with $R \sim 0.6-1$ (Perola et al. 2001, Matt et al 2000a, Lubinski and Zdziarski 2001). Conversely, the X-ray spectra of the type 2 sources are much less well defined due to the extra complexity of absorption: constraints on individual spectra are rather poor due to the limited photon statistics and provide a greater variety of spectral components (Matt et al. 2000b, Malaguti et al. 1999, Turner et al. 2000). One way to better constrain the hard-X properties is to consider their average spectra. When this is done, the spectrum of type 2 objects turns out to be substantially harder than that of type 1, which implies a lower energy cut-off (Zdziarski et al. 1995, 2000). However, this intrinsic difference in the spectrum of Seyferts 1 and 2 cannot be explained by the simplest version of the unified AGN model, providing its strongest challenge yet. Here, we study the average spectra of Seyfert 1 and 2 observed by *BeppoSAX* over the energy band 3-200 keV. The purpose is to determine the tightest constraints on both spectral shapes, to check if their

intrinsic continuum is indeed different and to discuss our findings in the framework of the unified theory.

6.2 Average Spectra

The *BeppoSAX* MECS data together with the PDS data analyzed in the previous chapter, have been used here to study the average 3-200 keV spectra of Seyfert 1s and Seyfert 2s in order to investigate their average spectral characteristics and the possible differences between the two classes. For this study the MECS data have been also considered to better constrain the spectral parameters, but the soft energy range (0.1-3 keV) has been excluded to avoid the problems introduced by the presence of soft excess. Firstly the Piccinotti Seyfert 1s (Fairall9, 3C120, NGC3783, NGC4593, MCG-6-30-15, NGC5548, MKN509, ESO141-G55, 3C445, NGC7469) and Seyfert 2s (NGC526A, NGC2992, NGC5506, ESO103-G35, NGC7172, NGC7314, NGC7582) have been added together to produce stacked spectra. Although for the Seyfert 1 objects the statistics were good and the results consistent with expectations, the situation was less clear for type 2 objects due to the more limited quality of the data. For this reason the Seyfert 2 sample has been widened to include all the Seyfert 2s having $N_H \leq 10^{23}$ atoms cm^{-2} and which were observed by *BeppoSAX* as of Dec 2000 (MCG-5-23-16, NGC1365, NGC2110, NGC 4258, NGC5252, NGC5674). NGC4151 and IC4329A are not included in the sum since they are so bright that they can strongly dominate the average spectrum. We also excluded from the Seyfert 2 sample sources with column density in excess of 10^{23} atoms cm^{-2} , in order to maintain a certain homogeneity in the absorption properties. The sum of the spectra has been obtained using the FTOOL's task 'mathpha', which performs aritmetical operations on the PHA (Pulse Height Analyser) datasets. The units in which the algebra is performed is COUNTS, so that in each spectral channel/bin of the detector the counts (N) have been added and the mean performed. The propagation and calculation of errors are obtained assuming a Gaussian distribution where the errors are the \sqrt{N} counts. The exposure time of the average PHA file is performed with a specified calculation from the exposure times of the input PHA files.

In tables 6.1 and 6.2 the spectral analysis performed is reported for Seyfert 1s and Seyfert 2s respectively. For both type 1 and type 2 samples we first fit the spectra with an absorbed simple power law in order to see all the spectral characteristics over the considered band (model 1), then a gaussian line is added (model 2) and, as in the previous chapter, the high energy band has been fitted first with the HIGHECUT (model 3) i.e. with no Compton reflection and finally with the PEXRAV model (last columns), where all the

components have been considered. For the Seyfert 1 galaxies the pexrav model has been used with two different inclination angles: $\cos\theta=0.45$, edge-on configuration (model 4) and $\cos\theta=0.87$, face-on configuration (model 4[†]), as suggested by Gondek et al. (1996) and Zdziarski et al. (2000); on the other hand since Seyfert 2s are most likely to be seen edge-on, only $\cos\theta=0.45$ has been assumed for this type of object.

6.3 Results of the average spectra

In the second column (model 1) of table 6.1 and 6.2 the parameters of the absorbed power law fits are listed. It is worth noting that, although the overall shape is similar for both types of galaxies, the best fit photon index for Seyfert 1 and 2 turns out to be significantly different: $1.87^{+0.01}_{-0.02}$ for Seyfert 1s and $1.77^{+0.02}_{-0.02}$ for Seyfert 2s. Obviously, Seyfert 2 galaxies are more absorbed than Seyfert 1 with an average column density of $\sim 4 \times 10^{22}$ atoms cm^{-2} , however some amount of absorption is also present in Seyfert 1 galaxies with $N_H \leq 10^{22}$ atoms cm^{-2} . A recent analysis of a sample of Seyfert 1s observed with *BeppoSAX* indicates that cold absorption of this amount is generally not present in this type of objects ($N_H \leq 10^{21}$ atoms cm^{-2}); however a warm absorber seems to be a common feature of type 1 objects, and is consistent with the presence of some absorption in our average spectrum (Perola et al. 2001). As expected, the absorbed power law provides an unsatisfactory fit and in figures 6.1 the data to model ratios are reported for both classes. From the ratios it is possible to see strong features over the entire 3-200 keV range considered: emission in excess at around 6.4 keV is clearly evident as well as a reflection hump around 30 keV and a possible cut-off in the spectra at higher energies. From a deeper inspection of the two ratios a different behaviour of the spectra at around 50 keV stands out, a weak excess of counts at this energy is present in the Seyfert 2 average spectrum but not in Seyfert 1s.

A significant improvement in the fits is given by the addition of the iron $K\alpha$ line (model 2) which is required by both spectra with a probability of 99.99% ($\Delta\chi^2=569.5$ with 3 d.o.f. for Seyfert 1s and $\Delta\chi^2=500.19$ with 3 d.o.f. for Seyfert 2s). The iron line values of both classes of objects are in agreement with the expected values, i.e. with reflection in cold material. The lines are located at 6.39 ± 0.04 keV in type 1 Seyferts with an equivalent width (EW) of 148^{+19}_{-18} eV and at $6.48^{+0.06}_{-0.1}$ keV in type 2 with EW of 189^{+26}_{-25} eV. It is worth noting that in both cases the iron $K\alpha$ line is slightly broad $\sigma_{\text{Sey1}} = 0.26^{+0.06}_{-0.05}$ and $\sigma_{\text{Sey2}} = 0.25^{+0.07}_{-0.02}$ (see figures 6.2). The broadness of the line maybe due to a redshift effect as sources with different z are summed together. The samples considered include 10 Seyfert 1s and 13 Seyfert 2s: of these 5 are Seyfert 1s and 3 are Seyfert 2 galaxies

which have redshift greater than 0.01, i.e. enough to determine a broadening of the line; in particular an important contribution to the line width could be given by Fairall 9 ($z=0.047$) to the Seyfert 1 average spectrum and by NGC5506 ($z=0.062$) to the Seyfert 2 spectrum. Note however, that an analysis of the composite ASCA spectrum of a sample of Seyfert 1 galaxies, indicates a similar average width ($\sigma=0.22\pm0.03$, Lubinski and Zdziarski 2001), possibly due to the presence of two components: a narrow one around 6.4 keV and a broader one bluewards. Similar results are emerging from Chandra and XMM data (see Matt et al. 2001 and references therein). However, a detailed analysis of the iron line is beyond the scope of this thesis.

We then tested the presence of the high energy cut-off in the average spectra and found that both fits significantly improve, the difference in χ^2 for one d.o.f. is 83.5 and 91.3 for Seyfert 1s and Seyfert 2s respectively. The probability that the fit improvements were not by chance (obtained using the F-test) is 99% for type 1 galaxies and >99% for type 2. Using the highecut model (see tables 6.1 and 6.2, model 3) we found a cut-off energy of $E_c=164^{+61}_{-24}$ keV for the type 1 objects and $E_c=114^{+31}_{-80}$ keV for type 2, which are compatible within errors with the results of Zdziarsky et al. (2000) on OSSE average spectra. The two cut-off energies found are well constrained and as already suggested by Zdziarsky et al (2000) this could indicate that the high energy cut-off is present in the individual Seyferts (type 1 and 2) in a relatively narrow range of energies otherwise the resulting average spectra would be a power law without cut-off. In figures 6.3 the data to model ratio considering only the high energy cut-off for Seyfert 1s (top) and Seyfert 2s (bottom) are reported. From both, the presence of the Compton reflection hump is evident, therefore this component has been introduced via the pexrav model in XSPEC (column 5 and 6 of tables 6.1 and column 5 of table 6.2). The addition of the Compton reflection component significantly improves the fit of the average spectrum of Seyfert 1s by $\Delta\chi^2=86.76$ (for 1 d.o.f.) as well as for the average spectrum of Seyfert 2s by $\Delta\chi^2=49.43$ (for one d.o.f.) which corresponds in both cases to a probability >99%. In the case of Seyfert 1 objects best-fit values are found using $\cos\theta=0.45$ (i.e. edge-on configuration), but there is no statistically significant difference ($\Delta\chi^2=3.36$) using $\cos\theta=0.87$. Note that we have assumed the reflection medium close to neutral and the abundances used are those of Anders and Ebihara (1982). The contour plots of the various best fit parameters for both types of objects and for Seyfert 1 for both inclination angles assumed, are shown in figures 6.4 (high energy cut-off versus photon index), figure 6.5 (reflection versus photon index) and figure 6.6 (reflection versus high energy cut-off). All confidence contours have been obtained by fixing the column density and all the parameters of the iron line to their best fit values. Decreasing the inclination angle (i.e. considering the face-on

configuration) the spectral characteristics of Seyfert 1s become more similar to Seyfert 2, the photon index decreases to $1.88^{+0.04}_{-0.03}$, as expected the amount of the reflected radiation decreases ($R=0.64^{+0.22}_{-0.19}$) and the cut-off energy (197^{+64}_{-40}) decreases too. It is evident from the figures and the tables that while the amount of reflection is consistent between the two types, the primary continuum is still significantly different: the average Seyfert 2 spectrum is substantially harder than that of Seyfert 1s and the cut-off is at lower energies. On the other hand, the average spectrum of the Seyfert 1s is perfectly canonical with $\Gamma=1.9$, reflection strength $R \sim 0.6$ (or 1 depending on the inclination angle assumed) and cut-off energy at around 200 keV. The iron line is confirmed at 6.4 keV and the equivalent width is 100-120 eV. Our results confirm the findings of Perola et al. (2001) on a sample of Seyfert 1 galaxies observed by *BeppoSAX* and analyzed individually with the same model. When their data are combined to get weighted mean values, these are very similar to our best fit parameters of table 6.1: $\Gamma=1.84\pm0.02$, $R=0.64\pm0.09$ (for $\cos\Theta=0.9$) and $E_c=130\pm20$ keV; their average line energy is at 6.44 ± 0.0 keV while the equivalent width is $EW=122\pm16$ eV. It is worth noting that if the iron line comes from the same medium as the Compton reflecting continuum, one would expect a simple relationship between R , Γ and EW , which for the average photon index of the Seyfert 1 galaxies and the reflection value obtained for $\cos\Theta=0.87$ provides an EW value very similar to that observed (see George and Fabian 1991 results rescaled to the Anders and Grevesse, 1993, abundances). Therefore, the observed EW is of the right order expected from the simultaneously measured strength of the reflection component confirming an origin in the accretion disc. The difference seen between Seyferts 1 and 2 is however troublesome as it is not easily reconciled with the Unified Theory, which is independently supported by a number of observational evidences. On the other hand the inter-dependence of the parameters in the *pexrav* model is well known: the same data could be fitted just as well with a steeper power law, a higher reflection component and a cut-off at higher energy. To test this possibility, we have imposed a photon index of 1.92 (i.e. equal to that obtained for the Seyfert 1s in the $\cos i=0.45$ configuration) to the Seyfert 2s and measured the contours of reflection strength against cut-off energy for this case. Figure 6.7 shows the results compared to the Seyfert 1 case while model 4[†] in table 6.2 provides the best fit parameters for this case. The cut-off energy turns out to be similar to that measured in type 1 objects but the R value is now much higher (≥ 2.6). A Compton reflection component as strong as this is unusual for Seyferts especially for Compton-thin Seyfert galaxies (Bassani et al. 1999a,b) and has not been observed even in the more extreme Compton thick objects (Matt et al. 2000b). A strong reflection component is however still possible if the X-ray emission is anisotropic and/or there is a time lag in

the response of the reflection flux to the variations of the source intensity (Capri et al. 1996, Weaver et al. 1996). However, following the same reasoning as for type 1 objects, the measured iron line EW is too low for the observed reflection strength especially if some contribution of the order of 30-40 eV is to be considered to account for the line component originating by transmission through a torus of column density of $N_H \sim 4 \times 10^{22}$ at cm^{-2} .

A model-independent way to verify the above two hypothesis (different spectral shape or different reflection component), is to measure the Seyfert 2 to Seyfert 1 ratio as a function of energy: more reflection in Seyfert 2 would produce a bump in the 10-50 keV band while a flatter power law with a lower cut-off energy would produce a deviation from 1 at lower and higher energies. The Seyfert 2 to Seyfert 1 ratio is shown in figure 6.8, which clearly excludes the presence of stronger reflection in type 2 objects. The deficit of counts at lower energies is only partly due to the different absorption found in the two samples, indicating either a difference in the intrinsic shape and/or the presence of extra absorption; similarly the high energy excess is probably due to a flatter slope and/or a lower cut-off energy.

Having excluded reflection as the possible cause of a flatter spectrum, the only other remaining way to steepen the Seyfert 2 spectrum and so save the fundamental principal of the unified theory, i.e. that objects of type 1 and 2 are intrinsically equal, is via a more complex absorption model than that assumed here. Complex absorbers have been observed in some individual source spectra (Malaguti et al. 1999, Vignali et al 1998, Turner et al. 2000, Guainazzi et al. 2001) and have recently been used to reconcile the spectrum of NGC4151 with the canonical Seyfert 1 spectrum (Zdziarski et al. 2001, Takahashi et al. 2001). We have therefore introduced in the Seyfert 2 fit an extra absorber that partially covers the source (table 6.3). The fit improves significantly at the 99% level for two extra degrees of freedom and provides average spectral parameters for the intrinsic continuum very similar to those measured in Seyfert 1. The contours of this extra column density and covering fraction are shown in figure 6.9 while the composite spectra of both types of Seyferts are compared in figure 6.10 where we have assumed model 4 ($\cos\Theta=0.45$) of table 6.1 for type 1 objects and the double absorption model of table 6.3 for type 2 objects.

With this model we are able to explain the deficit in counts (mainly due to the extra absorption) as well as the excess in counts (which disappears when a more canonical spectrum is assumed) observed in figure 6.8.

Table 6.1: Seyfert 1s - Sum

| Parameter | (1) | (2) | (3) | (4) ($\cos \theta=0.45$) | (4)($\cos \theta=0.45$) |
|----------------------|------------------------|------------------------|------------------------|----------------------------|---------------------------|
| $N_H \times 10^{22}$ | $1.62^{+0.14}_{-0.15}$ | $1.01^{+0.15}_{-0.17}$ | $0.39^{+0.21}_{-0.19}$ | $0.93^{+0.18}_{-0.18}$ | $0.87^{+0.18}_{-0.19}$ |
| Photon Index | $1.87^{+0.01}_{-0.02}$ | $1.85^{+0.01}_{-0.02}$ | $1.74^{+0.03}_{-0.03}$ | $1.92^{+0.04}_{-0.03}$ | $1.88^{+0.04}_{-0.03}$ |
| E_{fold} (keV) | - | - | 164^{+61}_{-24} | 216^{+75}_{-41} | 197^{+64}_{-40} |
| R | - | - | - | $1.25^{+0.38}_{-0.29}$ | $0.64^{+0.22}_{-0.19}$ |
| E_{line} (keV) | - | $6.39^{+0.04}_{-0.04}$ | $6.37^{+0.04}_{-0.03}$ | $6.37^{+0.03}_{-0.03}$ | $6.38^{+0.04}_{-0.04}$ |
| σ_{line} (eV) | - | $0.26^{+0.06}_{-0.05}$ | $0.25^{+0.07}_{-0.06}$ | $0.18^{+0.03}_{-0.14}$ | $0.22^{+0.06}_{-0.08}$ |
| EW (eV) | - | 148^{+19}_{-18} | 147^{+16}_{-16} | 106^{+18}_{-29} | 120^{+21}_{-20} |
| χ^2/dof | 826.97 (73) | 257.41 (70) | 173.88 (69) | 87.12 (68) | 90.48 (68) |
| χ^2_ν | 11.33 | 3.68 | 1.39 | 1.25 | 1.33 |

Notes: model (1) = wa*po, model (2) = wa*po+ga, model (3) = wa*(po+ga)*highcut;
model (4) = wa*(pexrav+ga)

Table 6.2: Seyfert 2s - Sum

| Parameter | (1) | (2) | (3) | (4)($\cos \theta=0.45$) | (4 [†]) |
|----------------------|------------------------|------------------------|------------------------|---------------------------|------------------------|
| $N_H \times 10^{22}$ | $4.98^{+0.22}_{-0.23}$ | $4.12^{+0.23}_{-0.22}$ | $3.16^{+0.32}_{-0.26}$ | $3.67^{+0.29}_{-0.27}$ | $3.83^{+0.24}_{-0.03}$ |
| Photon Index | $1.77^{+0.02}_{-0.02}$ | $1.74^{+0.02}_{-0.02}$ | $1.58^{+0.04}_{-0.04}$ | $1.75^{+0.06}_{-0.04}$ | 1.92 |
| E_{fold} (keV) | - | - | 114^{+31}_{-80} | 128^{+45}_{-24} | 221^{+94}_{-61} |
| R | - | - | - | $1.19^{+0.64}_{-0.35}$ | $3.02^{+0.28}_{-0.27}$ |
| E_{line} (keV) | - | $6.48^{+0.06}_{-0.1}$ | $6.46^{+0.06}_{-0.03}$ | $6.47^{+0.03}_{-0.04}$ | $6.44^{+0.04}_{-0.03}$ |
| σ_{line} (eV) | - | $0.25^{+0.07}_{-0.02}$ | $0.25^{+0.06}_{-0.07}$ | $0.21^{+0.06}_{-0.11}$ | $0.01^{+0.15}_{-0.01}$ |
| EW (eV) | - | 189^{+26}_{-25} | 188^{+24}_{-26} | 145^{+71}_{-36} | 97^{+17}_{-14} |
| χ^2/dof | 742.79 (73) | 242.62 (70) | 151.35 (69) | 101.92 (68) | 108.54 (69) |
| χ^2_ν | 10.17 | 3.47 | 2.19 | 1.5 | 1.57 |

Notes: model (1) = wa*po, model (2) = wa*po+ga, model (3) = wa*(po+ga)*highcut;
model (4) = wa*(pexrav+ga)



Table 6.3: Seyfert 2s - Double Absorption

| $N_H(1)$ | $N_H(2)$ | C_f | Γ | E_{fold} | R | E_{line} | σ_{line} | EW | χ^2/dof |
|------------------------|-------------------------|------------------------|------------------------|-------------------|------------------------|------------------------|------------------------|------------------|---------------------|
| $3.13^{+0.15}_{-0.19}$ | $27.05^{+7.45}_{-8.15}$ | $0.26^{+0.05}_{-0.08}$ | $1.89^{+0.03}_{-0.04}$ | 228^{+69}_{-45} | $0.93^{+0.37}_{-0.08}$ | $6.46^{+0.04}_{-0.03}$ | $0.13^{+0.05}_{-0.13}$ | 97^{+21}_{-12} | 93.38 (66) |

6.4 Discussion

We have measured with *BeppoSAX* the average spectra of Seyfert 1 galaxies confirming previous indication that these galaxies typically have a power law shape with photon index 1.9, a reflection component of strength $R \approx 0.6-1$ and a high energy cut-off which is now more clearly defined and located at around 200 keV. The possible range of these parameters seems to be relatively small otherwise each feature would be smeared out in the spectral summation and the resulting spectrum would look more like a simple power law. Seyfert 2s on the other hand, have an average spectrum which is substantially harder and with a lower energy cut-off than Seyfert 1s unless a complex absorption is assumed. The findings that the X-ray absorber is complex is not surprising: whether it consists of two column densities (one with $N_H \sim 3 \times 10^{22}$ totally covering the source and one with $N_H \sim 4 \times 10^{23}$ covering only half of the source) or more, whether the absorber/s is/are ionized or not and whether the covering fraction are exactly as measured here or different is beyond the scope of the present thesis. Here, it is important to stress that the average spectra of Seyferts 1 and 2 are different unless heavier and more complex absorption is present in type 2 objects with respect to type 1. Naively, this complex absorption could represent various clouds seen along the line of sight or two separate absorbing regions for example a starburst and the torus as recently indicated by Weaver et al. (2000), or inner and outer torii as suggested by Maiolino et al. (1995). What is clear is that multiple absorption is probably ubiquitous in Seyfert 2 galaxies otherwise the flattening of their average spectrum with respect to Seyfert 1s would not be so clear cut. Our results argue strongly for a very similar production mechanism not only in both types of Seyfert galaxies but in each individual object. They also strongly suggest that individual deviations from the canonical spectrum measured here are probably an artifact due to the wrong modelling of the absorption properties in the source as recently indicated also by a detailed analysis of the NGC4151 X-ray spectrum (Zdziarski et al. 2001 and Takahashi et al. 2001). Our results are also relevant for the synthesis of the X-ray background: Seyfert 2 spectra can now be taken to be similar to their type 1 counterparts in the AGN contribution estimates but absorption has to be considered more complex than usually assumed in these calculations.

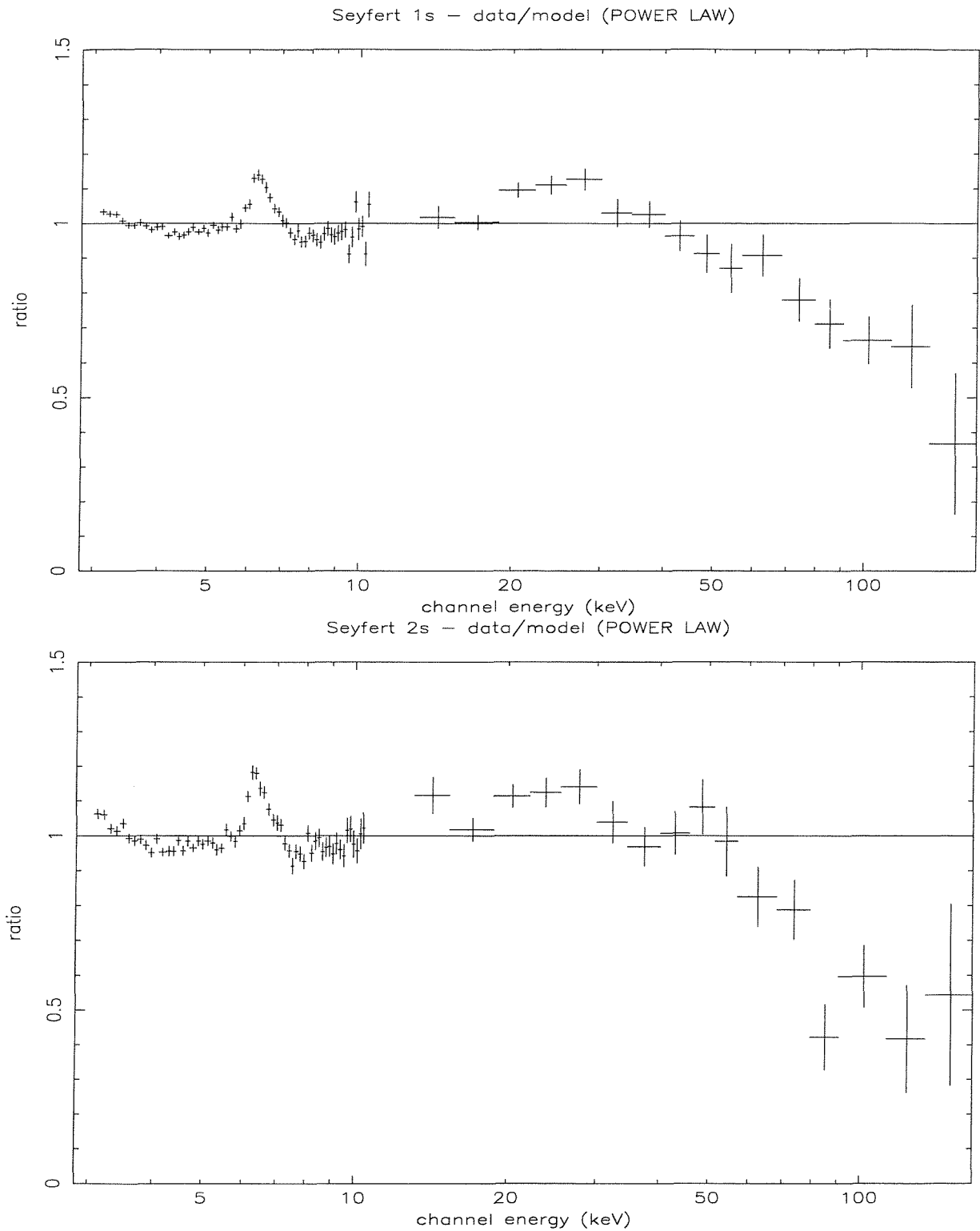


Figure 6.1: Data to model ($wa*po$) ratio over the 3-200 keV energy range for Seyfert 1 (top) and Seyfert 2 (bottom). The figures show the major spectral characteristics to be investigated in both type of objects

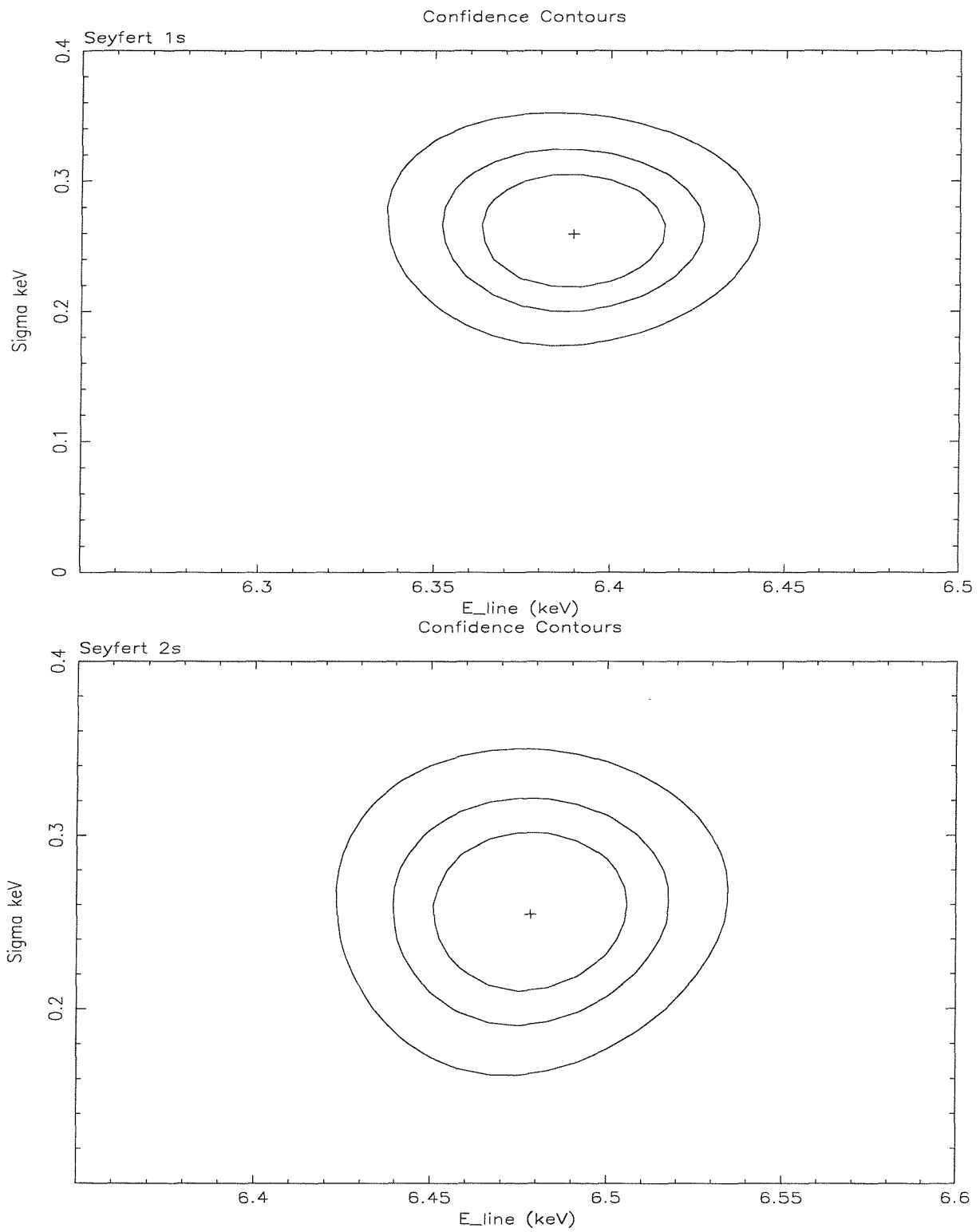


Figure 6.2: Confidence contours of iron line sigma versus energy line for Seyfert 1 (top) and Seyfert 2 (bottom)

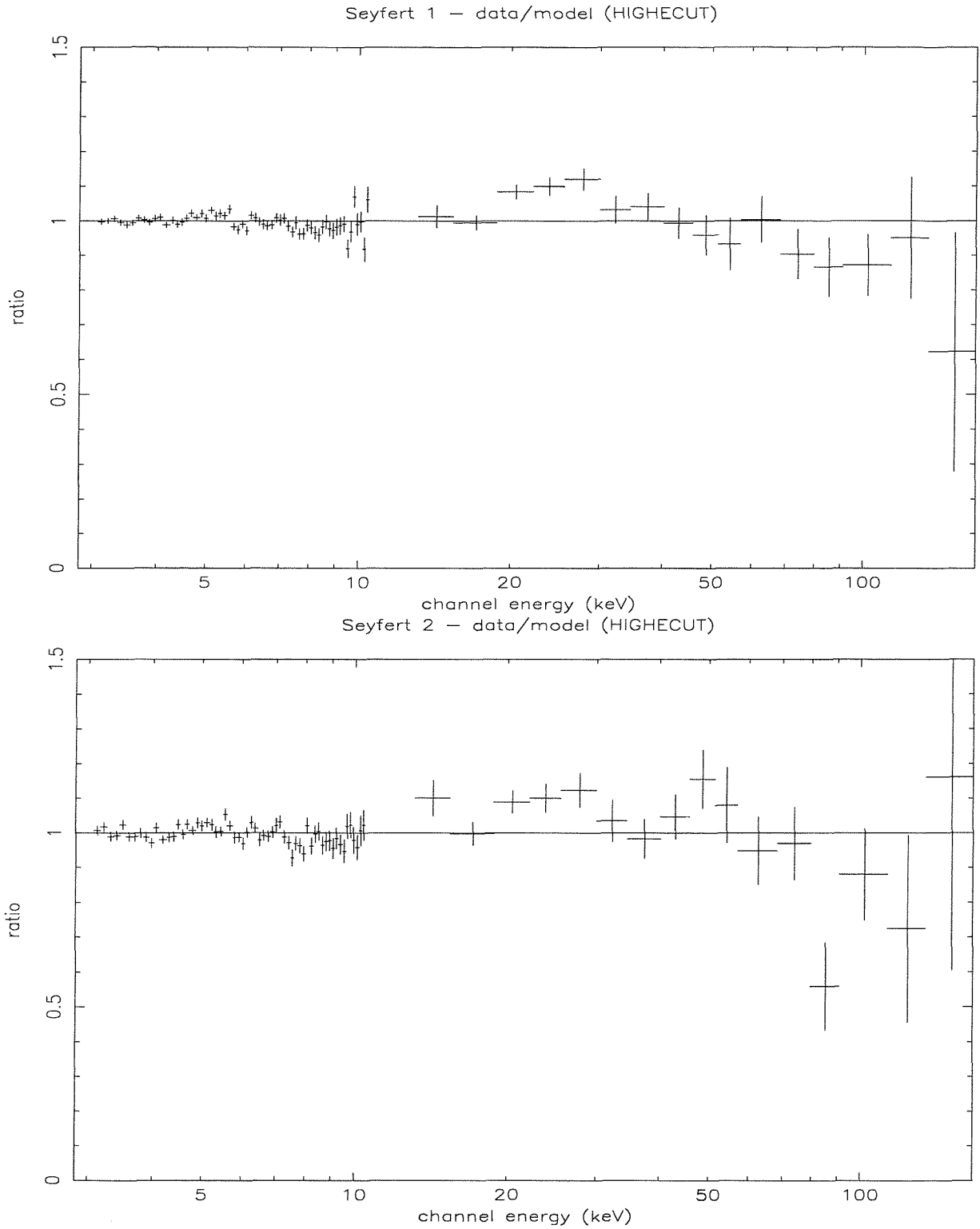


Figure 6.3: Data to model $[wa*(po+ga)*highcut]$ ratio for Seyfert 1 (top) and Seyfert 2 (bottom). The Compton reflection component around 30 keV is well evident in both classes.

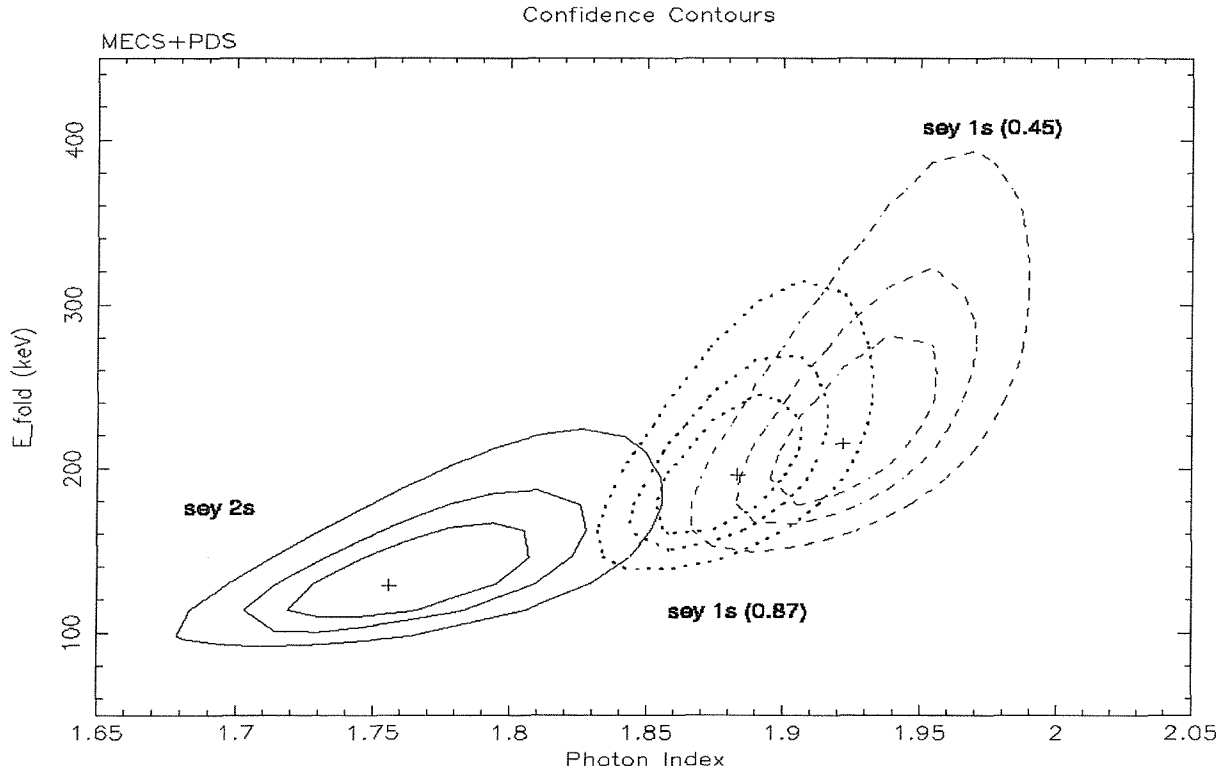


Figure 6.4: Confidence contours of high energy cut-off versus photon index. Solid lines are the 65%, 90% and 99% levels of the Seyfert 2s, the dashed lines are Seyfert 1s in edge-on configuration ($\cos\Theta=0.45$) and dotted lines are contours of Seyfert 1s in face-on configuration ($\cos\Theta=0.87$)

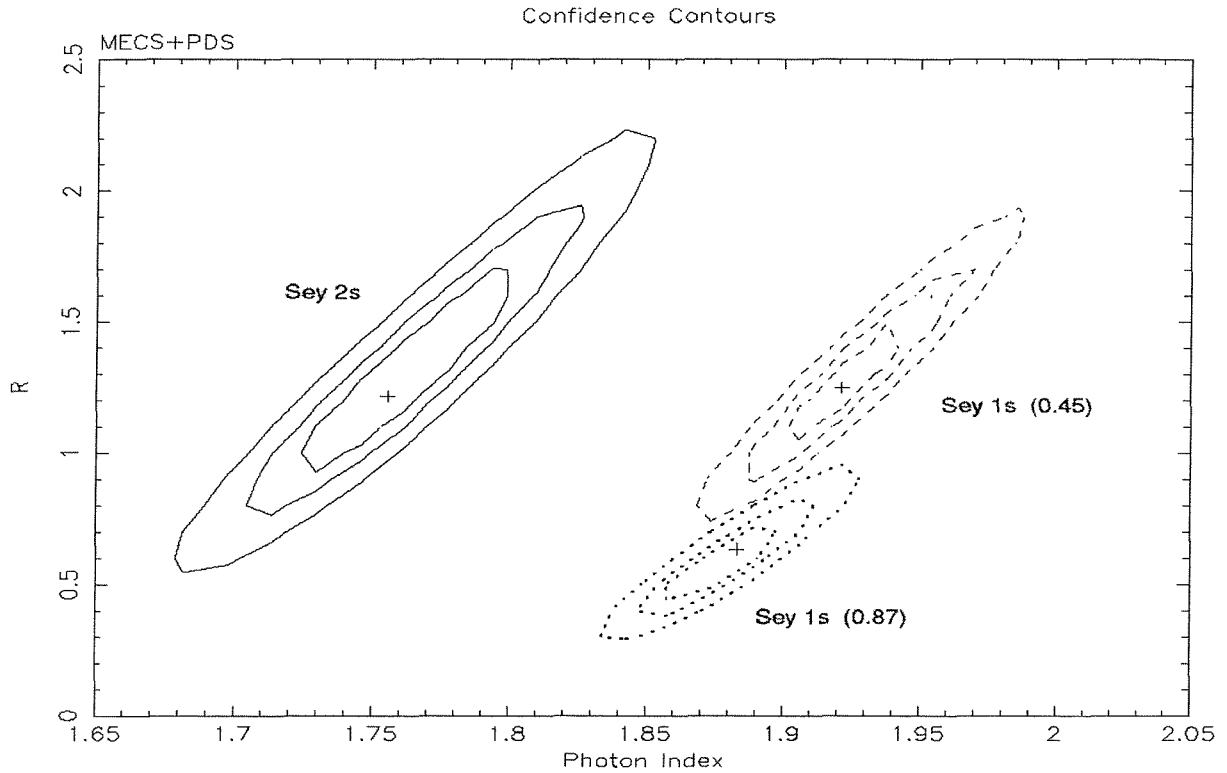


Figure 6.5: Confidence contours of Compton reflection versus photon index. Solid lines are the 65%, 90% and 99% levels of the Seyfert 2s, the dashed lines are Seyfert 1s in edge-on configuration ($\cos\Theta=0.45$) and dotted lines are contours of Seyfert 1s in face-on configuration ($\cos\Theta=0.87$)

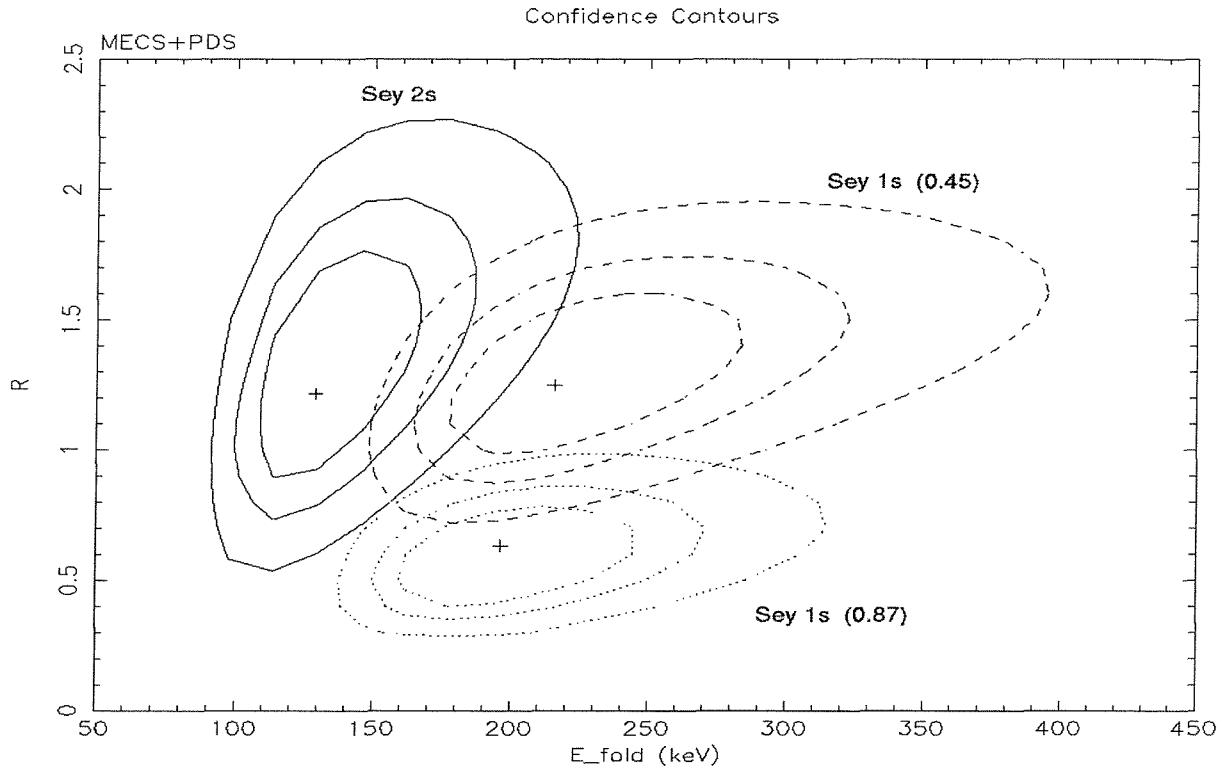


Figure 6.6: Confidence contours of Compton reflection versus high energy cut-off. Solid lines are the 65%, 90% and 99% levels of the Seyfert 2s. The dashed lines are Seyfert 1s in edge-on configuration ($\cos\Theta=0.45$) and dotted lines are contours of Seyfert 1s in face-on configuration ($\cos\Theta=0.87$)

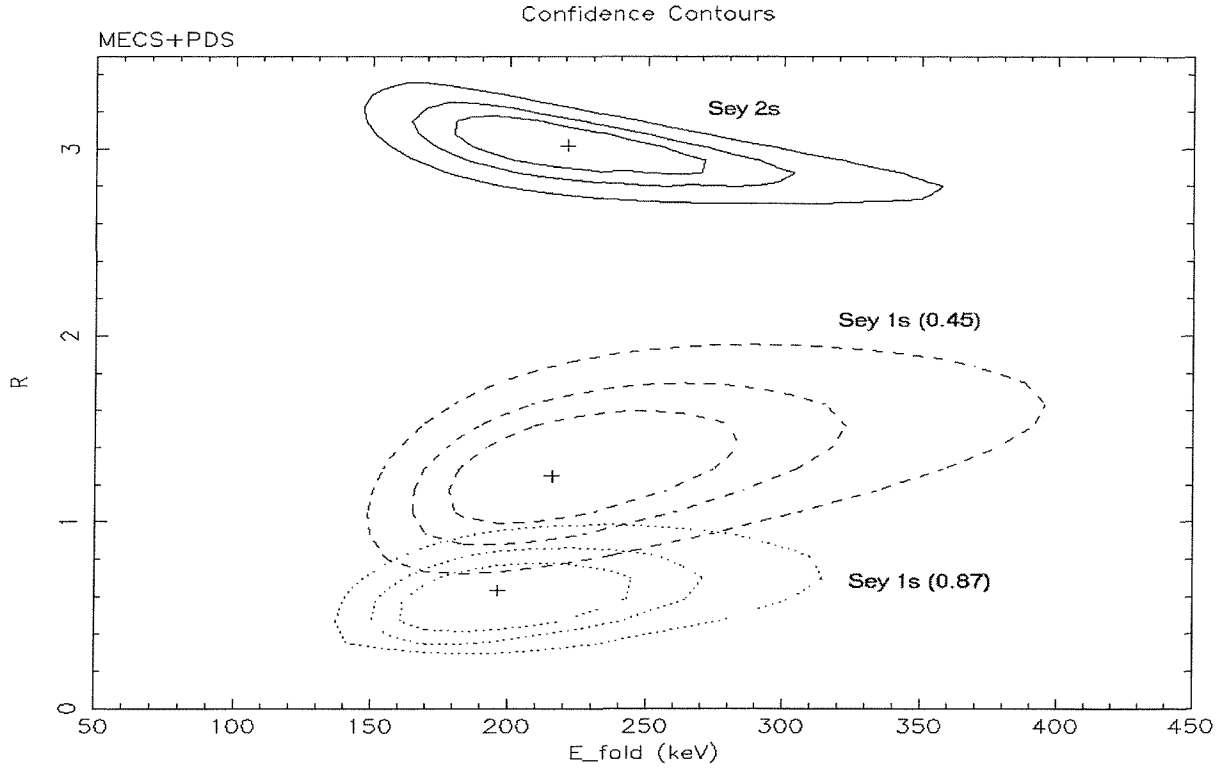


Figure 6.7: Confidence contours of Compton reflection versus high energy cut-off. Solid lines are the 65%, 90% and 99% levels of the Seyfert 2s with Γ fixed to 1.92 value, the dashed lines are Seyfert 1s in edge-on configuration ($\cos\Theta=0.45$) and dotted lines are contours of Seyfert 1s in face-on configuration ($\cos\Theta=0.87$)

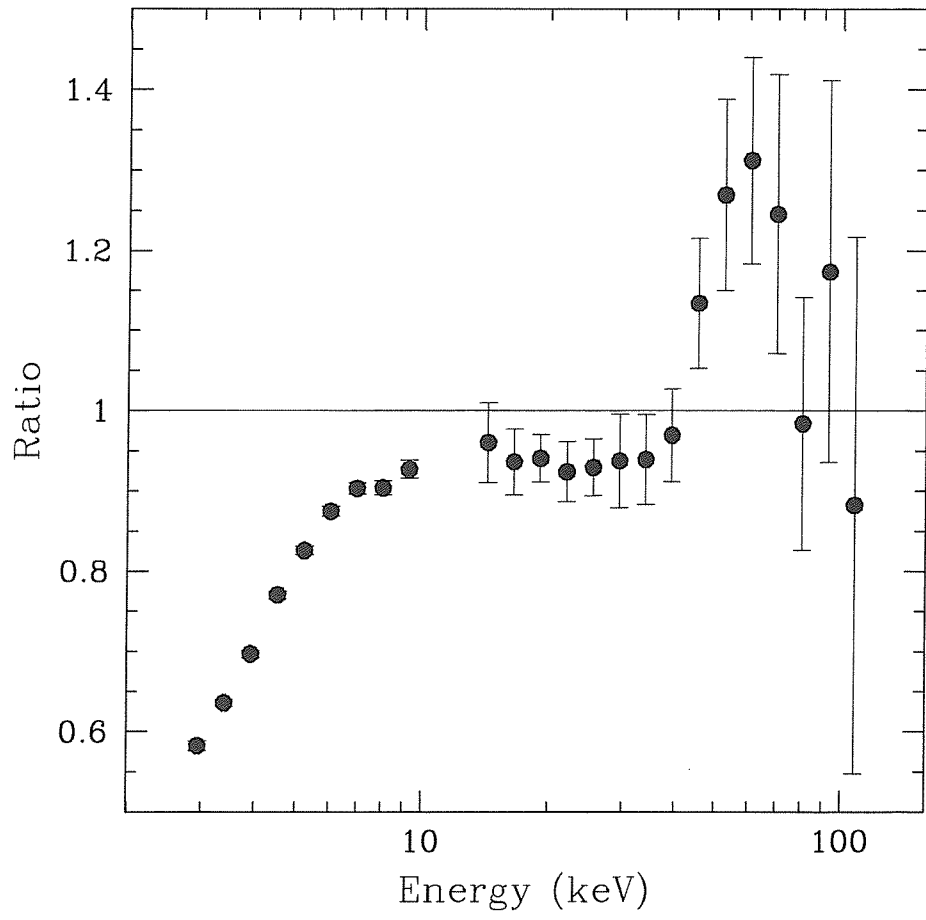


Figure 6.8: Ratio of Seyfert 2s/Seyfert 1s spectra

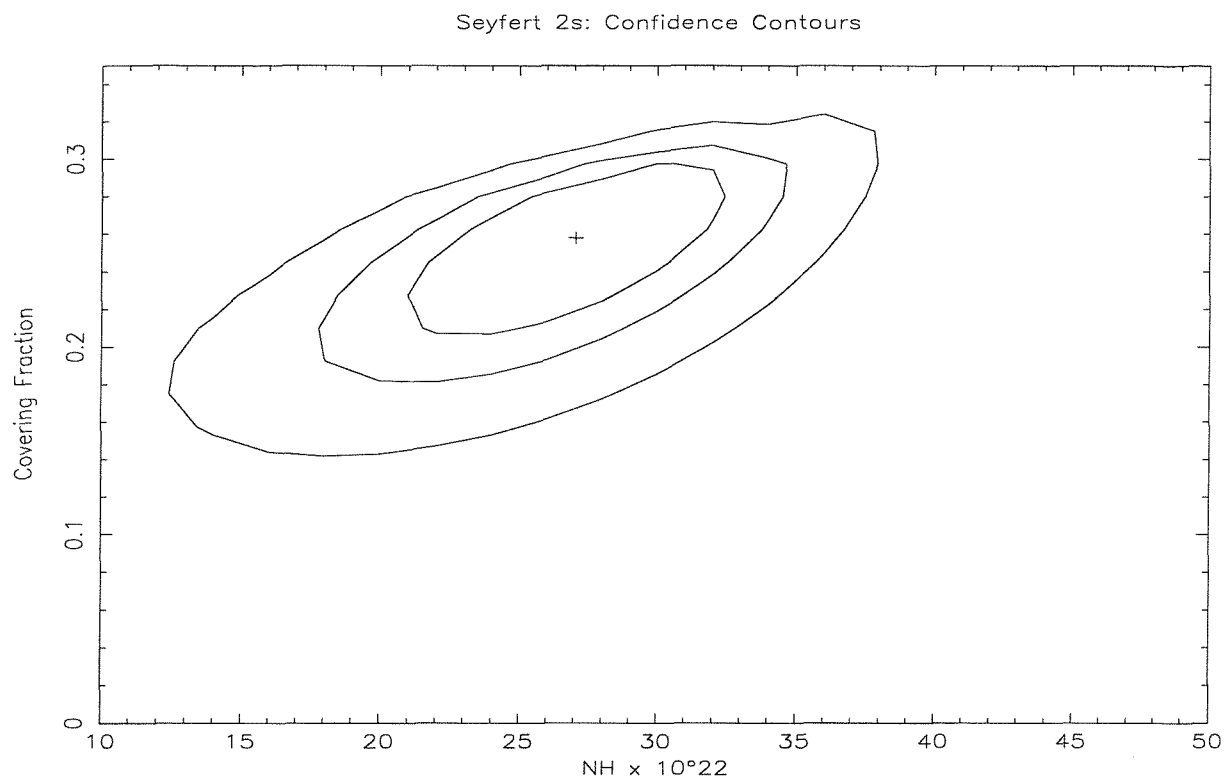
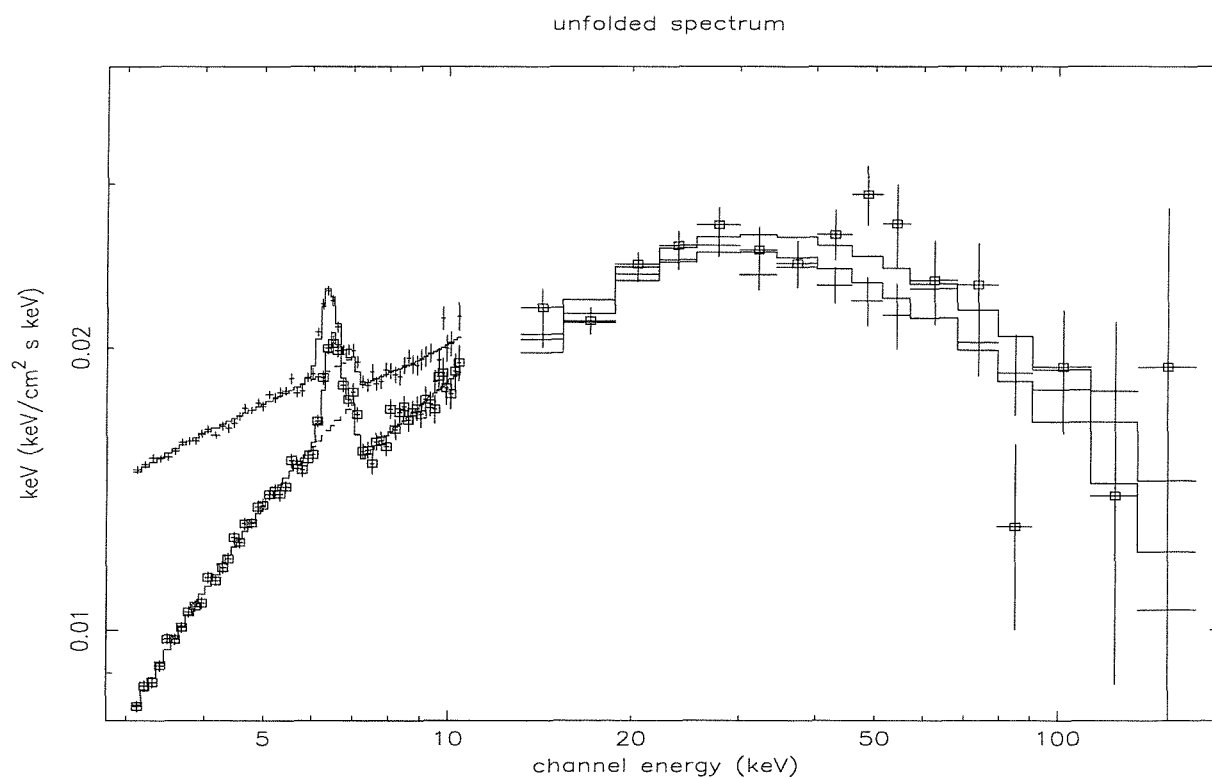
Figure 6.9: Confidence contours of N_H vs Cf for a double absorption model

Figure 6.10: Combined unfolded spectra of Seyfert 1s fitted with pexrav and Seyfert 2s (squares) fitted with double absorption plus pexrav

Chapter 7

Conclusions

7.1 BATSE results

The hard X-ray properties of active galactic nuclei have been studied in this thesis using data sets from two different satellites: ComptonGRO-BATSE (20-100 keV band) and *BeppoSAX* -PDS (20-200 keV band). The sample used for this investigation is the Piccinotti sample of AGN which is a complete X-ray (2-10 keV) selected sample composed of 30 Seyfert galaxies (of which 23 are of type 1 and 7 of type 2), one starburst galaxy (M82), 4 BL Lac objects and one QSO (3C273). The BATSE Earth occultation technique has been exploited to search for emission from the whole sample and nearly four years of observations (November 93- September 97) have been analyzed to extract a signal. The BATSE data reported in the ApJ publication (Malizia et al. 1999) and presented in this thesis, provided for the first time a systematic coverage at high energies of the whole Piccinotti sample. The main result of the BATSE data analysis is the detection of high energy emission from the majority of the sample sources: significant detection at $\geq 10\sigma$ level has been found only for NGC4151, 3C273 and NGC5506, while at the 5σ level the number of detections grows to 14. Marginal detections ($3 < \sigma < 5$) can be claimed for 13 sources, while only 9 were measured below the 3σ confidence level. Comparison between OSSE and BATSE data indicates that 6 objects are reported as hard X-ray emitting sources for the first time: ESO198-G24, H0917-074, ESO 103-G35, H1846-786, 3C 445 and MKN1152, all detected above the 3σ confidence level (Malizia et al. 1999); only successively *BeppoSAX* -PDS observations, most of which are not yet published, have confirmed these high energy emitters. Fluxes in the 20-100 keV energy band have been obtained by folding a single power law of photon index 1.75 for Seyfert galaxies, 3C273 and M82, and 2.25 for BL Lac objects, with the BATSE instrumental response function

and then computing weighted mean flux values over the whole observation period. In order to assess the reliability of our results and to investigate the approximate spectral shape of AGN in the BATSE energy band, a comparison with soft X-ray fluxes as well as with hard X-ray fluxes, has been performed.

BATSE flux estimates, however, are the result of a long integration period (years) and thus represent averaged values over this period, while observations with pointed instruments provide instantaneous flux measurements. This has been taken into account in the comparison with the low energy band by using in the 2–10 keV range mean flux values as estimated from data in the literature. We found that the canonical 1.7 power law which best represents the soft X-ray data gives also a good description of the spectrum in the 20–100 keV band. This result indicates that the reflection component which is responsible for flattening the intrinsic $\Gamma=1.9$ spectrum in the 2–10 keV band, is relevant also above 20 keV and present in most sample sources. Furthermore, BATSE observations imply that spectral breaks and/or steepening must occur preferentially above about 100 keV for consistency with our findings. This is confirmed by the subsequent analysis of BeppoSAX data. A comparison between BATSE and OSSE data has been also performed for all the sample sources for which contemporaneous observations were available. Our findings were that in the particular case of extragalactic studies the BATSE flux can be systematically higher than that seen by OSSE by as much as 35%. We have also compared BATSE data to BeppoSAX observations although in this case the comparison is hampered by the lack of simultaneous data. In this analysis we get many cases ($\sim 50\%$) in which the BATSE/SAX flux ratio is ~ 1 ; only in 8 cases is the flux higher in BATSE than in SAX by a factor of 2. We know, however, that in some of these sources (as in 3C273) variability could well explain this flux difference. In other cases, contamination by nearby objects could be responsible for excess emission in BATSE as in the case of M82 contaminated by M81 and 2A1219+305 contaminated by MKN766.

We have searched for variability of the Piccinotti sample with the BATSE data even if this is not an easy task, mainly due to the poor statistics found in a large fraction of the sources. To be conservative, for each source only the daily positive detections have been considered and then a bin of 30 days has been applied to improve the statistics. Afterwards with the χ^2 test we have verified if the selected data shows variations from the weighted mean value and so the associated probability of variability has been calculated. Among all 36 Piccinotti sources only NGC4151 and 3C273 are variable with a probability $>90\%$, but on the other hand only NGC4151, 3C273 and NGC5506, which is not found to be variable, have detections $>10\sigma$. Therefore, conclusive results on long timescale variability can not be given for the rest of the sample sources. It is however worth not-

ing, that BATSE timing analysis helps in identifying the trend of the source over long periods; furthermore BATSE monitoring includes also pointed observations contemporaneously with other satellites such as *BeppoSAX*. Simultaneous data are considered in order to frame a particular state of the source into the long look performed by BATSE. We have performed this study in the cases of 3C273 and MKN501.

7.2 *BeppoSAX* results

With BATSE only an average flux has been estimated over the observing period, while the good sensitivity of *BeppoSAX* -PDS has been exploited in order to study the spectral characteristics of all Piccinotti AGN observed and available in the public archive as of December 2000. A good fraction of sample sources (29) has been observed by *BeppoSAX*, and for several of them more than one observation is available. All sources, except for PKS0548-322, were detected at $\geq 3\sigma$ confidence level and, therefore, the 20-200 keV flux is reported for each individual observation while for PKS0548-322 a 2σ upper limit on the flux has been listed.

If with BATSE it was possible to study only the long term variability (timescale of months/years) of the brightest sources, with the PDS observations, possible high-energy variability on a shorter timescale (hours/day) has been investigated. Furthermore, the comparison of the variability results between *BeppoSAX* and BATSE has given us the opportunity to evaluate the behavior of the brightest sources of the Piccinotti sample on long timescales. As for the BATSE data the χ^2 test has been used on all the PDS observations assuming a bin of 5700 seconds i.e. the time of a *BeppoSAX* orbit. 11 sources were found to be variable with a probability $\geq 90\%$ in the 20-200 keV band over this timescale. Only for three of these sources, the well known variable sources NGC4151, 3C273 and MKN501, was variability on different timescales discussed, and when possible the comparison with soft X-ray (LECS-MECS) data has been performed. Although not highly detailed, the variability study performed in this thesis provides the interesting result that variation of the high energy emission is probably ubiquitous in Seyfert galaxies being present on both short and long timescales.

The PDS spectral analysis of the Piccinotti sample has been performed for all the *BeppoSAX* observations with detections $> 5\sigma$ for Seyfert galaxies and whenever possible for blazars. A simple power law model was used to fit the data in the 20–200 keV energy band finding that the photon indices are generally steep $\langle \Gamma \rangle = 1.98 \pm 0.01$ with no difference between Seyfert 1 and Seyfert 2 galaxies. To investigate more complex spectral shapes, a deeper analysis has been performed for all the Seyfert galaxies which have

a χ^2 value greater than 21 in the power law fit (this corresponds to a 90% probability that the model used is not a good fit to the data). For this sub-sample of 10 objects three more complex models have been used to fit the high energy data:

- Model 1: HIGHECUT model in the XSPEC package which corresponds to a power law with an high energy cut-off (i.e. with no reflection);
- Model 2: PEXRAV model, i.e. an exponentially cut-off power law spectrum reflected from neutral material where the high energy cut-off has been frozen to a value of 10000 keV (i.e. only the Compton reflection component has been assumed);
- Model 3: PEXRAV model with both the reflection and the high energy cut-off included but with the photon index fixed to 1.9.

NGC4151 and IC4329A have been studied separately since they are the brightest Seyferts of the sample and allow a more detailed analysis. In these cases thanks to the good statistics available, the pexrav model with the photon index free to vary has also been performed. When only model 1 is considered the high energy cut-off is found to be well constrained for all the sources of the sample and it is required by the data at 91-99% probability: the estimated values range between 24^{+30}_{-9} keV to 142^{+8}_{-27} keV. However, the photon indices are found to be unusually flat and in a few cases they have unacceptably low values, indicating that this model is not correct. For this reason, in model 2 the high energy cut-off was fixed to 10000 keV in order to analyze the relevance of the Compton reflection component. This component is required by the data at 96-99% confidence level, but the spectra are steeper ($\Gamma > 2$) than usually found in AGN, the reflection component is large ($R > 1.5$) and cannot be well constrained in a large fraction of the observations. Considering the results of model 1 and model 2 as well as the high probability that these components are separately required by the data, we argued that both are probably present in the 20-200 keV spectra and exploited model 3 to test this hypothesis. This model provides an improvement with respect to the simple power law model which is significant at the 99.99% confidence level, the reflection component ranges from 0.33 to 2.3, while the cut-off energy is found to lie in the interval 78-255 keV. In NGC4151 the cut-off values range between 52^{+26}_{-12} and 144^{+56}_{-34} keV while the reflection is not required by the data in the 1999 observation and has its maximum value of $R = 0.27^{+0.32}_{-0.22}$ in July 1996 data. In IC4329A we obtained an average high energy cut-off of 155^{+15}_{-10} keV and an average value of reflection of $0.6^{+0.4}_{-0.35}$.

It is important to note that our PDS results are in general agreement with *BeppoSAX* broad band findings. An important result of this thesis is the new identification of the X-ray

source previously identified with the Seyfert 1 H0917-074 (Piccinotti et al. 1982). From the quick look inspection of the *BeppoSAX* broad band spectrum of H0917-074 there was the indication of an apparent mismatch between the MECS and PDS data. The simplest explanation for this phenomenon was the presence of a contaminating serendipitous source in the PDS field of view. The region of the sky around H0917-074 was searched for possible high energy sources, and only one candidate was found in the Seyfert 2 galaxy MCG-01-24-12, the position of which lies also within the original HEAO1-A2 error box. MCG-01-24-12 was then pointed at by *BeppoSAX* NFI. The broad-band spectrum of the source is analyzed in detail in Malizia et al. (in preparation), here only the PDS data have been briefly presented. The PDS spectrum is consistent with an absorbed power law of photon index $\Gamma=2.23^{+0.57}_{-0.58}$ and a column density $N_H < 7 \times 10^{24} \text{ cm}^{-2}$.

Finally, all five blazars objects (PKS0548-322, 2A1219+305, 3C273, MKN501 and PKS2155-304) belonging to the Piccinotti sample have been observed by *BeppoSAX*. A simple power law describes well the data in all cases although the constraints on the parameters are not always good; the power-law slopes found are, in any case, consistent with the values obtained using the *BeppoSAX* broad band data. In all BL Lac objects the photon indices found are steep ($\Gamma > 2$) with the exception of 3C273 which is characterized by a flat photon index of 1.6-1.7. In the case of 3C273 and MKN501, a more detailed analysis was possible and a comparison with other high energy data has also been performed. A deep spectral analysis has been performed on the average spectrum of 3C273. A photon index of $1.7^{+0.03}_{-0.03}$ and an upper limit on the Compton reflection ($R < 0.1$) have been found, while the high energy cut-off is ruled out. In the case of MKN501, *BeppoSAX* observations confirm that the source significantly hardened when it brightened, in line with the expectations of the SSC model.

7.3 *BeppoSAX* average spectra

The *BeppoSAX* MECS data together with the PDS data, have been used in this thesis to study the average 3-200 keV spectra of Seyfert 1s and Seyfert 2s in order to investigate their medium spectral characteristics and the possible differences between the two classes. For this study the MECS data have also been considered to better constrain the spectral parameters taking a lower threshold of 3 keV to avoid the presence of the soft excess. The Seyfert 2 sample has been widened to include all Seyfert 2s having $N_H \leq 10^{23} \text{ atoms cm}^{-2}$ and which were observed by *BeppoSAX* as at Dec 2000, while NGC4151 and IC4329A were not added to the average Seyfert 1 spectrum since they are so bright that can strongly dominate over the other sources. A simple power law fit to the data

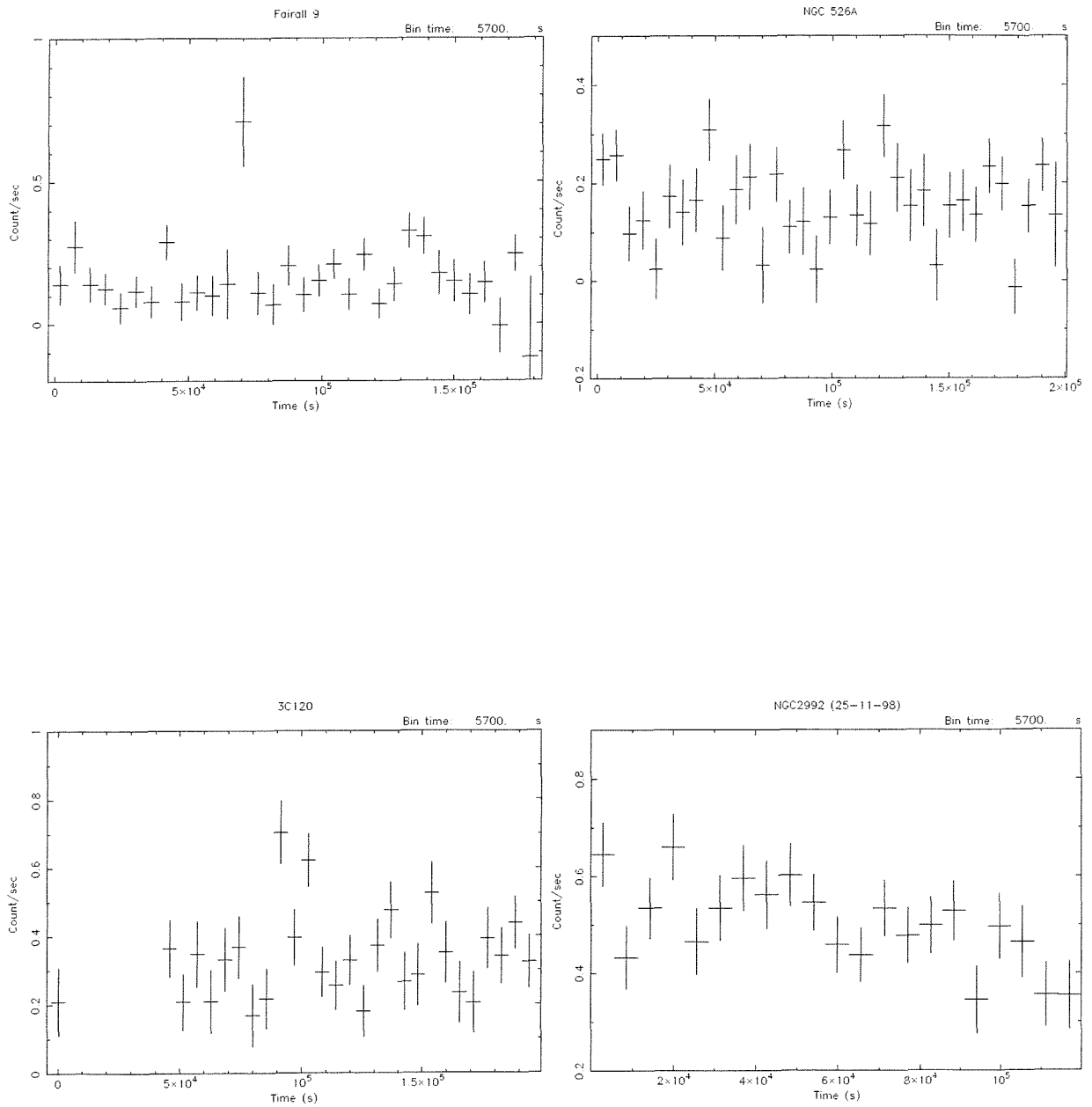
provides a photon index significantly different for the two classes: $1.87^{+0.01}_{-0.02}$ in Seyfert 1s and $1.77^{+0.02}_{-0.02}$ in Seyfert 2s. A significant improvement of the fits is given by the addition of the iron $K\alpha$ line at 6.4 keV which is required by both spectra with a probability of 99%. The iron line values of both classes of objects are similar ($EW \sim 150$ eV in Seyfert 1s and $EW \sim 190$ eV in Seyfert 2s) in agreement with the expected values, i.e. with reflection in cold material. It is worth noting that in both cases the iron $K\alpha$ line is slightly broad, this may be due to a redshift effect as sources with different z are summed together, but could also be intrinsic. These simple fits significantly improve (probability $>99\%$) with the addition of a high energy cut-off, located at $E_c=164^{+61}_{-24}$ keV in the type 1 objects and at $E_c=114^{+31}_{-80}$ keV in type 2. These values are compatible within errors with the results of OSSE average spectra (Zdziarski et al. 2001). In both spectra the presence of the Compton reflection hump is evident and the addition of this component improves the fit again with a probability $>99\%$. Although the amount of reflection is consistent between the two types of objects, the primary continuum is still significantly different: the average Seyfert 2 spectrum is substantially harder than that of Seyfert 1 and the cut-off is at lower energies. This difference between the two classes is problematic as it is not easily reconciled with the Unified Theory. In order to overcome this problem we have imposed a photon index of 1.92 (i.e. equal to that obtained for the Seyfert 1), to the Seyfert 2 and measured the contours of the reflection strength against the cut-off energy for this case. The cut-off energy turns out to be similar to that measured in type 1 objects but the R value is now much higher (≥ 2.6). The Seyfert 2 to Seyfert 1 ratio as a function of energy can be used as a model independent way to verify the above two hypothesis (different spectral shape or different reflection component). More reflection in Seyfert 2 would produce a bump in the 10-50 keV band while a flatter power law with a lower cut-off energy would produce a deviation from 1 at lower and higher energies. The Seyfert 2 to Seyfert 1 ratio clearly excludes the presence of stronger reflection in type 2 objects. Having excluded reflection as the possible cause of a flatter spectrum, the only other remaining way to steepen the Seyfert 2 spectrum and so save the fundamental principal of the unified theory, is via a more complex absorption model than the one assumed here. We have therefore introduced in the Seyfert 2 fit an extra absorber that partially covers the source. The fit improves significantly at the 99% level and provides average spectral parameters for the intrinsic continuum very similar to those measured in Seyfert 1s.

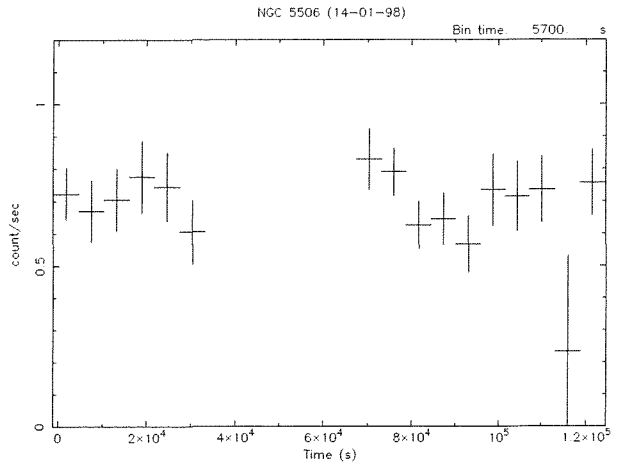
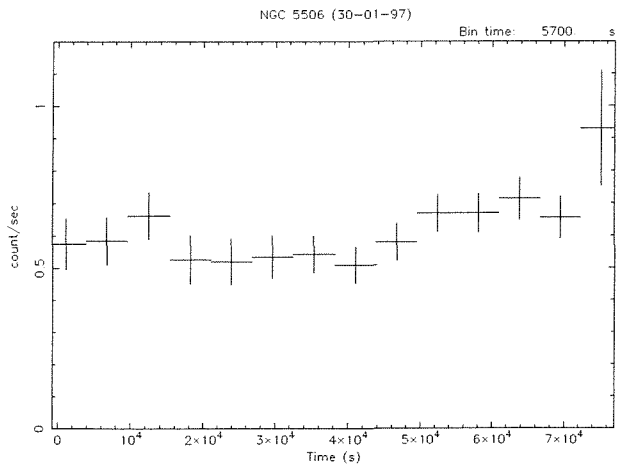
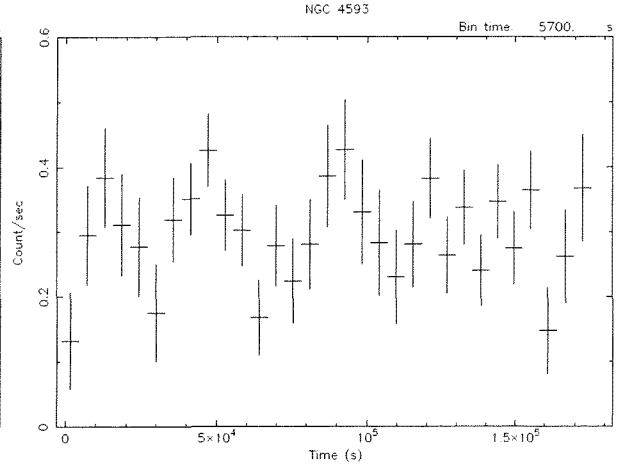
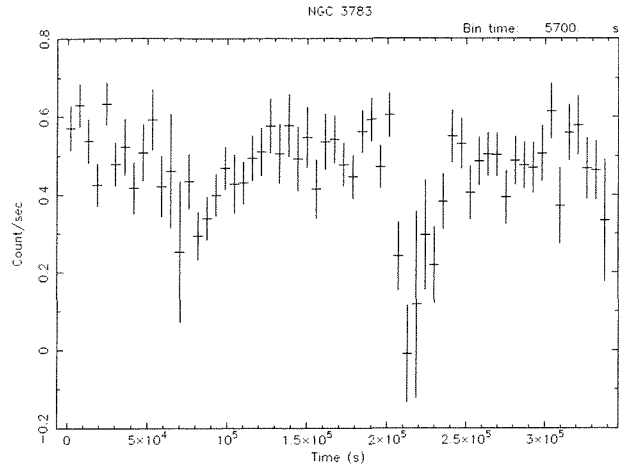
The findings that the X-ray absorber is complex is not surprising: whether it is made of two column densities (one with $N_H \sim 3 \times 10^{22}$ totally covering the source and one with $N_H \sim 4 \times 10^{23}$ covering only half of the source) or more, whether the absorber/s

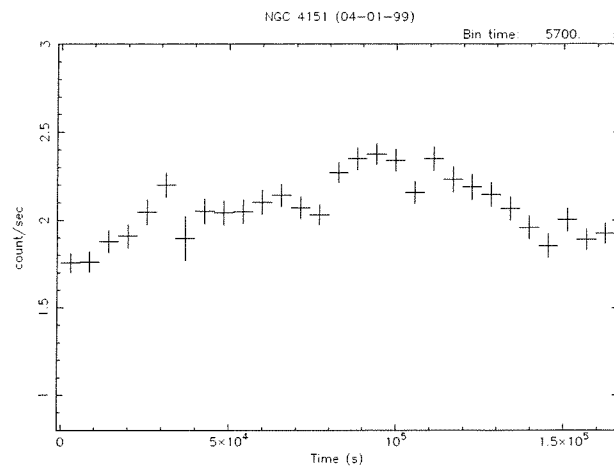
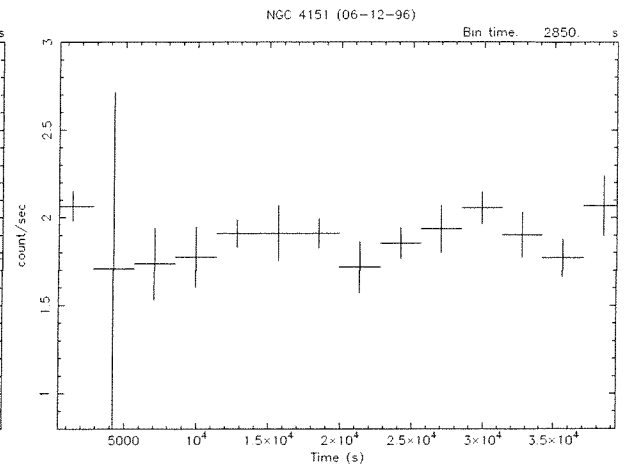
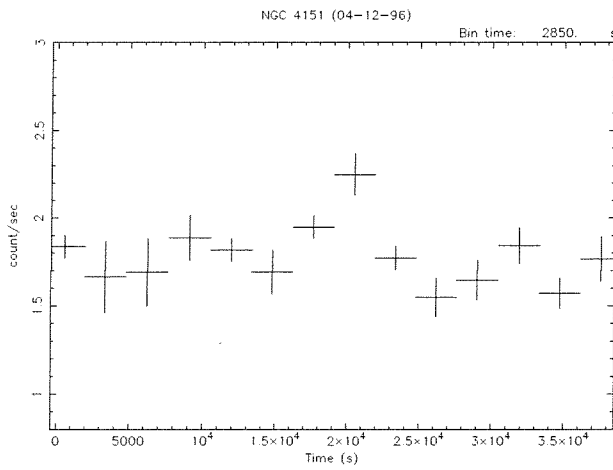
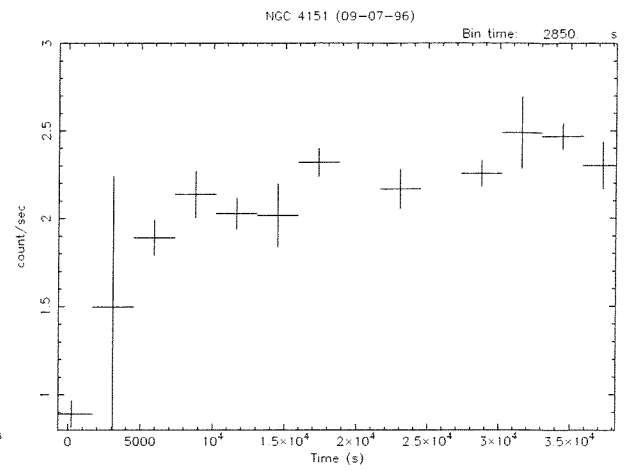
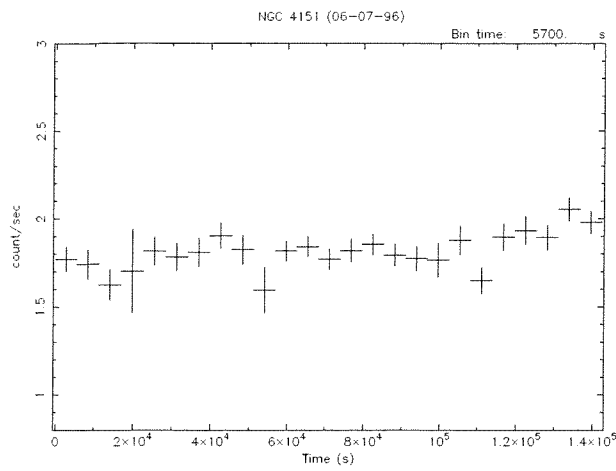
is/are ionized or not and whether the covering fraction are exactly as measured here or different is beyond the scope of the present thesis. Here, it is important to stress that the average spectra of Seyfert 1s and 2s are different unless heavier and more complex absorption is present in type 2 objects with respect to type 1. What is clear is that multiple absorption is probably ubiquitous in Seyfert 2 galaxies otherwise the flattening of their average spectrum with respect to Seyfert 1 would not be so clear cut. Our result argues strongly for a very similar production mechanism not only in both types of Seyfert galaxies but also in each individual object.

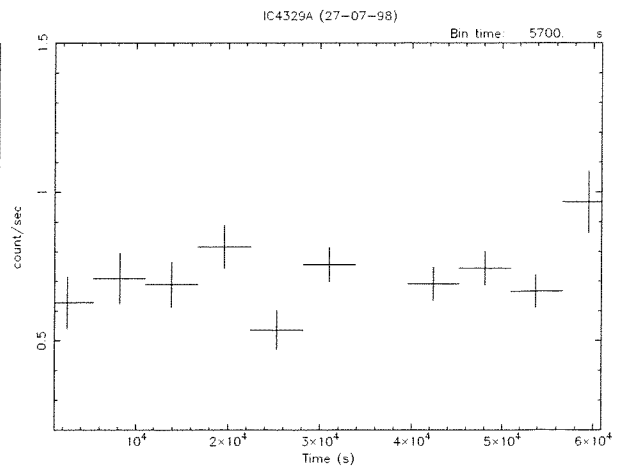
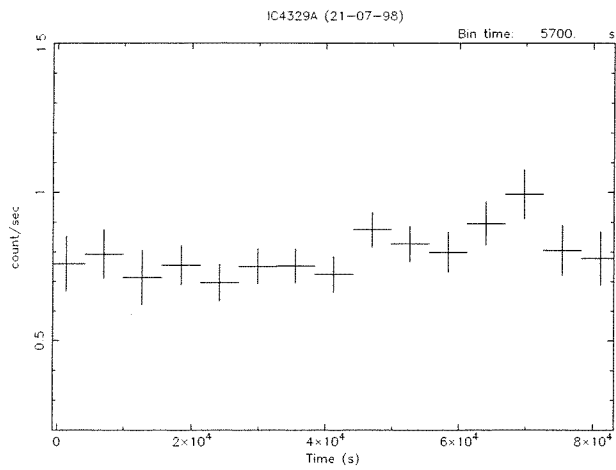
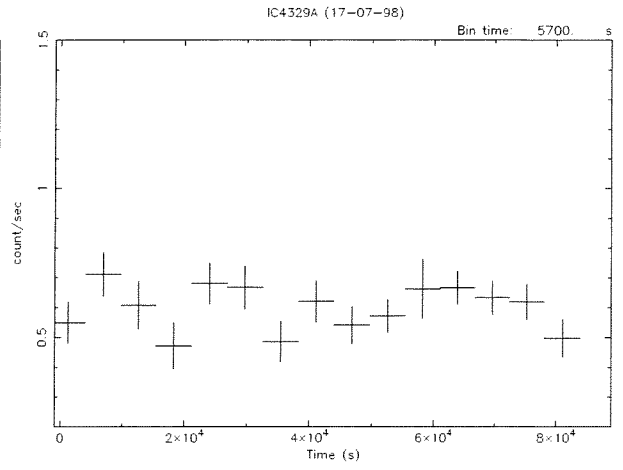
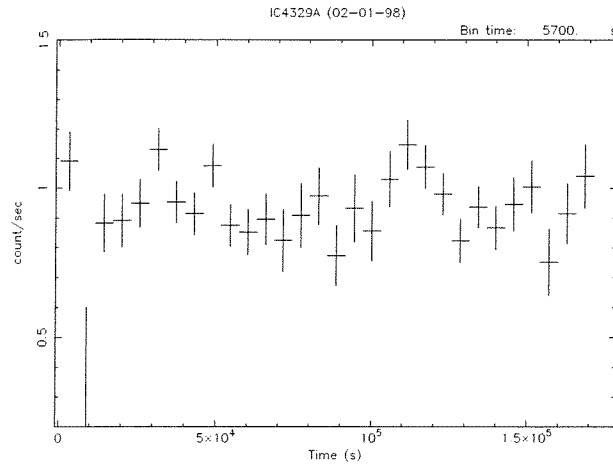
Appendix A

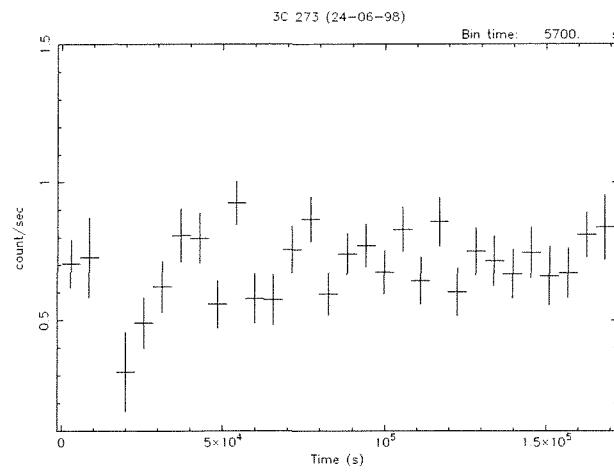
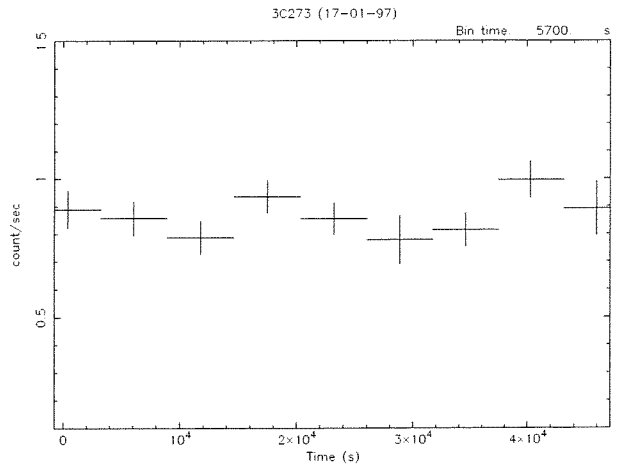
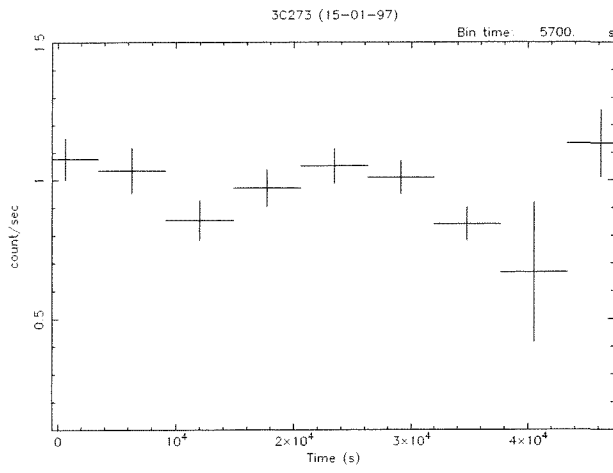
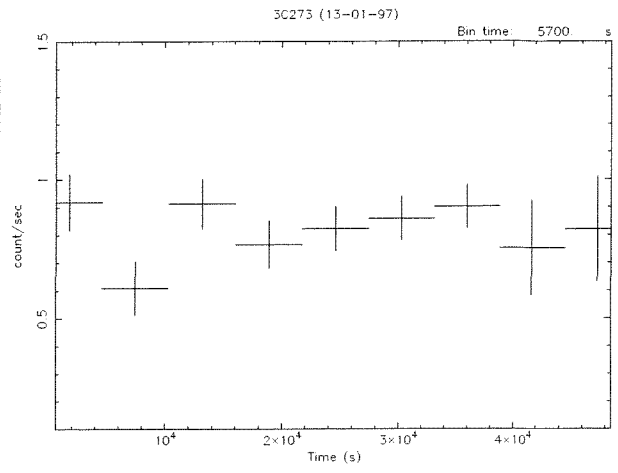
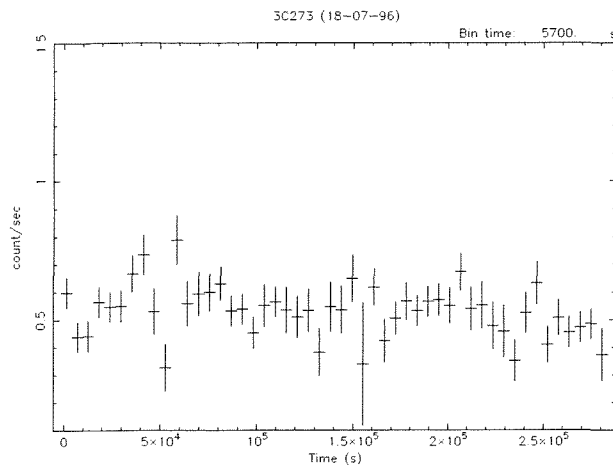
PDS Light Curves

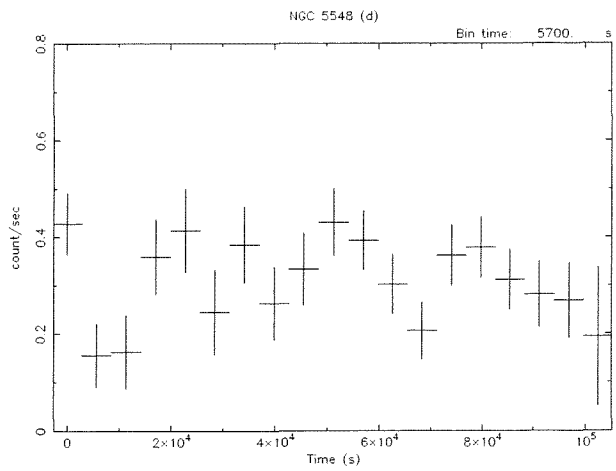
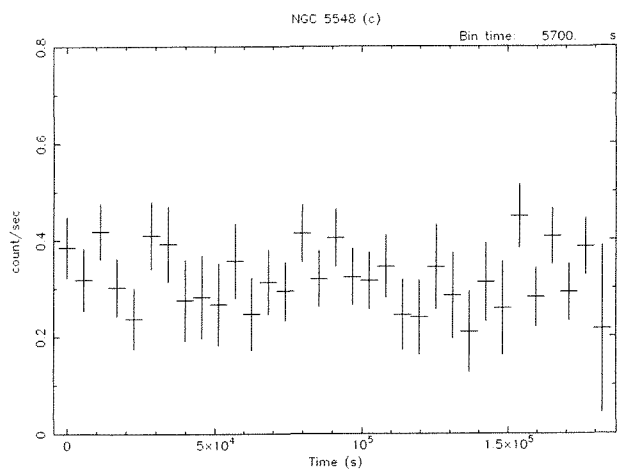
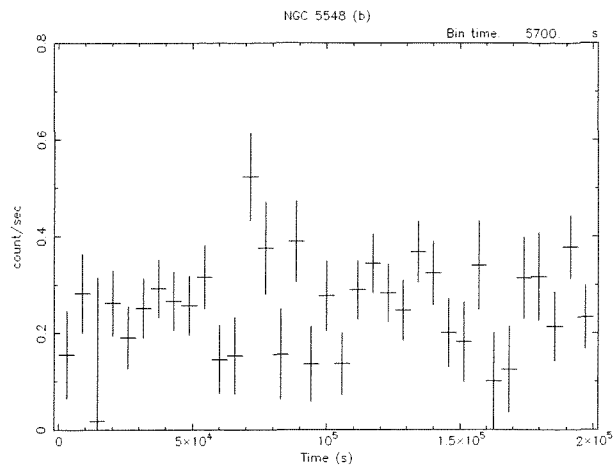
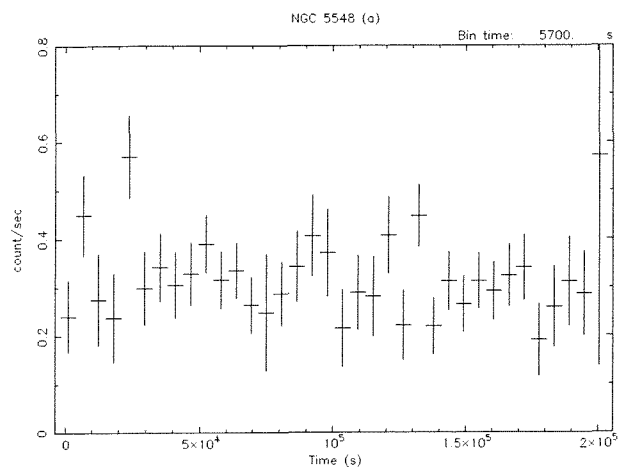


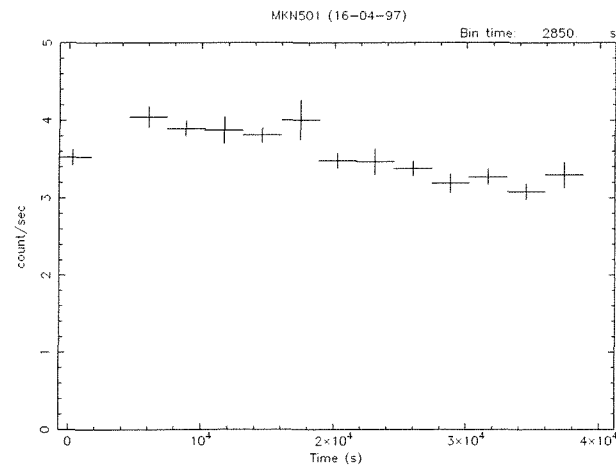
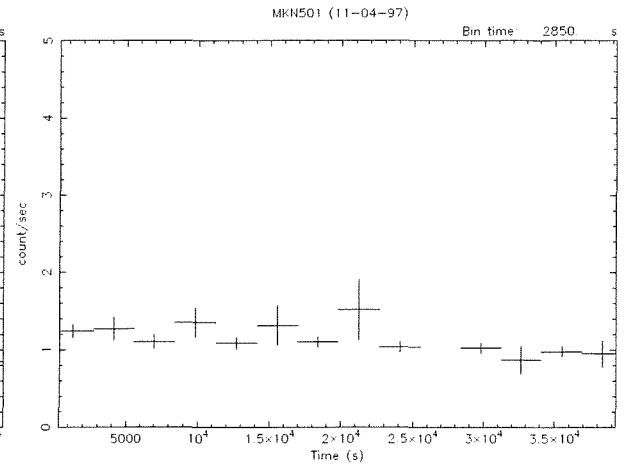
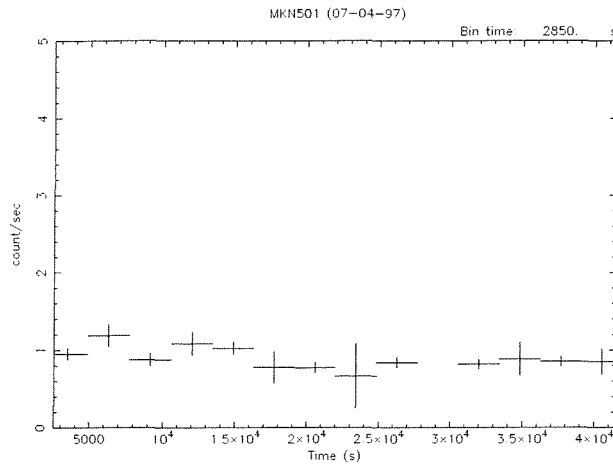


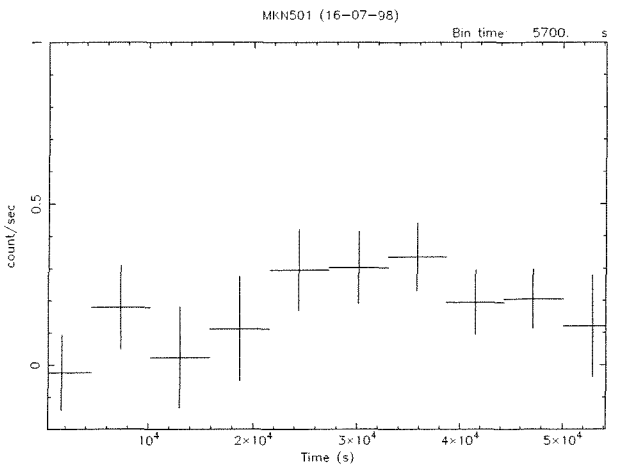
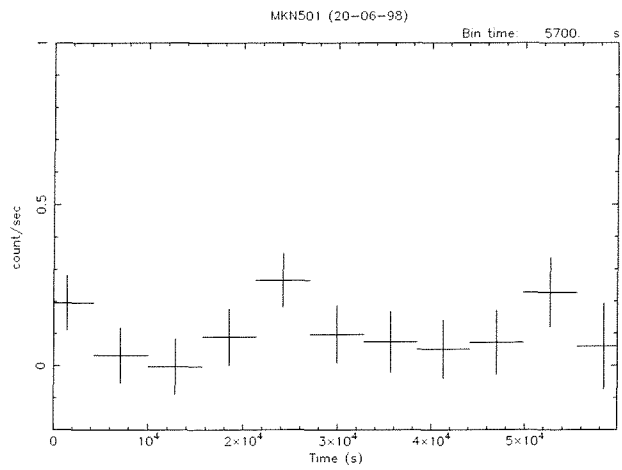
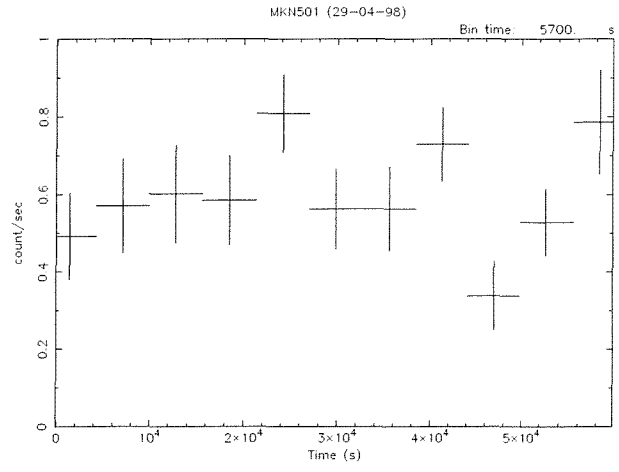
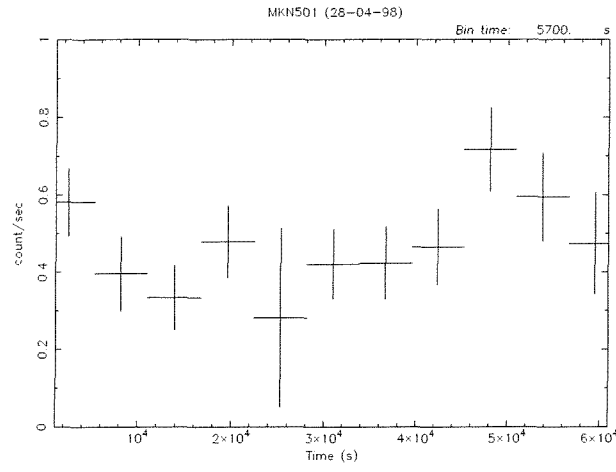


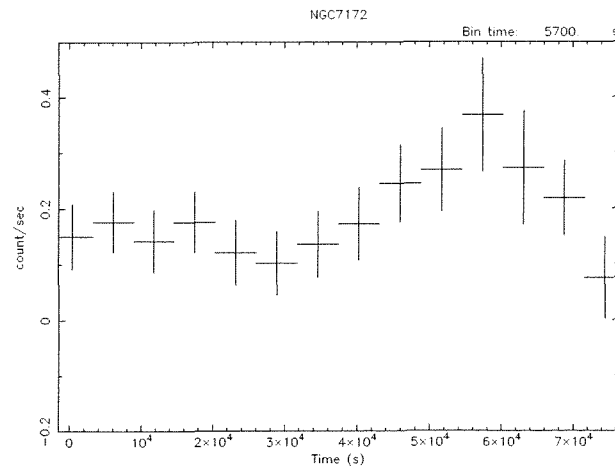
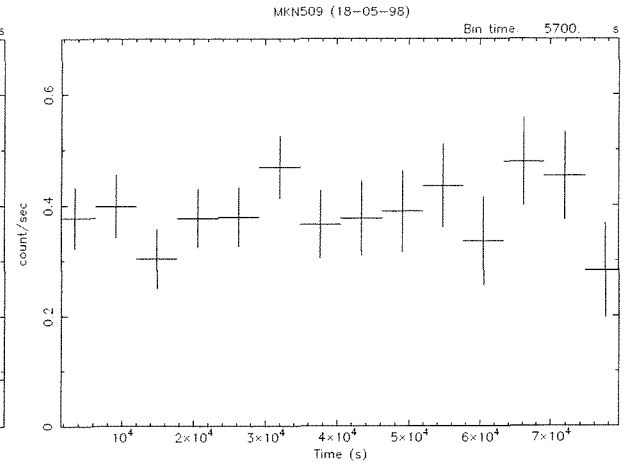
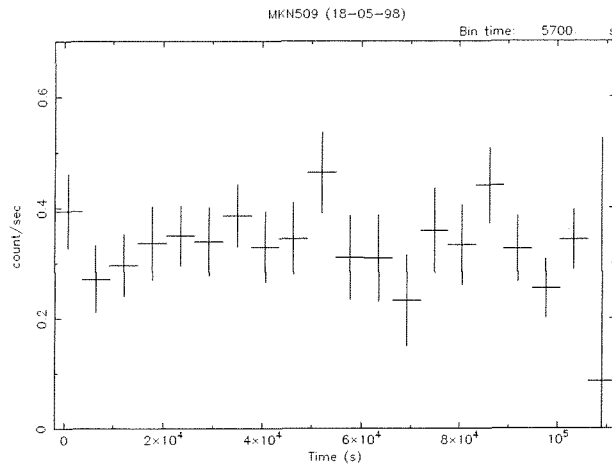
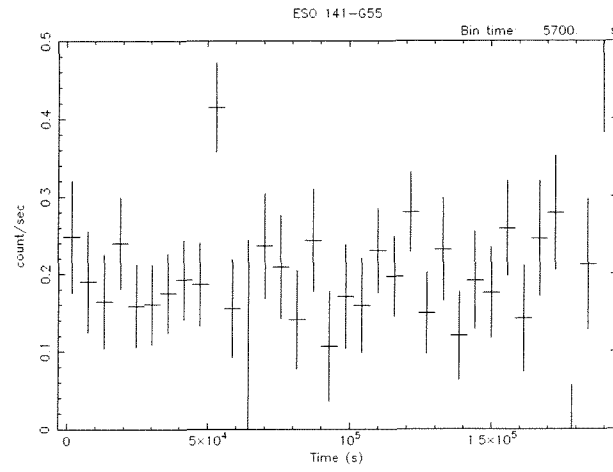


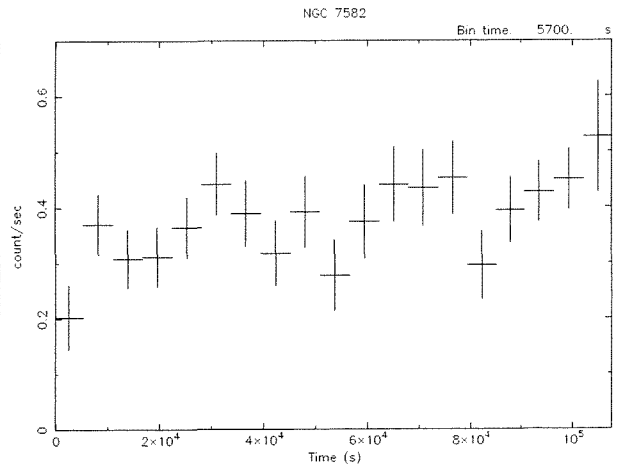
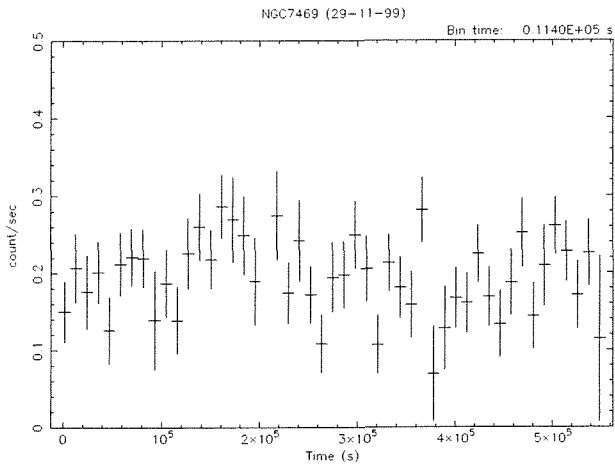
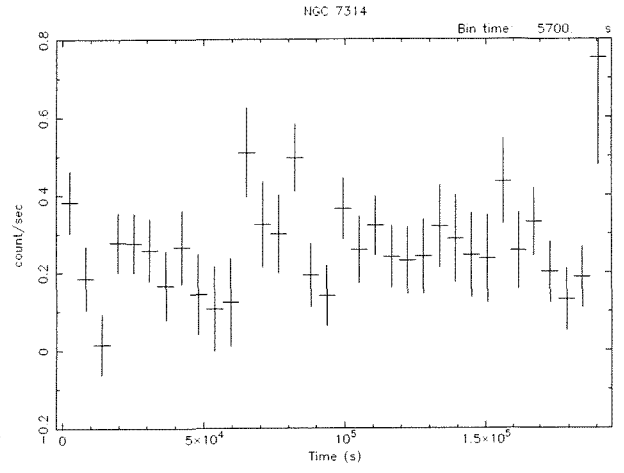
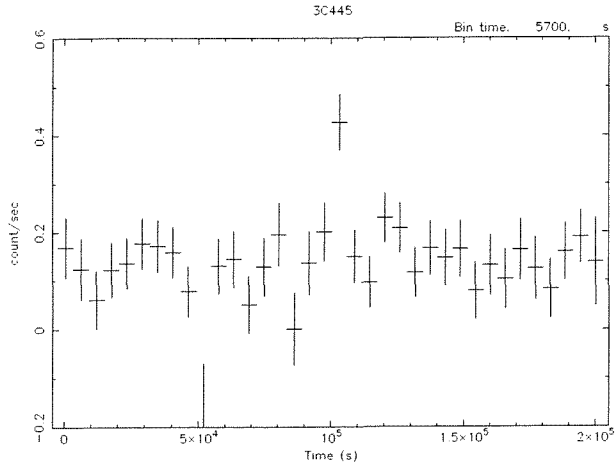






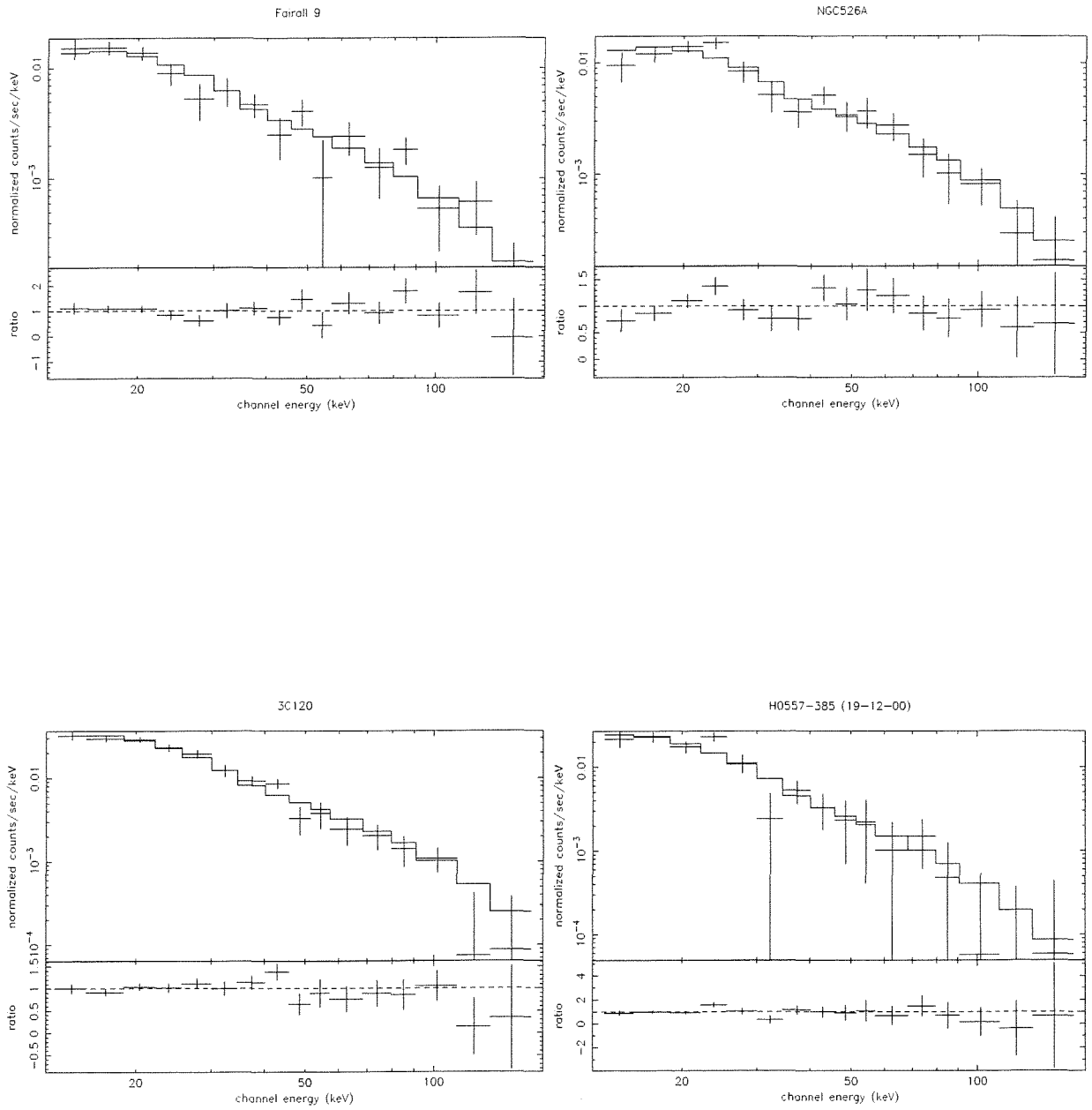


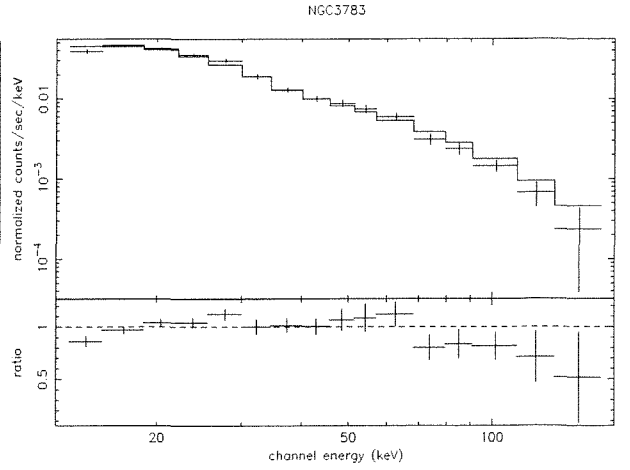
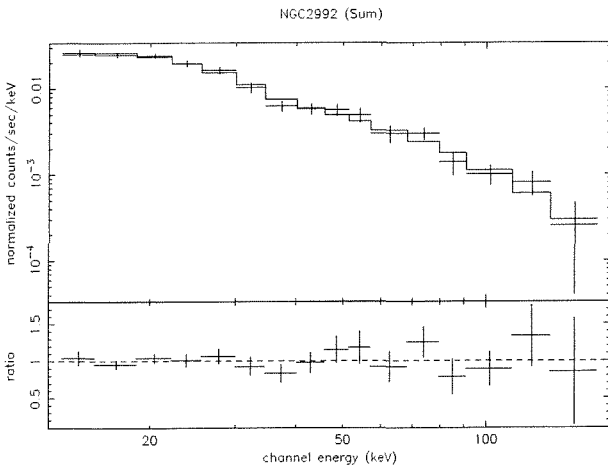
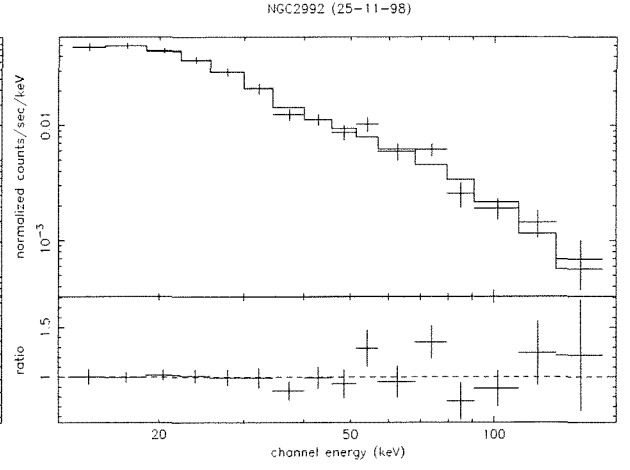
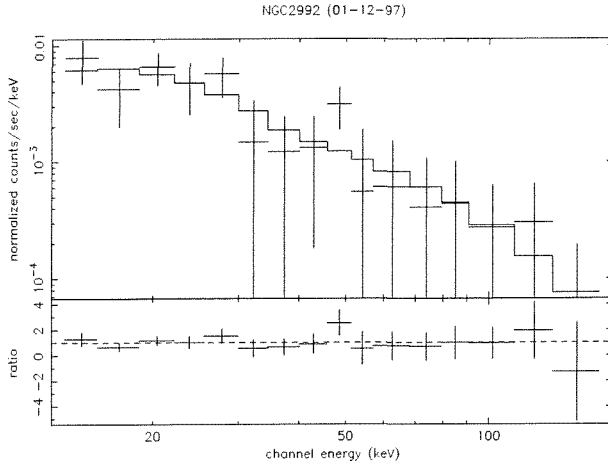
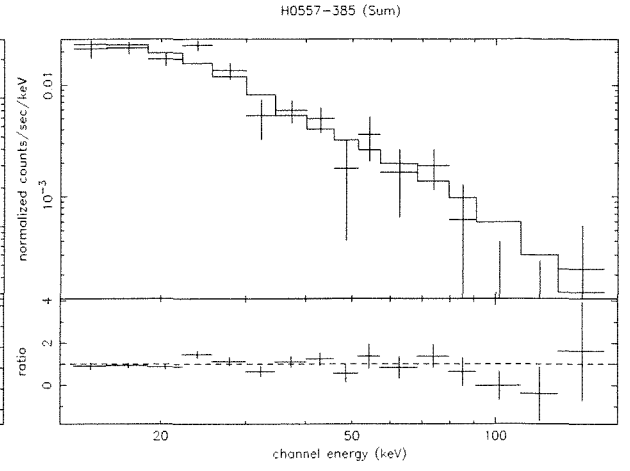
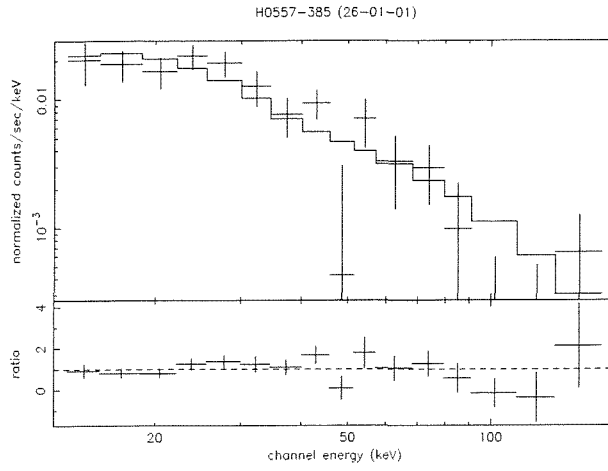


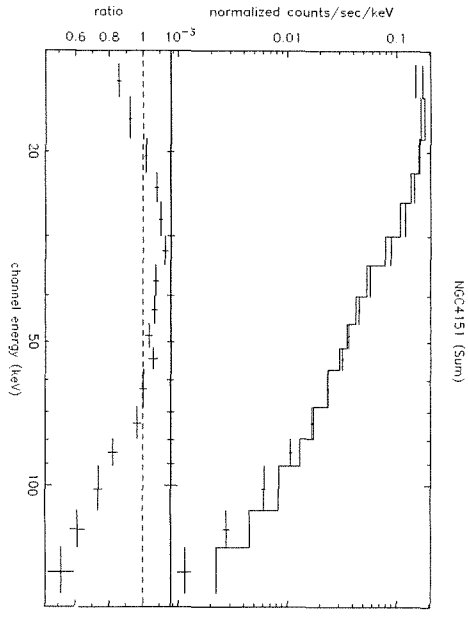
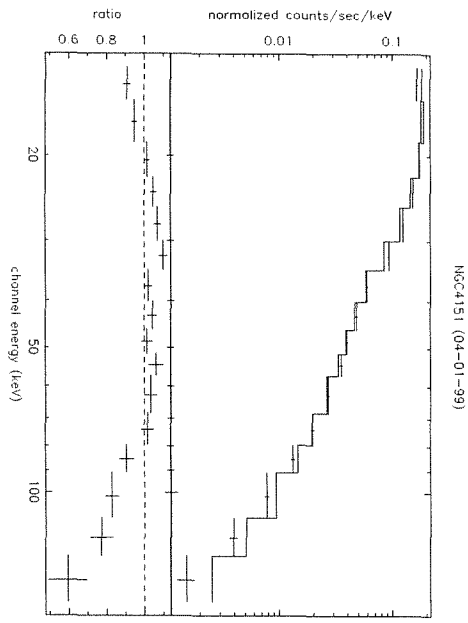
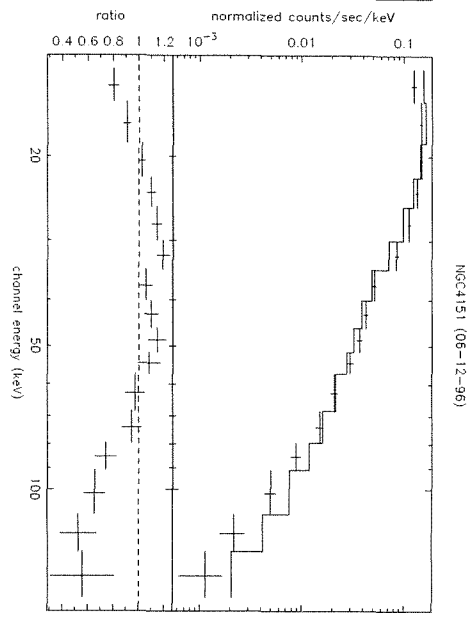
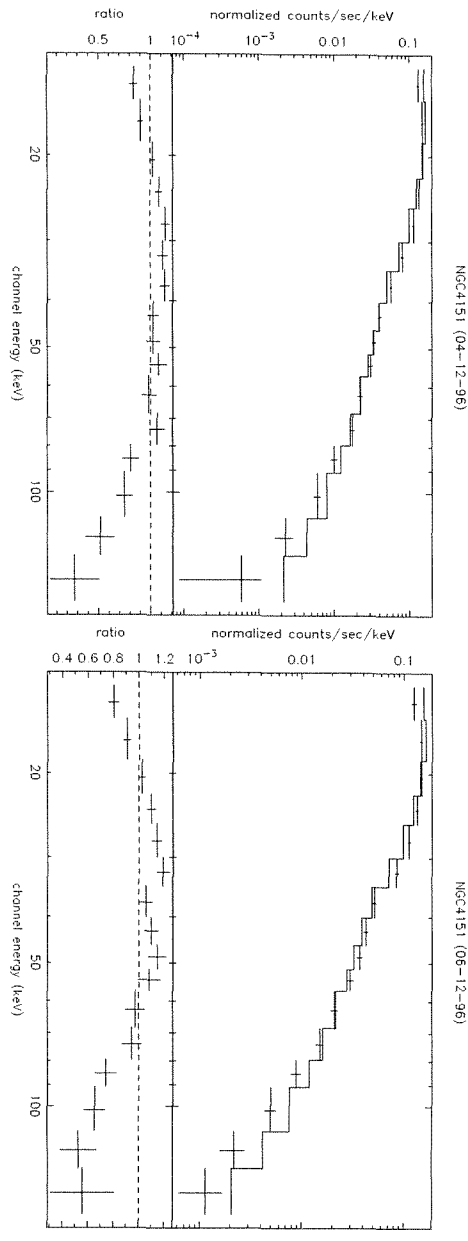
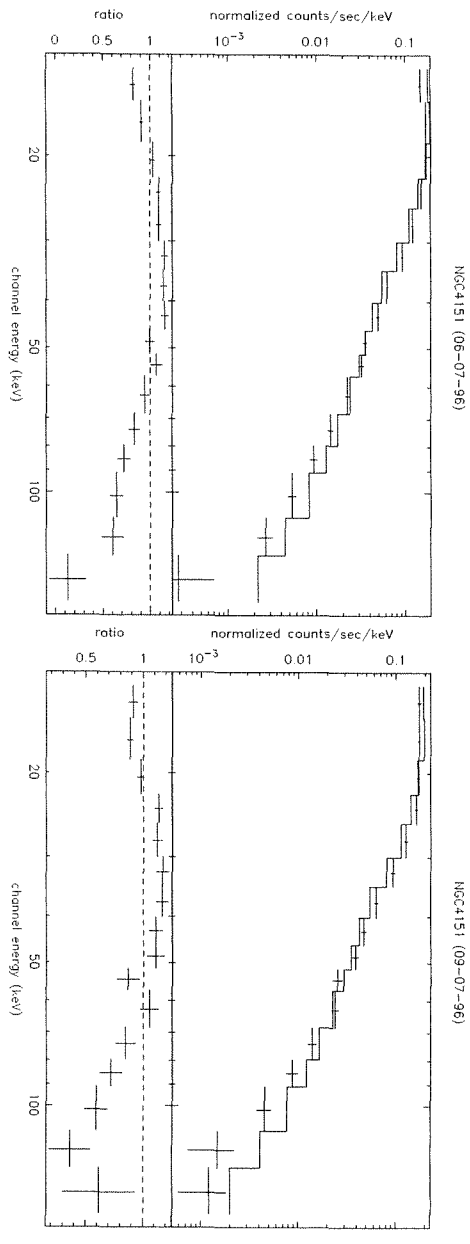


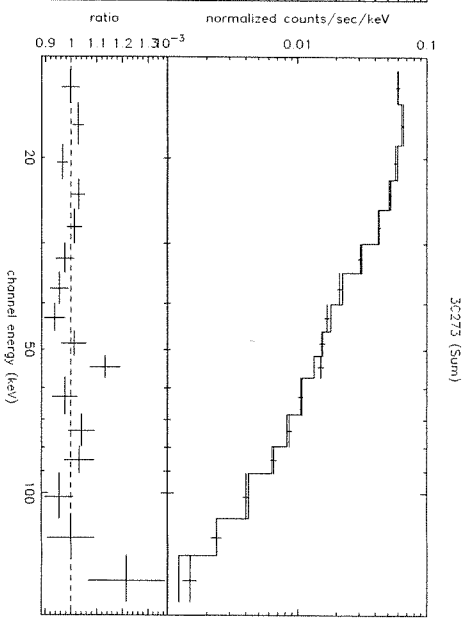
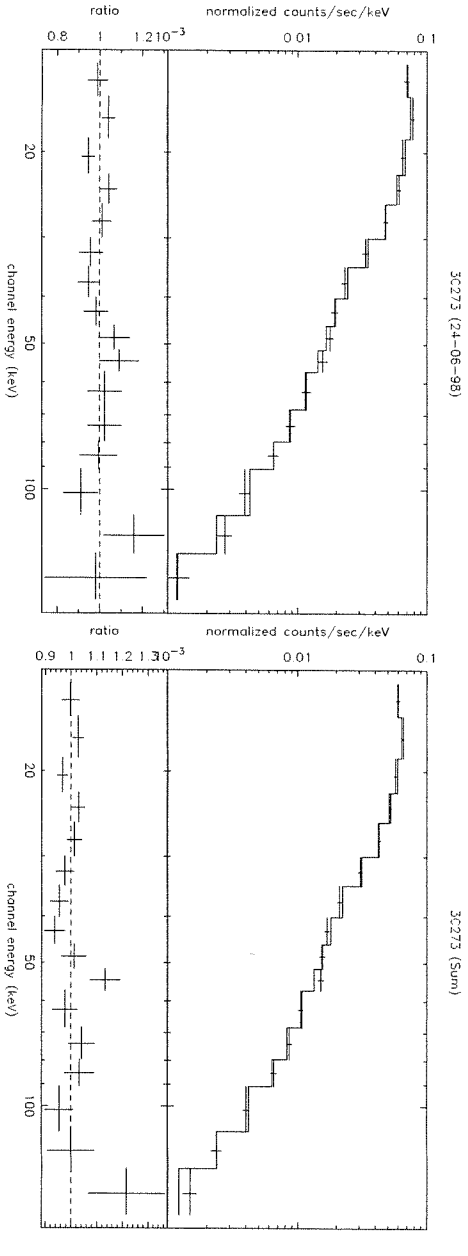
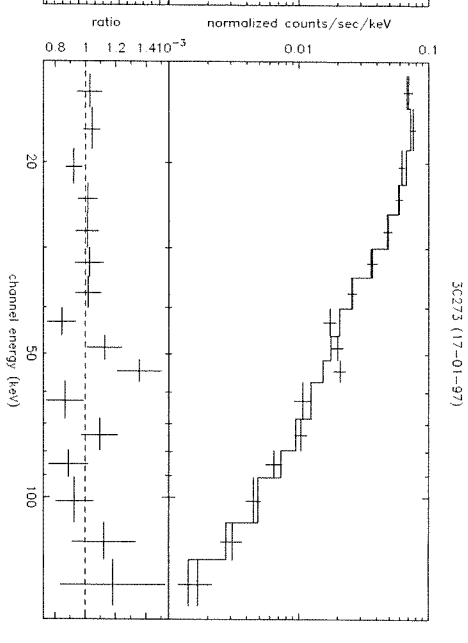
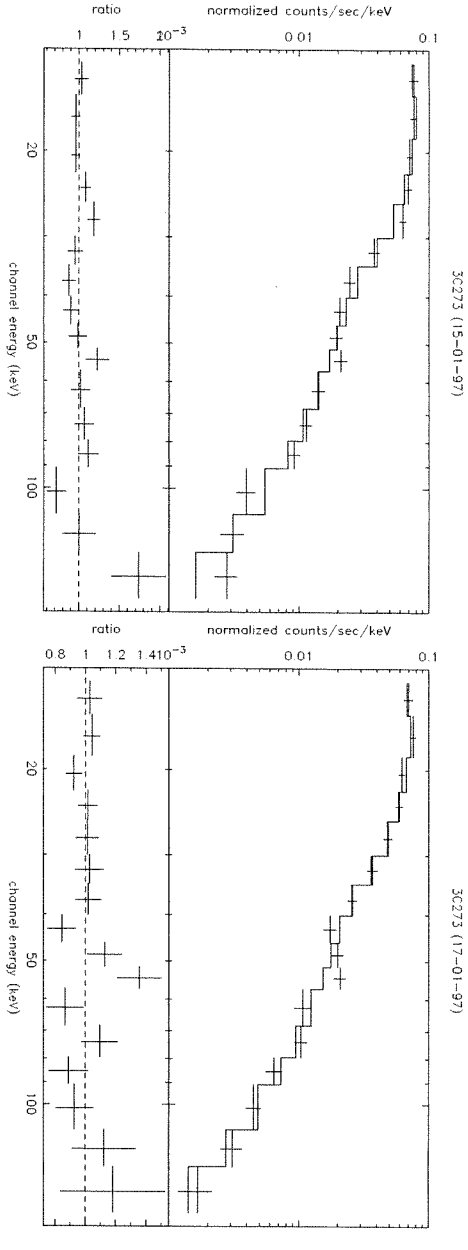
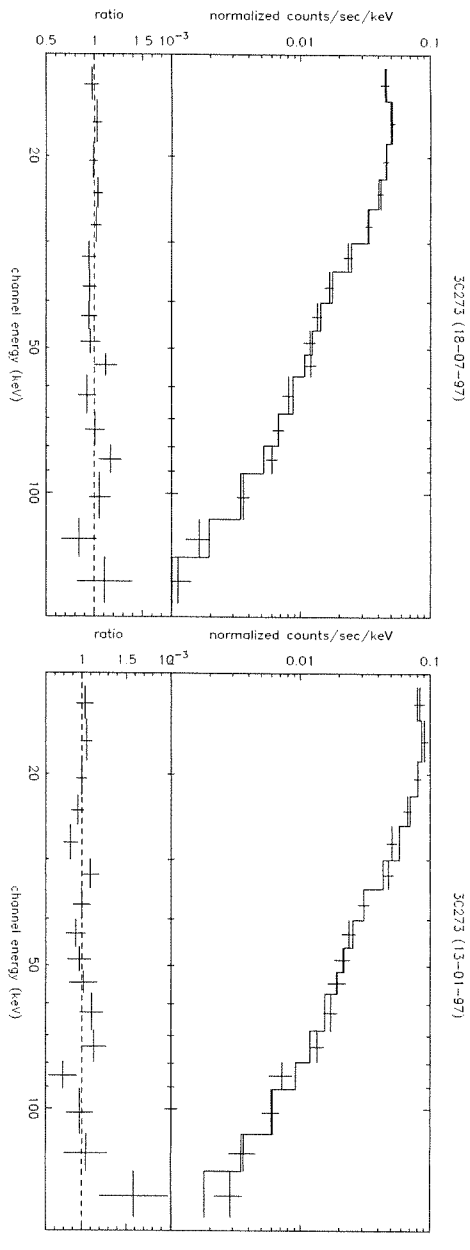
Appendix B

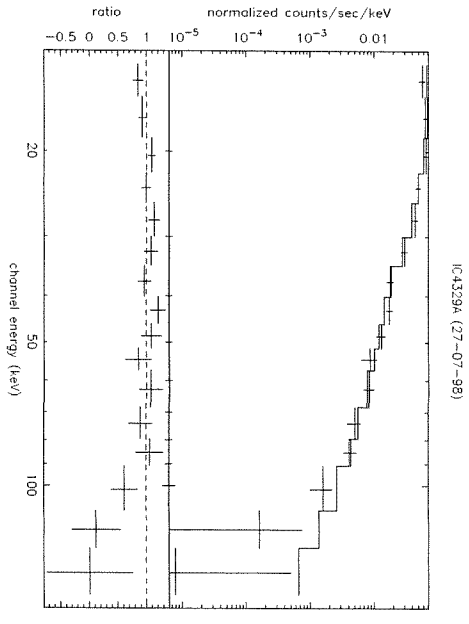
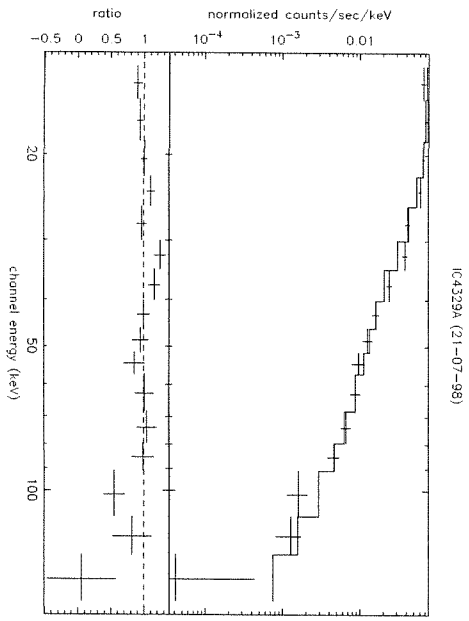
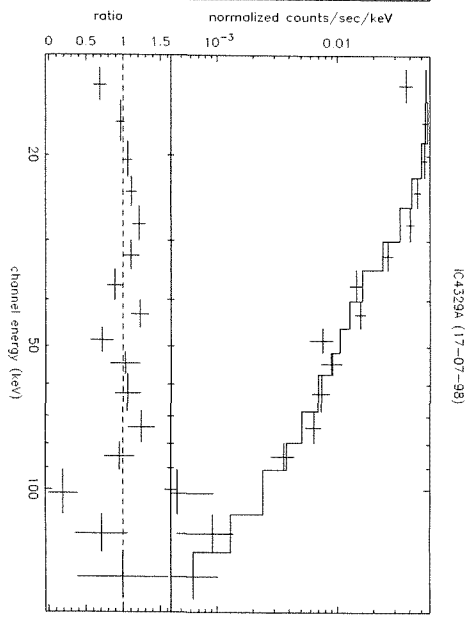
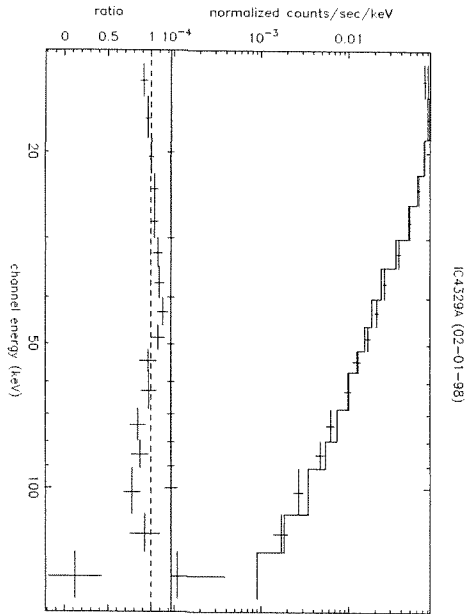
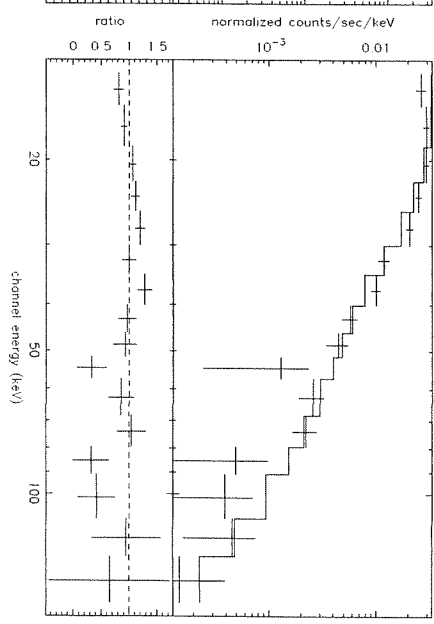
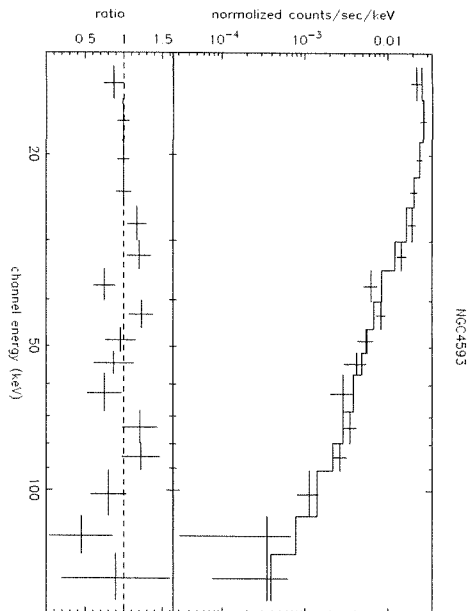
PDS Spectra

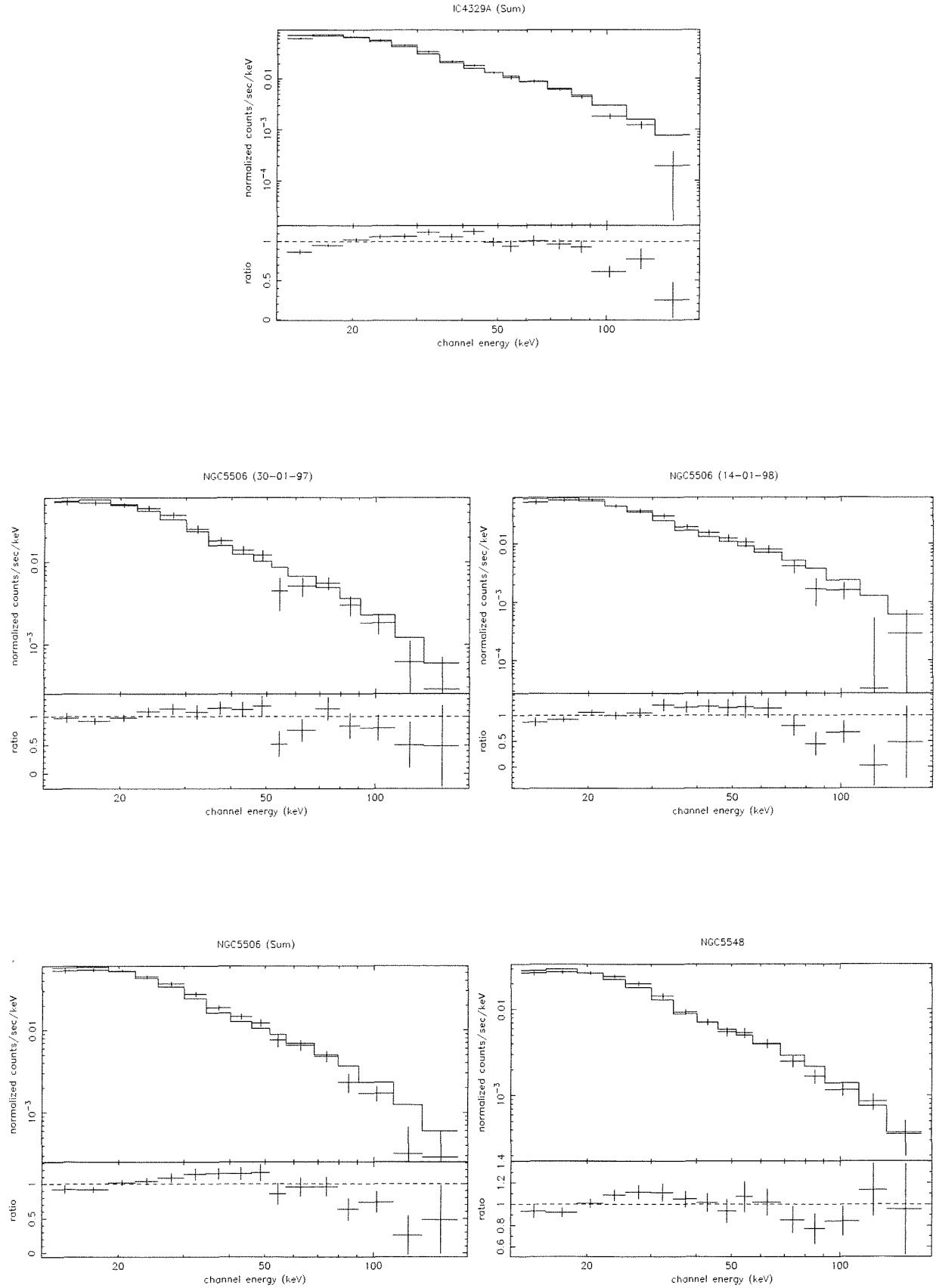


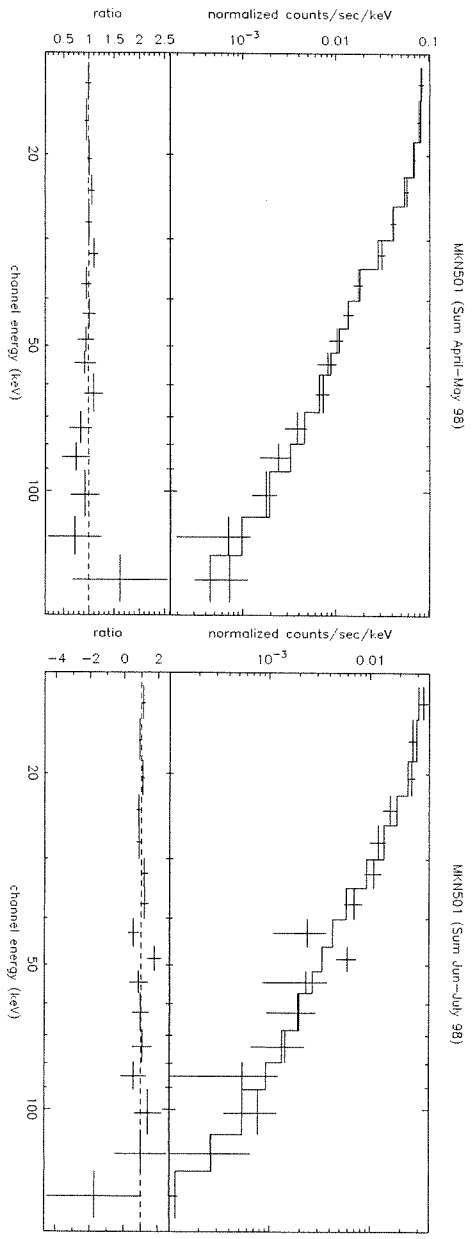
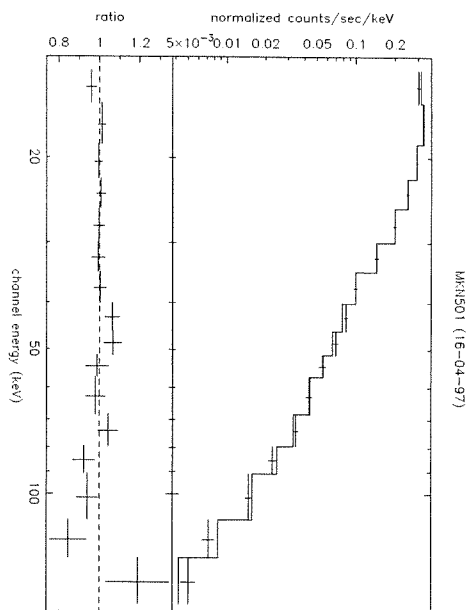
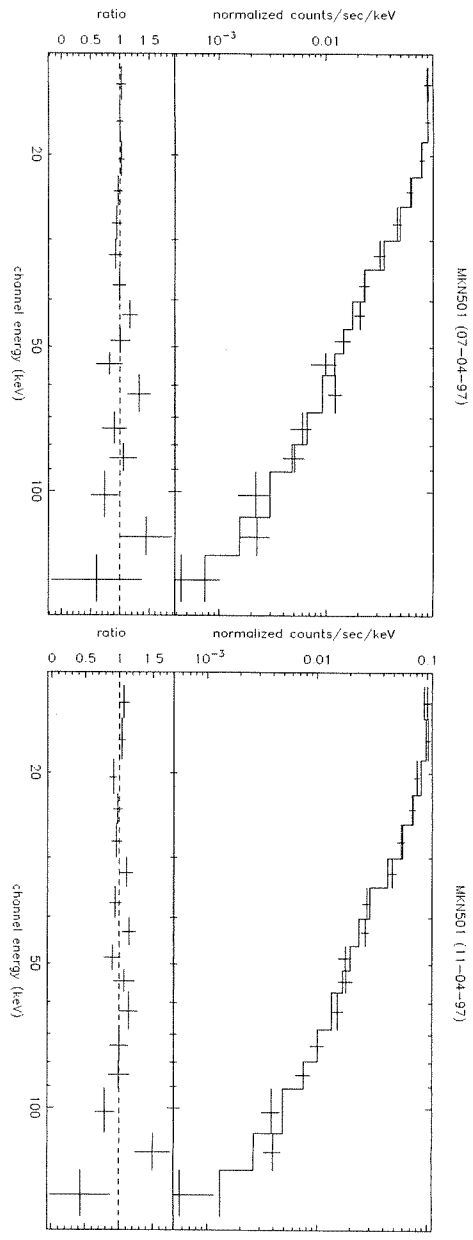


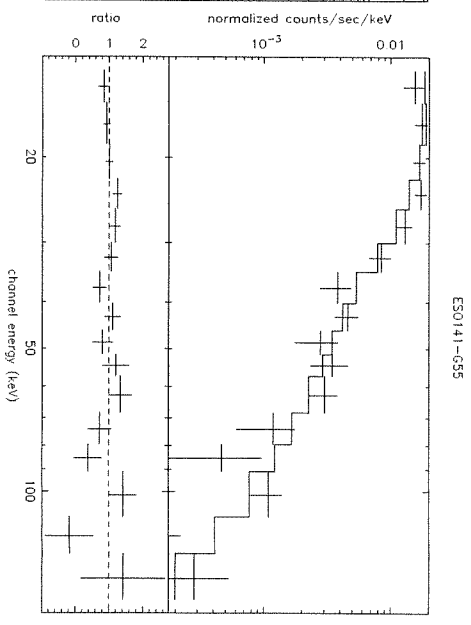
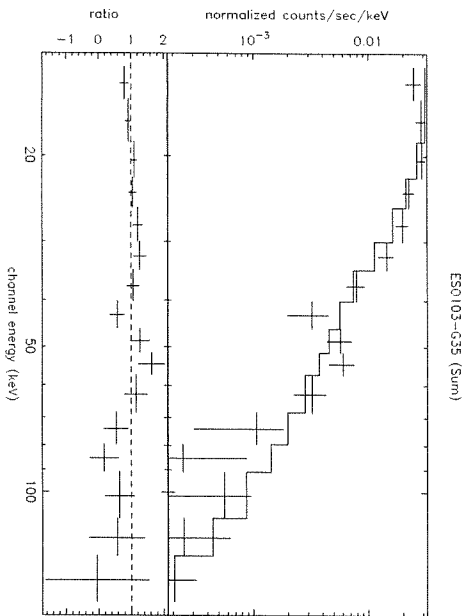
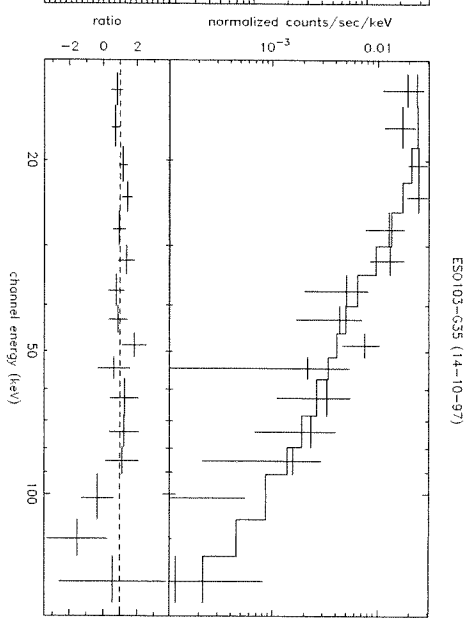
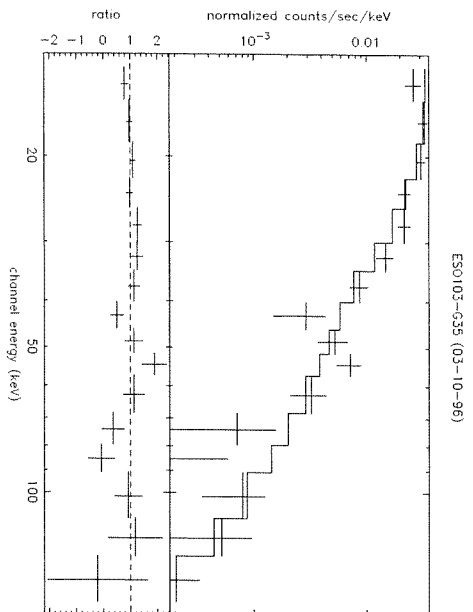
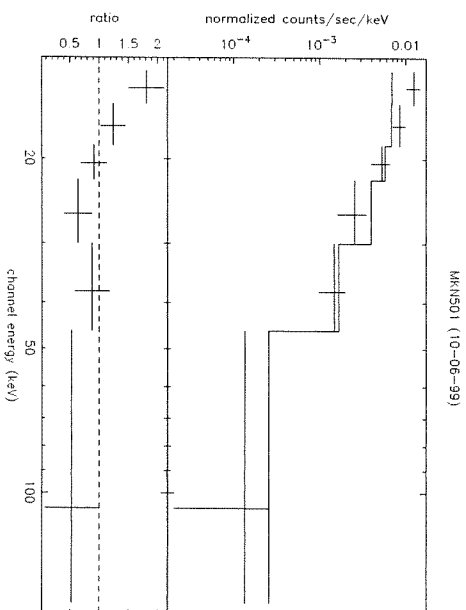


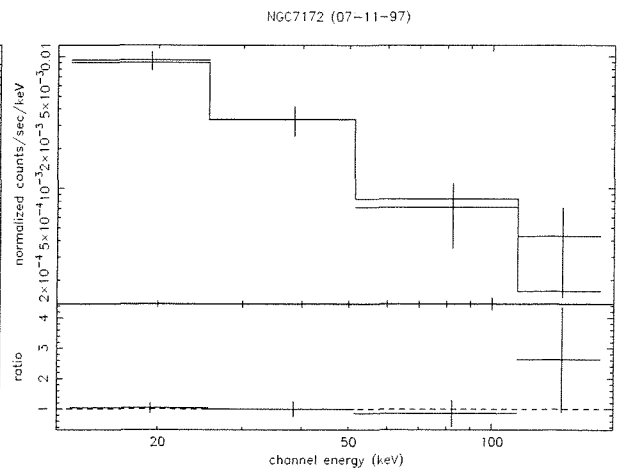
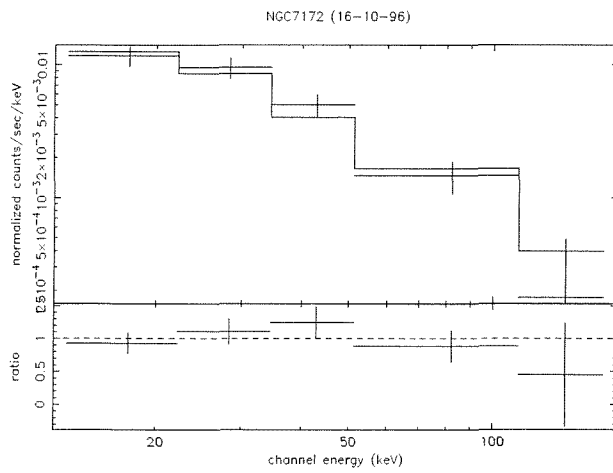
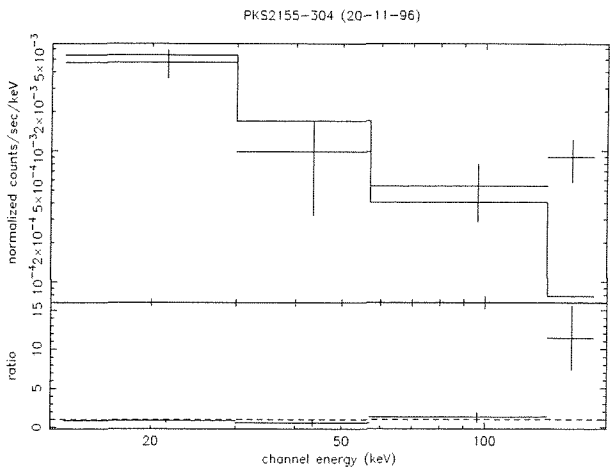
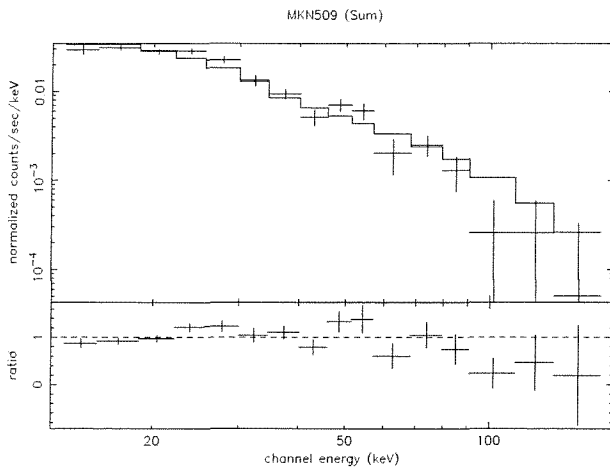
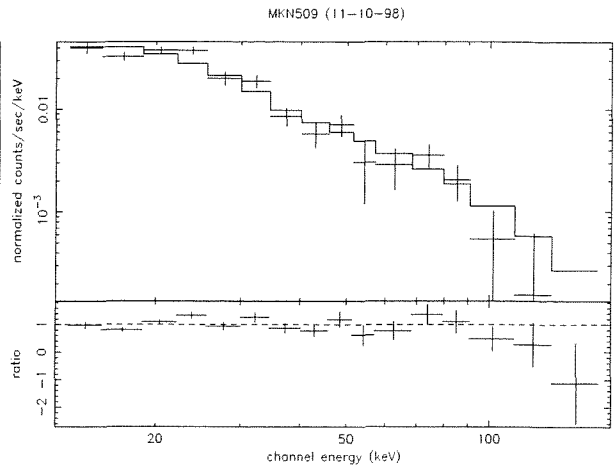
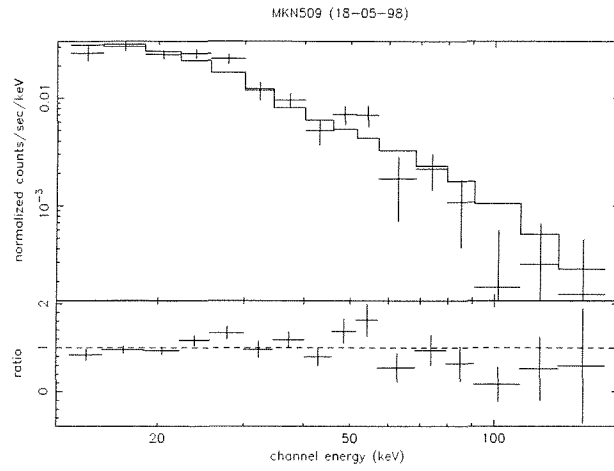


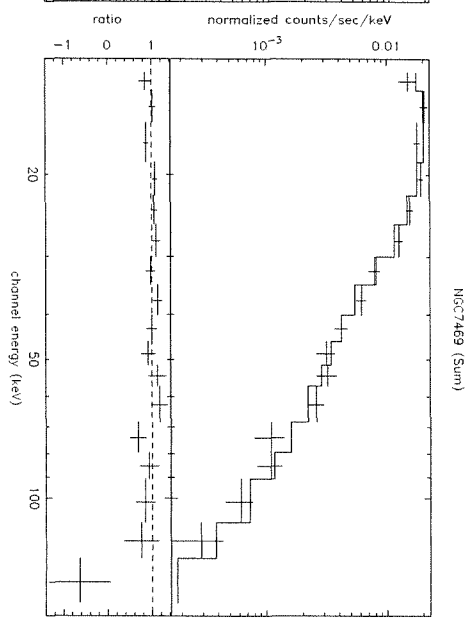
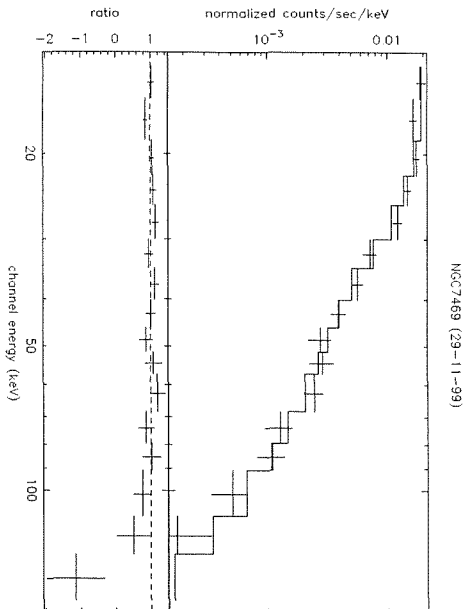
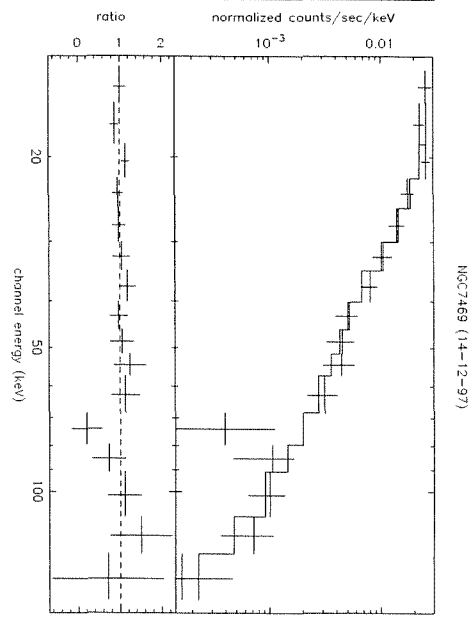
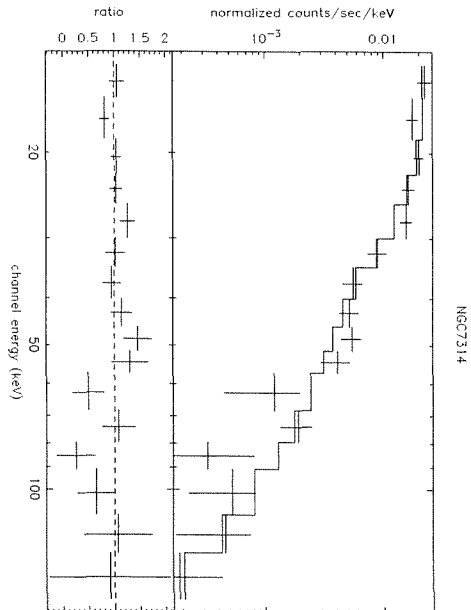
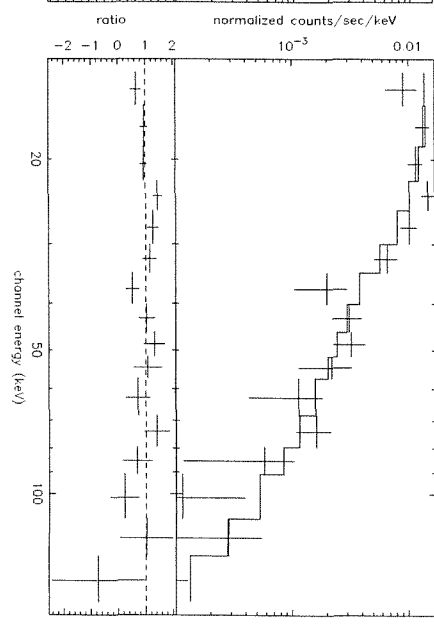
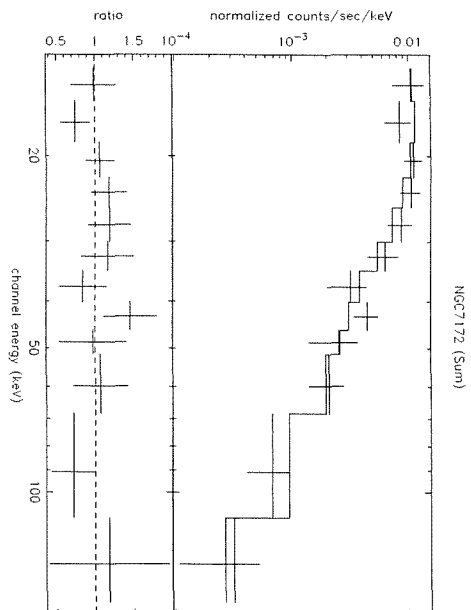


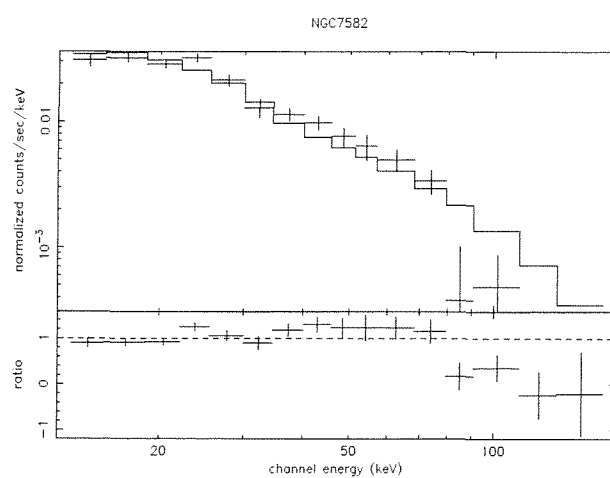












Bibliography

- [1] Anders, E., Ebihara, M. 1982, *Geochim. Cosmochim. Acta* 46, 2363
- [2] Anders, E., Grevesse, N. 1993, *Geochim. Cosmochim. Acta* 53, 197
- [3] Antonucci, R., and Miller, J. 1985, *ApJ*, 297, 621
- [4] Aschwanden, M. J., Schwartz, R. J, & Dennis, B. R. 1998, *ApJ*, 502, 468
- [5] Bassani, L., Dean, A. J., Di Cocco, G., and Perotti, F. 1985, *Proc. Manchester Conference on Active Galactic Nuclei*, 252
- [6] Bassani, L., Jourdain, E., Roques, J. P., Mandrou, P., Ballet, J., Cordier, B., et al. 1993, *A&AS*, 97, 89
- [7] Bassani, L., Malaguti, G., Jourdain, E., Roques, J. P., Johnson, W. N. 1995, *ApJ*, 444, L73
- [8] Bassani, L., Malaguti, G., Paciesas, W. S., Palumbo, G. G. C., Zhang, S. N. 1996, *A&AS*, 120, 559
- [9] Bassani, L., Cappi, M., Malaguti, G. 1999a, *Astr. Lett. and Communications*, Vol. 39, 41
- [10] Bassani, L., Cappi, M., Malaguti, G., Palumbo, G. G. C., Dadina, M., Comastri, A., et al. 1999b, *MmSAI*, 70, 65
- [11] Boella, G., Butler, R. C., Perola, G. C., Piro, L., Scarsi, L., Bleker, J. A. M. 1997a, *A&AS*, 122, 299
- [12] Boella, G., Chiappetti, L., Conti, G., Cusumano, G., Del Sordo, S., La Rosa, G., et al. 1997b, *A&AS*, 122, 327
- [13] Bowyer, C. S., et al. 1964, *Science*, 146, 912
- [14] Bowyer, C. S., Lampton, M., Mack, J., De Mendonca, F. 1970, *ApJ*, 161, L1

- [15] Brunner H., Lamer G., Worrall D. M., Staubert R., 1994, *A&A*, 287, 436
- [16] Campana, S., Stella, L., Mereghetti, S., Colpi, M., Tavani, M., Ricci, D. 1998, *ApJ*, 499, L65
- [17] Cappi, M., Mihara, T., Matsuoka, M., Hayashida, K., Weaver, K. A., Otani, C. 1996, *ApJ*, 458, 149
- [18] Cappi, M., Matsuoka M., Comastri A., Brinkmann W., Elvis M., Palumbo, G. G. C., Vignali C. 1997, *ApJ*, 478, 493
- [19] Cappi, M., Bassani, L., Comastri, A., Guainazzi, M., Maccacaro, T., Malaguti, G. et al. 1999a, *A&A*, 344, 857
- [20] Cappi, M., Bassani, L., Malaguti, G. 1999b, *Broad Band X-ray Spectra of Cosmic Sources*, Proceedings of the E1.1 Symposium of COSPAR, 815
- [21] Cappi, M., Persic M., Bassani L., Franceschini A., et al. 1999c, *A&A*, 350, 777
- [22] Catanese, M.; Bradbury, S. M.; Breslin, A. C.; Buckley, J. H.; Carter-Lewis, D. A.; Cawley, M. F.; et al. 1997, *ApJ*, 487, 143L
- [23] Chiappetti, L.; Maraschi, L.; Tavecchio, F.; Celotti, A.; Fossati, G.; Ghisellini, G.; et al. 1999, *ApJ*, 521, 552
- [24] Ciliegi, P., Bassani, L., Caroli, E. 1993, *ApJS*, 85, 111
- [25] Ciliegi, P., Bassani, L., Caroli, E. 1995, *ApJ*, 439, 80
- [26] Connaughton, V., Robinson C. R., McCollough M. L., and Laurent-Muehleisen S.A. 1998, in the Proc. of the meeting "BL Lac Phenomenon", Turku (Finland) 1998, Edited by L.O. Takalo & A. Sillanpaa, A.S.P. Conf. Ser. Vol. 159, p. 209
- [27] Costa, E., Frontera, F., Heise, J., Feroci, M., in 't Zand, J., Fiore, F., et al. 1997, *Nat.*, 387, 783
- [28] Costa E. 1998, *Nuclear Physics B (Proc. Suppl.)*, 69/1-3, 646
- [29] Costamante, L.; Ghisellini, G.; Giommi, P.; Tagliaferri, G.; Celotti, A.; Chiaberge, M.; et al. 2001, *A&A*, 371, 512
- [30] Costantini, E., Nicastro, F., Fruscione, A., Mathur, S., Comastri, A., Elvis, M., et al. 2000, *ApJ*, 544, 283

- [31] Courvoisier, T. J.-L., Turner, M. J. L., Robson, E. I., Gear, W. K., Staubert, R., Blecha, R., et al. 1987, A&A, 176, 197
- [32] Covino, S., Negueruela, I., Campana, S., Israel, G. L., Polcaro, V. F., Stella, L., Verrecchia, F. 2001, A&A, 374, 1009
- [33] Dadina, M.; Bassani, L.; Cappi, M.; Palumbo, G. G. C.; Piro, L.; Guainazzi, M.; Malaguti, G.; Di Cocco, G.; Trifoglio, M. 2001, A&A 370, 70
- [34] Dean, A. J., Bassani, L., Bird, A. J., Diallo, N., Lockley, J. J., Stephen, J. B., et al. 2001, submitted to MNRAS
- [35] Deans, S. R. 1983, The Radon Transform and Some of Its Applications (Wiley Press)
- [36] De Rosa, A., Piro, L., Nicastro, F., et al. 2001, in the Proc. of "X-Ray Astronomy '99", Bologna (Italy) 2000, Edited by N. E. White, G. Malaguti and G. G. C. Palumbo Vol. 599, p. 610
- [37] Done, C., Madejski, G. M., Smith, D. A. 1996, ApJ, 463, L63
- [38] Fabian, A. C. in the Proc. of "X-Ray Astronomy '99", Bologna (Italy) 2000, Edited by N. E. White, G. Malaguti and G. G. C. Palumbo Vol. 599, p. 93
- [39] Fairall, A. P., McHardy I. M., and Pye, J. P. 1982, MNRAS, 198, 13
- [40] Finger, M. H., Wilson, R. B., Harmon, B. A. 1996, ApJ, 459, 288
- [41] Fiore F., Guainazzi M., Grandi P. 1998, *BeppoSAX Cookbook*
- [42] Fiore, F., La Franca, F., Giommi, P., Elvis, M., Matt, G., Comastri, A., et al. 1999, MNRAS, 306, 55L
- [43] Fiore, F., Pellegrini, S., Matt, G., Antonelli, L. A., Comastri, A., Della Ceca, R., et al. 2001, ApJ, 556, 150
- [44] Fishman, G. J., Meegan, C. A., Wilson, R. B., Brock, M. N., Horack, J. M., Kouveliotou, C., et al. 1994, ApJS, 92, 229
- [45] Fossati, G., Maraschi, L., Celotti, A., Comastri, A., Ghisellini, G. 1998, MNRAS, 299, 433
- [46] Fossati, G., Celotti, A., Chiaberge, M., Zhang, Y. H., Chiappetti, L., Ghisellini, G., et al. 2000a, ApJ, 541, 153

- [47] Fossati, G., Celotti, A., Chiaberge, M., Zhang, Y. H., Chiappetti, L., Ghisellini, G., et al. 2000b, *ApJ*, 541, 166
- [48] Frontera F., Costa E., Dal Fiume D., et al. 1997 *A&AS*, 122, 357
- [49] George, I. M. and Fabian, A. C. 1991, *MNRASS* 249, 352
- [50] Ghisellini G., Maraschi, L. 1989, *ApJ*, 340, 181
- [51] Ghisellini G., Maraschi L., and Dondi L. 1996, *A&AS*, 120, 503
- [52] Ghisellini, G.; Celotti, A.; Fossati, G.; Maraschi, L.; Comastri, A. 1998, *MNRAS*, 301, 451
- [53] Ghisellini, G., Costamante, L., Tagliaferri, G., Maraschi, L., Celotti, A., Fossati, G., et al. 1999, *A&A*, 348, 63
- [54] Gilli, R., Maiolino, R., Marconi, A., Risaliti, G., Dadina, M., Weaver, K. A., Colbert, E. J. M. 2000, *A&A*, 355, 485
- [55] Giommi, P., Beuermann, K., Barr, P., Schwobe, A., Tagliaferri, G., and Thomas, H. C. 1989, *MNRAS*, 236, 375
- [56] Giommi, P., Barr, P., Garilli, B., Maccagni, D., and Pollock, A. M. T. 1990, *ApJ*, 356, 432
- [57] Giommi, P., Tagliaferri, G., Beuermann, K., Braduardi-Raymont, Brissenden, R., et al. 1991, *ApJ*, 378, 77
- [58] Giommi, P., Massaro, E., Chiappetti, L., Ferrara, E. C., Ghisellini, G., Jang, M., et al. 1999, *A&A*, 351, 59
- [59] Gondek, D.; Zdziarski, A. A.; Johnson, W. N.; George, I. M.; McNaron-Brown, K.; Magdziarz, P.; et al. 1996, *MNRAS*, 282, 646
- [60] Grandi, P., Palumbo, G. G. C., Tagliaferri, G., Giommi, P., Barr, P. 1992, *ApJS*, 82, 93
- [61] Grandi, P., 2000, in the *Proc. of "X-Ray Astronomy '99"*, Bologna (Italy) 2000, Edited by N. E. White, G. Malaguti and G. G. C. Palumbo Vol. 599, p. 130
- [62] Guainazzi, M., Mihara, T., Otani, C., Matsuoka, M. 1996, *PASJ*, 48, 781
- [63] Guainazzi, M., Matteuzzi, G. 1997, *SDC-TR-014*

- [64] Guainazzi, M., Nicastro, F., Fiore, F., Matt, G., McHardy, I., Orr, A., et al. 1998, MNRAS, 301, 1L
- [65] Guainazzi, M., Matt, G., Molendi, S., Orr, A., Fiore, F., Grandi, P., et al. 1999a, A&A, 341, 27L
- [66] Guainazzi, M., Perola, G. C., Matt, G., Nicastro, F., Bassani, L., Fiore, F., et al. 1999b, A&A, 346, 407
- [67] Guainazzi, M., Vacanti, G., Malizia, A., O’Flaherty, K. S., Palazzi, E., Parmar, A. N. 1999c, A&A, 242, 124
- [68] Guainazzi, M.; Marshall, W.; Parmar, A. N. 2001, MNRAS, 323, 75
- [69] Haardt, F.; Fossati, G.; Grandi, P.; Celotti, A.; Pian, E.; Ghisellini, G.; Malizia, A.; Maraschi, L.; et al. 1998, A&A, 340, 35
- [70] Hanson, C. G., Skinner, G. K., Eyles, C. J., Willmore, A. P. 1990, MNRAS, 242, 262
- [71] Harmon, B. A., Fishman, G. J., Wilson, C. A., Paciesas, W. S., Zhang, S. N., Finger, M. H., et al. 2001, ApJS, 138, 149
- [72] Huesman, R. H. et al. 1977, Donner Algorithms for Reconstruction Tomography, LBL Pub. 214, 42
- [73] Israel, G. L., Negueruela, I., Campana, S., Covino, S., Di Paola, A., Maxwell, D. H., et al. 2001, A&A, 371, 1018
- [74] Jager, R., Mels, W. A., Brinkman, A. C., Galama, M. Y., Goulooze, H., Heise, J., et al. 1997, A&AS, 125, 557
- [75] Johnson, W. N., et al. 1994, in The Second Symposium, ed. C. E. Fichtel et al. (New York: AIP) 515,
- [76] Johnson, W. N., Dermer, C. D., Kinzer, R. L., Kurfess, J. D.; Strickman, M. S., McNaron-Brown, K., et al. 1995, A&A, 445, 182
- [77] Johnson, W. N., McNaron-Brown, K., Kurfess, J. D., Zdziarski, A. A., Magdziarz, P., Gehrels, N. 1997, ApJ, 482, 173
- [78] Jourdain, E., Bassani, L., Bouchet, L., Mandrou, P., Ballet, J., Lebrun, F., et al. 1992, A&A, 256, 38L

- [79] Kinzer, R. L., Johnson, W. N., Dermer, C. D., Kurfess, J. D., Strickman, M. S., Grove, J. E., et al. 1995, *ApJ*, 449, 105
- [80] Kouveliotou, C., van Paradijs, J., Fishman, G. J., Briggs, M. S., Kommers, J., Harmon, B. A., et al. 1996, *Nat.*, 379, 799
- [81] Lamer, G. and Wagner, S. J. 1998, *A&A*, 331, L13
- [82] Landi, R.; Bassani, L.; Malaguti, G.; Cappi, M.; Comastri, A.; Dadina, M.; et al. 2001, *A&A*379, 46
- [83] Lawrence, A., Watson, M. G., Pounds, K. A., Elvis, M. 1987, *Nat.*, 325, 694
- [84] Levine, A. M., Lang, F. L., Lewin, W. H. G., Primini, F. A., Dobson, C. A., Doty, J. P., et al. 1984, *ApJS*, 54, 581
- [85] Lubinski, P. and Zdziarski, A. 2001, *MNRAS*, 323, L37
- [86] Magdziarz, P.; Zdziarski, A. 1995, *MNRAS*273, 837
- [87] Maiolino, R. and Rieke, G. H. 1995, *ApJ* 454, 95
- [88] Maiolino, R., Salvati, M., Bassani, L., Dadina, M., Della Ceca, R., Matt, G., et al. 1998, *A&A*, 338, 781
- [89] Maisack, M., Wood, K. S., Gruber, D. I. 1994, *A&A*, 284, 28
- [90] Malaguti, G.; Bassani, L.; Caroli, E. 1994, *ApJS*, 94, 517
- [91] Malaguti, G., Bassani, L., Cappi, M., Comastri, A., Di Cocco, G., Fabian, A. C., et al. 1999, *A&A* 342L, 41
- [92] Malizia, A., Bassani, L., Stephen, J. B., Malaguti, G., Palumbo, G. G. C. 1997, *ApJS*, 113, 311
- [93] Malizia, A., Bassani, L., Zhang, S. N., Dean, A. J., Paciesas, W. S., Palumbo, G. G. C. 1999, *ApJ*, 519, 637
- [94] Malizia, A., Bassani, L., Dean, A. J., McCollough, M., Stephen, J. B., Zhang, S. N., Paciesas, W. S. 2000a, *ApJ*, 531, 642
- [95] Malizia, A., Capalbi, M., Fiore, F., Giommi, P., Gandolfi, G., Tesseri, et al. 2000b, *MNRAS*, 312, 123
- [96] Malizia, A., Bassani, L.; Negueruela, I. 2000c, *A&A*, 359, 509

- [97] Mallozzi R. S. et al. 1993, AIP Conf. Proc. 280, 1122
- [98] Manzo G., Giarrusso S., Santangelo A., et al. 1997 A&AS, 122, 341
- [99] Marshall, F. E., Boldt, E. A., Mushotzky, R. F., Pravdo, S. H., Rothschild, R.E., and Serlemitsos, P. J. 1979, APJS, 40, 657
- [100] Matsuoka, M., Piro, L., Yamauchi, M., Murakami, T. 1990, ApJ, 361, 440
- [101] Matt, M., Pompilio, F., La Frenca, F., 1999, New Astronomy, Vol. 4, 191
- [102] Matt, G. 2000a, in the Proc. of "X-Ray Astronomy '99", Bologna (Italy) 2000, Edited by N. E. White, G. Malaguti and G. G. C. Palumbo Vol. 599, p. 209
- [103] Matt, G. , Fabian, A. C., Guainazzi, M., Iwasawa, K., Bassani, L., Malaguti, G. 2000b, MNRAS, 318, 173
- [104] Matt, G., Guainazzi, M., Perola, G. C., Fiore, F., Nicastro, F., Cappi, M., Piro, L. 2001, A&A, 377L, 31
- [105] Matt, G., Perola, G. C., Fiore, F.; Guainazzi, M., Nicastro, F., Piro, L. 2000c, A&A, 363, 863
- [106] McNaron-Brown, K., Johnson, W. N., Jung, G. V., Kinzer, R. L., Kurfess, J. D., Strickman, M. S., et. al. 1995, ApJ, 451, 575
- [107] McNaron-Brown, K., Johnson, W. N., Dermer, C. D., Kurfess, J. D. 1997, ApJ, 474, 85L
- [108] Meegan, C. A., Fishman, G. J., Wilson, R. B., Horack, J. M., Brock, M. N., Paciesas, W. S., et al. 1993, Nat. 355, 143
- [109] Miyaji, T., and Boldt, E. 1990, ApJ, 253, 3L
- [110] Much, R., Harmon, B. A., Nolan, P., Strickman, M. S., Bennett, K., Buccheri, R., et al. A&AS, 120, 703
- [111] Mukherjee R., Bertsch D. L., Bloom S. D., et al. 1997, ApJ, 490, 116
- [112] Nandra, K.; Pounds, K. A. 1994, MNRAS, 268, 405
- [113] Nandra, K.; George, I. M.; Mushotzky, R. F.; Turner, T. J.; Yaqoob, T. 1997, ApJ, 477, 602

- [114] Nicastro, F., Piro, L., De Rosa, A., Feroci, M., Grandi, P., Fiore, F., et al. 2000, ApJ, 536, 718
- [115] Padovani, P., Morganti, R., Siebert, J., Vagnetti, F., Cimatti, A. 1999, MNRAS, 304, 829
- [116] Parmar, A. N., Martin, D. D. E., Bavdaz, M., Favata, F., Kuulkers, E., Vacanti, G., et al. 1997, A&AS, 122, 309
- [117] Parsons, A. M., Gehrels, N., Paciesas, W. S., Harmon, B. A.; Fishman, G. J., Wilson, C. A., Zhang, S. N. 1998, ApJ, 501, 608
- [118] Pellegrini, S., Cappi, M., Bassani, L., Malaguti, G., Palumbo, G. G. C., Persic, M. 2000, A&A, 353, 447
- [119] Perola, G. C.; Matt, G.; Cappi, M.; Dal Fiume, D.; Fiore, F.; Guainazzi, M.; Mineo, T.; Molendi, S.; Nicastro, F.; Piro, L.; Stirpe, G. 1999, A&A, 351, 937
- [120] Perola, G. C.; Matt, G.; Fiore, F.; Grandi, P.; Guainazzi, M.; Haardt, F.; Maraschi, L.; Mineo, T.; Nicastro, F.; Piro, L. 2000 A&A, 358, 117
- [121] Perola, G. C., Matt, G., Cappi, M., Fiore, F., Guainazzi, M., Maraschi, L. et al. 2001, A&A, *submitted*
- [122] Petry, D., Bottcher, M., Connaughton, V., Lahteenmaki, A., Pursimo, T., Raiteri, C. M. et al. 2000, ApJ, 536, 755
- [123] Pian, E., Vacanti, G., Tagliaferri, G., Ghisellini, G., Maraschi, L., Treves, A., et al. 1998, ApJ, 492, L17
- [124] Piccinotti, G., Mushotzky, R. F., Boldt, E. A., Holt, S. S., Marshall, F. E., Serlemitsos, P. J., and Shafer, R. A. 1982, ApJ, 253, 485
- [125] Padovani, P., Giommi, P. 1995, ApJ, 444, 567
- [126] Padovani, P., Giommi, P. 1996, MNRAS, 279, 526
- [127] Piro, L. et al. 2001 *submitted*
- [128] Pian E., Vacanti, G., Tagliaferri G., et al., 1998 ApJ 492, L17
- [129] Polletta, M., Bassani, L., Malaguti, G., Palumbo, G. G. C., Caroli, E. 1996, APJS, 399

- [130] Pounds, K. A. 1990, MNRAS, 242, 20
- [131] Raiteri C. M., Ghisellini G., Villata M., De Francesco G., Lanteri L., Chiaberge M., et al. 1998, A&AS, 127, 445
- [132] Ramos, E., Kafatos, M., Fruscione, A., Bruhweiler, F. C., McHardy, I. M., Hartman, R. C., et al. 1997, ApJ, 482, 167
- [133] Rees, M., 1984, ARA&A, 22, 471
- [134] Risaliti, G.; Maiolino, R.; Salvati, M. 1999, ApJ, 522, 157
- [135] Rothschild, R. E., Mushotzky, R. F., Baity, W. A., Gruber, D. E., Matteson, J. L., and Peterson, L. E. 1983, ApJ, 269, 423
- [136] Rubin, B. C., Finger, M. H., Harmon, B. A., Paciesas, W. S., Fishman, G. J., Wilson, R. B., et al. 1996, ApJ, 459, 259
- [137] Sambruna, R. M., George, I. M., Mushotzky, R. F., Nandra, K., Turner, T. J. 1998, ApJ, 495, 749
- [138] Schartel, N., Schmidt, M., Fink, H. H., Hasinger, G., and Trumper, J. 1997, A&A, 495, 749
- [139] Shaw, S. E., Bird, A. J., Dean, A. J., Diallo, N., Ferguson, C., Knodlseder, J., et al. 2000, for publication in Proceedings of the 4th Integral Workshop, Alicante, Spain.
- [140] Tagliaferri, G., Angelini, L., Osborne, J. P. 1988, ApJ, 331, 113
- [141] Tagliaferri, G., Ghisellini, G., Giommi, P., Chiappetti, L., Maraschi, L., Celotti, A., et al. 2000, A&A, 354, 431
- [142] Takahashi T., Tashiro M., Madejeski G., et al. 1996, ApJ 470, 89
- [143] Takahashi T., Inoue, H., Dotani, T. 2001 submitted to PASJ
- [144] Tavecchio, F., Maraschi, L., Ghisellini, G., Celotti, A., Chiappetti, L., Comastri, A., et al. 2000, ApJ, 543, 535
- [145] Thompson D. J., Bertsch D. L., Dingus B. L. et al., 1993, ApJ, 415, 13L
- [146] Turner, T. J., and Pounds, K. A. 1989, MNRAS, 240, 833
- [147] Turner, T. J., Netzer, H., George I. M. 1996, ApJ, 463, 134

- [148] Turner, T. J., Perola, G. C., Fiore, F., Matt, G., George, I. M., Piro, L., Bassani, L. 2000, *ApJ*, 531, 245
- [149] Urry, C. M., Padovani, P. 1995, *PASP*, 107, 803
- [150] Uttley, P., McHardy, I. M., Papadakis, I. E., Cagnoni, I., Fruscione, A. 1998, *Nuclear Physics B (Proc. Suppl.)*, 69/1-3, 490
- [151] Vignali, C., Comastri, A., Stirpe, G. M., Cappi, M., Palumbo, G. G. C., et al. 1998, *ApJ* 333, 411
- [152] von Linde J., Borgeest U., Schramm K. J., Graser U., Heidt J., Hopp U., et al. 1993, *A&A*, 267L, 23
- [153] von Montigny, C., Aller, H., Aller, M., Bruhweiler, F., Collmar, W., Courvoisier, T. J.-L., et al. 1997, *ApJ*, 483, 161
- [154] Weaver, K. A., Nousek, J., Yaqoob, T., Mushotzky, R. F., Makino, F., Otani, C. 1996, *ApJ*, 457, 616
- [155] Weaver, K. A., Heckman, T. M., Dahlem, M. 2000, *ApJ* 534, 684
- [156] Westmore, M. J., Dean, A. J., Bassani, L., Bird, A. J., Diallo, N., Lockley, J. J., et al. 2000a, for publication in *Proceedings of the 4th Integral Workshop*, Alicante, Spain.
- [157] Westmore, M. J., Dean, A. J., Bassani, L., Bird, A. J., Diallo, N., Lockley, J. J., et al. 2000b, for publication in *Proceedings of the 4th Integral Workshop*, Alicante, Spain.
- [158] Westmore, M. J., Bassani, L., Bird, A. J., Dean, A. J., Diallo, N., Ferguson, C., et al. 2001, submitted to *MNRAS*
- [159] Wilkes, B. J., Mathur, S., Fiore, F., Antonelli, A., Nicastro, F. 2001, *ApJ*, 557, 492
- [160] Winkler C. 1996, *A&AS*, 120, 637
- [161] Wolter, A., Comastri, A., Ghisellini, G., Giommi, P., Guainazzi, M., Maccacaro, T., et al. 1998, *A&A*, 335, 899
- [162] Woods, P. M., Kouveliotou, C., van Paradijs, J., Briggs, M. S., Hurley, K., Gogus, E., et al. 1999, *ApJ*, 527, 47L
- [163] Zhang, S. N., Fishman, G. J., Harmon, B. A., Paciesas, W. S. 1993, *Nat.*, 366, 245

- [164] Zdziarski, A., Johnson, W. N., Done, C., Smith D., McNaron-Brown K. 1995, ApJ, 438, 63L
- [165] Zdziarski, A. A.; Lubinski, P.; Smith, D. A. 1999, MNRAS, 303, L11
- [166] Zdziarski, A. A., Poutanen, J., Johnson, W. N. 2000, ApJ, 542, 703
- [167] Zdziarski, A. A., Grandi, P. 2001, ApJ, 551, 186
- [168] Zdziarski, A. A., Leighly, K. M., Matsuoka, M., Cappi, M., Mihara, T. 2001, ApJL
submitted